Controlling crystallisation and the effect of interfaeial curvature

Jamieson, Matthew James

Controlling Crystallisation and the Effect of Interfacial Curvature

Matthew James Jamieson

A thesis submitted for the degree of Doctor of Philosophy at the University of Durham

2004

Table of Contents

Chapter 2. Crystallisation of DL-Aspartic Acid Under Nylon 6 Spread Films

Chapter 3. Monolayer Induced Crystallisation of Calcium Carbonate

Chapter 4. Ice Crystallisation in Oil-in-Water Emulsions

Controlling Crystallisation and the Effect of Interfacial Curvature

PhD Thesis

Matthew James Jamieson

Abstract

Crystallisation induced at the air-water planar interface and oil-water interface in emulsions is explored. DL-Aspartic acid crystallisation under nylon 6 spread films is studied by neutron reflectivity and ER-FTIR, and shows that the resulting crystallisation occurs within, rather than underneath the spread film layer. It is shown that 50% of the nylon 6 surface layer is composed of DL-aspartic acid, despite only 1-5% being visible to the naked eye. This is attributed to sub-visible crystalline nuclei embedded in the nylon 6 film layer, whose growth to visible dimensions is impeded by the surrounding nylon 6 film.

Calcium carbonate crystallisation induced by octadecanoic acid monolayers at moderate surface pressure is studied by GIXD and ER-FTIR and shows a tilting of the monolayer hydrocarbon chain towards the surface normal as crystallisation progresses. Addition of polyacrylic acid to the subphase results in formation of an amorphous calcium carbonate film under the monolayer, with no corresponding tilt of the monolayer hydrocarbon chain observed.

The crystallisation of ice induced by 1-heptacosanol at the oil-in-water (o/w) interface in emulsions is studied and shows that a high curvature interface is a less effective ice nucleator than the low curvature systems. A much better ice nucleating ability is even observed when the interfacial density of 1-heptacosanol is significantly less for the low curvature systems. This is attributed to the larger critical nucleus required for crystallisation induced at a high curvature interface and a poorer ability of the 1-heptacosanol to pack in a way that favours ice nucleation.

Glycine crystallisation in emulsions is shown for o/w and water-in oil (w/o) cases. Crystallisation in the o/w samples using Span surfactants typically show β-phase spherical crystal aggregates, whereas the o/w show β-phase crystals with elongated morphology. Systems prepared at the phase inversion boundary typically showed a poorer nucleating ability than analogous w/o and o/w emulsion systems. The use of water-soluble additives failed to alter the glycine polymorph, but use of octanoic acid did promote α glycine crystallisation and an unusual honeycomb structure due to the aggregation of octanoic acid attracted to the glycine crystals.

Acknowledgements

I owe a huge debt of gratitude towards my supervisor, Dr. Sharon Cooper. Without her support and patience, the work presented in this thesis would not have been possible. In particular, I thank Sharon for remaining available during her current period of maternity leave, when she was in no way obliged to remain so helpful.

Mr W. Doug Carswell is thanked for DSC support. Doug analysed in excess of 500 samples and showed a lot of interest in the ice crystallisation work. Mr Stuart Eggleston is also thanked for in-house X-ray and E-SEM support, often at very short notice.

Dr. Aline Miller is thanked for the deuterated nylon synthesis and for checking some of the initial neutron reflectivity model fitting. I also thank Prof. Randal Richards for his ideas and use of his neutron reflectivity programme, LAYERS. Thanks also to Dr. Stephen Holt and Dr. Graham Clark at the ISIS and Daresbury facilities respectively, and Dr. Matt Smith for helping with experiments on one of the Daresbury visits.

Finally I thank my brother Daniel and my sister and brother-in-law, Louise and Ben Whatling, for proof-reading the final document.

Memorandum

The work reported in this thesis was carried out at the Department of Chemistry at the University of Durham between October 2001 and August 2004. The work has not been submitted for any other degree and is the original work of the author except where acknowledged by an appropriate reference.

Financial Support

I gratefully acknowledge EPSRC funding for all work detailed in this thesis.

Chapter 1

General Background

This thesis describes a series of experiments aimed at inducing and controlling crystallisation by using surfactants. This chapter presents a general overview of background material relevant to the results (chapters 2 to 5) presented later. Each results chapter begins with more specific background material relevant to that particular section.

1.1 Crystallisation

1.1.1 Introduction to Crystallisation

The ordered manner in which atoms, ions or molecules come together to form a crystalline 3d array is of fundamental importance to scientists. Controlled crystallisation is critical in chemical industries for catalysts[1-3], polymers[4,5] and pharmaceuticals[6-10] among others[11-13].

A better knowledge of crystallisation processes is highly desirable. This will better enable the scientist to develop an optimal product. This might be through the control of crystal particle size, polymorph (section 1.1.5) or crystal habit. Equally this helps the scientist to understand how crystallisation can be inhibited, in cases such as oil pipeline mineralisation and scaling of domestic appliances, etc.

Biological systems exert impressive control over the crystallisation of inorganic species, which is termed biomineralisation (see section 3.1.1). These include calcium carbonate (shells[14-16]), magnetite (teeth enamel[17] & brain[18]) and apatite (bones[19,20]). Many of these are formed as composites[21-23], which allows exceptional mechanical properties.

Biological systems also exert excellent inhibitory qualities, such as the ability to prevent urinary and kidney stones[24,25].

The exceptional ability of biological systems to crystallise materials with such specificity has caused huge numbers of scientists to study these mechanisms extensively. Once these are understood, scientists will be better able to design novel strategies for the crystallisation of synthetic species with exceptional properties.

Emulsion crystallisation is increasingly of interest to crystal engineers. The crystallisation of glycine[26-28], calcium carbonate[29-31], fats[32-35] and other materials[36-39] in emulsions have been reported in recent years. Emulsions can give crystals of well defined size/morphology, and potentially allow better polymorph control by limiting the influence of non-specific nucleators such as foreign particulates or vessel surfaces[26].

1.1.2 Driving Forces in Crystallisation

First consider the phase diagram of a single component system in pressure-temperature coordinates (figure 1.1). Two phases are in equilibrium along each of the lines, and three phases are simultaneously in equilibrium at the triple point, labelled O.

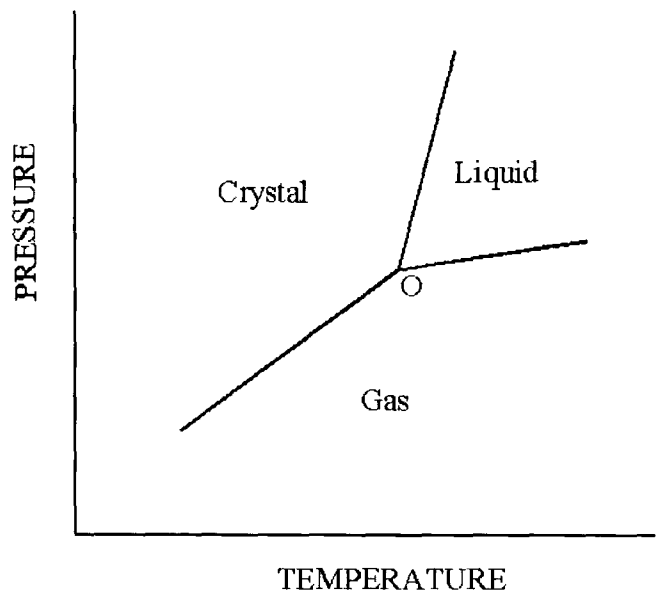

Figure 1.1. Pressure versus temperature phase diagram for a single component system.

The crystal phase is thermodynamically favoured at low temperature and high pressures, whereas the gas phase is stable at high temperature and low pressure. Applying pressure to a system with 2 phases at equilibrium, i.e. along one of the lines, will make the gas or liquid unstable with respect to the infinitely large crystal. The difference between the chemical potentials of the gas/liquid and the crystal is known as the supersaturation, $\Delta\mu$. The supersaturation is the driving force for the phase transition, i.e., a measure of whether crystallisation will occur.

1.1.3 Supersaturation

Figure 1.2 represents the chemical potential versus pressure for the vapour/crystal equilibrium line presented in figure 1.1. p_o represents the equilibrium pressure at point X. Changes in chemical potential with pressure for the vapour phase follow a logarithmic relationship, while the chemical potential of the crystal phase is related linearly to pressure, p, and the molecular volume, v_c.

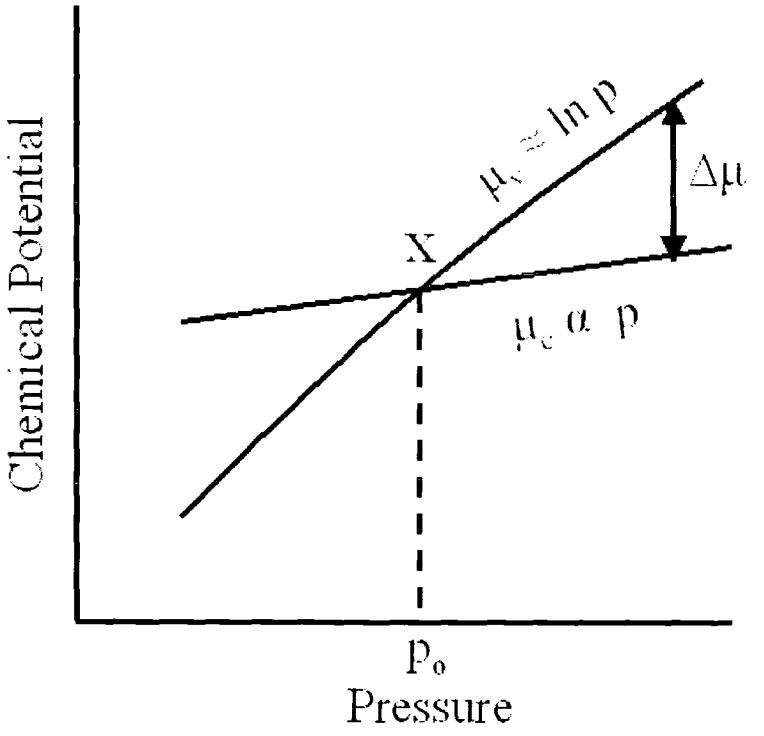

Figure 1.2. Illustration of the dependence of chemical potential on pressure for the vapour/crystal equilibrium line illustrated in figure 1.1.

The difference in chemical potentials, i.e. the supersaturation, $\Delta\mu$, is calculated from:

$$\Delta\mu = k_B T \ln \frac{p}{p_O} \qquad \text{[Eqn. 1.1]}$$

where p is the actual pressure, and p_o is the equilibrium pressure of the infinitely large crystal at any given temperature, T. Similarly, for crystallisation from solutions:

$$\Delta\mu = k_B T \ln \frac{s}{s_{sat}} \qquad \text{[Eqn. 1.2]}$$

where s is the actual concentration, and s_{sat} is the saturation concentration of solute, respectively.

Figure 1.3 shows an equivalent diagram of chemical potential versus temperature for the liquid/crystal equilibrium boundary. Clearly for this case, the two phase equilibrium point at atmospheric pressure is the melting temperature, T_m.

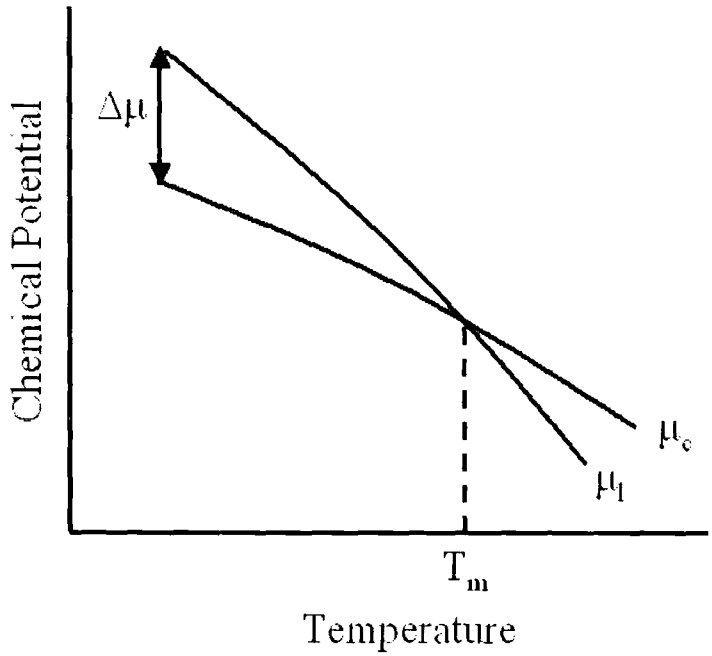

Figure 1.3. An illustration of the change in chemical potential with temperature along the liquid/crystal equilibrium line in figure 1.1.

The supersaturation for this case is:

$$\Delta\mu = \frac{\Delta H_m}{T_m}\Delta T \qquad \text{[Eqn. 1.3]}$$

where ΔH_m is the enthalpy of melting and ΔT represents the change in temperature, $T_m - T$.

In practical terms for the work presented in this thesis, the percentage supersaturation, $\mu\%$, is more useful and is defined as:

$$\mu\% = \frac{s - s_{sat}}{s_{sat}} \times 100\% \qquad \text{[Eqn. 1.4]}$$

1.1.4 Equilibrium of Finite Phases

The previous section dealt with infinitely large phases. This is clearly of limited relevance at the beginning of a crystallisation process, which begins with tiny crystalline nuclei. The cases where the interfaces are not planar must therefore be considered, and the effect of size on the thermodynamic equilibrium.

LaPlace Pressure

Consider the pressure impinging on a curved interface. The pressure on the concave side of an interface will always be greater than the pressure at the convex side. This is related by the LaPlace equation:

$$p_l - p_v = \frac{2\gamma}{r} \qquad \text{[Eqn. 1.5]}$$

where γ is the surface tension of the infinitely large liquid phase, r is the droplet radius and p_l and p_v are the pressures of the liquid and vapour phases, respectively. When the boundary is flat, i.e. $r \rightarrow \infty$, $p_l = p_v$.

The overall external force exerted on the droplet is $4\pi r^2 p_v$ from the vapour phase and $8\pi r\gamma$ due to the surface tension. This equals the force due to internal pressure, $4\pi r^2 \gamma p_l$

Thus the LaPlace pressure, $p_L = p_l - p_v$, is due to the surface tension of the small droplet.

So for an arbitrary surface described by orthogonal radii r_1 and r_2:

$$p_l - p_v = \gamma\left(\frac{1}{r_1} - \frac{1}{r_2}\right) \qquad \text{[Eqn. 1.6]}$$

Gibbs-Thomson Equation

Consider the transfer of molecules from a liquid to a finite solid phase. At equilibrium:

$$\Delta G = \mu_v dn_v + \mu_l dn_l + \gamma dS = 0 \qquad \text{[Eqn. 1.7]}$$

where n_v and n_l are the number of moles of molecules in the vapour and liquid phases, respectively, and γS is a surface energy term with S equal to the surface area. ΔG is the Gibbs free energy of the phase transition and μ_l and μ_v are the chemical potentials of the liquid and vapour phases respectively.

Assuming the system is closed, then $n_v + n_l$ is constant and $dn_v + dn_l = 0$. Hence:

$$\Delta\mu = \gamma \frac{dS}{dn_l} \qquad \text{[Eqn. 1.8]}$$

Substituting for $n_l = 4\pi r^3/3v_c$, where v_c is the molecular volume, then the Gibbs-Thomson equation is derived:

$$\Delta\mu = \frac{2\gamma v_c}{r} \qquad \text{[Eqn. 1.9]}$$

1.1.5 Polymorphism

Definition of Polymorphism

McCrone[40] described polymorphism as "a solid crystalline phase of a given compound resulting from the possibility of at least two crystalline arrangements of the molecules of that compound in the solid state". More simply, polymorphism is the ability of a compound to exhibit more than one crystal structure. For differences in crystal structure of pure elements, the term allotropy is preferred. Polymorphism was defined in the 19th century by Mitscherlich, and the first organic example, benzamide, was identified in 1832. It can affect even the simplest compounds, such as HgI_2 and glycine, which display two and three polymorphs, respectively. More complex molecules, such as pharmaceuticals can have many more polymorphs[41,42].

In chemical industries, the demand for high yield production means processes are often operated far from equilibrium. This can cause products to crystallise in a metastable or less stable form, which can transform to more stable crystal forms with time. Finding the most suitable solid form is a major part of the research effort, especially in the pharmaceutical industry.

Computational Prediction of Crystal Structures and Polymorphism

Computational predictions of crystal structure and polymorphism have been undertaken, but are a long way from being useful[43,44]. There are many commercial programmes available, including CRYSCA, DMAREL, MOLPAK, MPA, PROMET and UPACK. Most of these are iterative and based on lattice energy minimisations, but MOLPAK and PROMET proceed by determining high density packing or changing the crystal structure until common symmetry operators in organic crystal chemistry are found.

Random tests of molecules in the Cambridge Structural Database show that many of the programmes listed above identify one stable polymorph, but are not yet sophisticated enough to identify all polymorphs of compounds with many thermodynamically favoured crystal structures. More recently, it has been shown that crude thermodynamic

approaches appear to overestimate the propensity of a compound to polymorphism, which might be improved by incorporating kinetic factors[45].

Structure-Property Relationships

The crystal structure of a compound significantly affects its physical properties. Calcium carbonate shows three anhydrous polymorphs (see chapter 3), which display very different solubilities and crystal morphologies. In the pharmaceutical industry, the polymorph of the active ingredient is critical to the marketability of the product. Different polymorphs offer different stabilities (and solubilities), which affect the shelf life and bio-availability to the patient[46].

At a very simple level, the inorganic compound HgI_2 can exist as an orthorhombic or tetragonal structure. The orthorhombic structure is yellow and the tetragonal, red. Even long chain hydrocarbons can display polymorphism, which significantly affects the physical properties[47].

Polymorph Control

Of fundamental importance in understanding crystallisation of polymorphs is an appreciation of the combined kinetic and structural factors that control the appearance of available polymorphic forms[48]. Acidifying the solvent (see introduction to chapter 5) or seeding can induce growth of the desired form. Well-organised monolayers of surfactant can also induce growth of a specific polymorph (see chapter 3). Mann et al. showed that an ordered monolayer of octadecanoic acid will induce vaterite formation at low supersaturation, whereas calcite will form under the same monolayer at higher supersaturation[49]. Clearly if a choice of polymorphs is possible for a compound, only those that are supersaturated will crystallise.

Kinetic control of polymorphism is equally valid. DiMasi et al[50] controversially proposed that kinetics were responsible for the growth of different polymorphs of calcium carbonate under monolayers of octadecanoic acid, despite extensive evidence that other factors are relevant (see chapter 3). Others have shown kinetic factors can affect the crystal structure of semi-crystalline polymers, such as polypropylene[51].

Inhibiting polymorphic change is equally important. Sjolin[52] showed that ammonium nitrate cakes on polymorph transformation. In this case, the kinetics of the polymorph transformation depend on the crystal size[53].

Ostwald's Rule of Stages

Ostwald proposed that a crystallising system progresses from the supersaturated state to equilibrium in stages, with each stage representing the smallest possible change in free energy. This means that a crystal of the most stable polymorph would have moved through each of the less stable possible crystal structures before finally reaching equilibrium.

This concept was observed and reported extensively in german scientific literature between 1870 and 1914[54]. This is long before the development of nucleation theory and is still useful as Ostwald's rule is typically obeyed, but exceptions do occur.

1.2 Classical Nucleation Theory

1.2.1 Classical Homogeneous Nucleation Theory

Volmer and Weber[128] first presented classical nucleation theory. This theory is presented in sections 1.2.1 and 1.2.2, based on textbooks by Markov[129] and Davey and Garside[130].

By definition, homogeneous nucleation occurs in the absence of a foreign substrate, so a new phase must form from a parent phase. This requires the creation of an interface between the two phases. The creation of this interface requires an amount of work related to the interfacial tension of the interface, and so for crystallisation to occur, an energy barrier must be exceeded. The size of this barrier can be found as follows.

The free energy of formation, ΔG, for a cluster containing i monomer units, is

$$\Delta G_i = -i(\Delta\mu) + \sum_n \gamma_n A_n \qquad \text{[Eqn. 1.10]}$$

where $\Sigma\gamma_n A_n$ is the interfacial energy.

For a spherical cluster of radius r, this is represented as:

$$\Delta G_i = -\frac{4\pi r^3}{3v_c}(\Delta\mu) + 4\pi r^2\gamma \qquad \text{[Eqn. 1.11]}$$

Plotting ΔG_i versus r shows a maximum at $r = r^*$, (figure 1.4) which is the radius of the critical nucleus. This shows that only aggregates of a certain size, termed critical nuclei, will be stable and tend to grow into the condensed phase. Thus crystallisation can be considered a two-phase process, involving formation of critical nuclei followed by crystal growth on these nuclei up to macroscopic dimensions.

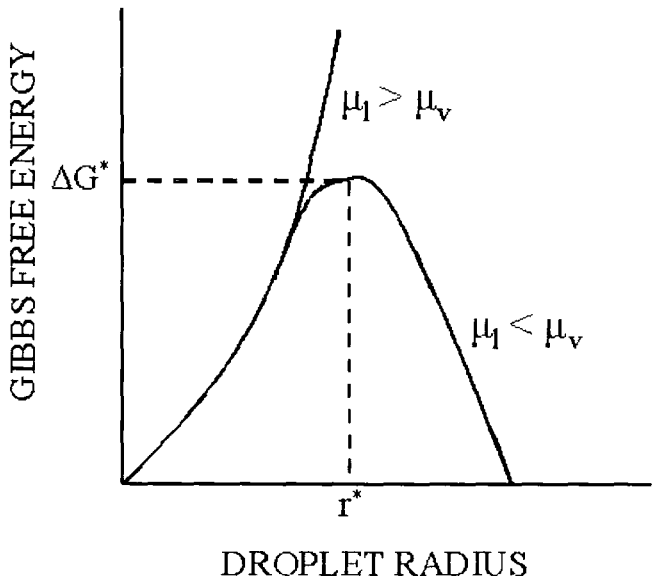

Figure 1.4 Illustration of Gibbs free energy required for formation of a critical nucleus, of radius r^*.

By differentiating ΔG_i with respect to r and equating to zero for this maximum condition, we find:

$$\frac{d\Delta G_i}{dr} = -\frac{4\pi r^2}{v_c}(\Delta\mu) + 8\pi r\gamma \qquad \text{[Eqn. 1.12]}$$

this gives $r^* = \frac{2\gamma v_c}{\Delta\mu}$ i.e. the Gibbs-Thomson equation [Eqn. 1.9]

Substituting the Gibbs-Thomson equation into equation 1.11 gives the magnitude of the energy barrier, i.e. the Gibbs free energy, ΔG^*, for formation of the critical nucleus:

$$\Delta G^* = \frac{16\pi\gamma^3 v_c^2}{3\Delta\mu^2} \qquad \text{[Eqn. 1.13]}$$

The rate of nucleation, J, is considered as a two stage process:

1) The formation of a near equilibrium concentration of critical nuclei, $n(i^*)$
2) The impingement at a rate W^* of the condensable species on the critical nuclei to eventually form bulk condensate.

Hence:

$$J = W^* n(i^*) \qquad \text{[Eqn. 1.14]}$$

where $n(i^*)$ is:

$$n(i^*) = n\exp\left[\frac{-\Delta G^*}{k_B T}\right] \qquad \text{[Eqn. 1.15]}$$

and n is the concentration of crystallising species.

Overall, the nucleation rate, J, is represented by:

$$J = \Omega\exp\left[-\frac{\Delta G^*}{k_B T}\right] \qquad \text{[Eqn. 1.16]}$$

The pre-exponential factor, Ω varies little with supersaturation, Δμ, hence it can often be treated as a constant. Typically Ω is considered in the range $10^{25} - 10^{35}$ $cm^{-3}s^{-1}$ for the case of homogeneous nucleation from aqueous solution. The form of equation 1.16 is such that J remains negligibly small until the supersaturation reaches a critical limit known as the Ostwald metastable limit (section 1.2.3).

1.2.2 Heterogeneous Nucleation and Cap-Shaped Nuclei

Heterogeneous nucleation typically proceeds at a significantly greater rate than the homogeneous case and occurs when the crystallising species adsorbs on a foreign substrate.

This is illustrated in figure 1.5, where r is the radius of the nucleus and γ represents the surface tension. Subscripts v, x and s refer to the vapour, nucleus and substrate respectively. θ is the contact angle, which is calculated from the Young's Equation:

$$\cos\theta = \frac{\gamma_{sv} - \gamma_{sx}}{\gamma_{vx}} \qquad \text{[Eqn. 1.17]}$$

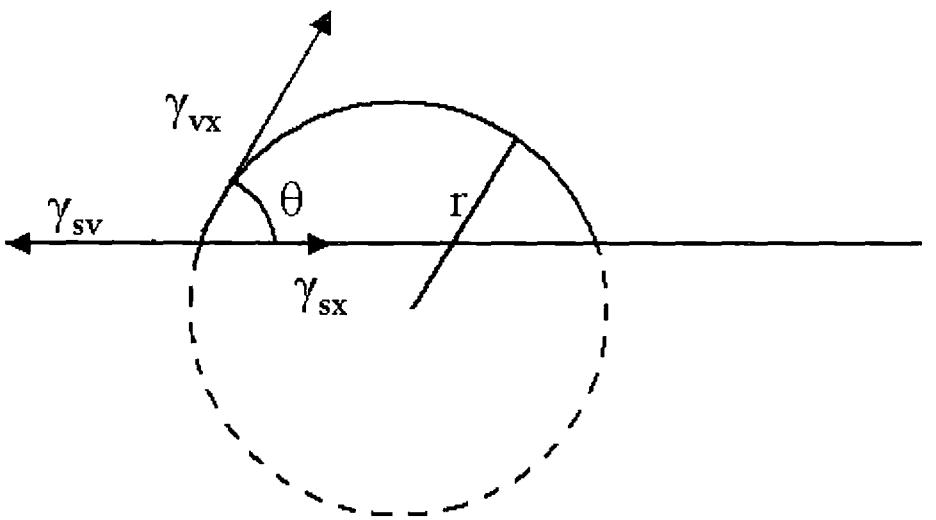

Figure 1.5. Illustration of a cap shaped nucleus on a planar heterogeneous substrate.

r^* and ΔG^* are determined in the same manner as for homogeneous nucleation, where the cluster is considered as a bulk crystal and terms are included to account for its surface, i.e.:

$$\Delta G_i = -\frac{4}{3v_c}\pi r^3 \Delta\mu\left(\frac{2-3\cos\theta+\cos^3\theta}{4}\right)$$

$$+4\left(\frac{1-\cos\theta}{2}\right)\pi r^2\gamma_{vx}+\pi r^2\sin^2\theta(\gamma_{sx}-\gamma_{sv}) \qquad \text{[Eqn. 1.18]}$$

substituting for $\gamma_{sx} - \gamma_{sv}$ from the Young's equation [1.17] gives:

$$\Delta G_i = -\frac{4\pi r^3\Delta\mu}{3v_c}f(\theta)+4f(\theta)\pi r^2\gamma_{vx} \qquad \text{[Eqn. 1.19]}$$

where $$f(\theta)=\frac{2-3\cos\theta+\cos^3\theta}{4} \qquad \text{[Eqn. 1.20]}$$

Maximising ΔG_i with respect to r gives:

$$r^* = \frac{2\gamma_{vx}v_c}{\Delta\mu} \quad \text{(the Gibbs-Thomson equation)} \qquad \text{[Eqn. 1.9]}$$

or incorporating temperature [from Eqn 1.3]:

$$r^* = \frac{2\gamma_{vx}v_cT_m}{\Delta H_m(T_m-T)} \qquad \text{[Eqn. 1.21]}$$

and

$$\Delta G^*_{Het} = \frac{16\pi\gamma_{vx}^3v_c^2}{3\Delta\mu^2}f(\theta) = \frac{\sum_n A_n\gamma_n}{3} = \Delta G^*_{Hom}\frac{V^*_{Het}}{V^*_{Hom}} \qquad \text{[Eqn. 1.22]}$$

where V^*_{Het} and V^*_{Hom} are the volumes of the critical nuclei for the heterogeneous and homogeneous nucleation cases, respectively.

For the case where $\theta = 180°$, the homogeneous value of ΔG^* is obtained. When $\theta = 0°$, complete wetting occurs and no nucleation barrier is predicted. However, in this case, a 2d monolayer disc is predicted (figure 1.6), and so equation 1.22 is not valid.

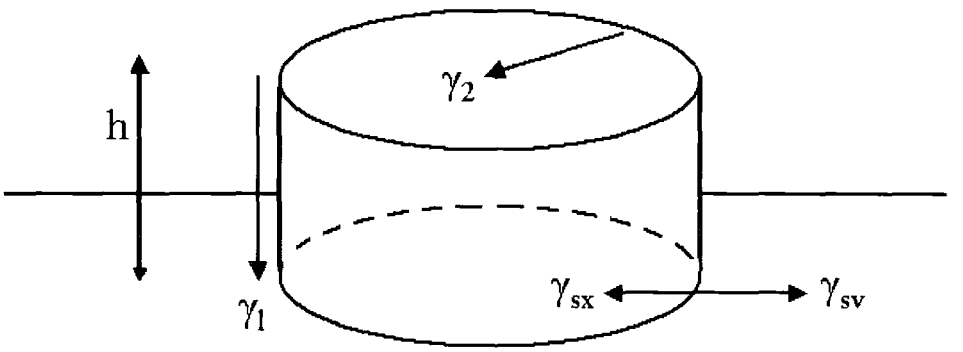

Figure 1.6. Illustration of 2d monolayer disc showing the interfacial tensions.

For the 2d monolayer disc:

$$\Delta G_i = -\frac{\pi r^2 h}{v_c}\Delta\mu + \pi r^2\gamma_2 + \pi r^2(\gamma_{sx} - \gamma_{sv}) + 2\pi r h\gamma_1 \quad \text{[Eqn. 1.23]}$$

$$= -\frac{\pi r^2 h}{v_c}\Delta\mu + \pi r^2(\gamma_2 + \gamma_{sx} - \gamma_{sv}) + 2\pi r h\gamma_l \quad \text{[Eqn. 1.24]}$$

where h is a constant equal to the height of the monolayer perpendicular to the substrate surface. From the maximum ΔG_i value, it is found that for this case:

$$\Delta G^* = \frac{\pi h\gamma_1^2}{(\Delta\mu / v_c) - \left[(\gamma_{sx} + \gamma_2 - \gamma_{sv})/h\right]} = \pi r^* h\gamma_1 \quad \text{[Eqn. 1.25]}$$

The nucleation rate for the heterogeneous case is calculated from:

$$J_{Het} = \Omega_{Het} \exp\left[\frac{-\Delta G^*_{Het}}{k_B T}\right] \qquad \text{[Eqn. 1.26]}$$

Typical values of Ω_{Het} are 10^{17} to 10^{22} $cm^{-2}s^{-1}$ for crystallisation from aqueous solution, see page 229. As with the homogeneous case, this varies little with change in supersaturation, and is often treated as a constant.

1.2.3 The Ostwald Metastable Limit

The form of equation 1.26 is such that the nucleation rate, J, can be set to one nucleus per cm^2/s (or ln J = 0) at the critical supersaturation level. This is also referred to as the Ostwald Metastable Limit.

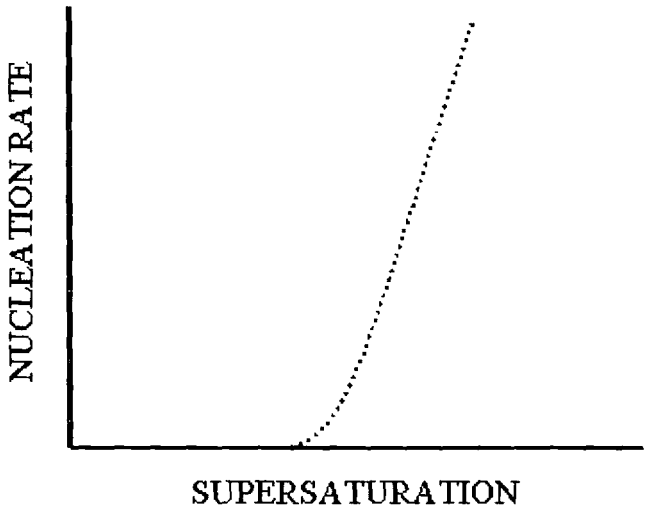

Figure 1.7. Illustration of the rapid increase in nucleation rate at the Ostwald metastable limit of supersaturation.

This allows an estimate of the highest temperature at which crystal nucleation will occur when cooling a supersaturated solution. This is demonstrated in chapter 4.

1.2.4 Improvements to, and Omissions in, Classical Nucleation Theory

Classical nucleation theory can be improved by the incorporation of terms to account for the following, if appropriate.

Statistical Mechanical Terms

The classical expression for ΔG^* considers the critical nucleus as stationary bulk condensate. Small aggregates of vapour atoms, however, would be expected to translate and rotate, so that statistical mechanical terms for these motions should also be included[55-61]. These terms are collectively known as the replacement term.

Zeldovich Factor[62,63]

The Zeldovich factor, Z, gives the steady-state concentration of critical nuclei, rather than the equilibrium concentration of critical nuclei. This is achieved by also considering in the evaluation of $n(i^*)$ the loss of critical nuclei by both growth to macroscopic droplets and evaporation to become sub-critical nuclei. The Z value is approximately 0.1 to 0.01 for most cases of nucleation from the vapour[59].

Thermal Non-Accommodation[64]

Every time a cluster grows by the addition of an atom, its temperature will rise due to the liberated enthalpy of crystallisation. Hence the cluster will be more likely to evaporate.

Quasi-Adsorption of Impingement Atoms[65]

This considers the scenario where an adatom re-evaporates before equilibrating with the surface.

Time Dependent Nucleation (Time Lag)[66]

Time is required for the steady-state concentration of critical nuclei to arise, and up to this point, the nucleation rates will be time dependent. The time delay between a

supersaturation occurring and the production of the steady state concentration of critical nuclei is termed nucleation time lag. Often this is much less than one second in duration, and so can be ignored.

Correction for Small Critical Nuclei at High Supersaturations[67]

For spherical particles the surface tension will tend to decrease with decreasing size. For anisotropic crystals (where the critical nucleus will not in general be spherical), edge and corner effects may also become important for very small nuclei.

Strain or Dislocations

The critical nucleus may have some relatively large additional energy terms due to strain or dislocations, if the lattice dimensions of the substrate and critical nucleus differ greatly.

Classical nucleation theory is often adequate to describe crystallisation in different systems. However, for the heterogeneous case, the substrate is assumed to be rigid and flat, which is clearly not the case for crystallisation induced by surfactants. Consequently, in this thesis we will begin to investigate whether classical nucleation theory can be extended to model these systems.

1.3 Crystal Growth

1.3.1 Equilibrium Shape of Crystals

For crystals, the surface free energy is generally anisotropic. Consequently, the equilibrium shape of a crystal will not be spherical, but can be determined by the Gibbs-Wulff theorem[68].

Gibbs and Curie proposed that the equilibrium shape of a crystal, is given by the condition that the total surface Gibbs function of formation, should be a minimum for a constant volume of crystal[69,70], i.e.

$$d\sum_n A_n\gamma_n = \sum_n \gamma_n dA_n = 0 \qquad \text{[Eqn. 1.27]}$$

where A_n is the area of face n and γ_n is the surface tension of face n.

The surface tension is assumed to be constant across the face and independent of crystal shape.

Wulff showed that by assuming a fixed point, of distance Y_n from face n, that the ratio γ_n/Y_n is constant[68]. This allows determination of the equilibrium shape of the crystal from a Wulff plot (figure 1.8).

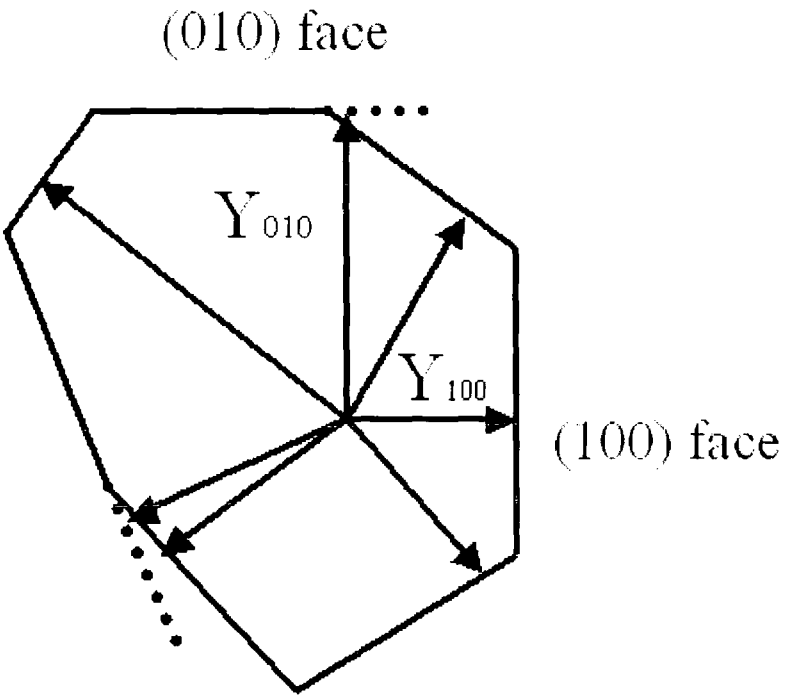

Figure 1.8. Illustration of a Wulff plot. According to the theory, the product $Y_{100}*\gamma_{100}$ is equivalent to $Y_{010}*\gamma_{010}$.

In a Wulff plot, vectors are drawn normal to all possible crystallographic faces from an arbitrary point, and the distances proportional to γ_n are marked on the vectors. Planes normal to the vectors are constructed through the marks and the resulting polyhedron is the equilibrium form. As a consequence, faces with the lowest surface tension dominate

the shape of the equilibrium crystal. This would be the (100) face for the hypothetical crystal illustrated in figure 1.8.

1.3.2 Epitaxial Growth

Epitaxy is the term applied to describe the oriented growth of a material on another[71]. Early crystallisation theories describe the necessity of a similar lattice structure between the substrate and the overgrowth. A lattice mismatch parameter was introduced, which remains important in modern epitaxial theories. A good lattice match certainly makes epitaxial deposition likely, but there is growing evidence that epitaxial growth may still occur, even in the absence of a good lattice match[72-75]. Epitaxial growth is now considered likely if a particular overgrowth orientation minimises the interfacial energy of the system.

1.3.3 Monolayer Induced Crystallisation

Surfactant monolayers will spontaneously organise at the air-water interface. These provide a well-defined matrix, which can be compressed and systematically varied as required. Not only do monolayers give a well-defined heterogeneous surface for crystallisation studies, but they also often induce oriented growth of crystallising species, i.e. a specific crystallographic plane is observed parallel to the substrate.

Monolayer-induced crystallisation has been studied extensively[76] since Lahav et al.[77] showed that specific polymorphs of glycine can be crystallised under a model template. Examples include monolayer induced calcite[78], DL-aspartic acid[79], L-asparagine monohydrate[80], sodium chloride[81], para-hydroxybenzoic acid[82,83] and ice crystallisation[84]. Scientists have developed such an understanding in this area that species are now specifically designed to promote the more complex crystallisation of proteins[85].

1.3.4 Atomic View of Crystal Growth

The mechanism of crystal growth is determined by the structure of the crystal face, i.e. the degree of roughness. As illustrated in the previous section, the faces of lowest surface tension determine the equilibrium shape of a crystal. A face at an angle to these low energy faces will consist of terraces and steps. These crystal faces can be divided into three groups:

- Flat faces, parallel to at least two dense atomic rows.
- Stepped faces, parallel to one dense atomic row.
- Kinked faces, not parallel to any dense atomic row.

These faces are illustrated in figure 1.9.

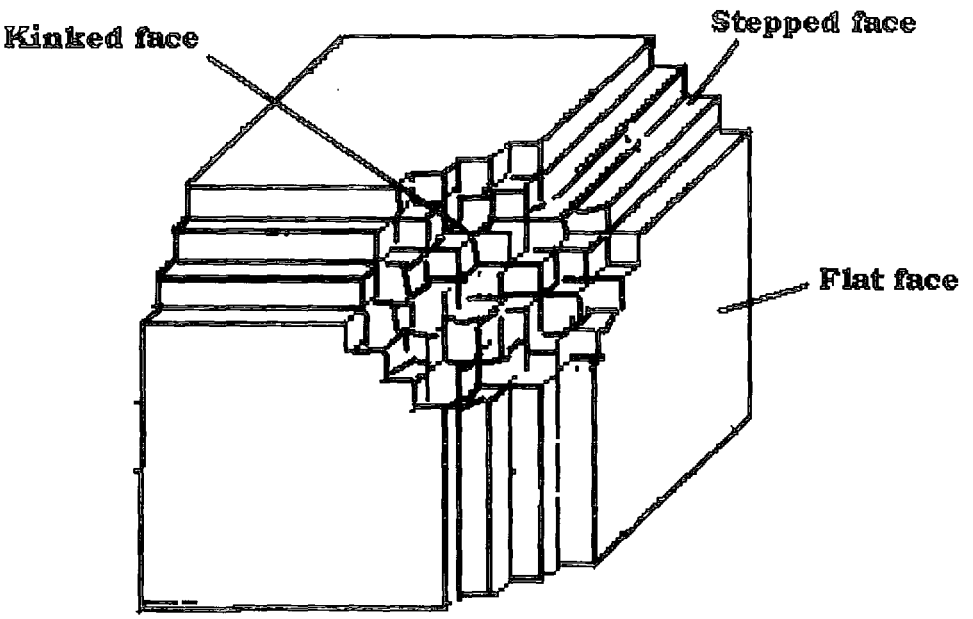

Figure 1.9. Illustration of the three categories of crystal face that determine crystal growth.

The kink position is important because it determines the equilibrium of an infinitely large crystal. This is because an equal number of intermolecular bonds are formed and broken when molecules adsorb and desorb from this position, respectively. If a system

is supersaturated, it is favourable for an adatom arriving at the kink site to be incorporated into the crystal.

The increasing importance of entropy at elevated temperatures means that flat faces undergo a surface roughening transition at a critical temperature, referred to as the roughening temperature, T_r. Above T_r, flat and stepped faces have a high density of kink sites (they are atomically rough) and can grow continuously.

In these circumstances, the growth rate, η, is linearly proportional to the supersaturation, i.e:

$$\eta = \lambda \Delta \mu \qquad \text{[Eqn. 1.28]}$$

For crystallisation from aqueous solution, however, temperatures are below T_r, and so growth mechanisms on atomically flat faces must be considered.

1.3.5 Layer Growth of Flat Faces Below T_r

Below the roughening temperature, T_r, it will not be favourable for an adatom to become incorporated into the flat crystal faces. Two distinct mechanisms can be identified.

2d Nuclei Formation

2d nuclei form, which is the rate determining step, and spread until the crystal face is completely covered. Formation of another layer requires formation of a new critical nucleus.

The rate of 2d nucleation is given by:

$$\eta = \Omega_{2d} \exp\left(-\frac{\Delta G^*_{2d}}{k_B T} \right) \qquad \text{[Eqn. 1.29]}$$

From ΔG^* for a monolayer disc, see Eqn. 1.25, we find:

$$\eta = \Omega_{2d} \exp\left(-\frac{\pi h v_c \gamma^2}{\Delta\mu k_B T}\right) \qquad \text{[Eqn. 1.30]}$$

At higher supersaturations, the face can grow via a multi-nucleation mechanism caused by many 2d nucleation sites developing. As the supersaturation increases, the 2d critical nuclei become so small, and the density of these becomes so great, that arriving atoms can be incorporated at virtually any site. This is known as kinetic roughening[86].

Screw Dislocation Growth

Experiments have shown that crystal growth proceeds at supersaturation significantly lower than that required for 2d nucleation growth. A spiral growth mechanism was proposed by Burton, Cabrera and Frank (BCF)[87,88] where there is lateral movement of steps arising from screw dislocations (effectively creating kink sites), see figure 1.10.

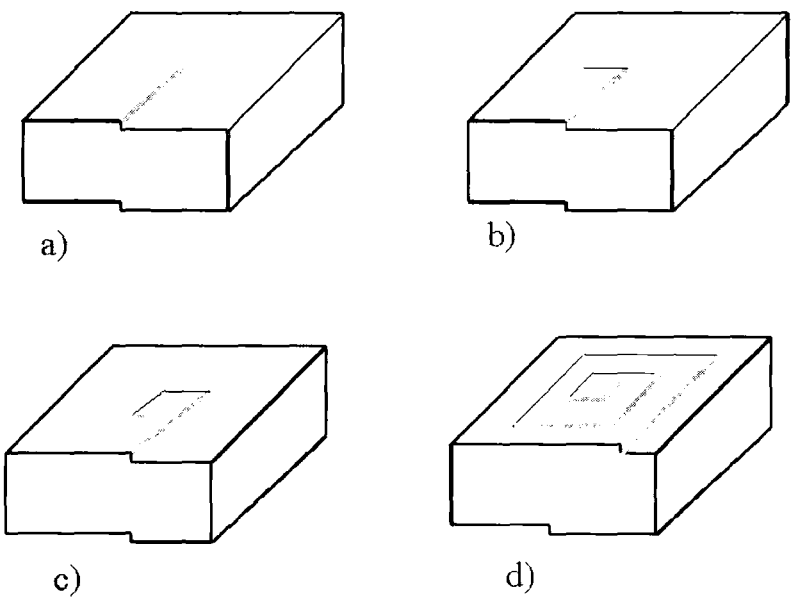

Figure 1.10. a) – d) gradual dislocation of an initially smooth crystal face, such that kink sites are formed over time allowing adatoms to be incorporated into the crystal, (assuming a supersaturated system).

Scientists have now shown this dislocation mechanism in operation by SEM[89-91].

Burton, Cabrera and Frank (BCF) developed the theory of screw dislocation crystal growth and found that:

$$\eta = C(\sigma^2 / \sigma_c)\tanh(\sigma_c / \sigma) \qquad \text{[Eqn. 1.31]}$$

where: η is the growth rate, σ is the supersaturation parameter $\Delta\mu/k_BT$, σ_c is the characteristic supersaturation of the system and C is a rate constant.

Two limiting cases can be distinguished:

At low $\Delta\mu$, $\sigma_c >> \sigma$, hence $\tanh(\sigma_c/\sigma) \rightarrow 1$. This is the BCF parabolic law:

$$\eta = C(\sigma^2 / \sigma_c) \qquad \text{[Eqn. 1.32]}$$

At $\Delta\mu$ sufficiently higher than σ_c, $\tanh(x \rightarrow 0) = x$, hence the BCF linear growth rate is obtained:

$$\eta = C\sigma \qquad \text{[Eqn. 1.33]}$$

At low supersaturation, the spiral growth mechanism dominates. At moderate supersaturation, both the dislocation and 2d nuclei processes will operate (figure 1.11).

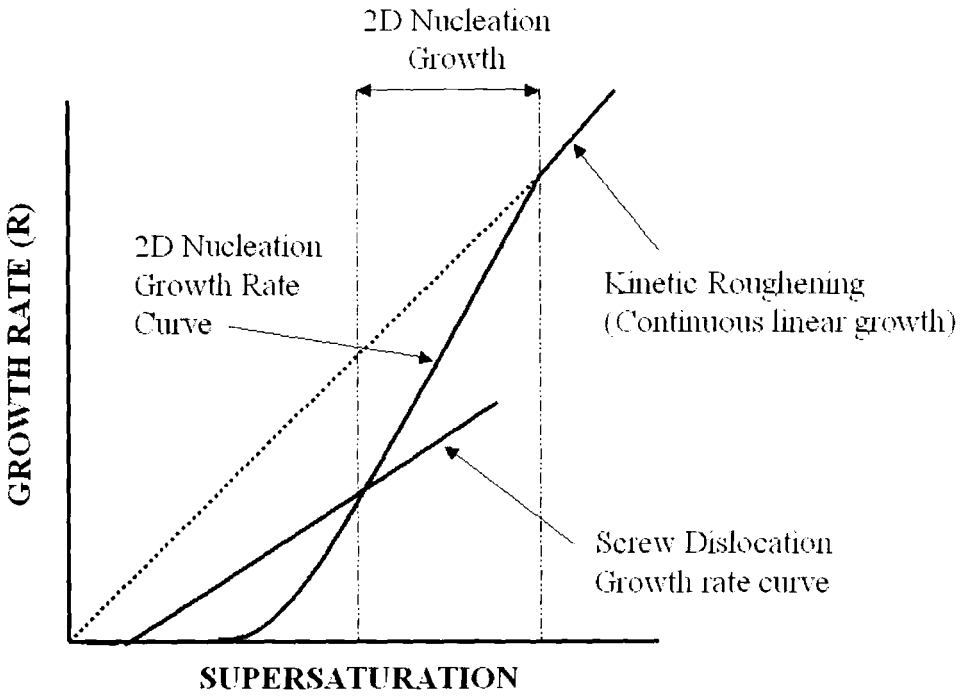

Figure 1.11. Illustration of growth rate of flat faces vs. supersaturation for different growth mechanisms.

1.3.6 Inhibition of Crystal Growth

Inhibition of crystal growth is of particular interest to scientists. For instance, calcium oxalate is a major component of kidney stones. While keyhole surgery has made the physical removal of these stones more comfortable than open surgery, a greater understanding of kidney stone development might eliminate the need for surgery altogether. This could lead to the development of agents that prevent the build up of stones in patients known to be susceptible to the condition.

There is a connection between growth inhibition and nucleation promotion. This depends upon whether an additive is aggregated or not, therefore an emulsion system can potentially act as either a crystallisation promoter or inhibitor[92]. For instance, if the additive aggregates to form an ordered surface, nucleation is favoured provided that the crystallising material is adsorbed onto this surface.

1.4 Background to Emulsions

1.4.1 Crystallisation in Emulsions

Heterogeneous processes typically dominate crystallisation. The influence of foreign surfaces responsible for heterogeneous nucleation can be minimised by reducing the volume of the supersaturated solution so that impurities are less likely to be present. As a consequence, homogeneous nucleation can be studied. Emulsions can clearly offer this limited volume and give an ideal opportunity to successfully control the polymorph by reducing the chance of unwanted heterogeneous processes. There is also the potential to control particle size, simply by limiting the crystal growth to within the droplet.

Crystallisation can take place at curved surfaces. Examples are the synthesis of mesoporous catalysts in oil/water emulsions and biomineralisation, such as shells and skeletons (section 3.1.1). As will be explored in chapter 4, a flat interface enhances crystallisation, but the influence of a curved surface is less clear. In the context of gaining an understanding of the effect of interfacial curvature, emulsions offer an excellent model system, provided emulsions of various droplet diameters can be made.

There are also cases where crystallisation of species in emulsions is believed to be induced by the surfactant[26,93-95] such that heterogeneous rather than homogeneous nucleation occurs.

1.4.2 Types of Emulsions

Colloidal type systems are typically categorised as microemulsions, nanoemulsions and emulsions, which have diameters of approximately 10 nm, 20 – 500 nm and > 500 nm, respectively. Generally speaking, due to scattering of light, nanoemulsions give a translucent blue appearance, microemulsions are colourless and emulsions appear white. In simplest terms, these systems can be categorised as oil-in-water, (o/w), or water-in-oil (w/o). The droplets are often referred to as the disperse phase and the continuous phase is commonly termed the dispersion medium.

1.4.3 Stability of Emulsions

Ostwald Ripening and Coalescence

Microemulsions are thermodynamically stable, since the interfacial tension is low and is offset by the entropy of dispersion of the globules. Systems of larger droplet diameters are only kinetically stable, and develop into separate phases over time.

Ostwald ripening and coalescence are two distinct mechanisms of gradual degradation in emulsions. Ostwald ripening[96-99] is driven by the difference in LaPlace pressure, p_L, of droplets of different radii, see equation 1.6, and the increased stability of smaller droplets, as shown by the Gibbs-Thomson equation. In particular,

$$p_L = \gamma\left(\frac{1}{r_1} + \frac{1}{r_2}\right) \qquad \text{[Eqn. 1.34]}$$

where γ is the interfacial tension and r_1 and r_2 are the radii of curvature of a deformed emulsion droplet.

Breaking of the droplets is feasible if the deforming force exceeds the LaPlace pressure. It can be inferred from the LaPlace relationship that a smaller droplet size requires a greater energy input (or more surfactant) to lower γ. Even in the absence of droplet rupture, larger droplets will tend to grow at the expense of smaller ones, due to the increased solubility of the material in the latter.

In the case of coalescence, the thin film between the droplets ruptures, causing them to fuse. Whether a coalescence or Ostwald ripening mechanism is predominantly operating is easily identified[100]; Ostwald ripening alone leads to a narrow size distribution and a growth rate that gradually vanishes. In the case of coalescence, the polydispersity increases.

Coagulation, Flocculation and Creaming

Coagulation is the term used to describe the formation of aggregates in an unstable emulsion or colloidal system. Some authors distinguish between coagulation and flocculation, with the latter referring to reversible aggregation and implying the formation of a loose or open network. If the coagulum density is lower than the surrounding medium, which is usually the case for oil-in water systems, the aggregate accumulates at the top. This is the effect known as creaming.

1.4.4 Surfactant Properties

Surfactants are surface active species which are amphiphilic, containing groups of opposite polarity and solubilising tendencies. In simplest terms they possess a hydrophilic and a lipophilic segment, e.g. a non-polar segment such as an aliphatic or aromatic hydrocarbon residue, and an ionic or polar group (e.g. hydroxyl, carboxyl) that interacts strongly with water.

Figure 1.12 illustrates the action of a surfactant. The aliphatic tail is lipophilic, causing the polar headgroups to face outward towards the continuous water phase. This surface activity gives emulsions significantly enhanced stability due to decreased interfacial tension between the oil and aqueous phases.

Figure 1.12 Illustration of an oil droplet stabilised by surfactant.

Micelles and the Critical Micelle Concentration (CMC)

As described in the previous section, emulsions are usually stabilised by surfactants. Surfactants in solution are often association colloids, which tend to form aggregates of colloidal dimensions. These aggregates are known as micelles, which exist in equilibrium with the monomeric molecules from which they are formed.

There is a relatively small range of concentrations separating the limit below which virtually no micelles are detected and the limit above, where virtually all additional surfactant molecules form micelles. Graphs of properties such as surface tension, turbidity and conductivity against surfactant concentration display sharp gradient changes in this concentration range. By extrapolating the loci of such a property above and below this range until they intersect, a value may be obtained, which is referred to as the critical micelle concentration (CMC).

1.4.5 Emulsion Preparation Methods

Emulsions are thermodynamically unstable, and hence energy must be input for their formation.

High Energy Preparation Methods

From the LaPlace relationship, or consideration of the energy required to form the interfacial region, it can be seen that the smaller the droplet size, the greater the energy input or surfactant quantity required to break up the larger droplets. Consequently, emulsion production (diameter approximately 1 μm) is less costly than nanoemulsion formation. Industrial manufacture of nanoemulsions is typically by high pressure methods. Ultrasonic emulsification can also be applied, but is only successful for relatively small-scale manufacture[101].

Low Energy Preparation Methods

For emulsions stabilised with non-ionic surfactants, low energy emulsification methods take advantage of the phase inversion temperature, PIT. This method is widely used in

industry[102,103] and relies on the variation in solubility of polyoxyethylene based non-ionic surfactants with temperature. Brij ® materials are typical of surfactants possessing this inversion property with temperature.

At low temperature, the non-ionic surfactant forms oil swollen micellar solution phases (o/w), whereas at higher temperature, water swollen reverse micelles are observed (w/o). At an intermediate temperature, the PIT (sometimes called the HLB temperature) a bicontinous phase exists with a water with oil common phase and excess amounts of oil or water existing as pure phases.

Relatively low interfacial tensions[104,105] are achieved at the PIT, hence droplet break-up is possible with very little energy input, and very small droplet sizes are achieved[106]. Other low energy methods take advantage of the phase transitions that occur on changing the emulsion composition at constant temperature[107-111], see chapter 4.

1.4.6 Non-ionic Surfactants and the HLB Scale of Amphiphilic Character[112]

The HLB scale was developed by Griffin[113] to describe the properties of non-ionic surfactants. The HLB numbers are an expression of the hydrophile/lipophile balance (HLB) and are an indication of the properties of a surfactant and its potential applications (see table 1.1). Generally speaking, a high HLB number indicates a more polar surfactant. These HLB values are illustrated further in table 1.2 for the surfactants used in the research presented in this thesis.

HLB	Application
1 – 3.5	Antifoams
3.5 - 8	Water-in-oil emulsions
7 – 9	Wetting and spreading agents
8 - 16	Oil-in-water emulsions
13 - 16	Detergents
15 - 40	Solubilisers

Table 1.1. HLB ranges and the typical applications for surfactants with that property.

Surfactant	HLB Value
Brij 30	9.7
Brij 52	5.0
Tween 80	15.0
Tween 20	16.7
Span 20	8.6
Span 80	4.3

Table 1.2. Commonly used surfactants and their HLB values.

Span surfactants are increasingly useful as they are sugar based and offer low toxicity. For a mixture of surfactants, a simple addition of the HLB is taken with each component multiplied by its weight fraction, i.e.

$$HLB = W_A \varpi_A + W_B \varpi_B \qquad \text{[Eqn. 1.35]}$$

where W_x is the weight fraction of surfactant x and ϖ_x is the HLB of pure surfactant x.

Mixtures of surfactants are known to offer improved stability[114], even if an optimal HLB would appear to be given by a pure surfactant. Tween surfactants are complex

sugar-oleic acid derivatives (figure 1.13). Figure 1.14 illustrates the structure of Brij and Span surfactants.

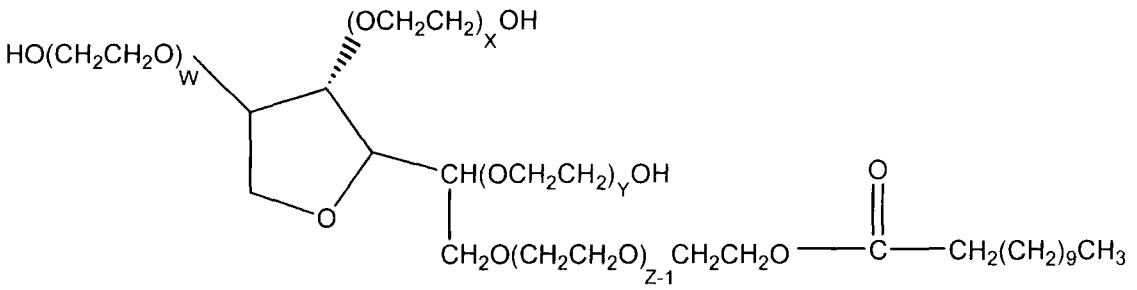

sum of w + x + y + z = 20

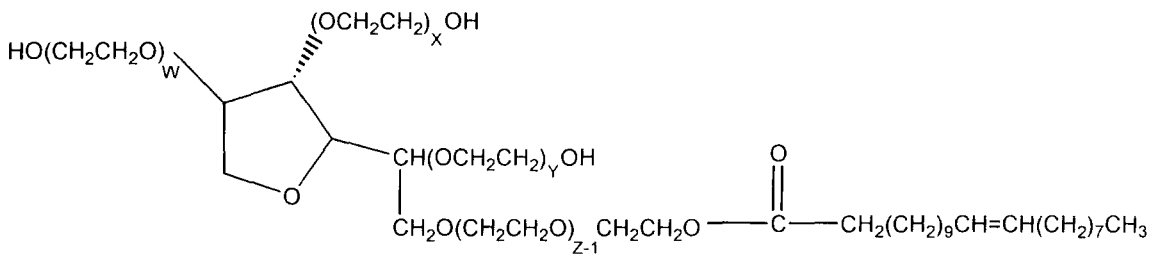

sum of w + x + y + z = 20

Figure 1.13. Illustration of the chemical structure of Tween 20 (top) and Tween 80 (bottom).

Brij 30 (where n ≈ 4)

Brij 52 where (where n ≈ 2)

Span 80

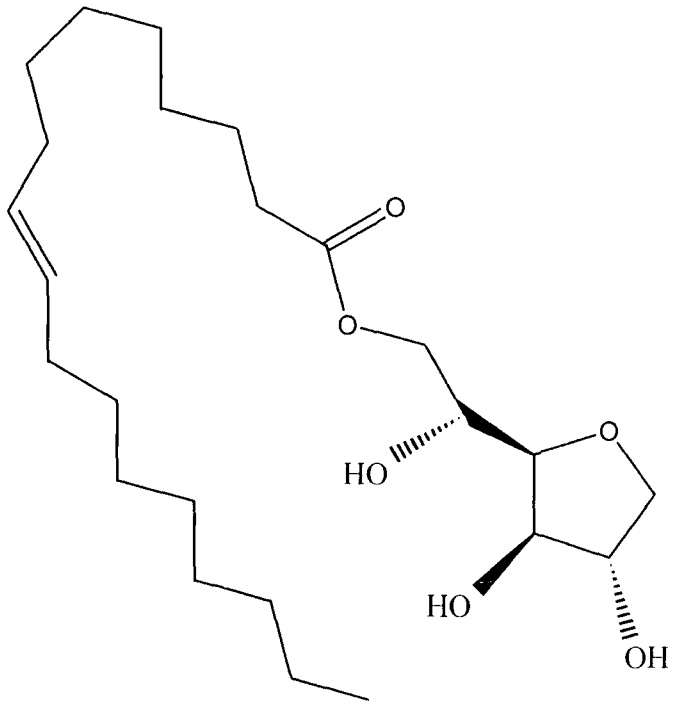

Span 20

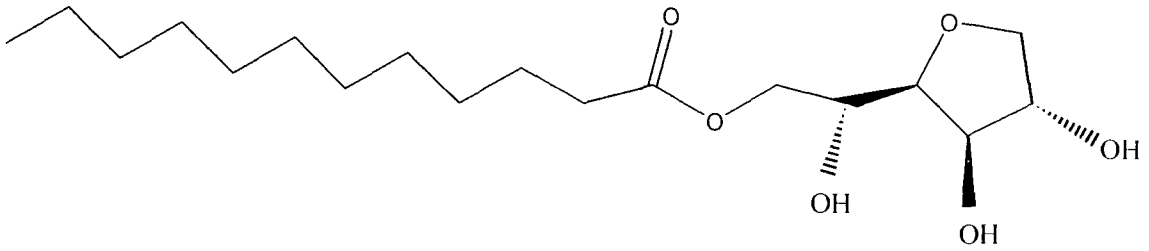

Figure 1.14. Structures of Brij and Span surfactants.

1.5 Reflectivity

Chapters 2 and 3 detail crystallisation studies at the planar interface. Reflectivity offers the ideal opportunity to study changes in the planar substrate that may help induce the crystallisation. Chapter 2 includes neutron reflectivity data, for which some understanding of reflectivity theory is useful. Chapters 2 and 3 also include external reflectance FTIR (ER-FTIR) data, for which the same optical principles apply.

1.5.1 Theory of Reflectivity

External reflection FTIR, X-ray reflectivity and neutron reflectivity follow the same fundamental laws of optics. A brief review of reflectivity theory is presented here based on publications by Higgins & Benoit[115] and Lekner[116].

The refractive index governs the reflection of radiation by surfaces and interfaces. An interface is defined as the position between media of two different refractive indices. The refractive index, N_i, of medium i can be given by:

$$N_i = 1 - \delta + i\beta \qquad \text{[Eqn. 1.36]}$$

where $1 - \delta$ is the real part of the refractive index, and $i\beta$ is the complex absorption coefficient. This equation has its counterpart in neutron and x-ray optics. For neutrons:

$$N_i = 1 - \frac{\lambda^2 \rho_i}{2\pi} + \frac{i\lambda n_i \sigma_a}{4\pi} \qquad \text{[Eqn. 1.37]}$$

where n_i is the atomic number density, ρ_i is the scattering length density (SLD) of species i, σ_a is the absorption cross-section and λ is the neutron wavelength. With the exception of a small number of inorganic elements, the absorption cross-section is effectively zero, *i.e.* $\sigma_a = 0$ so the complex number term can be dropped to give:

$$N_i = 1 - \frac{\lambda^2 \rho_i}{2\pi} \qquad \text{[Eqn. 1.38]}$$

For x-rays the equivalent expression is:

$$N_i = 1 - \frac{\lambda^2 \rho_e r_o}{2\pi} + \frac{i\tau\lambda}{4\pi} \qquad \text{[Eqn. 1.39]}$$

where λ is the x-ray wavelength, ρ_e is the electron density of the material, r_0 is the electron radius and τ is the mass absorption coefficient.

The equivalent expression for optical wavelengths is:

$$N_i = N_j + ik_j \qquad \text{[Eqn. 1.40]}$$

where N_j is the real refractive index and k_j is the absorption constant.

N_i for X-rays is typically ≤ 1, whereas for optical and infrared wavelengths, $N_i \geq 1$.

At an interface of two media possessing different refractive indices, radiation will undergo reflection and refraction as illustrated in figure 1.15. The angle by which the incident beam is refracted is dictated by the ratio of the refracted indices of the media. Figure 1.15 illustrates these processes, where N_1 and N_2 are the refractive indices of media 1 and 2, respectively, and θ_1 and θ_2 are the angles of incidence and refraction, respectively.

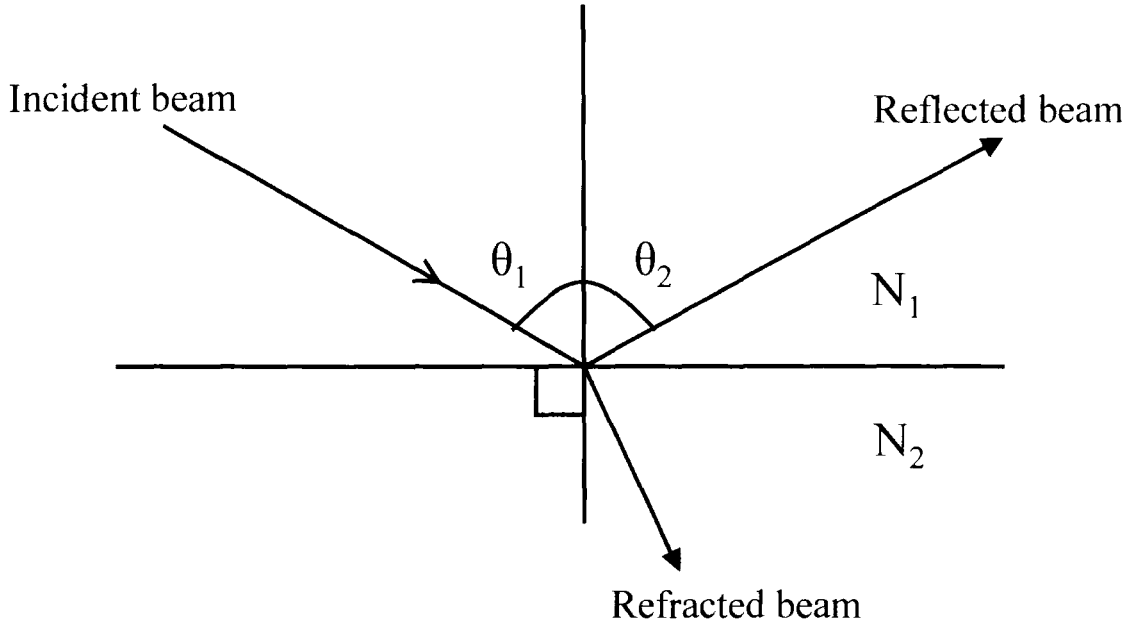

Figure 1.15 Diagram of incident radiation on a flat interface between two media, illustrating the reflected and refracted beams.

Figure 1.15 shows radiation incident on an interface between two infinitely thick media, where the interface is infinitely sharp. The beam can be either reflected, at an angle, θ_1, equal to that of the incident beam, or refracted with an angle according to the Snell-Descartes Law:

$$N_1 \sin\theta_1 = N_2 \sin\theta_2 \qquad \text{[Eqn. 1.41]}$$

If the refractive indices are greater than 1, total internal reflection can occur. Total internal reflection will occur at a critical glancing angle of incidence, θ_g, if the refractive index of the medium (N_2) is greater than the refractive index of the surface (N_1). This angle is given by:

$$\theta_g = \arcsin\frac{N_1}{N_2} \qquad \text{[Eqn. 1.42]}$$

When $N_2 > N_1$, there will be no refracted component and only an evanescent wave will penetrate the surface[117]. According to the Snell-Descartes Law, $\theta_1 < \theta_2$ hence $N_1 < N_2$.

If the refractive indices are less than 1 (i.e. in the case of scattering of X-rays), then total external reflectance may occur. For total external reflectance to occur, the incident beam must be at or below a critical angle, θ_c, with θ measured relative to the surface. $\cos \theta_c = N$ (if θ_c is measured relative to the surface) for reflection off a surface in air/vacuum. Considering neutron reflectivity, other than for a small number of inorganic materials and compounds with a very high proportion of hydrogen, ρ is positive and N for neutrons is less than unity.

Since $1 - N$ is typically in the order of 10^{-6} for X-ray and neutron reflectivity, θ_c is very small. $(1-\cos \theta_c) \sim (\theta_c^2 / 2)$, since

$$Cos\theta = 1 - \frac{\theta^2}{2!} + \frac{\theta^4}{4!} - \frac{\theta^6}{6!} + \ldots\ldots\ldots\ldots \qquad \text{[Eqn. 1.43]}$$

Hence for neutron reflectivity, from equation 1.38:

$$\frac{\theta_c}{\lambda} = \sqrt{\frac{\rho_b}{\pi}} \qquad \text{[Eqn. 1.44]}$$

Or for X-rays, (equation 1.39)

$$\frac{\theta_c}{\lambda} = \sqrt{\frac{\rho_e r_o}{\pi}} \qquad \text{[Eqn. 1.45]}$$

In the construction of reflectivities, it is convenient to use the wavevector, k of the incident radiation. k is related to Q, the scattering vector, which is the fundamental variable in X-ray and neutron reflectometry, by:

$$Q = 2k = \frac{4\pi}{\lambda} \sin\theta \qquad \text{[Eqn. 1.46]}$$

where λ is the wavelength of the neutrons or X-rays. Using these equations, a sample containing *m* discrete layers can be considered. Layer 1 is defined as the medium surrounding the sample, usually air. The coefficient for reflection of the interface between layers 1 and 2 is given by the Fresnel formula:

$$r_{12} = \frac{k_1 - k_2}{k_1 + k_2} \qquad \text{[Eqn. 1.47]}$$

where k_1 and k_2 are the wavevectors of layers 1 and 2, respectively. The reflectivity, R, is then given by:

$$R = \left| \frac{r_{12} + r_{23} \exp(2i\beta)}{1 + r_{12} r_{23} \exp(2i\beta)} \right|^2 \qquad \text{[Eqn. 1.48]}$$

where r_{ij} are the Fresnel reflectances calculated for each interface and β is a function of the film thickness and wavelength defined by:

$$\beta = 2\pi \left(\frac{d}{\lambda} \right) N_2 \cos\theta \qquad \text{[Eqn. 1.49]}$$

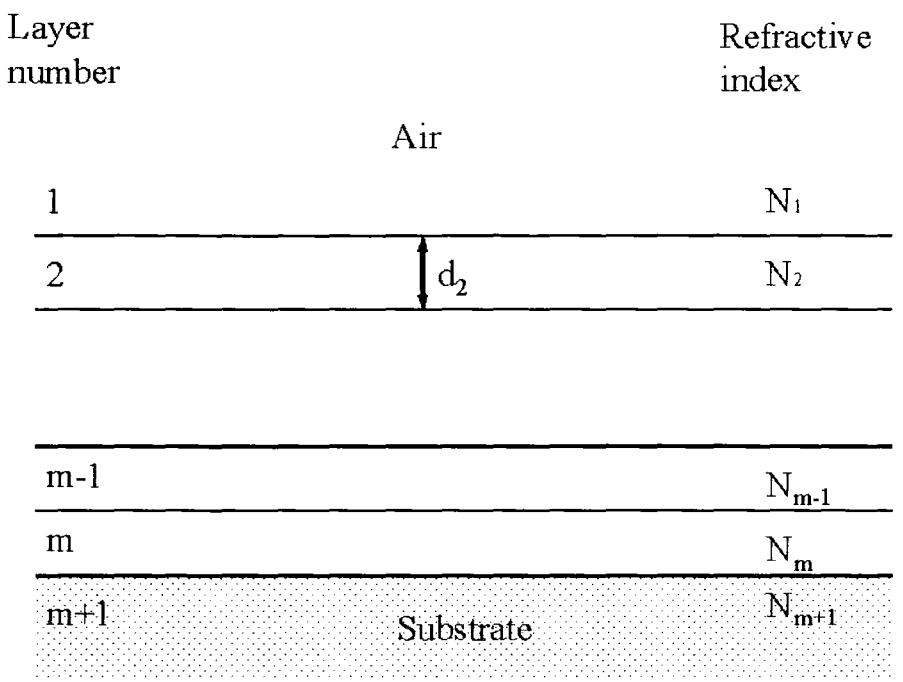

Figure 1.16. Schematic diagram of a sample composed of m discrete layers each with a thickness, d_i, and refractive index, N_i.

1.5.2 Introduction to Neutron Reflectivity Experiments

There has been a burst of activity in the study of surface and interfacial behaviour of materials by neutron reflectivity in the last decade. A comprehensive review by Dietrich and Haase[118] details a number of recent developments in the use of neutron reflectivity. This increase in the popularity of the technique is due to advances in the design of the reflectometers[119] and in the methods of data analysis.

Neutron reflectivity explores the composition variation normal to the surface reflecting the neutrons, offering spatial resolution on the Angstrom scale. This technique has advantages over X-ray diffraction in that there are considerable reflectivity differences between different elements and isotopes of elements. This enables the scientist to determine the composition of the layer of interest. Neutron reflectivity relies very heavily, however, on models that can prove time consuming.

The neutron reflectivity differences between hydrogen and deuterium are particularly striking. This proves invaluable in neutron reflectivity studies since deuteration, or part deuteration, of materials results in large changes in reflectivity without altering the behaviour of the system. The coherent scattering length, b, which is a measure of the interaction between an incoming neutron and the nucleus of the atom[120], varies at random across the periodic table, not only in magnitude, but also in sign for the case of hydrogen and deuterium. This is illustrated in table 1.3.

Atom	Coherent scattering length/ 10^{-4} Å
^{1}H	-3.74
^{2}H	6.67
^{16}O	5.80
^{18}O	5.84
^{14}N	9.37
^{15}N	6.44
^{12}C	6.65
^{13}C	6.19

Table 1.3. Coherent scattering lengths for selected elements[121].

So deuteration of one of the components provides an immediate contrast for neutron reflectivity experiments.

The scattering length density (SLD), ρ, of a material is given by:

$$\rho = \sum b_i n_i \qquad \text{[Eqn. 1.50]}$$

where n_i = number density of species i, and Σb_i = sum of the coherent scattering lengths of atoms in species i.

A more useful expression, particularly for polymers is:

$$\rho = \frac{\sum b_i D_i N_A}{M_i} \qquad \text{[Eqn. 1.51]}$$

where Σb_i is the sum of the monomer unit atomic coherent scattering lengths, D_i is the bulk compound density, N_A is the Avogadro constant and M_i is the compound molar mass (or monomer unit molar mass).

Scattering length densities for species relevant in this thesis are given in table 1.4, which illustrates the significant effect on SLD, of deuterating a species.

Material	SLD Hydrogenated /10^{-6} Å^{-2}	SLD Deuterated /10^{-6} Å^{-2}
Nylon-6	0.87	7.91
DL-aspartic acid	2.46	4.56
Water	-0.56	6.39

Table 1.4 Examples of SLD values for deuterated and hydrogenous samples.

For studies of crystallisation from an aqueous phase, a combination of D_2O and H_2O can give a subphase of zero scattering length density. This is commonly referred to as null reflecting water (NRW).

1.5.3 Neutron Reflectivity Data Analysis

In general, there are two methods of analysing neutron reflectivity data.

The kinematic approximation method has not proved widely useful in the interpretation of polymeric data[115]. This assumes that the interactions between neutrons and nuclei are very weak, so that single scattering events occur, which is not true close to the critical angle. The second method is model fitting, which has been shown to work for a wide variety of systems.

The relationships of Fresnel and Snell-Descarte can be used to derive expressions for the reflectivity profiles of simple systems. The optical matrix method developed by Born and Wolf[122] is the most widely used fitting method. In this approach, the reflection between layers is summed together, as a histogram of discrete layers. A matrix for each layer is created.

Abeles is one of the most widely used solutions to the optical matrix approach[123]. In this method, a characteristic matrix is defined for each discrete layer. For the mth layer, the matrix is:

$$c_m = \begin{bmatrix} \cos\beta_m & -(i/\kappa_m)\sin\beta_m \\ -i\kappa_m \sin\beta_m & \cos\beta_m \end{bmatrix} \qquad \text{[Eqn. 1.52]}$$

where $\kappa_m = N_m \sin\theta_m$ and β is from equation 1.49.

Matrices are calculated for each individual layer. An overall sample matrix M with m layers is defined as the product of the individual matrices from which the reflectivity is then obtained, i.e.

$$M = [M_1][M_2][M_3].....[M_n] \qquad \text{[Eqn. 1.53]}$$

The result is a 2 x 2 matrix:

$$M = \begin{bmatrix} M_{11} & M_{12} \\ M_{21} & M_{22} \end{bmatrix} \qquad \text{[Eqn. 1.54]}$$

and the reflectivity obtained from the relationship is:

$$R = \left| \frac{(M_{11} + M_{12}\kappa_s)\kappa_a - (M_{21} + M_{22})\kappa_s}{(M_{11} + M_{12}\kappa_s)\kappa_a + (M_{21} + M_{22})\kappa_s} \right|^2 \qquad \text{[Eqn. 1.55]}$$

where subscript *a* refers to the outer medium (air) and *s* refers to the final substrate. This solution is easily accessible from computational analysis and is suited to the modelling of reflectivity profiles from samples with complex internal layer structure.

1.6 Project Aims

The aims of this project are to investigate further the mechanisms that control crystallisation, and thereby develop crystallisation theory. For instance, there is growing evidence[72-75,79,124] that surfactant induced heterogeneous crystallisation proceeds via rearrangement of the surfactant layer. This differs from the conventional model that assumes crystallisation proceeds on a rigid substrate, and is most favourable on a substrate that offers a good epitaxial match with the crystallising species. The studies presented here explore this aspect and the effects of interfacial curvature.

Calcium carbonate crystallisation at the planar interface, induced by surfactant monolayers, has been studied extensively in recent years. The conditions that give calcite, rather than the metastable forms vaterite and aragonite, are well documented. There is limited knowledge, however, of the processes the monolayer undergoes to facilitate crystallisation. In this work, the findings of previous authors are confirmed and the octadecanoic acid monolayer studied by external reflectance FTIR and grazing incidence X-ray diffraction (GIXD) during crystallisation. The GIXD studies are repeated at different surface pressures to see if this affects the behaviour of the monolayer. The effect of polyacrylic acid, a crystal inhibitor, is also investigated. These studies aim to give an insight into the possible rearrangement of the octadecanoic acid monolayer during calcite crystallisation, as proposed by Ahn et al.[124] from external reflectance FTIR studies.

Similarly, the crystallisation of dl-aspartic acid under nylon 6 spread films is explored by neutron reflectivity and ER-FTIR. Neutron reflectivity is able to determine layer thicknesses and compositions, as crystallisation progresses. Data are therefore presented with the aim of showing changes in the structure of the nylon 6 spread film and the growth of dl-aspartic acid layers as crystallisation progresses. These data were

recently presented in Langmuir[79], and as far as I am aware, there is only one other published study of crystallisation by neutron reflectivity[125].

While crystallisation at planar interfaces is relatively well understood, there is a limited understanding of the effects of crystallisation at curved interfaces. Indeed, the need for further studies of crystallisation induced at curved interfaces was highlighted recently by Davey[126] and Cacciuto et al[127]. This gap in our understanding of crystallisation is therefore highly topical at present, and the emulsion crystallisation data presented in chapters 4 and 5 go some way in helping our understanding in this area.

Emulsions offer an excellent model system for interfacial crystallisation at curved interfaces and although there have been many studies of emulsion crystallisation in recent years, none has quantified curvature effects. Chapter 4 presents a systematic study of the crystallisation temperature of ice induced by additives at curved interfaces. Data from emulsions of different droplet diameters are presented, and the interfacial additive density discussed. This section aims not only to show the differences between curved and planar interfaces, but also to explore whether classical nucleation theory is sufficient to predict the differences in crystallisation at curved and planar interfaces.

Finally, with reference to the results from the ice curvature studies, the crystallisation of glycine in emulsions is examined, and the effect of concave and convex interfaces compared. Oil-in-water and water-in-oil emulsions are developed, and the effect of the relative curvature in each, assessed. The data in chapter 5 therefore aims to improve our understanding of the influence of curved interfaces on solute crystallisation.

References

(1) Jones, M. D.; Paz, F. A. A.; Davies, J. E.; Johnson, B. F. G.; Klinowski, J. *Acta. Cryst E-Struct. Rep.* **2003**, *59*, M1091-M1093.

(2) Brown, A. S. C.; Hargreaves, J. S. J.; Taylor, S. H. *Cat. Letts.* **1999**, *57*, 109-113.

(3) Chary, K. V. R.; Bhaskar, T.; Seela, K. K.; Lakshmi, K. S.; Reddy, K. R. *Applied Catalysis A-General* **2001**, *208*, 291-305.

(4) Sun, Y. M.; Spence, R. E. V. H.; Piers, W. E.; Parvez, M.; Yap, G. P. A. *J. Am. Chem. Soc.* **1997**, *119*, 5132-5143.

(5) Milani, B.; Stabon, E.; Zangrando, E.; Mestroni, G.; Sommazzi, A.; Zannoni, C. *Inorganica Chimica Acta* **2003**, *349*, 209-216.

(6) Brittain, H. G. *Polymorphism in Pharmaceutical Solids*; Marcel Dekker, 1999.

(7) Stanek, J.; Caravatti, G.; Frei, J.; Furet, P.; Mett, H.; Schneider, P.; Regenass, U. *J. Med. Chem* **1993**, *36*, 2168-.

(8) Karfunkel, H. R.; Wu, Z. J.; Burkhard, A.; Rihs, G.; Sinnreich, D.; Bürger, H. M.; Stanek, J. *Acta. Cryst.* **1996**, *B52*, 555-.

(9) Haleblia, J.; McCrone, W. *J. Pharm. Sci.* **1969**, *58*, 911.

(10) Behme, R. J.; Brooke, D.; Farney, R. F.; Kensler, T. T. *J. Pharm. Sci.* **1985**, *74*, 1041-1046.

(11) Kaduk, J. A.; Golab, J. T.; Leusen, F. J. J. *Cryst. Eng.* **1998**, *1*, 277-290.

(12) Karfunkel, H. R.; Rohde, B.; Leusen, F. J. J.; Gdanitz, R. J.; Rihs, G. *J. Comp. Chem.* **1993**, *14*, 1125-1135.

(13) Davey, R. J.; Cardew, P. T.; McEwan, D.; Sadler, D. E. *J. Cryst. Growth* **1986**, *79*, 648-653.

(14) Mann, S.; Webb, J.; Williams, R. J. P. *Biomineralization: Chemical and Biochemical Perspectives*; Weinheim, 1989.

(15) Sarashina, I.; Endo, K. *American Mineralogist* **1988**, *83*, 1510-1515.

(16) Falini, G.; Albeck, S.; Weiner, S.; Addadi, L. *Science* **1996**, *271*, 67-69.

(17) Farina, M.; Schemmel, A.; Weissmuller, G.; Cruz, R.; Kachar, B.; Bisch, P. M. *J. Struct. Biol.* **1999**, *125*, 39-49.

(18) Kirschvink, J. L.; Kobayashi-Kirschvink, A.; Woodford, B. J. *Proc Nat. Acad. Sci USA* **1992**, *89*, 7683-7687.

(19) Danilchenko, S. N.; Moseke, C.; Sukhodub, L. F.; Sulkio-Cleff, B. *Cryst. Res. & Tech.* **2004**, *39*, 71-77.

(20) Wu, P.; Zeng, Y. Z.; Wang, C. M. *Biomaterials* **2004**, *25*, 1123-1130.

(21) Belcher, A. M.; Hansma, P. K.; Stucky, G. D.; Morse, D. E. *Acta Materalia* **1998**, *46*, 733-736.

(22) Bond, G. M.; Richman, R. H.; McNaughton, W. P. *J. Mater. Eng. & Performance.* **1995**, *4*, 334-345.

(23) Huo, Q. S.; Margolese, D. I.; Ciesla, U.; Feng, P. Y.; Gier, T. E.; Sieger, P.; Leon, R.; Petroff, P. M.; Schuth, F.; Stucky, G. D. *Nature* **1994**, *368*, 317-321.

(24) Gebhardt, M. *J. Cryst. Growth.* **1973**, *20*, 6-12.

(25) Khan, S. R. *J. Urology* **1993**, *150*, 239-245.

(26) Allen, K.; Davey, R. J.; Ferrari, E.; Towler, C.; Jones, M. O.; Pritchard, R. G. *Cryst. Growth & Design* **2002**, *2*, 523-527.

(27) Yano, J.; Furedi-Milhofer, H.; Wachtel, E.; Garti, N. *Langmuir* **2000**, *16*, 9996-10004.

(28) Yano, J.; Furedi-Milhofer, H.; Wachtel, E.; Garti, N. *Langmuir* **2000**, *16*, 1005-1014.

(29) Li, M.; Lebeau, B.; Mann, S. *Adv. Mat.* **2003**, *15*, 2032-2035.

(30) Walsh, D.; Lebeau, B.; Mann, S. *Adv. Mat.* **1999**, *11*, 324-328.

(31) Hirai, T.; Hariguchi, S.; Komasawa, I.; Davey, R. J. *Langmuir* **1997**, *13*, 6650-6653.

(32) Dickinson, E.; McClements, D. J.; Povey, M. J. W. *J. Coll & Interf. Sci.* **1991**, *142*, 103-110.

(33) McClements, D. J.; Dickinson, E.; Dungan, S. R.; Kinsella, J. E.; Ma, J. G.; Povey, M. J. W. *J. Coll & Interf. Sci.* **1993**, *160*, 293-297.

(34) Kashchiev, D.; Kaneko, N.; Sato, K. *J. Coll & Interf. Sci.* **1998**, *208*, 166-177.

(35) Kaneko, N.; Horie, T.; Ueno, S.; Yano, J.; Katsuragi, T.; Sato, K. *J. Cryst. Growth* **1999**, *197*, 263-270.

(36) Dutta, P. K.; Jakupca, M.; Reddy, K. S.; Salvati, L. *Nature* **1995**, *374*, 44-46.

(37) Pileni, M. P.; Lisiecki, I.; Motte, L.; Petit, C.; Tanori, J.; Moumen, N., 1995 (1998), 289-304. In *Micelles, Microemulsions, and Monolayers: Science and Technology, [International Symposium on Micelles, Microemulsions, and Monolayers]*; Shah, D. O., Ed.; Dekker: Pierre and Marie Curie University, Paris, Fr., 1995 (1998); pp 289-304.

(38) Furedi-Milhofer, H.; Garti, N.; Kamyshny, A. *J. Cryst. Growth* **1999**, *198/9 (II)*, 1365-1370.

(39) Popovitz-Biro, R.; Wang, J. L.; Majewski, J.; Shavit, E.; Leiserowitz, L.; Lahav, M. *J. Am. Chem. Soc.* **1994**, *116*, 1179-1191.

(40) McCrone, W. C.; Fox, D.; Labes, M. M.; Weissberger, A., Eds.; Interscience: New York, 1965; Vol. 2, pp 725-767.

(41) Almarsson, O.; Hickey, M. B.; Peterson, M. L.; Morissette, S. L.; Soukasene, S.; McNulty, C.; Tawa, M.; MacPhee, J. M.; Remenar, J. F. *Cryst. Growth & Design* **2003**, *3*, 927-933.

(42) Borka, L.; Haleblian, J. K. *Acta Pharmaceutica Jugoslavica* **1990**, *40*, 71-94 and references therein.

(43) Gavezzotti, A. *Acc. Chem. Res.* **1994**, *27*, 309-314.

(44) Lommerse, J. P. M.; Motherwell, W. D. S.; Ammon, H. L.; Dunitz, J. D.; Gavezzotti, A.; Hofmann, D. W. M.; Leusen, F. J. J.; Mooij, W. T. M.; Price, S. L.; Schweizer, B.; Schmidt, M. U.; van Eijck, B. P.; Verwer, P.; Williams, D. E. *Acta. Cryst B - Struct. Sci.* **2000**, *56*, 697-714.

(45) Price, S. L. *Advanced Drug Delivery Reviews* **2004**, *56*, 301-319.

(46) Amidon, G. L.; Lennernas, H.; Shah, V. P.; Crison, J. R. *Pharm. Res.* **1995**, *12*, 413-420.

(47) Kobayashi, M.; Kobayashi, T.; Cho, Y.; Kaneko, F. *Makromol. Chemie, Macromol. Symp.* **1986**, *5*, 1-20.

(48) Blagden, N.; Davey, R. J.; Lieberman, H. F.; Williams, L.; Payne, R.; Roberts, R.; Rowe, R.; Docherty, R. *J. Chem. Soc. - Far. Trans.* **1998**, *94*, 1035-1044.

(49) Rajam, S.; Heywood, B. R.; Walker, J. B. A.; Mann, S.; Davey, R. J.; Birchall, J. D. *J. Chem. Soc.; Far. Trans.* **1991**, *87*, 727-734.

(50) DiMasi, E.; Olszta, M. J.; Patel, V. M.; Gower, L. B. *CrystEngComm* **2003**, *5*, 346-350.

(51) Alamo, R. G.; Kim, M. H.; Galante, M. J.; Isasi, J. R.; Mandelkern, L. *Macromol.* **1999**, *32*, 4050-4064.

(52) Sjolin, C. *J. Agricultural & Food Chem.* **1972**, *20*, 895.

(53) Cardew, P. T.; Davey, R. J.; Ruddick, A. J. *J. Chem. Soc. - Far. Trans. II* **1984**, *80*, 659-668.

(54) Bernstein, J.; Davey, R. J.; Henck, J. O. *Angewandte Chemie - Int. Ed.* **1999**, *38*, 3441-3461.

(55) Gibbs, J. *On the Equilibrium of Heterogeneous Substances*: New York, 1928; Vol. 1.

(56) Frenkel, J. *Kinetic Theory of Liquids*; Oxford University Press: Oxford, 1946.

(57) Rodebush, W. *Chem. Revs.* **1949**, *44*, 269-276.

(58) Lothe, J.; Pound, G. *J. Chem. Phys.* **1962**, *36*, 2080-.

(59) Lothe, J.; Pound, G. In *Nucleation*; Zettlemoyer, M., Ed.: New York, 1969; p 120.

(60) Reiss, H. *Adv. Coll. & Interf. Sci.* **1977**, *7*, 1-66.

(61) Russel, K.; Lothe, J.; Pound, G.; Proceedings of the International Symposium on Condensation and Evaporation of Solids Rutner, G., Hirth, Gordon & Breach, Ed.: New York., 1964.

(62) Zeldovich, J. *Acta Physicochim* **1943**, *18*, 1.

(63) Chan, K. S.; Lee, J. K.; Shiflet, G. J.; Russell, K. C.; Aaronson, H. I. *Metallurgical Transactions A: Physical Metallurgy and Materials Science* **1978**, *9A*, 1016-1017.

(64) Sigsbee, R.; Pound, G. *Adv. Coll. & Interf. Sci.* **1967**, *1*, 335.

(65) Venables, J. A. *Thin Solid Films* **1973**, *18*, S11-14.

(66) Shizgal, B.; Barrett, J. C. *J. Chem. Phys.* **1989**, *91*, 6505-6518.

(67) Chukanov, V. N.; Korobitsin, B. A. *High Temperatures - High Pressures* **1997**, *29*, 319-325.

(68) Wulff, G. *Z Kristallogr.* **1901**, *34*, 449.

(69) Gibb, J. *On the Equilibrium of Heterogeneous Substances p 55*; Longmans: New York, 1928; Vol. 1.

(70) Curie, P. *Bull. Soc. Franc. Mineral* **1885**, *8*, 49.

(71) Royer, L. *Bull. Soc. Franc. Mineral* **1928**, *51*, 7.

(72) Cooper, S. J.; Sessions, R. B.; Lubetkin, S. D. *J. Am. Chem. Soc.* **1998**, *120*, 2090-2098.

(73) Backov, R.; Lee, C. M.; Khan, S. R.; Mingotaud, C.; Fanucci, G. E.; Talham, D. R. *Langmuir* **2000**, *16*, 6013-6019.

(74) Volkmer, D.; Fricke, M.; Vollhardt, D.; ., S. S. *J. Chem. Soc., Dalton Trans.* **2002**, *24*, 4547-4554.

(75) Ouyang, J. M.; P., D. S. *Dalton Trans.* **2003**, *14*, 2846-2851.

(76) Rapaport, H.; Kuzmenko, I.; Berfeld, M.; Kjaer, K.; Als-Nielsen, J.; Popovitz-Biro, R.; Weissbuch, I.; Lahav, M.; Leiserowitz, L. *J. Phys. Chem. B* **2000**, *104*, 1399-1428.

(77) Lahav, M.; Landau, E. M.; Grayer Wolf, S.; Levanon, L.; Leiserowitz, L.; Sagiv, J. *J. Am. Chem. Soc.* **1989**, *111*, 1436-1445.

(78) Naka, K.; Chujo, Y. *Chem. Mat.* **2001**, *13*, 3245-3259.

(79) Jamieson, M. J.; Cooper, S. J.; Miller, A. F.; Holt, S. A. *Langmuir* **2004**, *20*, 3593-3600.

(80) Cooper, S. J. *Langmuir* **2002**, *18*, 3749-3753.

(81) Lahav, M.; Weissbuch, I.; Popovitz-Biro, R.; Levanon, M.; Leiserowitz, L.; Sagiv, J. *Mol. Cryst. Liq. Cryst.* **1986**, *134*, 323-325.

(82) Weissbuch, I.; Berkovic, G.; Yam, R.; Als-Nielsen, J.; Kjaer, K.; Lahav, M.; Leiserowitz, L. *J. Phys. Chem.* **1995**, *99*, 6036-6045.

(83) Weissbuch, I.; Berkovic, G.; Leiserowitz, L.; Lahav, M. *J. Am. Chem. Soc.* **1990**, *112*, 5874-5875.

(84) Popovitz-Biro, R.; Majewski, J.; Wang, J. L.; Leiserowitz, L.; Lahav, M.; Kjaer, K.; Als-Nielsen, J. *Thin Films*, *20*, 145-181.

(85) Maloney, K.; Schief, W. R.; Pack, D. W.; Frey, W.; Arnold, F. H.; Vogel, V. *Coord. Chem. Rev.* **1999**, *183*, 3-18.

(86) Halpin-Healy, T.; Zhang, Y. C. *Phys. Reps. - Rev. Sec. Phys. Letts.* **1995**, *254*, 215-415.

(87) Burton, W. K.; Cabrera, N.; Frank, F. C. *Nature* **1949**, *163*, 398-399.

(88) Burton, W.; Cabrera, N.; Frank, F. *Phil. Trans. of the Royal Soc.of London, A - Math. & Phys. Sci.* **1951**, *243*, 299-358.

(89) Yamaguchi, H.; Homma, Y. *J. Cryst. Growth* **1999**, *201*, 124-127.

(90) Yin, L.; Li, M.; Sun, D.; Li, F.; Hao, Z.; Dong, X. *J. Mats. Sci. & Tech.* **2002**, *18*, 66-68.

(91) Singh, R.; Samanta, S.; Narlikar, A.; Trigunayat, G. *J. Cryst. Growth* **2000**, *213*, 70-74.

(92) Cooper, S. J. *CrystEngComm* **2001**, *56*, 1-4.

(93) Skoda, W.; van den Tempel, M. *J. Coll Sci.* **1963**, *18*, 568-584.

(94) Davey, R. J.; Hilton, A. M.; Garside, J.; de la Feunte, M.; Edmondson, M.; Rainford, P. *J. Chem. Soc. - Far. Trans.* **1996**, *92*, 1927-1933.

(95) Lim, G. K.; Wang, J.; Ng, S. C.; Gan, L. M. *Langmuir* **1999**, *15*, 7472-7477.

(96) Ostwald, W. *Lehrbruck der Allgemeinen Chemie*: Leipzig, Germany., 1896; Vol. 2 Part 1.

(97) Ostwald, W. *Z. Phys. Chem.* **1897**, *22*, 289.

(98) Ng, J. D.; Lorber, B.; Witz, J.; Theobald, D. A.; Kern, D.; Giege, R. *J. Cryst. Growth* **1996**, *168*, 50-62.

(99) Boistelle, R.; Astier, J. P. *J. Cryst. Growth* **1988**, *90*, 14-30.

(100) Schmitt, V.; Cattelet, C.; Leal-Calderon, F. *Langmuir* **2004**, *20*, 46-52.

(101) Solans, C.; Esquena, J.; Forgiarini, A. M.; Uson, N.; Morales, D.; Izquierdo, P.; Azemar, N.; Garcia-Celma, M. J. *Surfactant Science Series* **2003**, *109*, 525-554.

(102) In *Surfactants in Cosmetics*; Rieger, M.; Rhein, L. D., Eds.; Marcel Dekker: New York, 1997; pp 105-125.

(103) In *Modern Aspects of Emulsion Science*; Binks, B. P., Ed.; Royal Society of Chemistry: Cambridge, 1998; pp 395-426.

(104) Kunieda, H.; Friberg, S. E. *Bull. Chem. Soc. Japan* **1981**, *54*, 1010-1014.

(105) Kunieda, H.; Shinoda, K. *Bull. Chem. Soc. Japan* **1982**, *55*, 1777-1781.

(106) Friberg, S.; Solans, C. *J. Coll & Interf. Sci.* **1978**, *66*, 367-368.

(107) Sagitani, H. In *Organized Solutions*; Friberg, S. E.; Lindman, B., Eds.; Marcel Dekker: New York, 1992; pp 259-271.

(108) Forgiarini, A.; Esquena, J.; González, C.; Solans, C. *Prog. Colloid Polym. Sci.* **2000**, *115*, 36-39.

(109) Rang, M. J.; Miller, C. A. *J. Coll & Interf. Sci.* **1999**, *209*, 179-192.

(110) Forgiarini, A.; Esquena, J.; González, C.; Solans, C. *Langmuir* **2001**, *17*, 2076-2083.

(111) Forgiarini, A.; Esquena, J.; González, C.; Solans, C. *Prog. Coll. Polym. Sci.* **2001**, *118*, 184-189.

(112) Fennel Evans, D.; Wennerstrom, H.; VCH: New York, 1994; pp Chapter 11, 470-473.

(113) Griffin, W. C. *J. Soc. Cosmetic Chem.* **1954**, *5*, 249.

(114) Bibette, J.; Leal-Calderon, F.; Schmitt, V.; Poulin, P. *Emulsion Science: Basic Principles - An Overview*; Springer-Verlag: Berlin, 2003.

(115) Higgins, J. S.; Benoit, H. C. *Polymers and Neutron Scattering*; Clarendon Press, 1994.

(116) Lekner, J. *Theory of Reflection*; Martinus Nijhoff: Dordrecht, 1987.

(117) Dosch, H. *Critical Phenomena at Surfaces and Interfaces: Evanescent x-ray and neutron scattering*; Springer, 1992; Vol. 126.

(118) Dietrich, S.; Haase, A. *Phys. Reps.* **1995**, *260*, 1-138.

(119) Penfold, J.; Richardson, R. M.; Zarbakhsh, A.; Webster, J. R. P.; Bucknall, D. G.; Rennie, A. R.; Jones, R. A. L.; Cosgrove, T.; Thomas, R. K.; Higgins, J. S.; Fletcher, P. D. I.; Dickinson, E.; Roser, S. J.; McLure, I. A.; Hillman, A. R.; Richards, R. W.; Staples, E. J.; Burgess, A. N.; Simister, E. A.; White, J. W. *J. Chem. Soc. - Far. Trans.* **1997**, *93*, 3899-3917.

(120) Koester, L. *Neutron Interferometry*; Oxford Science Publications, 1979.

(121) Sears, V. F. *Neutron News* **1992**, *3*, 29-37.

(122) Born, M.; Wolf, E. *Principles of Optics*; Pergamon Press, 1980.

(123) Abeles, F. *J. de Phys.* **1950**, *11*, 310.

(124) Ahn, D. J.; Berman, A.; Charych, D. *J. Phys. Chem* **1996**, *100*, 12455-12461.

(125) Weygand , M.; Kjaer, K.; Howes, P. B.; Wetzer, B.; Pum, D.; Sleytr, U. B.; Lösche, M. *J. Phys. Chem. B* **2002**, *106*, 5793-5799.

(126) Davey, R. J. *Nature* **2004**, *428*, 374-375.

(127) Cacciuto, A.; Auer, S.; Frenkel, D. *Nature* **2004**, *428*, 404-406.

(128) Volmer, M.; Weber, A. *Z. Phys. Chem.* **1926**, *119*, 277.

(129) Markov, I. V. *Crystal Growth for Beginners*, **1995**, World Scientific, N.J.

(130) Davey, R.J.; Garside, J. *From Molecules to Crystallizers, an Introduction to Crystallization*, **2000**, Oxford University Press.

Chapter 2

Crystallisation of DL-Aspartic Acid Under Nylon 6 Spread Films

2.1 Introduction and Objective

In this chapter, the crystallisation of DL-aspartic acid under nylon 6 spread films is investigated by neutron reflectivity. The neutron reflectivity data are supported by external reflectance FTIR and optical microscopy studies. A summary of the data presented in this chapter was recently published in Langmuir[1].

Landau et al. first reported the ability of a monolayer to induce highly specific crystallisation at the air-water interface[2]. The resulting crystallisation was thought to occur via the ordered surfactant transmitting a corresponding order to the adsorbed crystallising material. Mann et al.[3] reported the importance of stereochemical matching for calcite crystallisation beneath monolayers and others have detailed similar results for biologically important organic species[4-6]. Subsequent work[7-10] has also shown that the crystallisation rate can be maximised under less well-ordered, more compressible films, particularly if there is a lattice mismatch between the film and crystallising species.

Consequently, this chapter details an investigation of the crystallisation of an important amino acid, DL-aspartic acid, under a nylon 6 spread film, for which geometric matching does not occur. Nylon 6 is a good model compound for proteins, and in particular, is easily deuterated, to provide optimal contrast in neutron reflectivity studies.

The structure of nylon 6 6 spread films at the air-water interface is well documented. The analogous nylon 6 spread film is expected to behave in a similar manner. Lahav et al.[11] studied nylon 6 6 by grazing incidence X-ray diffraction (GIXD) at film concentrations of 1.5 mg m^{-2} and found chain-folded hydrogen-bonded sheets similar to those present in the bulk crystal. Within the sheets, the distance in the hydrogen-bond

direction is considerably longer than that in the chain direction, and hence a fibrillar-type texture is observed. The sheets are parallel to the water surface, with an average of 5 - 6 sheets stacking to produce a multilayer film, corresponding to a thickness of approximately 20 Å. Others[12,13] have shown by surface pressure, surface potential and compression hysteresis that the existence of microfibrils, promoted by hydrogen-bonding of the amide group, results in a collapse of the film into a 3 dimensional structure at only 60 $Å^2$ per repeat unit (compared to a limiting area of ~30 $Å^2$ per repeat unit). External reflection FTIR studies on this system confirmed the presence and same orientation of the hydrogen-bonded sheets at surface concentration of 0.6 to 5.5 mg m^{-2}, whilst ESEM studies showed the fibrils to be ~ 600 - 800 nm in length and 20 nm wide[14]. The fibrils are interspersed by the aqueous phase, becoming increasingly close-packed as the film is compressed. Full fibrillar coverage is only achieved, however, by overcompressing to surface concentrations of approximately 4 mg m^{-2}.

There is comprehensive literature on the engineering of crystalline architectures at the air-aqueous interface, using techniques such as FTIR[15,16], GIXD[17], fluorescence probe microscopy[18] and Brewster angle microscopy[19]. In contrast, there is very little information regarding the depth-profiling of crystallising species beneath monolayers, which neutron reflectivity can provide. A recent study by Weygand et al.[20] used a combination of X-ray and neutron reflectivity to provide evidence for a structural reorganisation of the phospholipid headgroups during the binding and recrystallisation of a bacterial S-layer protein, but I am not aware of any other studies of crystallisation by neutron reflectivity.

2.2 Neutron Reflectivity

2.2.1 Scattering Length Densities

Recall from chapter 1 that the scattering length density (SLD), ρ, of a material is given by:

$$\rho = \sum b_i n_i \qquad \text{[Eqn. 1.50]}$$

where n_i is the number density of atomic species *i*, and $\sum b_i$ is the sum of the coherent scattering lengths of atoms in species i.

The neutron scattering length *b* is a nuclear property describing the interaction between the neutron and the atomic nucleus. All values of *b* used in the calculations in this chapter are as listed in Neutron News[21].

For hydrogenous and heavy water, the scattering length densities are -0.56×10^{-6} Å^{-2} and 6.39×10^{-6} Å^{-2}, respectively, so as mentioned in chapter 1, an appropriate combination of H_2O and D_2O (92.05 : 7.95) will give an aqueous phase of zero effective scattering length density (ρ). This is referred to as null reflecting water (NRW).

2.2.2 Consideration of Labile Protons

For both nylon 6 (N6) and DL-aspartic acid (ASP), the value of ρ will depend on the nature of the subphase. This is due to labile protons; for N6 the amide proton is labile. For ASP, the labile protons are contained in the carboxylic acid, carboxylate and ammonium groups. NRW is composed of 92.05 % H_2O and 7.95% D_2O, so for species on NRW, it is assumed that 92.05% of the labile deuterium species will exchange with the subphase and as such the deuterated nylon 6 (D-N6) layer is assumed to be principally $C_6D_{10}HNO$. Hence hydrogen/deuterium exchange is unlikely to make a considerable impact on the composition of the undeuterated nylon 6 (H-N6) spread film or DL-aspartic acid (H-ASP). For hydrogenous species on (or dissolved in) D_2O, there will be significant proton exchanges, which must be considered in the calculation of scattering length densities for these species.

The labile proton exchanges with the subphase are illustrated in figures 2.1 a & 2.1b.

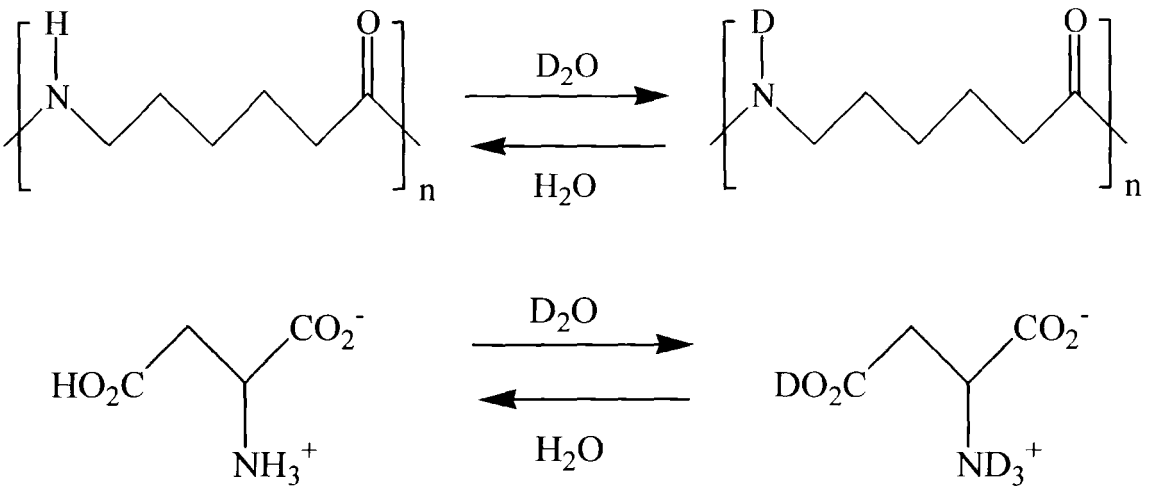

Figures 2.1 a (top) & 2.1b (bottom). Illustration of the impact of labile proton exchange between the subphase and nylon 6 and DL-aspartic acid, respectively.

The scattering length density values calculated for the species discussed in this section for different subphases (D_2O or NRW) are given in table 2.1. Amorphous nylon 6 has a less dense structure than its crystalline analogue, hence two different values of ρ are given for this material.

Material	ρ on NRW/10^{-6} Å^{-2}	ρ on D_2O/10^{-6} Å^{-2}
Crystalline D-N6	7.39	8.00
Amorphous D-N6	6.92	7.47
Crystalline H-N6	0.88	1.52
Amorphous H-N6	0.83	1.42
H-ASP	2.46	5.54
D-ASP	4.78	7.87

Table 2.1. Values of scattering length density, ρ, for nylon 6 and DL-aspartic acid on different subphases.

The scattering length density of the subphase will also be affected by the solute. This effect will be well within experimental error, however, as even at the highest solute concentration discussed in this work, the DL-aspartic acid represents only approximately 2% of the total mass of solution. It has therefore been excluded from any calculations. This value of ~2% will also decrease with time, becoming even less significant as the crystallisation progresses.

Scattering length densities for the systems studied in this chapter are given in table 2.2.

Material	System 1. H-N6 on D_2O ρ / 10^{-6} Å^{-2}	System 2. H-N6 on sat H-ASP in D_2O ρ / 10^{-6} Å^{-2}	System 3. D-N6 on sat H-ASP in D_2O ρ / 10^{-6} Å^{-2}	System 4. H-N6 on 125% ss H-ASP in D_2O ρ / 10^{-6} Å^{-2}	System 5. D-N6 on 150% ss H-ASP in D_2O ρ / 10^{-6} Å^{-2}	System 6. D-N6 on 150% ss H-ASP in NRW ρ / 10^{-6} Å^{-2}
D-N6 (amorphous)	-	-	8.00 (7.47)	-	8.00 (7.47)	7.39 (6.92)
H-N6 (amorphous)	1.52 (1.42)	1.52 (1.42)	-	1.52 (1.42)	-	-
H-ASP	-	5.54	5.54	5.54	5.54	2.46
D_2O	6.39	6.39	6.39	6.39	6.39	-
NRW	-	-	-	-	-	0.00

Table 2.2. Scattering length densities, ρ, considering the influence of labile protons for the species discussed in this chapter.

2.2.3 Neutron Reflectivity Data Fitting

The theory behind neutron reflectometry was introduced in Chapter 1. Brief details of the data fitting method employed here are detailed below. More intensive mathematical treatment of this data fitting method is available elsewhere[22-25]. Data were fitted by the

Abeles[26,27] solution to the optical matrix method[28]. Recall that, a characteristic matrix is defined for each layer. For the mth layer, the matrix is:

$$c_m = \begin{bmatrix} \cos\beta_m & -(i/\kappa_m)\sin\beta_m \\ -i\kappa_m \sin\beta_m & \cos\beta_m \end{bmatrix} \qquad \text{[Eqn. 1.52]}$$

where $\kappa_m = N_m \sin\theta_m$

and $$\beta_m = 2\pi\left(\frac{d}{\lambda}\right)N_m \sin\theta_m \qquad \text{[Eqn. 1.49]}$$

d is the layer thickness, θ_m is the angle of the incident beam, β_m is the optical path length of layer m and N_m is the refractive index of layer m. Optical matrices are calculated for each individual layer and incorporated[29] with a Gaussian roughness[30]:

$$r_m = r_m^f \exp(-0.5 Q_m Q_{m-1} < \sigma^2 >) \qquad \text{[Eqn. 2.1]}$$

where $<\sigma^2>$ is the mean squared roughness and r_m^f is the Fresnel reflectance of the mth layer.

Data were fitted by the Abeles solution to the optical matrix method, using LAYERS, an enhanced version of RWRDOC. This is in-house software written by Prof. R.W. Richards, which enables the user to modify the roughness values for each individual layer, in addition to layer thickness and SLD values.

LAYERS gives a fit index, which is calculated from the following:

$$R_e = \frac{1}{N-p}\sum (R_{\exp}(Q) - R_{calc}(Q))^2 \qquad \text{[Eqn. 2.2]}$$

where N = no of data points, p = number of parameters in the model, and $R_{exp}(Q)$ and $R_{calc}(Q)$ are experimental and calculated reflectivities at scattering vector Q. While data fitting, the aim was to keep R_e as low as possible. Typically, the R_e value for a best fit lies in the order of 10^{-2}.

LAYERS treats air as having a scattering length density of 0 by default. Air is denoted as layer 1, with subsequent layers numbered sequentially as illustrated in figure 2.2.

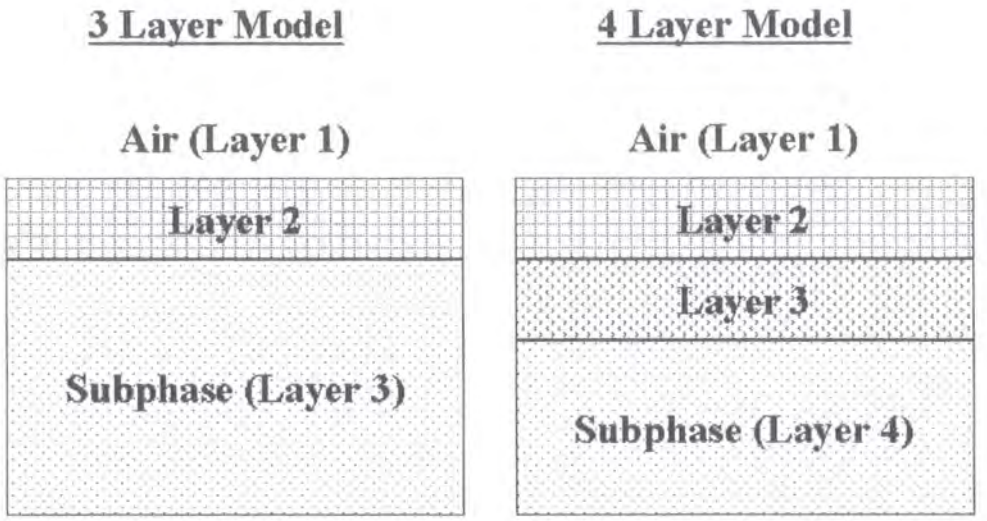

Figure 2.2. Schematic illustrating the numbering of different layers as treated by the model fitting program, LAYERS.

2.2.4 Determination of Layer Composition

The SLD, ρ, of any given layer is the sum of the total scattering length of the components present, i.e. for this system:

$$\rho = \varphi_{N6}\rho_{N6} + \varphi_{Water}\rho_{Water} + \varphi_{Asp}\rho_{Asp} \qquad \text{[Eqn. 2.3]}$$

where φ_i is the volume fraction of component i. For this system:

$$\varphi_{Asp} + \varphi_{Water} + \varphi_{N6} = 1 \qquad \text{[Eqn. 2.4]}$$

Equations 2.3 and 2.4 are combined and rearranged to:

$$\varphi_{Asp} = \frac{\rho - \varphi_{N6}\rho_{N6} - \rho_{Water}(1 - \varphi_{N6})}{\rho_{Asp} - \rho_{Water}} \quad \text{[Eqn. 2.5]}$$

$$\varphi_{Water} = \frac{\rho - \varphi_{N6}\rho_{N6} - \rho_{Asp}(1 - \varphi_{N6})}{\rho_{Water} - \rho_{Asp}} \quad \text{[Eqn. 2.6]}$$

where ρ is the effective layer scattering length density derived from LAYERS, and ρ_i and φ_i are the SLD and volume fraction of component i, respectively. Except in cases where one component has a volume fraction equal to zero, these equations have an infinite number of solutions. However, it can be assumed that the insoluble nylon 6 is entirely contained in layer 2, and so this allows calculation of φ_{N6} for this layer. Substituting this calculated value for φ_{N6} in equations 2.5 and 2.6 produces a unique solution for the volume fractions of DL-aspartic acid and water. This is because the thickness of the layer is derived from LAYERS, and the quantity of N6 added is known.

2.2.5 Amorphous vs. Crystalline Nylon 6

Volume fraction values for nylon 6 in the film layer were calculated assuming it was 100% crystalline, or 100% amorphous, with the values for the latter case given in brackets in italic. It is probable that the nylon 6 is more crystalline than amorphous, and the data displayed later in this chapter support this.

For H-N6, assuming no intervening water, spread film thicknesses of 16 Å and 17 Å are expected for the crystalline and amorphous cases, respectively, based on the quantity of nylon 6 added. For the deuterated species, thicknesses of 14 Å and 15 Å are expected for the crystalline and amorphous species respectively.

2.3 Experimental

2.3.1 Neutron Reflectometer (SURF) and Data Acquisition

Neutron reflectivity was introduced in section 1.5.2. Neutron reflectivity data were acquired on the SURF neutron reflectometer at the Rutherford Laboratories, Oxon (see figure 2.3). In neutron reflectivity there are two possible modes of measurement. The fundamental variable, the wavevector, k, depends on θ and λ. Data can be acquired by fixing λ and measuring θ, or by fixing θ and measuring λ. SURF is typical of many time-of-flight neutron reflectometers across the world, based on the latter of these data acquisition methods.

SURF was specifically designed for the study of liquid surfaces and has a horizontal sample geometry and an inclined beam 1.5° from the horizontal. This is the region applicable to analysis of monolayer structure at the air-water interface[31]. The neutrons pass through choppers to select the wavelength range. This is collimated by coarse jaws and then finely collimated between two sets of jaws to achieve the beam size and required resolution.

The beam profile and intensity is monitored before reaching the sample using a scintillator detector. Post-sample, the background noise is suppressed by two further slits. SURF has a wavelength range of 0.55 - 6.8 Å, with the disc chopper working at 50 Hz. At 50 Hz, this yields a wavevector range, Q (= 2k), range of 0.026 to 0.60 $Å^{-1}$, which is the optimum range for liquid surface measurements.

Data were acquired at fixed incident angles of 0.8° and 1.5°. Data at the 2 incident angles were combined into a single reflectivity profile and calibrated with respect to D_2O data. Each combined data profile acquisition time was approximately 2 hours.

Data were acquired with Drs. Sharon Cooper and Aline Miller. The station manager was Dr. Stephen Holt.

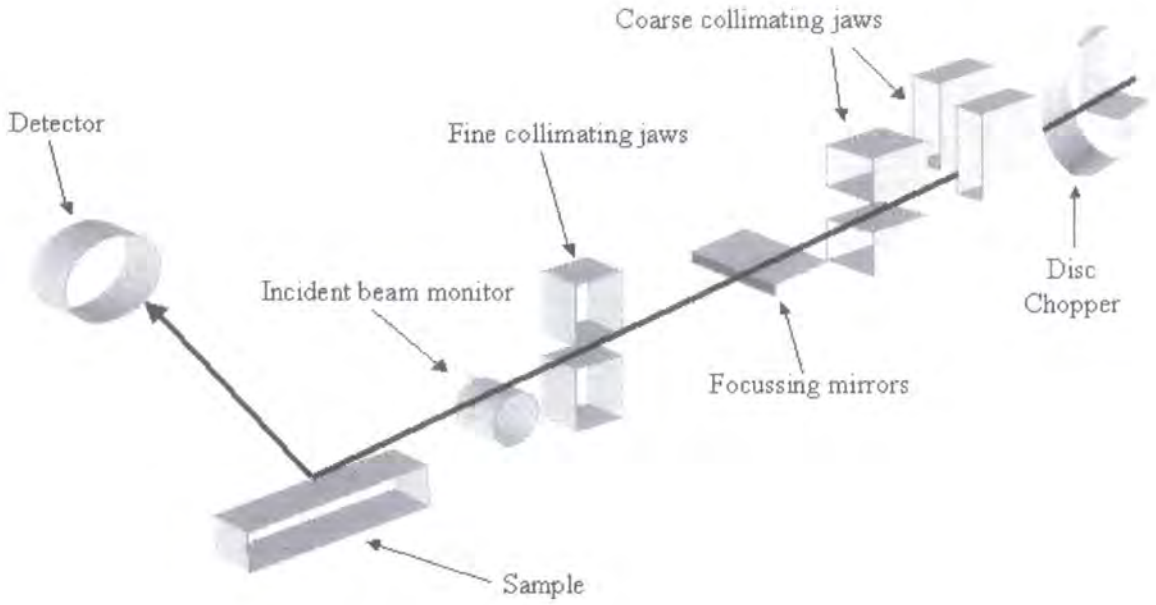

Figure 2.3. Diagram of SURF time-of-flight neutron reflectometer at the ISIS, Rutherford Appleton Laboratory.

Crystallisation experiments were performed in a rectangular Nima Langmuir trough (30 x 20 cm), which was mounted on an anti-vibration table and enclosed by a Perspex box to minimise contamination, evaporation and H/D exchange between the subphase and atmosphere. The well-collimated neutron beam entered and exited the enclosing box via quartz windows.

2.3.2 Materials

The following materials were used, with no further purification required. Hydrogenous DL-aspartic acid (99%, BDH), deuterated DL-aspartic acid (Aldrich), hydrogenous nylon 6 (Aldrich), and heavy water (Aldrich). Deuterated nylon 6 was polymerised by standard methods[32] from deuterated caprolactam (Aldrich) by Dr. Aline Miller at the Cavendish Laboratories, Cambridge.

2.3.3 Supersaturated Solutions

Solubility of DL-Aspartic Acid

Recall that the percentage supersaturation, μ%, is defined as:

$$\mu\% = \frac{s - s_{sat}}{s_{sat}} \times 100\% \qquad \text{[Eqn. 1.4]}$$

where s is the quantity of material in solution and s_{sat} is the literature saturation level.

The solubility of DL-aspartic acid at 298K is 0.778 g per 100 g water. Other values for s_{sat} are derived from the relationship:

$$\ln(S) = -3568.8\left(\frac{1}{T}\right) + 11.734 \qquad \text{[Eqn. 2.7]}$$

where S = solubility of DL-aspartic acid in 100g water, since the solubility data given in the literature[33] are consistent with this equation, as shown in figure 2.4.

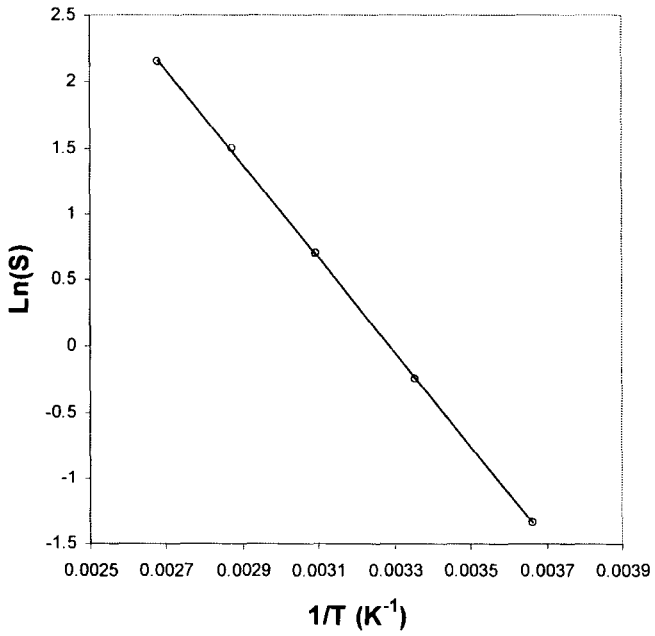

Figure 2.4. Graph of the solubility of DL-aspartic acid in water at various temperatures[33].

Preparation of Supersaturated Solutions

DL-aspartic acid solutions were prepared by weighing the required amount of material and adding ultrapure water with a resistivity of 18 MΩ cm provided by a UHQ water filtration unit. This mixture was heated on a thermostated hot plate to at least 10 °C above the saturation temperature for 2 hours. The resulting solution was filtered through a 0.2 μm filter to ensure removal of any undissolved nuclei, and the filtrate was returned to 10 °C above the saturation temperature for a further hour. This solution was allowed to cool slowly to ambient temperature. Typically, solutions were considered suitable for crystallisation experiments if no spontaneous formation of crystals was observed after >12 hours.

2.3.4 Crystallisation Experiments

Langmuir Trough

Except in the case of ER-FTIR experiments, all planar crystallisation studies were performed in Nima PTFE troughs (see example in figure 2.5). The sample area dimensions are ~12 x 8 cm or 30 x 20 cm, which hold ~ 100 cm^3 or 250 cm^3 solution, respectively when filled, so that a convex meniscus is formed. The smaller trough has custom-made legs and a partial glass base to enable light transmission for microscopy studies.

The barriers are mechanically driven together to enable compression of spread films. The barrier positions are measured manually at their widest point, and this value inputted in the software. The barrier positions can then be controlled through the software, which automatically calculates the area between the barriers. This also allows calculation of the surfactant limiting area through isotherm experiments.

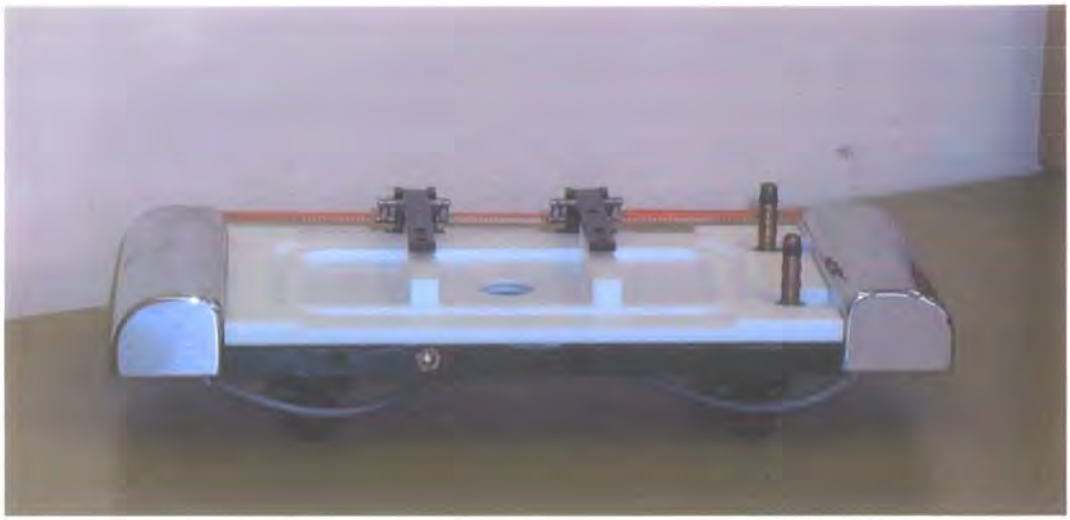

Figure 2.5 Image of 12 x 8 cm Nima Langmuir trough.

Cleaning of Trough and Subphase

The trough was cleaned twice with hot (~95 °C) UHQ water and wiped with chloroform. Prior to monolayer deposition, the subphase surface was cleaned with a suction unit and the surface was considered sufficiently clean when driving the barriers together resulted in a maximum surface pressure change of less than 0.5 mN/m.

2.3.5 Deposition of Spread Films

Film Solutions

Film materials were dissolved in a 2:3 (v/v) formic acid/chloroform mixture at a concentration of approximately 1 mg/ml. Solutions were added by microsyringe and the solvent allowed to evaporate, leaving a residual monolayer or film. Following evaporation of solvent, the barriers were driven together until the desired surface pressure of the spread film or monolayer was attained.

Surface Pressure Measurements

The surface pressure of the spread films was measured with a Wilhelmy plate balance. This was controlled through the Nima software and calibrated by ensuring that a 100

mg weight gave a tensiometer reading of 48.3 mN/m. Surface pressure readings were also checked on pure water, where a reading of 72 mN/m is expected at ambient temperature. The Wilhelmy plate was a purpose made filter paper, which dipped into the trough solution and was connected to the balance with a copper 'S' wire. A new plate was used for each experiment.

The nylon 6 films were spread onto ultrapure water and DL-aspartic acid solution subphases contained in the Nima Langmuir trough, which was thermostated via a water bath to a temperature of 25 °C ± 0.2°C. A full compression cycle of the subphase was completed to ensure a clean surface, prior to the addition of the nylon 6 solution. 30 µl of the solution, which contained ~ 1 mg/ml of nylon in the 2:3 (v/v) formic acid/chloroform solution, were added drop-wise to the subphase surface. After the solvent had evaporated (~ 5 minutes), the trough barriers were driven together to give a surface pressure, π = 3 m Nm^{-1}, corresponding to a surface concentration of ~1.8 mg/m^2. The nylon 6 films were relatively stable, equilibrating at π ~ 2.5 m Nm^{-1}.

2.3.6 Optical Microscopy

Optical microscopy is an invaluable technique in crystallisation studies. By using polarised light, the technique can assess the refractive index variation within a sample, i.e. the birefringence. This also enables the scientist to study liquid crystals and assess homogeneity of samples (see chapter 4).

The equipment used was an Olympus MX50 (see figure 2.6) equipped with a fixed 10x lens and optional 10x and 50x glass objectives, described in this thesis as low and high magnification, respectively. These enable observation of features greater than ~ 2 µm. The microscope also has a first order retardation plate and variable light flux to complement the light polariser.

Optical microscopy was also used to study crystal morphology and orientation (chapter 3) and the larger emulsion droplet sizes (chapters 4 and 5). It was also used in conjunction with a controlled temperature stage to assess ice crystallisation temperatures and verify that liquid crystals were not present in the emulsions (chapter 4).

Figure 2.6. Image of optical microscope, equipped with Linkam controlled temperature stage.

2.3.7 FTIR Spectroscopy

A Brief Introduction to IR Spectroscopy

The infrared region of the electromagnetic spectrum (λ = 100 to 1 μm) corresponds to the energies of molecular vibrations and rotations. Electromagnetic radiation with wavelengths between 16 and 2.5 μm corresponds to the separation between adjacent vibrational energy states in molecules, and is the region of most use for structure determination.

The IR beam is composed of a range of frequencies. As these are absorbed, the molecule is excited from its ground state to a higher one. This causes chemical groups to vibrate and rotate in one of a few modes (bending, twisting, wagging, scissoring, etc). Each vibrational mode has a set frequency as determined by the quantum mechanical nature of the chemical system. Infrared spectroscopy is therefore well suited to the identification of specific chemical groups. Each compound typically has a large number of specific vibrations available to it, which means an FTIR spectrum can differentiate a sample from almost any other compound.

Traditionally, FTIR spectroscopy was used by chemists and in quality control environments as a method of product identity confirmation. The development of new technologies, however, such as ATR-FTIR, FTIR microscopy and external reflection FTIR, among others, mean this type of spectroscopy is now widely used to probe more specialist system features.

External Reflectance FTIR (ER-FTIR)

Early work using external reflectance infrared was limited to thin films on solid substrates. The advent of Fourier transform instruments, and improvements in detector technology now allow the acquisition of external reflectance spectra from monolayers with good signal-to-noise over a reasonable time period. ER-FTIR is now a powerful technique commonly applied to study monolayers on aqueous subphases[15,34-40] and metallic substrates[41-43] and has even been applied to monolayers and sub-monolayers on semiconductors[44-46] and glassy carbon[46,47].

A typical experimental set-up is illustrated in figure 2.7. There are fixed mirrors after the source and in front of the detector. The source beam is reflected up to a concave mirror and onto the sample. The reflected signal from the sample is then reflected towards the final mirror, which directs the signal into the detector.

The angle of incidence, Φ, is measured relative to the surface normal and can be varied between ~5 and 85°, to best suit the substrate used.

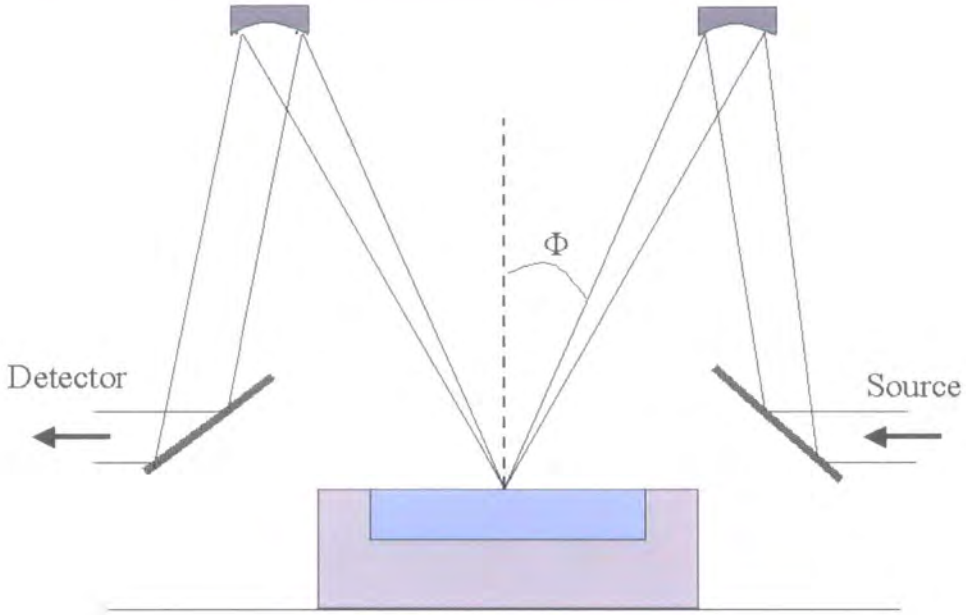

Figure 2.7. Illustration of ER-FTIR accessory.

ER-FTIR Equipment

External reflection FTIR studies were undertaken using a Spec-Ac monolayer accessory (figure 2.8) in the sample chamber of a Nicolet Nexus spectrometer (figure 2.9). The spectrometer was equipped with a liquid nitrogen cooled HgCdTe detector and operated with Omnic software. The Spec-Ac accessory is equipped with a removable Teflon trough, which has a manually moveable barrier for compression of the spread films.

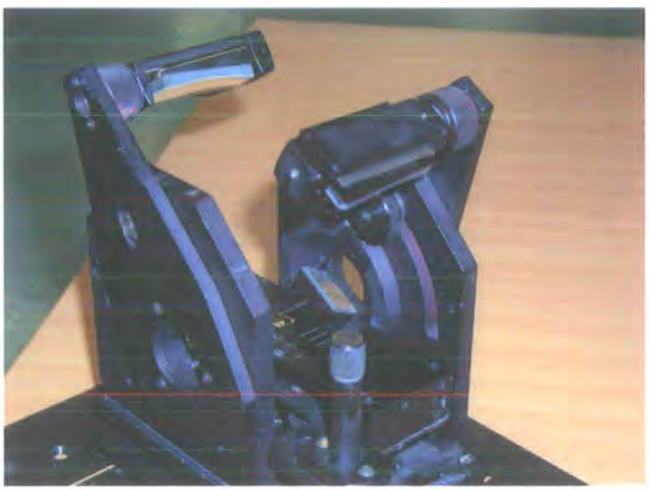

Figure 2.8. Image of Spec-Ac external reflectance accessory. The concave mirrors and the planar mirror after the source are visible.

The HgCdTe detector, commonly described as MCT-A, offers better sensitivity than the MCT-B equivalent, but at the expense of spectral range (4000 – 750 cm^{-1} versus 4000 - 650 cm^{-1}).

ER-FTIR Data Collection

N6 Films were spread from ~1 mg ml^{-1} formic acid/chloroform (2:3 v/v) solutions. Sufficient quantity of the film material was spread on a clean subphase surface and compressed to achieve the required surface pressures. 512 scans were collected for each spectrum from 4000 to 650 cm^{-1} at a resolution of 4 cm^{-1}. The spectra were ratioed against the background spectrum taken on the clean subphase surface immediately prior to the film spreading. All the resulting spectra display raw data.

Figure 2.9. Picture of Nicolet Nexus FTIR bench.

For the monolayer on water experiments, Φ was fixed at 30°, but this can be varied as appropriate to enable data collection from various species. The mirrors at the top of the arms were adjusted until the maximum signal was received at the detector. Typically, 512 scans were acquired, but 128 scans were sufficient for many of the exploratory experiments.

An initial background file was acquired from a blank (no monolayer added) subphase and subtracted from the subsequent data. Hence data become increasingly affected

during lengthy experiments (>2 hours) by changes in atmospheric conditions over time, and bands attributed to carbon dioxide and water vapour begin to affect data quality and obscure sample bands in the same region.

2.4 Neutron Reflectivity Results

2.4.1 Nylon 6 on Heavy Water

Figure 2.10 shows the neutron reflectivity data acquired for H-N6 on pure heavy water (system 1). The solid line is the best model fit. The values derived from LAYERS are given in table 2.3, with calculated volume fractions, φ, for nylon 6 and water.

Timepoint	$\rho/10^{-6}$ Å^{-2}	Roughness/ Å	Thickness/Å	φ_{N6}	φ_{Water}
0 - 2 hrs	3.7	13	30	0.54 *(0.57)*	0.46 *(0.43)*

Table 2.3. SLD (ρ), roughness, layer thickness and volume fractions derived for H-N6 on D_2O (system 1). Volume fractions data in parentheses assume the N6 is 100% amorphous.

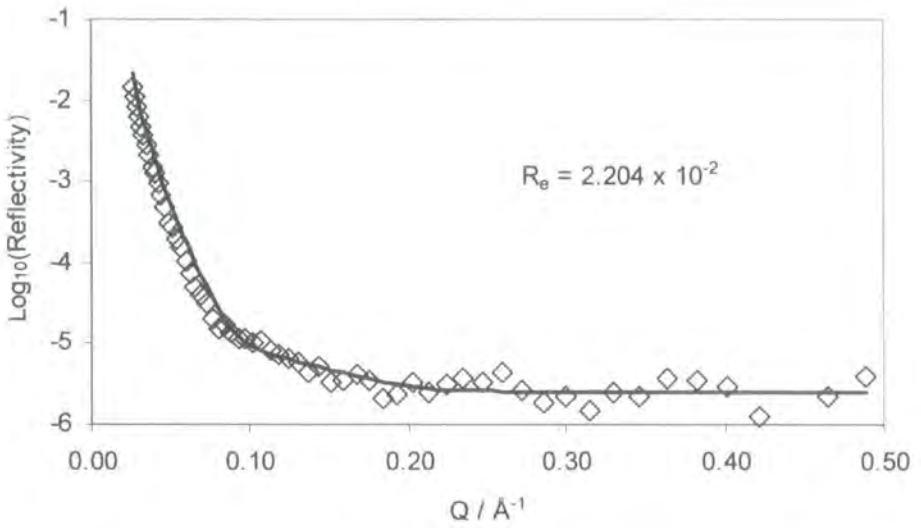

Figure 2.10. Neutron reflectivity profile and best fit (solid line) for H-N6 on pure D_2O.

The smooth nature of the best fit curve is consistent with a diffuse layer, i.e. there are no sharp interfaces for this system. The data are consistent with the findings summarised for nylon 6 6 in the introduction to this chapter. In particular, the volume fractions and thickness values derived from the best model fit are consistent with the fibrils being interspersed by the aqueous phase.

2.4.2 Saturated Systems

Two saturated systems were studied; H-N6 (system 2) and D-N6 (system 3) on H-ASP in D_2O. No crystallisation was observed (or expected) for these systems, and the data demonstrate that the effect of the solute on the spread N6 film is limited, since the results were similar to nylon 6 on water.

Timepoint	$\rho/10^{-6}$ Å^{-2}	Roughness/ Å	Thickness/ Å	φ_{N6}	φ_{Water}	φ_{Asp}
0-2 hrs	4.1	12	35	0.53 *(0.66)*	0.47 *(0.49)*	0.00 *(-0.15)*

Table 2.4. SLD, roughness, layer thickness and volume fractions (φ) derived for H-N6 on saturated H-ASP in D_2O (system 2). Volume fractions data in parentheses assume the N6 is 100% amorphous.

The best model fit data for system 2, hydrogenous nylon 6 on saturated DL-aspartic acid in D_2O, are presented in table 2.4, and further support the view that nylon 6 is principally crystalline for this system, because a negative volume fraction is derived for DL-aspartic acid if nylon 6 is assumed to be amorphous. The best model fit vs. observed data are illustrated in figure 2.11.

Best model fit data and observed vs. model data for system 3, deuterated nylon 6 on saturated H-ASP in D_2O, are illustrated in table 2.5 and figure 2.12. Once again, a

negative volume fraction is derived for DL-aspartic acid if the nylon 6 is assumed to be amorphous.

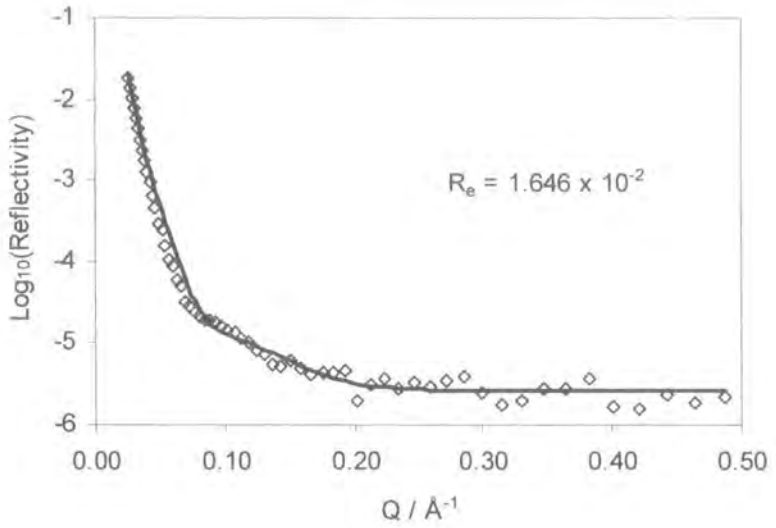

Figure 2.11. Neutron reflectivity profile and best model fit (solid line) for H-N6 on saturated H-ASP in D_2O.

Timepoint	ρ/10^{-6} Å^{-2}	Roughness/ Å	Thickness/Å	φ_{N6}	φ_{Water}	φ_{Asp}
0-2 hrs	7.15	10	27	0.53 *(0.56)*	0.45 *(0.62)*	0.01 *(-0.18)*

Table 2.5. SLD, roughness, layer thickness and volume fractions derived for D-N6 on saturated H-ASP in D_2O. Volume fractions data in parentheses assume the N6 is 100% amorphous.

The data for the deuterated and hydrogenous nylon on a saturated subphase show good agreement. Both data sets show smooth curves, indicating a diffuse layer, and model fits indicate that the nylon is interspersed by an approximately equal volume fraction of water, as observed for the pure water subphase (system 1).

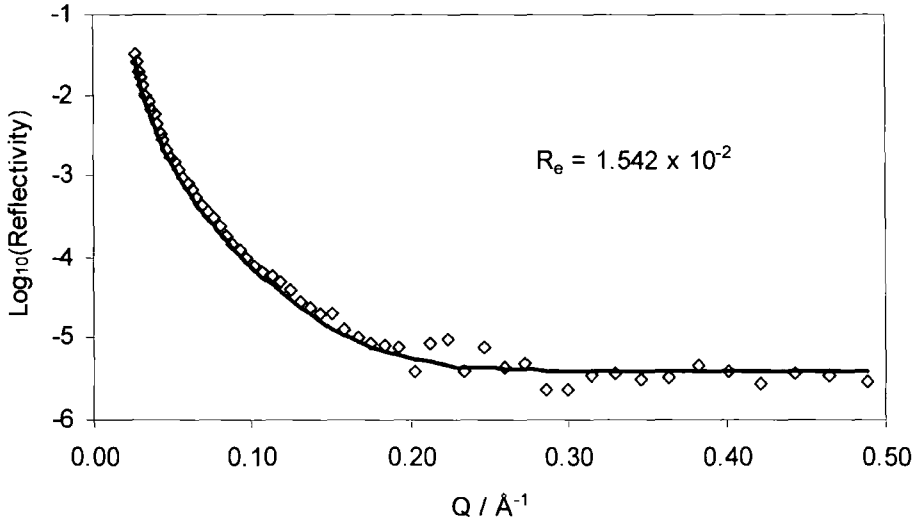

Figure 2.12 Neutron reflectivity profile and best model fit (solid line) for D-N6 on saturated H-ASP in D_2O.

2.4.3 125% Supersaturated Systems

Initial crystallisation experiments were undertaken at a supersaturation of 125%. This system was analysed over an 8 hour period, but no crystallisation was observed and no significant difference in reflectivity profile is noted (figure 2.13). Attempts to model these data were made with a 4 layer model, as it was expected that there might be DL-aspartic acid crystallising underneath the nylon 6 spread film.

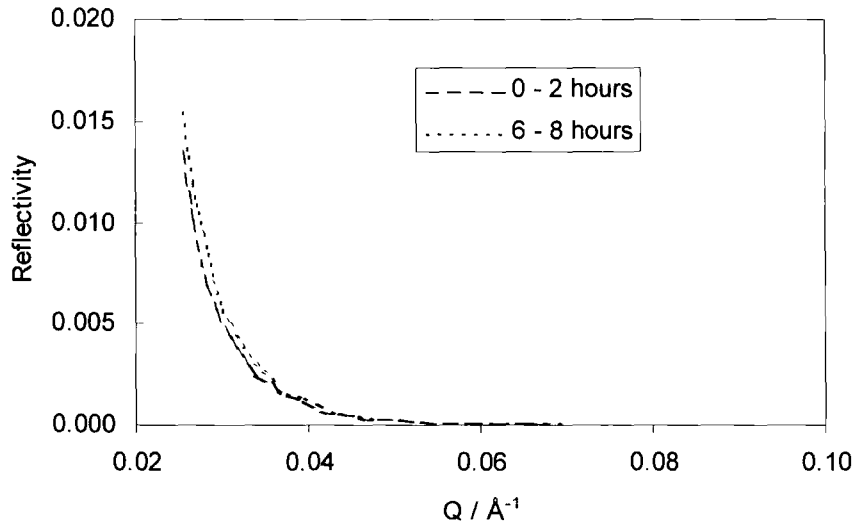

Figure 2.13. H-N6 on 125% supersaturated hydrogenous DL-aspartic acid in D_2O, analysed over an 8 hour period, illustrating negligible change.

Best model fit data using a 4 layer model, where layer 1 is air ($\rho = 0$) and layer 4 is assumed to be pure subphase are detailed in table 2.6 for the 0 – 2 hour data set. This shows a volume fraction for DL-aspartic acid of 1% at most in layer 2. Layer 3 gives a value for ρ consistent with pure subphase ($\rho = 6.39 \times 10^{-6}$ Å^{-2}, see table 2.2), giving no evidence for the crystallisation of DL-aspartic acid.

Timepoint	Layer	$\rho/10^{-6}$ Å^{-2}	Roughness/ Å	Thickness/ Å	φ_{N6}	φ_{Water}	φ_{Asp}
0–2 hours	2	4.11	12	34	0.47 *(0.50)*	0.50 *(0.72)*	0.01 *(-0.22)*
	3	6.39	32	10	0.00	1.00	0.00

Table 2.6. SLD (ρ), roughness, layer thickness and volume fractions derived for H-N6 on 125% supersaturated H-ASP in D_2O. This is for a 4 layer model where the 4th layer is pure subphase. Volume fractions data in parentheses assume the N6 is 100% amorphous.

Since layer 3 is effectively equivalent to layer 4, it is better to consider a 3 layer model. This is because considering an artificial (or non-existent) discrete layer with artificial thickness, etc, compromises the quality of the data by increasing the number of parameters that are modified by LAYERS. An increasing number of layers will give a better fit, but as few layers as possible should be considered to eliminate misleading results caused by introducing unnecessary adjustable parameters such as thickness and roughness for two layers that are essentially homogeneous.

Table 2.7 gives values derived at the 0 – 2 hours timepoint on this system using a three layer model. The same values of ρ, roughness, and layer thickness give a good fit at the 6 – 8 hours timepoint (compare figures 2.14 and 2.15) indicating a negligible change over time for this system.

Timepoint	Layer	$\rho/10^{-6}$ Å	Roughness/ Å	Thickness/ Å	φ_{N6}	φ_{Water}	φ_{Asp}
0–2 hours	2	4.11	12	34	0.47 *(0.50)*	0.50 *(0.72)*	0.01 *(-0.22)*

Table 2.7. SLD, roughness, layer thickness and volume fractions derived for H-N6 on 125% supersaturated H-ASP in D_2O. This is for a 3 layer model where layer 3 is pure subphase. Volume fractions data in parentheses assume the N6 is 100% amorphous.

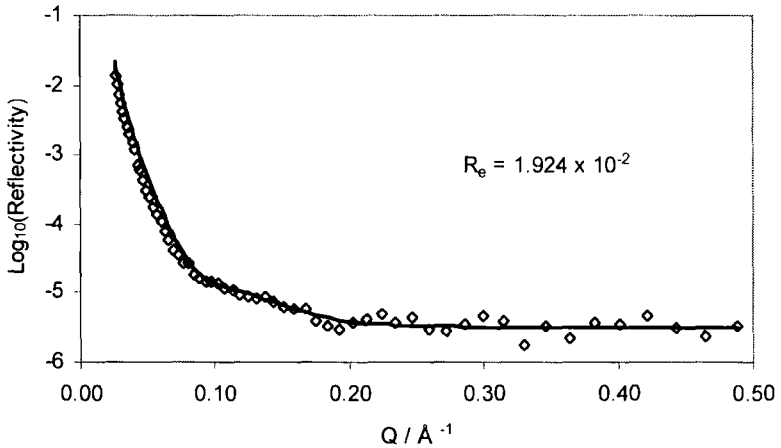

Figure 2.14. Representation of fitted and observed data at time-point 1 (0 – 2 hours) for H-N6 on 125% supersaturated H-ASP in D_2O, using a 4 layer model where layer 4 is pure subphase.

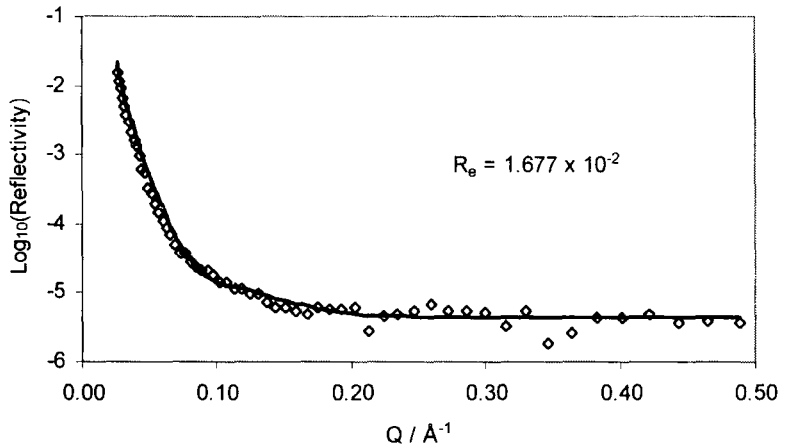

Figure 2.15. Representation of fitted and observed data at time-point 4 (6 – 8 hours) for H-N6 on 125% supersaturated H-ASP in D_2O, using a 3 layer model where layer 3 is pure subphase.

2.4.4 150% Supersaturated Systems

Given that even after 8 hours, no change in reflectivity profile was seen at supersaturation levels of 125%, 150% supersaturated systems were used for subsequent neutron reflectivity studies. Two contrasting N6 on aqueous DL-aspartic acid solutions were studied.

These crystallising systems are:

- D-N6 on 150% H-ASP in D_2O (system 5).
- H-N6 on 150% H-ASP in NRW (system 6).

The relevant values of ρ for these systems were summarised in table 2.2.

System 5 was studied over four time-points at intervals of approximately two hours, while system 6 was studied over a total 6 hour period (3 x 2 hour timepoints). For systems supersaturated at 150%, the crystallisation of the DL-aspartic acid under the monolayer was easily visible to the naked eye after approximately ten hours. Visible surface coverage values are described more fully in section 2.5. Figure 2.16 illustrates the changing reflectivity profile over 8 hours for the D-N6 on 150% H-ASP in D_2O (system 5). It can be seen that changes in reflectivity profile were apparent over this timescale showing that the 150% supersaturation level was appropriate for neutron reflectivity studies.

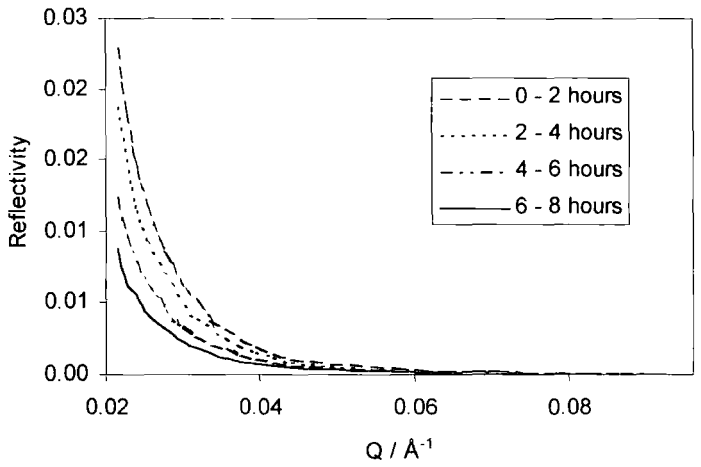

Figure 2.16. D-N6 on 150% supersaturated H-ASP in D_2O over 4 timepoints. This figure illustrates the change in reflectivity during this experiment as crystallisation progresses.

System 5. Four Layer Fit.

Figures 2.17a – 2.17d illustrate best model fit and observed data for four layer fits on system 5. Significantly, the raw data show smooth curves consistent with a diffuse layer as observed for the non-crystallising systems detailed earlier. The model fit data derived are given in table 2.8. At 0 – 2 hours, the data are consistent with those acquired for N6 on water and N6 on saturated subphase systems (sections 2.4.1. & 2.4.2). There is no evidence for crystallisation of the DL-aspartic acid and the data indicate a diffuse layer of nylon 6 interspersed with the aqueous phase. The 0 – 2 hours data (See table 2.8) show that layer 3 is consistent with subphase, hence a 3 layer and not a 4 layer model is appropriate for this system. The data at 2 – 4 hours, however, show 10% DL-aspartic acid by volume of layer 3 consistent with DL-aspartic acid crystallisation under the nylon layer. However, within the "nylon 6" layer 2 there is more DL-aspartic acid, namely 24% by volume, which has displaced some of the water previously present. The best-fit data derived at 4 - 6 hours are very significant. These show no evidence for DL-aspartic acid within layer 3 as seen at 2 – 4 hours, but rather a swelling of layer 2 and incorporation of 39% DL-aspartic acid within this nylon 6 layer. Layer 3 is consistent with D_2O, i.e. the same as layer 4, showing again that a 3 layer model is more appropriate.

Timepoint	Layer Number	ρ/ 10^{-6} Å^{-2}	Thickness / Å	Roughness / Å	φ_{N6}	φ_{Water}	φ_{Asp}
0 – 2 hours	2	7.00	34	9	0.41 *(0.44)*	0.58 *(0.71)*	0.01 *(-0.15)*
	3	6.42	16	3	0.00	1.00	0.00
2 – 4 hours	2	6.81	36	12	0.39 *(0.42)*	0.37 *(0.54)*	0.24 *(0.04)*
	3	6.12	15	4	0.00	0.90	0.10
4 – 6 hours	2	6.54	50	17	0.28 *(0.30)*	0.33 *(0.49)*	0.39 *(0.21)*
	3	6.39	17	6	0.00	1.00	0.00

Table 2.8. SLD (ρ), Roughness and thickness values derived for D-N6 on 150% supersaturated H-ASP in D_2O (system 5). This is a 4 layer fit, where the 4th layer is the subphase. Volume fractions data in parentheses assume the N6 is 100% amorphous.

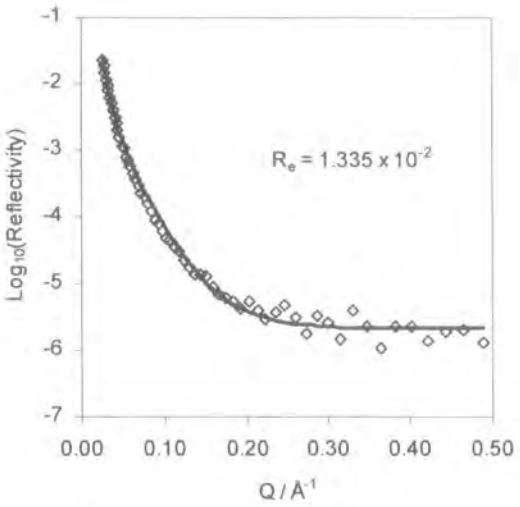

a) 0 – 2 hrs

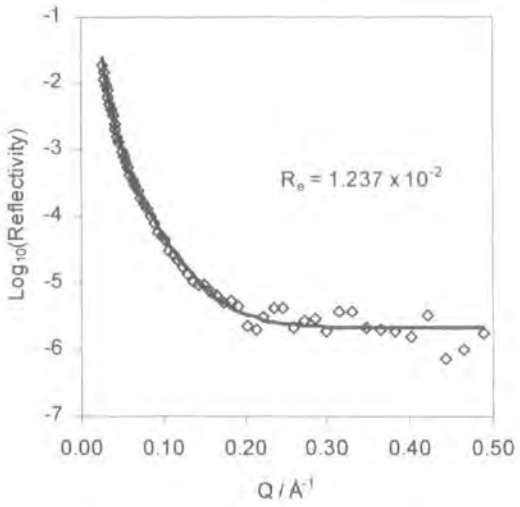

b) 2 – 4 hrs

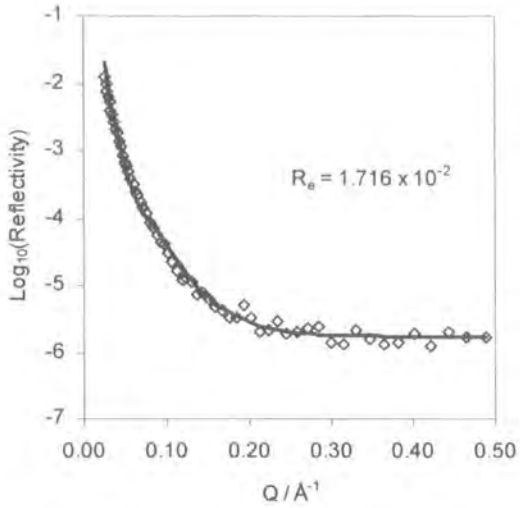

c) 4 – 6 hrs

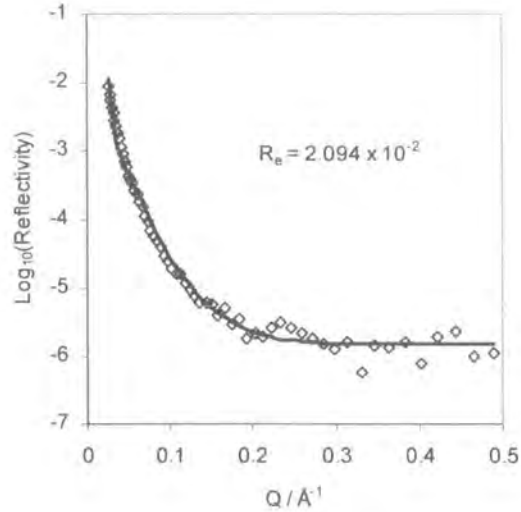

d) 6 – 8hrs

Figures 2.17a - 2.17d. Representation of best model fit (solid line) and observed data at 4 time-points for system 5. These data are fitted by a 4 layer model, assuming layer 1 is air and layer 4 is subphase, however for timepoint 6 –8 hrs, the resulting best fit corresponds to a 3 layer model, as the 3rd and 4th layer had identical compositions.

So it appears that the DL-aspartic acid crystallises on the nylon layer and then becomes widely dispersed within the layer. As crystallisation progresses, the layer increases in thickness, becoming a single layer. At 6 – 8 hours, layer 3 is again consistent with D_2O and hence a 3 layer model fit was attempted for this system for all data sets acquired.

Table 2.9 summarises the best model fit data using a 3 layer model for system 5 at all timepoints. These show very similar volume fractions for layer 2 to those found for the 4 layer data described earlier. Figures 2.18a – 2.18d show graphs of best model fit vs. raw data, showing that the agreement using the 3 layer model system is just as good as for the 4 layer model previously adopted.

Timepoint	$\rho/10^{-6}$ Å^{-2}	Roughness/ Å	Thickness/Å	φ_{N6}	φ_{Water}	φ_{Asp}
0 - 2 hrs	7.01	9	35	0.40 *(0.43)*	0.60 *(0.76)*	0.00 *(-0.18)*
2 - 4 hrs	6.81	9	39	0.36 *(0.38)*	0.41 *(0.62)*	0.23 *(0.00)*
4 - 6 hrs	6.54	17	50	0.28 *(0.30)*	0.33 *(0.49)*	0.39 *(0.21)*
6 - 8 hrs	6.18	26	81	0.17 *(0.19)*	0.30 *(0.33)*	0.53 *(0.48)*

Table 2.9. Best model fit data for layer 2 using a 3 layer model for D-N6 on 150% supersaturated H-ASP in D_2O. Volume fractions data in parentheses assume the N6 is 100% amorphous.

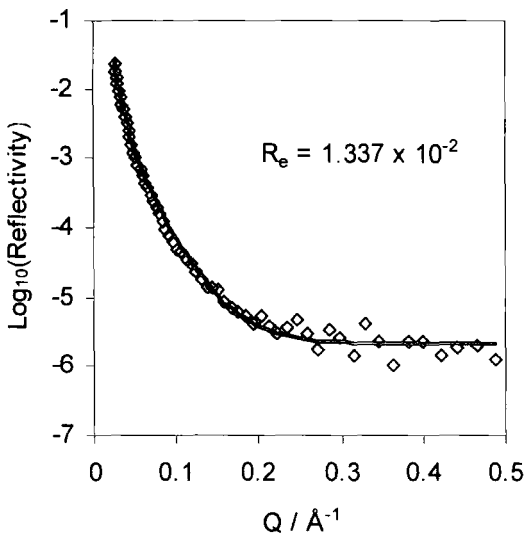

a) 0 – 2 hrs

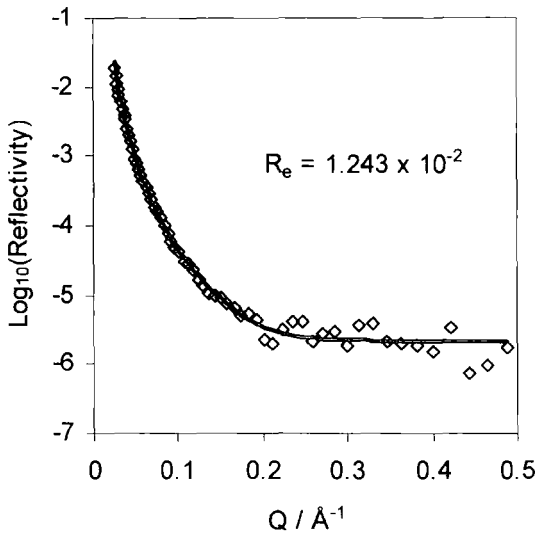

b) 2 – 4 hrs

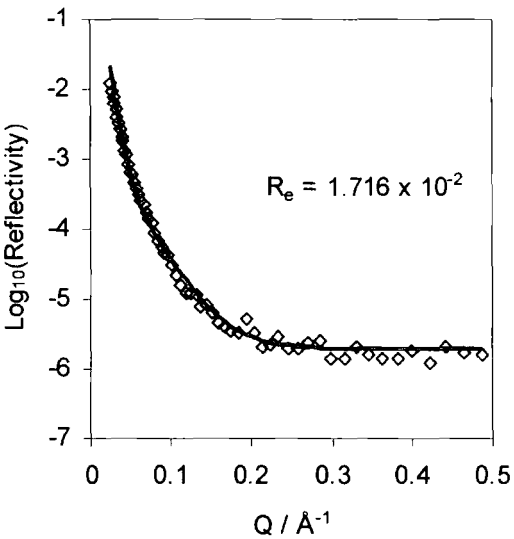

c) 4 – 6 hrs

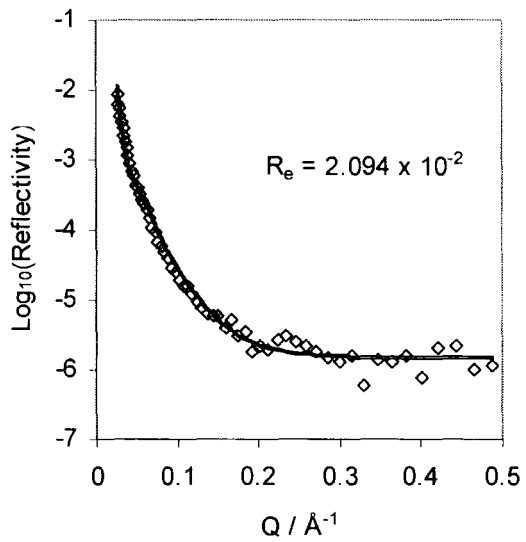

d) 6 – 8 hrs

Figures 2.18a – 2.18d. Graphs of model fit (solid line) vs. raw data for system 5 (D-N6 on 150% supersaturated H-ASP in D_2O) assuming a three layer model.

Since the 3 and 4 layer best model fits for system 5 are equally good to the naked eye (figures 2.17a-d vs 2.18a-d) and give very similar R_e best fit values, figures 2.19 and 2.20 compare the SLD profile for this system on penetrating the surface for the 4 and 3 layer model fits.

For the 4 layer model, figure 2.19 shows a dip in the SLD at ~ 50 Å below the surface for the 2 - 4 hour data set, indicating the crystallisation of a very small amount of DL-aspartic acid beneath, as well as within the nylon 6 layer, whereas this feature is absent in the 3 layer model at this timepoint. Ultimately, it is impossible to say whether the indication here that DL-aspartic acid has crystallised underneath the nylon 6 is real or a consequence of limited contrast in ρ, (6.18 vs. 7.01 $Å^{-2}$). Furthermore, this dip is not seen in the subsequent 4 layer model timepoints. Consequently, it is not possible to confirm at present whether this thin 15 Å layer containing 10% DL-aspartic acid is a real feature of the crystallisation process or an artefact of the 4 layer model that arises due to the limited contrast between layers 2 and 3. It is apparent, however, irrespective of whether a 4 or 3 layer model is adopted, that the majority of the DL-aspartic acid adsorption and crystallisation occurs within and not beneath the nylon 6 layer, causing the swelling of this layer. Thus both models show that the vast majority of DL-aspartic acid adsorption and crystallisation occurs within the nylon 6 film layer, and hence the system is better represented by using a 3 layer model.

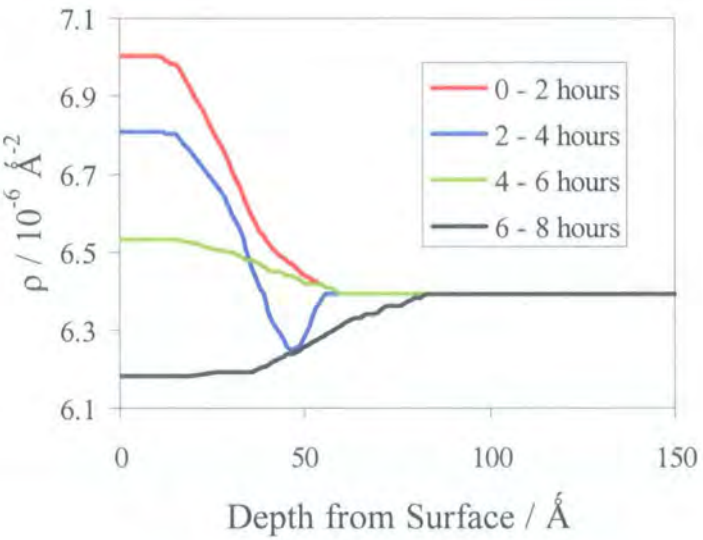

Figure 2.19. Illustration of the change in scattering length density on penetrating the surface for system 5, according to the 4 layer model fit data.

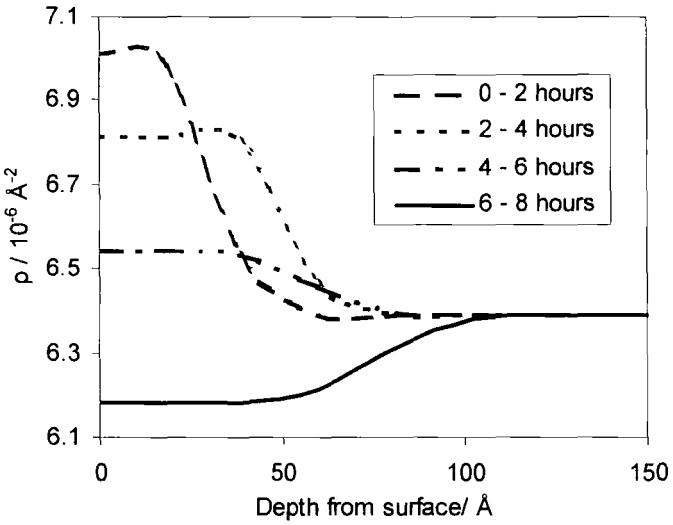

Figure 2.20. Illustration of the change in scattering length density on penetrating the surface for system 5, according to the 3 layer model fit data.

Furthermore, if the DL-aspartic acid layer beneath the nylon 6 film was the predominant crystallisation mechanism then we would expect ~10% crystal coverage on the surface because further growth from the underlying solution on these crystals would be unimpeded by the presence of nylon 6 film. The optical microscopy studies detailed later in section 2.5, however, show the crystal surface coverage is below this value, again confirming that the 3-layer model is the more appropriate.

System 6 D-N6 on H-ASP in NRW

The last crystallising system studied was deuterated nylon 6 on hydrogenous DL-aspartic acid in null reflecting water (system 6).

System 6 provides significantly greater contrast in scattering length density, which helped to resolve the issue of whether there is any crystallisation of DL-aspartic acid underneath the film layer. However, these data are inherently noisier than for D_2O subphases due to the incoherent backscatter caused by the 92% of H_2O in the subphase. For this NRW system, layer 3 in the 4 layer model was always consistent with NRW at all three timepoints, i.e. a 3 layer model was most appropriate for this system at all timepoints. Hence only the 3 layer model data are displayed here (figures 2.21a - 2.21c).

Since the system cannot be modeled using 4 layers, these data do not show any evidence for DL-aspartic acid crystallising underneath the nylon layer. The only evidence for DL-aspartic acid is within the nylon 6 layer (layer 2). At the 2 – 4 and 4 - 6 hour measurements, layer 2 has swelled but there is no evidence for DL-aspartic acid crystallising in layer 3. Figure 2.22 shows the change in SLD on penetrating the surface at the three timepoints for this system.

Timepoint	ρ / 10^{-6} Å^{-2}	Roughness/ Å	Thickness/Å	φ_{N6}	φ_{Water}	φ_{Asp}
0-2 hrs	2.80	16	34	0.41 *(0.44)*	0.59 *(0.66)*	0.00 *(-0.10)*
2-4 hrs	2.48	28	55	0.25 *(0.27)*	0.49 *(0.48)*	0.26 *(0.25)*
4-6 hrs	2.00	40	100	0.14 *(0.15)*	0.51 *(0.45)*	0.35 *(0.40)*

Table 2.10. SLD, Roughness and thickness values derived for D-N6 on 150 % supersaturated H-ASP in NRW. This is for a 3 layer model fit. Volume fractions data in parentheses assume the N6 is 100% amorphous.

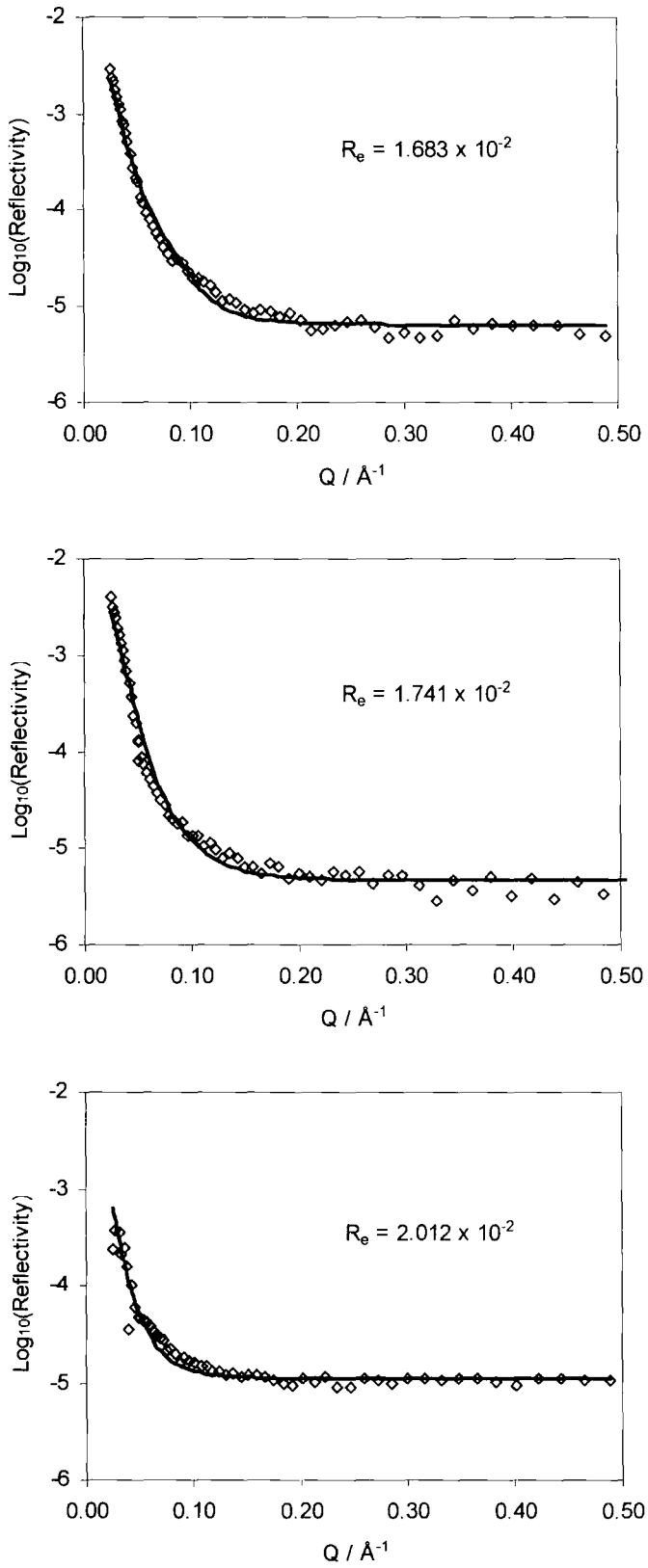

Figure 2.21. 3 layer model. D-N6 on 150% supersaturated hydrogenous DL-aspartic acid in NRW (system 6). Top is 0 – 2 hrs, middle 2 - 4 hrs and bottom 4 – 6 hrs.

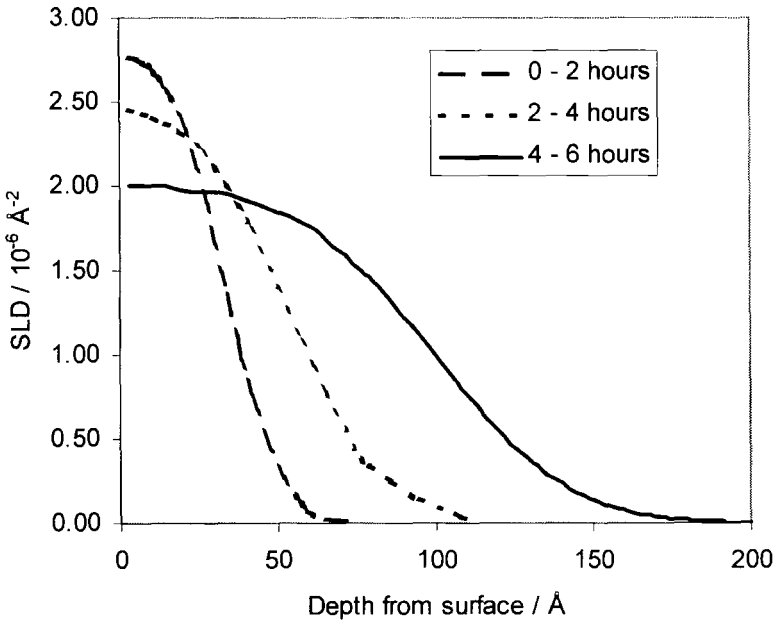

Figure 2.22. Illustration of change in SLD profile against depth from surface for D-N6 on 150% supersaturated H-ASP in NRW.

2.4.5 Discussion of Neutron Reflectivity Data

The neutron reflectivity data for nylon 6 on pure water show evidence for a diffuse film layer interspersed with an approximately equal volume of water. This is consistent with the structure for nylon 6 6 spread on aqueous subphases, as was described in the introduction to this chapter.

The neutron reflectivity data presented here demonstrate that this diffuse nylon structure is unaffected by a saturated, or 125% supersaturated subphase. The model fits offer no evidence for crystallisation in the 125% supersaturated system, even after 8 hours have elapsed, which agrees with the lack of visible crystallisation observed.

The 150% supersaturated system visibly crystallised and the neutron reflectivity data show that this occurs predominantly within and not underneath the nylon 6 spread film as might have initially been expected. Figures 2.23 and 2.24 illustrate the change in the "film" layer thickness and composition that arises from the preferred 3-layer model for both of the

crystallising 150% supersaturated systems. These show good agreement except that the crystallisation for system 6 appears to be progressing at a slightly greater rate. This good agreement is highlighted in table 2.11, which compares the data acquired for the crystallising systems, assuming that the nylon 6 is crystalline. The assumption of crystalline nylon 6 is justified because negative volume fractions are derived for DL-aspartic acid when the spread film is assumed to be amorphous.

Timepoint	System	Thickness/ Å	φ_{N6}	φ_{Water}	φ_{Asp}
0 – 2 hours	4	35	0.40	0.60	0.00
	5	34	0.41	0.59	0.00
2 – 4 hours	4	39	0.36	0.41	0.23
	5	55	0.25	0.49	0.26
4 – 6 hours	4	50	0.28	0.33	0.39
	5	100	0.14	0.51	0.35
6 – 8 hours	4	81	0.17	0.30	0.53
	5	n/a	n/a	n/a	n/a

Table 2.11. Comparison of model fit data derived for systems 5 and 6.

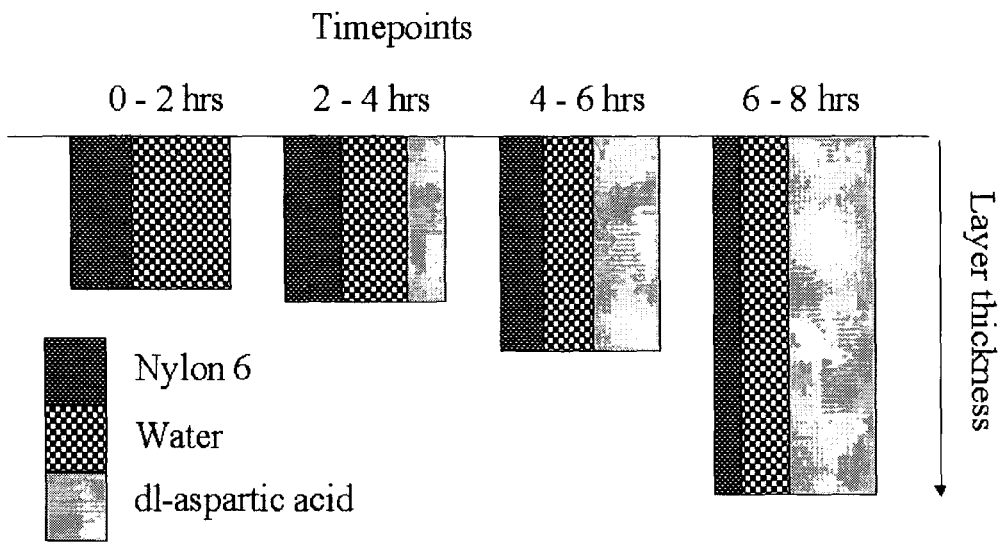

Figure 2.23. Illustration of the surface layer composition over 4 timepoints for D-N6 on 150% supersaturated H-ASP in D_2O (system 5).

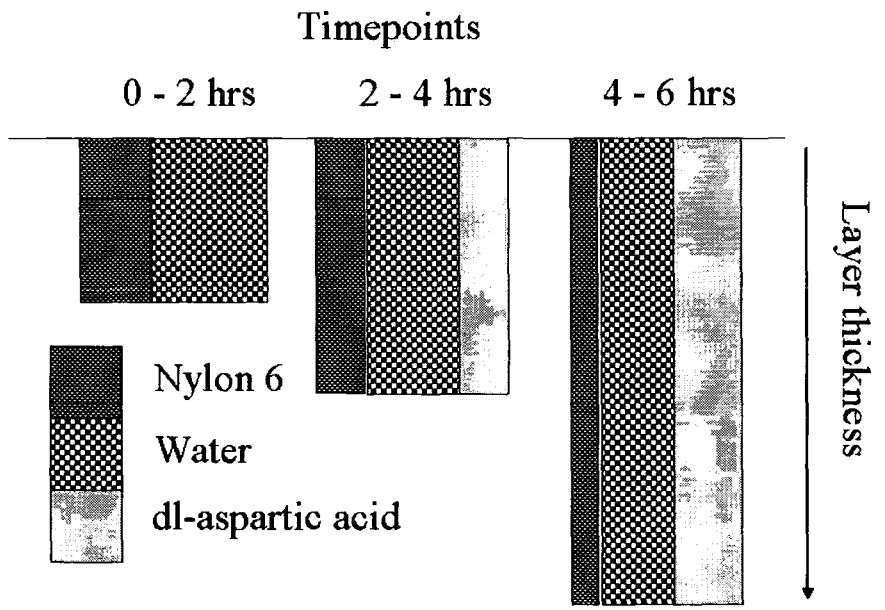

Figure 2.24. Illustration of the surface layer composition over 3 timepoints for D-N6 on 150% supersaturated H-ASP in NRW (system 6).

2.5 Optical Microscopy Studies; Surface Coverage

Optical microscopy studies were conducted to provide further insight into the crystallisation of DL-aspartic acid induced by the nylon 6 film. 150% supersaturated DL-aspartic acid in Milli-Q water solutions were prepared as described in section 2.3.3. These were placed in a medium Nima trough of dimensions approximately 12 cm x 8 cm and a full compression cycle was undertaken to ensure that the surface was clean. 10 µl of 1 mg/cm^3 nylon 6 in $HCO_2H/CHCl_3$ (2:3) was added and compressed to 70 cm^2. As for the neutron reflectivity studies, this gave a surface reading of ~ 3 mN/m which equilibrated at approximately 2.5 mN/m. This density of nylon is equivalent to that used in the neutron experiments.

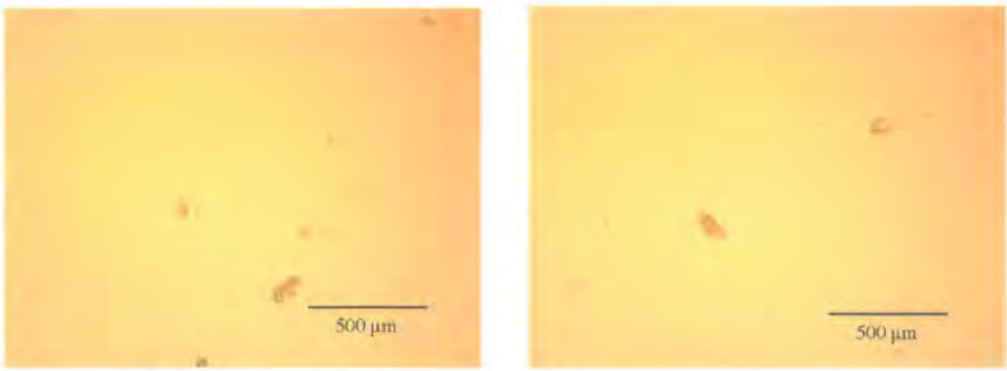

Figures 2.25 a & b. Images of DL-aspartic acid growth under nylon 6 spread films as viewed at low magnification.

Figures 2.25 a and b are typical images viewed at low magnification of DL-aspartic acid growth under a nylon 6 spread film 8 hours after film deposition. These images suggest that visible crystal coverage at the surface is in the order of only 1%. The neutron reflectivity data indicated significant (~50%) incorporation of DL-aspartic acid within the nylon 6 layer, but this significant adsorption does not result in a corresponding degree of visible crystallisation. One might therefore conclude that most of the DL-aspartic acid, known to have been adsorbed into the film layer from the neutron reflectivity data, exist as sub-visible crystalline nuclei embedded within the nylon 6 film.

Additional views of crystal clusters at low and high magnification are shown in figures 2.26 and 2.27, respectively. These images were obtained 8 hours after film deposition.

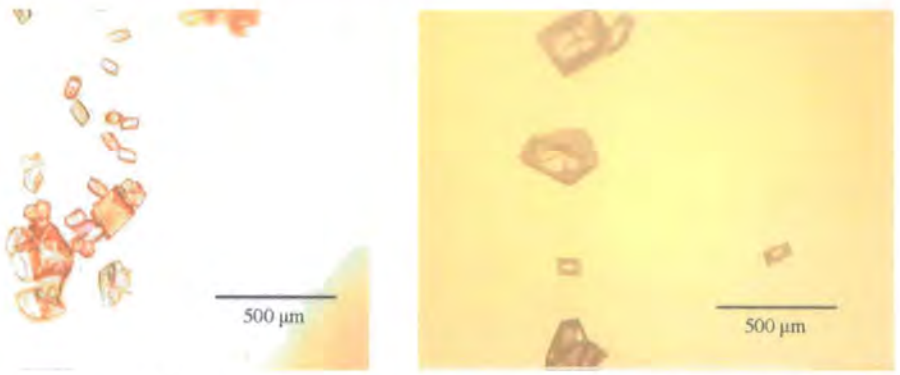

Figure 2.26. Images of DL-aspartic acid clusters under a nylon 6 spread film viewed at low magnification.

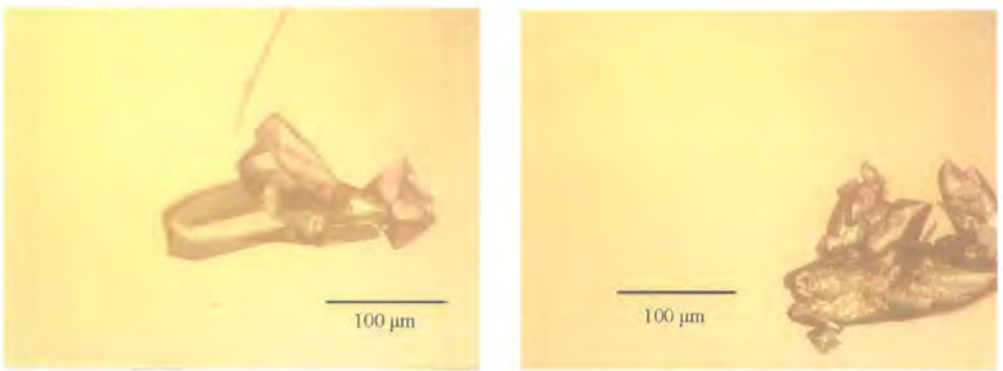

Figure 2.27. Images of DL-aspartic acid clusters under nylon 6 spread film viewed at high magnification.

The high magnification data show a tendency for crystals to become aggregated, and show a range of crystal sizes. The data displayed here for areas where crystallisation density was high, also show relatively low visible crystal coverage at the surface, when compared to the data acquired by neutron reflectivity.

2.6 External Reflection FTIR Studies

2.6.1 Introduction

The finding that significant adsorption of DL-aspartic acid occurred within the nylon 6 film despite the far more limited visible crystallisation observed was quite surprising. Hence to gain further insight into the film-induced crystallisation process, the crystallisation of DL-aspartic acid beneath nylon 6 was followed in situ using external reflection FTIR. All species were undeuterated. Table 2.12 lists the observed band positions attributable to the

nylon 6 film and DL-aspartic acid crystals, together with their corresponding band assignments.

Nylon 6 Film Bands	DL-Aspartic Acid Bands Seen Prior to Visible Crystal Formation	DL-Aspartic Acid Bands Seen on Visible Crystal Formation	Assignment and Reference
		853 s	CH_2 rock[48]
		893 s	CC stretch[48]
		986 w	CC stretch[48]
	1071 w, broad	1071 s	CN stretch[48]
	1117 vw, broad	1117 m or w	NH_3^+ rocking[48]
	1141 w, broad	1141 m	NH_3^+ rocking[48]
1171 vw			CH_2 twist/wag[30]
1202 w			Amide III & CH_2 wag / CH_2 twist/wag[30]
	1213 w, broad	1213 vs	CH_2 twist?[48]
1265 w			Amide III & CH_2 wag[30]
		1313 s	CH_2 wagging[48]
		1349 s*	CH bend[48]
1543 s*			Amide II[30]
1639 s*			Amide I[30]
		2851 vw, broad	CH_2 symmetric stretch[48]
2865 w, broad			CH_2 symmetric stretch[30]
		2920 vw, broad	CH_2 asymmetric stretch[48]
2930 w, v broad			CH_2 asymmetric stretch[30]
		3134 w, broad	NH_3^+ asymmetric stretch[48]
3304 m			NH stretch[30]

* These bands become increasingly obscured by the increasing water vapour bands that arise as the background spectrum taken at the start of the experiment ages.

Table 2.12. Observed external reflection FTIR bands for nylon 6 and DL-aspartic acid.

Figures 2.28 and 2.29 compare attenuated total reflectance (ATR) spectra for solid DL-aspartic acid and nylon 6 at wavenumbers ranging from 1800 – 750 cm^{-1} and 4000 – 750 cm^{-1}, respectively. ER-FTIR experiments on nylon 6 spread films at the air-water interface show that the nylon 6 film bands occur at similar positions to those observed for nylon 6 6 spread films and the solid nylon 6, and so are consistent with the film adopting a hydrogen-bonded sheet structure parallel to the film surface akin to the sheet structure found in its bulk α-phase crystal[30]. The absence of so-called 'amorphous' bands at ~1124 cm^{-1} and 983 cm^{-1} also support the view that the film is not predominantly amorphous, although a very weak band at 1170 cm^{-1}, controversially attributed to the amorphous phase is just discernable[49]. The DL-aspartic acid bands have been assigned with reference to published l-aspartic acid crystal transmission data[48], since data for DL-aspartic acid crystals could not be found in the literature; hence these are only tentative assignments.

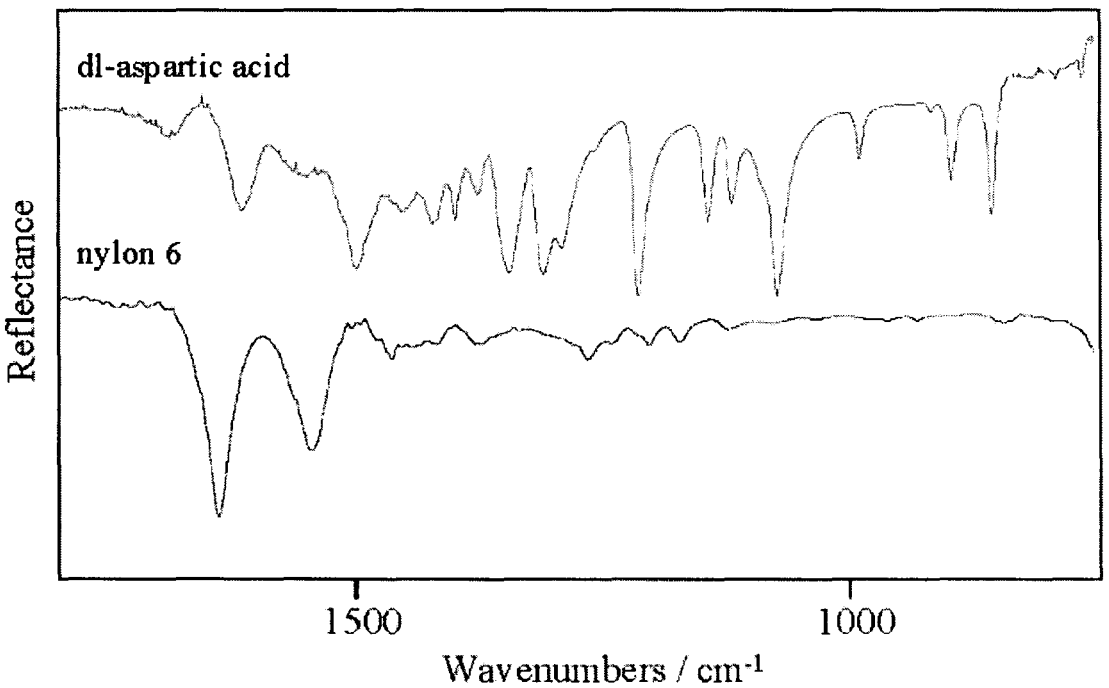

Figure 2.28. FTIR spectra (1800 – 750 cm^{-1}) of DL-aspartic acid and nylon 6 acquired on the thunderdome ATR accessory.

ER-FTIR spectra were acquired from the nylon 6 film and 150% supersaturated DL-aspartic acid systems at an incidence angle of 30° at 4 cm^{-1} resolution over 512 scans.

The sample was contained in a PTFE micro-trough of dimensions approximately 2 cm x 10 cm. 150% supersaturated solutions were prepared as described in section 2.3.3 and films were spread and compressed as described in each section below.

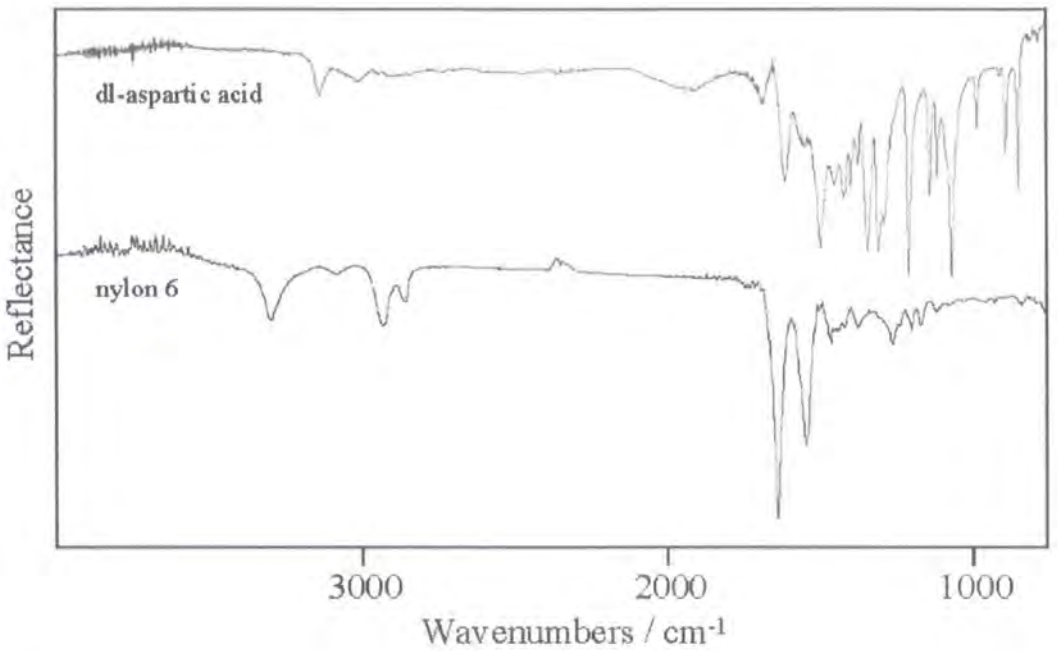

Figure 2.29 Full range FTIR spectra (4000 – 750 cm^{-1}) of DL-aspartic acid and nylon 6 acquired on the thunderdome ATR accessory.

2.6.2 Crystal Growth Experiment

10 µl of nylon 6 in $HCO_2H/CHCl_3$ (2:3) at a concentration of 0.25 mg/cm^3 were spread on clean subphase and compressed to 15 cm^2. This nylon density corresponds to that used in the neutron reflectivity experiments.

After 90 - 120 minutes, which was prior to any visible crystal formation, weak bands were observed at approximately 1213 cm^{-1}, 1141 cm^{-1}, 1117 cm^{-1} and 1071 cm^{-1}, see figures 2.30a and 2.30b. These values correspond to band positions expected for DL-aspartic acid, and therefore provide further evidence for the incorporation of DL-aspartic acid material into the film layer, as found in the neutron reflectivity studies. Of these bands, the 1213 cm^{-1}, 1141 cm^{-1} and 1071 cm^{-1} were the more intense, although the 1213 cm^{-1} band was partially obscured by the 1202 cm^{-1} amide III band of the nylon 6 film.

No other bands attributed to DL-aspartic acid bands were discernable, though the 1350 cm^{-1} to 1700 cm^{-1} region was obscured by water vapour bands, so the presence of further bands in this region cannot be ruled out. These weak bands, observed prior to any visible crystal formation, increased slightly in intensity over time, again without any observable crystal formation occurring in the beam-sampled region, see figures 2.30a and 2.30b. The emergence of one further band associated with DL-aspartic acid at 986 cm^{-1} was also just discernible in the 150-minute data shown in figure 2.30b. No spectral changes were observed for features attributed to the nylon 6 spread film during this period of pre-visible crystallisation.

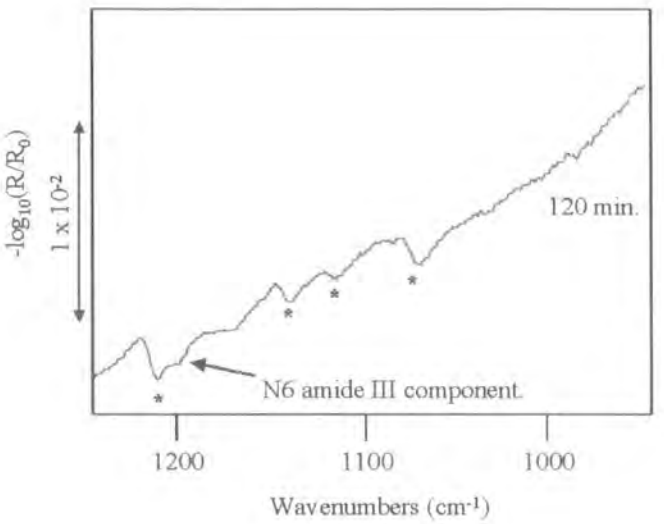

Figure 2.30a. ER- FTIR data (1250 – 950 cm^{-1}) at 120 min. showing the occurrence of weak DL-aspartic acid bands prior to any visible crystal formation after film spreading. Weak DL-aspartic acid bands are asterisked.

In order to determine the extent of the occurrence of these weak bands, ten film-covered areas of the sample were randomly selected that were apparently crystal-free from visual observation. These regions also revealed the weak bands associated with DL-aspartic acid in six of the ten cases. The widespread occurrence of these weak DL-aspartic acid bands are consistent with the neutron reflectivity data, which showed a significant incorporation of DL-aspartic acid material within the film layer, despite the relatively low visible crystal surface coverage obtained after 8 hours (see section 2.5). These data therefore support the hypothesis that the majority of the adsorbed DL-aspartic acid material remains as sub-visible clusters. Similar conclusions were reached by Ahn et al.[15] to explain the large scale

intensity changes observed in film IR bands on calcite crystallisation, despite only ~5-15% of the surface becoming covered with calcite crystals.

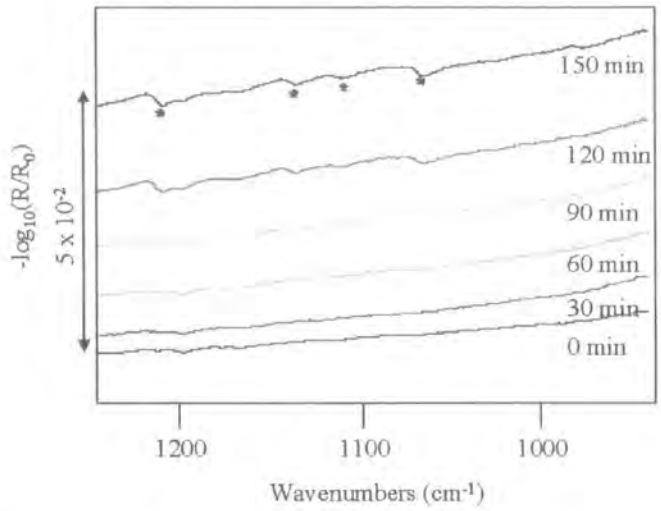

Figure 2.30b ER- FTIR data (1250 – 950 cm^{-1}) at 0 – 150 min showing the gradual appearance of the weak DL-aspartic acid bands.

Upon visible formation of DL-aspartic acid crystals on the beam-sampled surface there is a sharpening, and large increase in the intensity of the weak signals at 1213 cm^{-1}, 1141 cm^{-1}, 1117 cm^{-1} and 1071 cm^{-1}, see figure 2.31, together with the appearance of many more crystalline bands, as listed in table 2.12.

Figures 2.32a and 2.32b show the 3500 - 2800 cm^{-1} and 1400 - 950 cm^{-1} spectral data obtained in a region showing the visible crystallisation of DL-aspartic acid; not only are the DL-aspartic acid bands readily seen, but it is also evident from figure 2.32a that the nylon 6 NH stretch at 3304 cm^{-1} increases dramatically in intensity as the crystallisation proceeds. The weaker bands at ~ 2900 cm^{-1} attributed to nylon 6 methylene stretches also increase slightly in intensity. An intensity increase is also apparent for the nylon 6 amide I at 1637 cm^{-1}, although the extent of the increase is harder to discern due to the overlapping water vapour bands; indeed the latter obscure the amide II band at 1541 cm^{-1} to such a degree that the observation of any intensity increases for this band are precluded. The weakness and close proximity to stronger DL-aspartic acid crystalline bands also makes it difficult to discern the extent of intensity changes for the nylon 6 amide III bands at 1265 cm^{-1} and

1202 cm^{-1}. Nevertheless, the intensity of these amide III bands does appear to increase also.

It was difficult to observe these synergistic nylon 6 film and crystallising DL-aspartic acid changes regularly, though, because this required the crystals to grow within the small ~mm^2 region sampled by the IR beam. More typically, crystals grew outside the area sampled by the beam, necessitating careful movement of the trough so that IR data from these regions could be compared with regions without crystals. Comparison of these regions often, but certainly not always, displayed similar film band increases in the visible crystal regions.

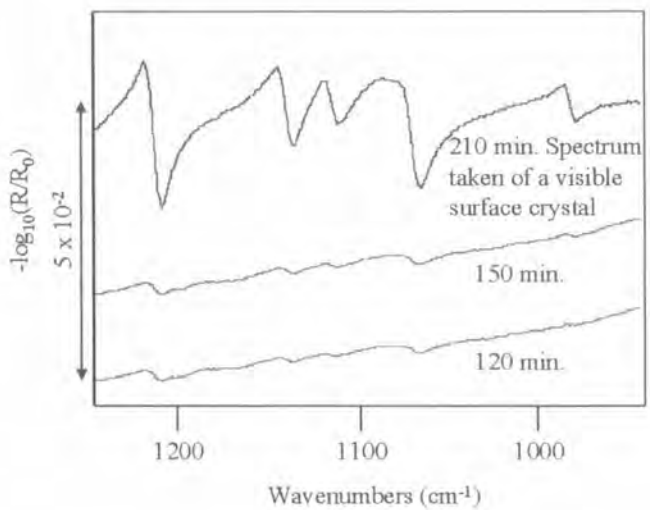

Figure 2.31. ER-FTIR data, comparing the sharper, more intense DL-aspartic acid bands found in regions of visible crystal formation with the weak DL-aspartic acid bands often seen in regions devoid of visible crystal formation.

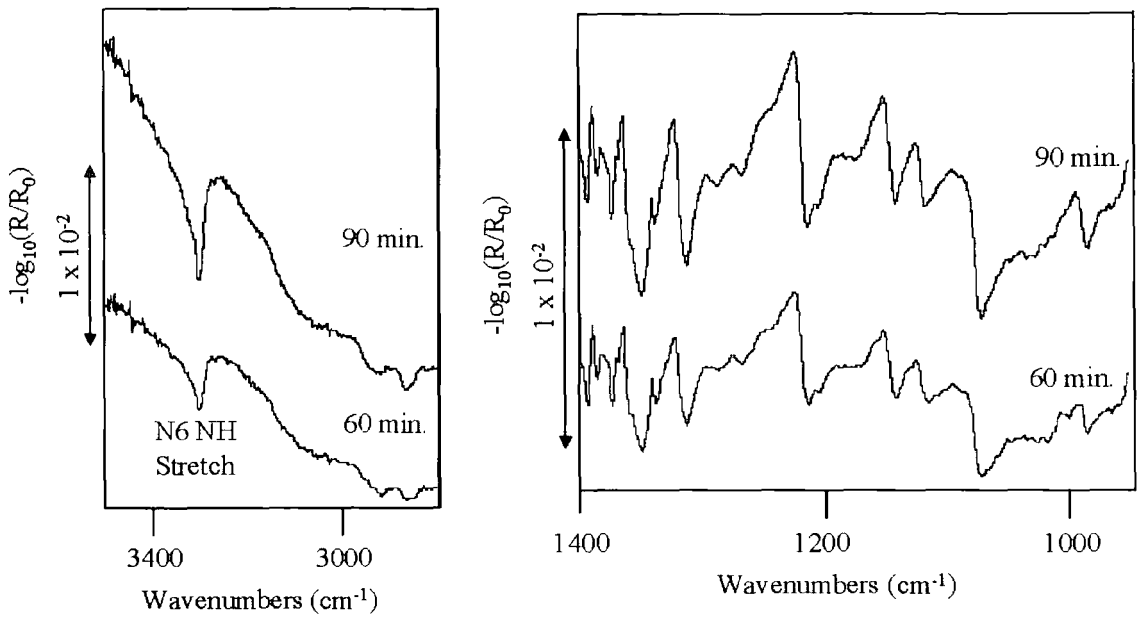

Figure 2.32a (left) & 2.32b (right). Intensity changes observed in the nylon 6 NH film band during visible DL-aspartic acid crystal growth/dissolution. 2.32a shows the 3500-2800 cm^{-1} and 2.32b is 1400-950 cm^{-1} during the visible crystallisation of DL-aspartic acid. Each spectrum is labelled with the time elapsed after spreading of the nylon 6 film.

2.6.3 Dissolution Experiment

In order to better understand the increase in the NH stretch and other film bands during the crystallisation process, a "reverse" experiment was attempted. The aim was to monitor the change in FTIR spectra acquired from a single crystal upon dissolution by the replacement of the saturated solution with ~50% by volume of water. Care was taken to ensure that the dissolution process would progress sufficiently quickly by using hot water, so that the crystal would not move out of the beam. However, the temperature of the water added was limited to 60 °C to ensure dissolution of the nylon 6 spread film did not also occur.

Data were acquired by carefully sliding the trough along its platform, until a crystal was located in the IR beam. Then part of the saturated solution was removed from behind the barrier, and replaced with hot water. The resulting dissolution of the DL-aspartic acid crystal was monitored by acquiring spectra every 10 minutes.

The data obtained, see figures 2.33a 2.33b, clearly show the decrease in the nylon 6 NH stretch film band as the DL-aspartic acid crystal dissolves. This confirms the reversibility of the synergistic process that occurs during the film-induced DL-aspartic acid crystallisation.

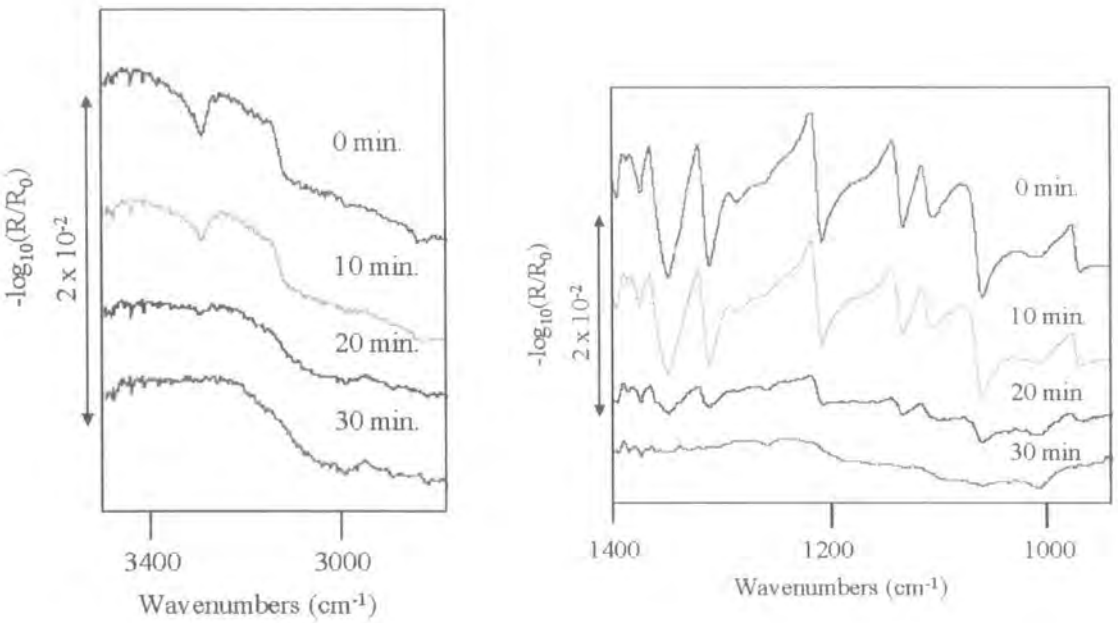

Figures 2.33a (left) and 2.33b (right) show the 3500 - 2800 cm^{-1} and 1400 - 950 cm^{-1} spectra during the visible dissolution of a DL-aspartic acid crystal. The minute values indicated refer to the time elapsed after adding pure water to dissolve the crystal.

2.6.4 Discussion of the ER-FTIR Data

In the case of ER-FTIR studies with an incidence angle of 30°, bands due to groups vibrating parallel to the interface contribute more to a spectrum at the air-water interface, because the magnitude of the electric vector perpendicular to the interface is very low[35,36]. Band intensity increases/decreases can therefore arise due to molecular reorientations that cause that particular vibration to become more/less parallel to the interface.

Such an interpretation has previously been given for intensity changes observed during crystallisation beneath non-polymeric films, where it has been shown that the reorientation decreased the lattice mismatch between the film and underlying crystal face, and hence aided the crystallisation process[15]. However, the polymeric film in this study could of course be accumulating around the growing crystal, without necessarily reorienting itself to

a significant extent, and this would also lead to the same observed film band intensity increases. As was discussed in the introduction to this chapter, the hydrogen-bonded sheets of nylon 6 are expected to lie parallel to the aqueous surface, which would already give a maximum intensity for the NH stretch for a crystalline, or mainly crystalline nylon 6 film. Except for the asymmetric methylene stretches, all the other nylon 6 bands listed in table 2.12 also have their transition dipole moments parallel to the surface for a mainly crystalline film, hence these bands should also be at a maximum intensity initially. Therefore, since all the nylon 6 bands appear to increase/decrease in intensity in unison during DL-aspartic acid crystallisation/dissolution, this does suggest that the film accumulation process is a more likely explanation for the observed intensity changes. Some reorientation of the film will also occur during this accumulation process, but this is unlikely to be extensive since the increase in the NH stretch would be far less evident if the NH stretching vibration was no longer approximately parallel to the aqueous surface.

Film accumulation around the DL-aspartic acid crystals is not definitive proof that the accumulation occurs due to the favourable interaction between the nylon 6 film and DL-aspartic acid crystal. The increased band intensities could be caused by the additional weight of the crystal as it grows, causing the surface to be depressed, with additional polymeric material then filling the recess formed. If infilling was the main cause of the film accumulation in the visible crystal regions, however, this effect would be expected for all the larger crystals growing beneath the film, which is not the case. Also the favourable adsorption of the nylon 6 film on the DL-aspartic acid crystals is consistent, 1) with the DL-aspartic acid material becoming incorporated within, and not below the nylon 6 film, and 2) the suggestion based on the limited visual crystallisation observed, that subsequent growth of many crystallites has been hindered by the film adsorption caused by the mutual DL-aspartic acid-nylon 6 attraction.

2.6.5 Rigid film

To help establish whether a more compressible film aids the crystallisation process, by its ability to rearrange to maximise its interaction with adsorbed DL-aspartic acid clusters, experiments were carried out to assess the impact of a rigid film on the crystallisation of DL-aspartic acid.

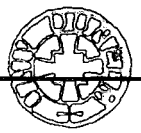

20 µl of nylon 6 dissolved in formic acid/chloroform (2:3) at a concentration of 1 mg cm^{-3} was added to the supersaturated subphase and compressed to 5 cm^2. This amount of nylon 6 is a 16-fold increase in the density used for all other experiments detailed in this chapter, and would significantly inhibit any rearrangement of the film.

Figure 2.34 shows spectra acquired for this system over an 8 hour period. After 8 hours, sharp intense bands associated with DL-aspartic acid would have been expected under a less rigid film, but only very weak bands were observed. There was very little variation in the nature of the spectra acquired on moving the sample, and there were no crystals visible to the naked eye.

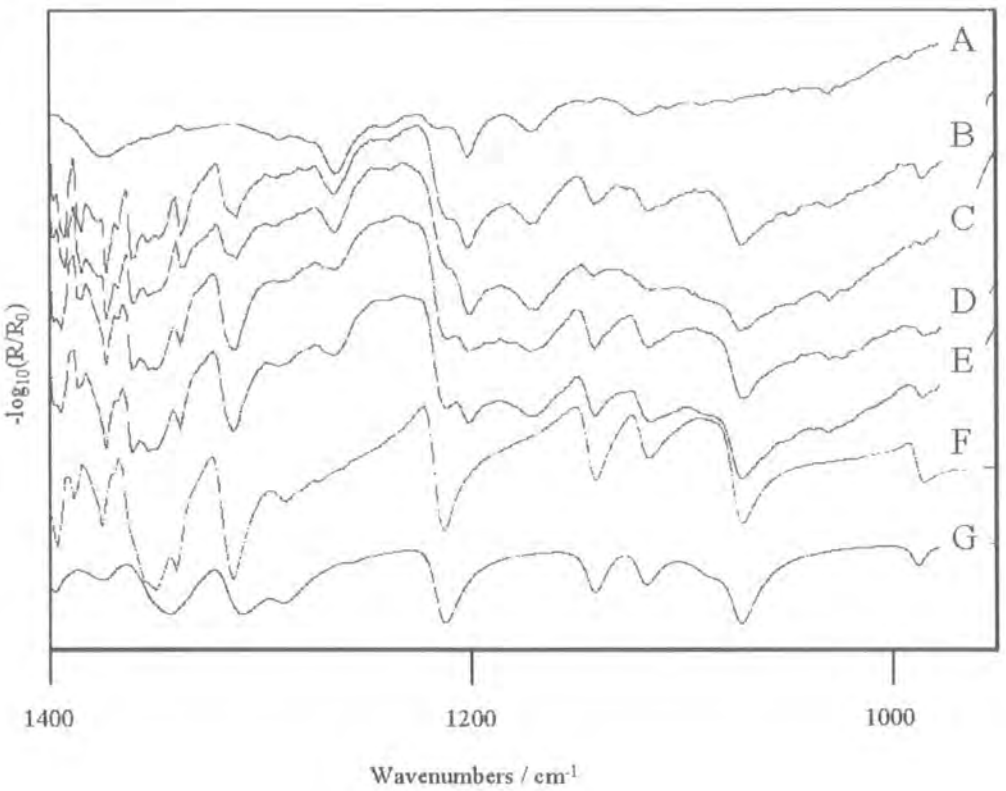

Figure 2.34. Spectral range 1400 – 950cm^{-1}. Crystallisation of DL-aspartic acid under a rigid nylon 6 film. Spectra A – E are at 0, 2, 4, 6 and 8 hours respectively. Spectrum F is a typical example of DL-aspartic acid under a less rigid film at 6 hours and spectrum G is pure DL-aspartic acid data acquired on the thunderdome accessory.

Intense DL-aspartic acid bands were only observed after approximately 24 hours, at which time there was substantial evaporation of the water, and significant crystallisation at the base of the trough. Consequently, the nucleating ability of the nylon 6 film is substantially decreased for this far more rigid film. This may be evidence that film compressibility is important in the nucleation process. Alternatively, the reduced crystallisation may be a consequence of the lack of water interdispersed between the nylon 6 film at these high concentrations, which would limit the ability of the DL-aspartic acid to be adsorbed within this film layer. Hence, DL-aspartic acid cluster adsorption may only be possible beneath the film layer, which as we have seen previously in the neutron reflectivity studies, does not occur to a significant degree.

2.7 Conclusions

Neutron reflectivity was used to follow the crystallisation of 150% supersaturated DL-aspartic acid under nylon 6 spread films with the aim of providing information about the composition and thickness of the interfacial region during the early stages of crystal growth. The data revealed the incorporation of significant quantities of DL-aspartic acid *within* the nylon 6 layer, rather than the existence of discrete film and crystal layers.

Neutron reflectivity data show that after 8 hours, the DL-aspartic acid could comprise over 50% of the interfacial film layer. Optical microscopy studies indicate that accumulation of further DL-aspartic acid material to produce microscopic/macroscopic crystals occurred, but on a more limited scale, culminating in ~1% crystal coverage of the surface over the same period.

These observations suggest that a large proportion of the incorporated DL-aspartic acid material is of sub-critical nucleus size and/or that subsequent film absorption upon the nuclei impedes their further growth to visible dimensions. These neutron reflectivity data are supported by external reflection FTIR studies in which very weak bands attributable to DL-aspartic acid are observed in surface regions devoid of visible crystals. In regions with visible crystals, much larger and sharper DL-aspartic acid bands are seen.

Changes in the intensity of the nylon 6 NH stretch and other nylon 6 bands are often observed during the visible crystallisation and dissolution of DL-aspartic acid, and are consistent with the reversible accumulation of the nylon 6 film around the growing crystals. Crystallisation of DL-aspartic acid is not observed at the 150% supersaturation level if a far more rigid film is used. This may be evidence that film compressibility is important for the nucleation stage, so that the film can maximise its interaction with any adsorbed DL-aspartic acid clusters. However, if film rearrangement does occur, it does not result in a significant rearrangement of the nylon 6 hydrogen-bonded sheets parallel to the surface.

References

(1) Jamieson, M. J.; Cooper, S. J.; Miller, A. F.; Holt, S. A. *Langmuir* **2004**, *20*, 3593-3600.

(2) Lahav, M.; Landau, E. M. *Nature* **1985**, *318*, 353.

(3) Heywood, B. R.; Mann, S. *Adv. Mater.* **1994**, *6*, 9-20.

(4) Mann, S.; Heywood, B. R.; Rajam, S.; Walker, J. B. A. *ACS Symposium Series* **1991**, *444*, 28-41.

(5) Ma, C. L.; Lu, H. B.; Wang, R. Z.; Zhou, L. F.; Cui, F. Z.; Qian, F. J. *Cryst. Growth* **1997**, *173*, 141-149.

(6) Lochhead, M. J.; Letellier, S. R.; Vogel, V. *J. Phys. Chem. B*, *101*, 10821-10827.

(7) Cooper, S. J.; Sessions, R. B.; Lubetkin, S. D. *J. Am. Chem. Soc.* **1998**, *120*, 2090-2098.

(8) Backov, R.; Lee, C. M.; Khan, S. R.; Mingotaud, C.; Fanucci, G. E.; Talham, D. R. *Langmuir* **2000**, *16*, 6013-6019.

(9) Volkmer, D.; Fricke, M.; Vollhardt, D.; ., S. S. *J. Chem. Soc., Dalton Trans.* **2002**, *24*, 4547-4554.

(10) Ouyang, J. M.; P., D. S. *Dalton Trans.* **2003**, *14*, 2846-2851.

(11) Popovitz-Biro, R.; Edgar, R.; Weissbuch, I.; Lavie, R.; Cohen, S.; Kjaer, K.; Als-Nielsen, J.; Wassermann, E.; Leiserowitz, L.; Lahav, M.-. *Acta Polym.* **1998**, *49*, 626-635.

(12) Wang, L. F.; Kou, J. F.; Chen, C. Y. *Mater. Chem. Phys.* **1995**, *40*, 197.

(13) Wang, L. F.; Kou, J. F.; Chen, C. Y. *Colloid Polym. Sci.* **1995**, *273*, 16.

(14) Miller, A. F.; Cooper, S. J. *Langmuir* **2002**, *18*, 1310-1317.

(15) Ahn, D. J.; Berman, A.; Charych, D. *J. Phys. Chem* **1996**, *100*, 12455-12461.

(16) Cooper, S. J. *Langmuir* **2002**, *18*, 3749-3753.

(17) Rapaport, H.; Kuzmenko, I.; Berfeld, M.; Kjaer, K.; Als-Nielsen, J.; Popovitz-Biro, R.; Weissbuch, I.; Lahav, M.; Leiserowitz, L. *J. Phys. Chem. B* **2000**, *104*, 1399-1428.

(18) Mowald, H. *Reports on Progress in Physics* **1993**, *56*, 653-685.

(19) Li, B.; Liu, Y.; Lu, N.; Yu, J. H.; Bai, Y. B.; Pang, W. Q.; Xu, R. R. *Langmuir* **1999**, *15*, 4837-4841.

(20) Weygand , M.; Kjaer, K.; Howes, P. B.; Wetzer, B.; Pum, D.; Sleytr, U. B.; Lösche, M. *J. Phys. Chem. B* **2002**, *106*, 5793-5799.

(21) Sears, V. F. *Neutron News* **1992**, *3*, 29-37.

(22) Penfold, J.; Richardson, R. M.; Zarbakhsh, A.; Webster, J. R. P.; Bucknall, D. G.; Rennie, A. R.; Jones, R. A. L.; Cosgrove, T.; Thomas, R. K.; Higgins, J. S.; Fletcher, P. D. I.; Dickinson, E.; Roser, S. J.; McLure, I. A.; Hillman, A. R.; Richards, R. W.; Staples, E. J.; Burgess, A. N.; Simister, E. A.; White, J. W. *J. Chem. Soc. - Far. Trans.* **1997**, *93*, 3899-3917.

(23) Penfold, J.; Thomas, R. K. *Jnl. Phys. - Cond. Matter* **1990**, *2*, 1369-1412.

(24) Jones, R. A.; Richards, R. W. *Polymers at Surfaces and Interfaces*; Cambridge University Press, 1999.

(25) Lovell, M. R.; Richardson, R. M. *Current Opinion in Colloid & Interface Science* **1999**, *4*, 197-204.

(26) Born, M.; Wolf, E. *Principles of Optics*; Pergamon Press, 1980.

(27) Nevot, L.; Croce, P. *Phys. Appl.* **1980**, *15*, 761.

(28) Pynn, R. *Physica B* **1992**, *45*, 602-612.

(29) Cowley, R. A.; Ryan, T. W. *J. Phys. D., Appl. Phys.* **1987**, *20*, 61-68.

(30) Rotter, G.; Ishida, H. *J. Polym. Sci.: Part B* **1992**, *30*, 489-495.

(31) Lu, J. R.; Hromadova, M.; Simister, E. A.; Thomas, R. K.; Penfold, J. *J. Phys. Chem.* **1994**, *98*, 11519.

(32) Carraher Jnr., C. E. *J. Chem. Educ.* **1978**, *55*, 51-52.

(33) *CRC Handbook of Physics and Chemistry*, 82nd ed., 2001.

(34) Berman, A.; Ahn, D. J.; Lio, A.; Salmeron, M.; Reichert, A.; Charych, D. *Science* **1995**, *269*, 515-518.

(35) Gericke, A.; Huhnerfuss, H. *J. Phys. Chem.* **1993**, *97*, 12899-12908.

(36) Hasegawa, T.; Nishijo, J. *Langmuir* **2002**, *18*, 4758-4764.

(37) Ren, Y.; Kato, T. *Langmuir* **2002**, *17*, 6699-6705.

(38) Dluhy, R. A. *J. Phys. Chem.* **1986**, *90*, 1373-1379.

(39) Dluhy, R. A.; Cornell, D. G. *J. Phys. Chem.* **1985**, *89*, 3195-3197.

(40) Ren, Y.; Meuse, C. W.; Hsu, S. L.; Stidham, H. D. *J. Phys. Chem.* **1994**, *98*, 8424-8430.

(41) Osman, M. A.; Suter, U. W. *Chem. Mater.* **2002**, *14*, 4408-4415.

(42) Buffeteau, T.; Blaudez, D.; Pere, E.; Desbat, B. *J. Phys. Chem. B.* **1999**, *103*, 5020-5027.

(43) Mielczarski, J. A. *J. Phys. Chem* **1993**, *97*, 2649-2663.

(44) Mielczarski, J. A.; Yoon, R. H. *Langmuir* **1991**, *7*, 101.

(45) Yen, Y. S.; Wong, J. S. *J. Phys. Chem.* **1989**, *93*, 7208.

(46) Parikh, A. N.; Allara, D. L. *J. Chem. Phys.* **1992**, *96*, 15.

(47) Porter, M. D.; Bright, T. B.; Allara, D. L.; Kuwana, T. *Anal. Chem.* **1986**, *58*, 2461.

(48) Lopez Navarrete, J. T.; Hernandez, V.; Ramirez, F. *J. Biopolymers* **1994**, *34*, 1065-1077.

(49) Vasanthan, N.; Salem, D. R. *J. Polym. Sci.: Part B* **2001**, *39*, 536-547.

Chapter 3

Monolayer Induced Crystallisation of Calcium Carbonate

3.1 Introduction

3.1.1 Biomineralisation and the Significance of Calcium Carbonate

Biomineralisation is the formation of minerals by living organisms. These range from the crystals formed by bacteria, to bone formation in the rhinoceros or elephant. The size of biominerals thus spans nanometres to metres. The function of biominerals varies from gravity perception to the temporary storage of ions, but the principal business of this topic is the biosynthesis of materials with optimised mechanical properties such as bones, teeth and shells. An impressive feature of biomineralisation is the ability to generate single crystals of exact morphology generation after generation[1]. Calcium carbonate is one of the most abundant biominerals, representing 4% by mass of the earth's crust; hence it is not surprising it features so widely in organic species. Calcium compounds exist in a large number of plants and animals, principally as phosphates and carbonates, but also as citrates and oxalates.

The study of biomineralisation is a relatively new, but highly interdisciplinary research field. The huge number of scientists studying the role of calcium carbonate in biological systems[2-9] is indicative of the importance of understanding the sophisticated crystallisation processes in nature. Biomineralisation processes, such as the production of shells, teeth and bone, rely on complex processes that are not well understood by scientists. As a result, simple biological systems, such as algal calcification[10] are studied in order to develop a better understanding of more sophisticated natural processes.

3.1.2 The Crystal Structure of Calcium Carbonate Polymorphs, Natural Occurrences and Properties

Calcium carbonate exists in 6 solid forms, as detailed in table 3.1. In sharp contrast, only one crystalline form is known for each of $SrCO_3$ and $BaCO_3$. It is therefore all the more impressive that calcium carbonate features so significantly in organic systems and is crystallised with such specificity.

Form	Organism/Function	Chemical Formula
Amorphous	Plants/Ca store	$CaCO_3.nH_2O$
Hexahydrate	Not stable – transforms to vaterite[11].	$CaCO_3.6H_2O$
Monohydrate	Bacteria	$CaCO_3.H_2O$
Vaterite	Ascidans/Spicules	$CaCO_3$
Aragonite	Fish/Gravity device Molluscs/Exoskeleton	$CaCO_3$
Calcite.	Algae/Exoskeletons Trilobites/Eye lens	$CaCO_3$

Table 3.1 The solid forms of calcium carbonate and the organisms where these polymorphs are found.

A comprehensive list of the occurrences of calcium carbonates for different classes of bacteria, plants, algae and animals was reported by Lowenstam[12].

The hexahydrate form is unstable under normal conditions, transforming quickly to vaterite, but biological occurrences of this polymorph have been reported[13] for mollusc shells, otoliths (earstones) of fish and human gall stones. Crystalline anhydrous calcium carbonate has three different crystal structures and symmetries. The unit cell of aragonite is orthorhombic, for vaterite it is hexagonal and for calcite, trigonal. All seven crystal systems are illustrated in figure 3.1.

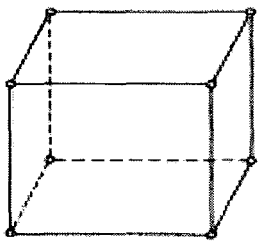

Tetragonal

$a = b \neq c$

$\alpha = \beta = \gamma = 90^\circ$

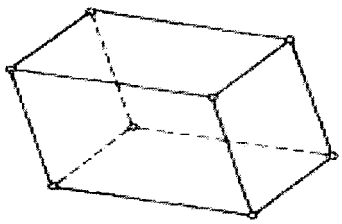

Triclinic

$a \neq b \neq c$

$\alpha \neq \beta \neq \gamma$

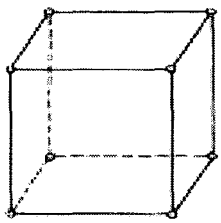

Cubic

$a = b = c$

$\alpha = \beta = \gamma = 90^\circ$

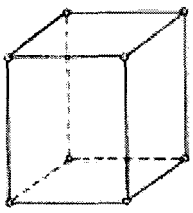

Orthorhombic

$a \neq b \neq c$

$\alpha = \beta = \gamma = 90^\circ$

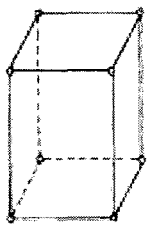

Monoclinic

$a \neq b \neq c$

$\alpha = \gamma;\ \beta > 90^\circ$

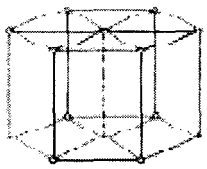

Hexagonal

$a = b = c$

$\alpha = \beta = 90^\circ \quad \gamma = 120^\circ$

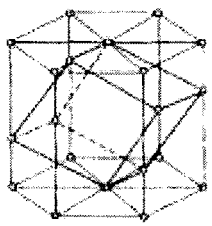

Trigonal

$a = b = c$

$\alpha = \beta = \gamma \neq 90^\circ$

Figure 3.1 An illustration of all seven crystal systems.

Vaterite is the most soluble polymorph of calcium carbonate and calcite the least[14]. Consequently, vaterite is the least stable polymorph, which only precipitates in the presence of specific additives[15]. Vaterite transforms into the most thermodynamically stable form, calcite, via a solvent-mediated process[16], and is not commonly found in organisms[17]. Figure 3.2 illustrates the unit cell axes and lattice positions for calcite.

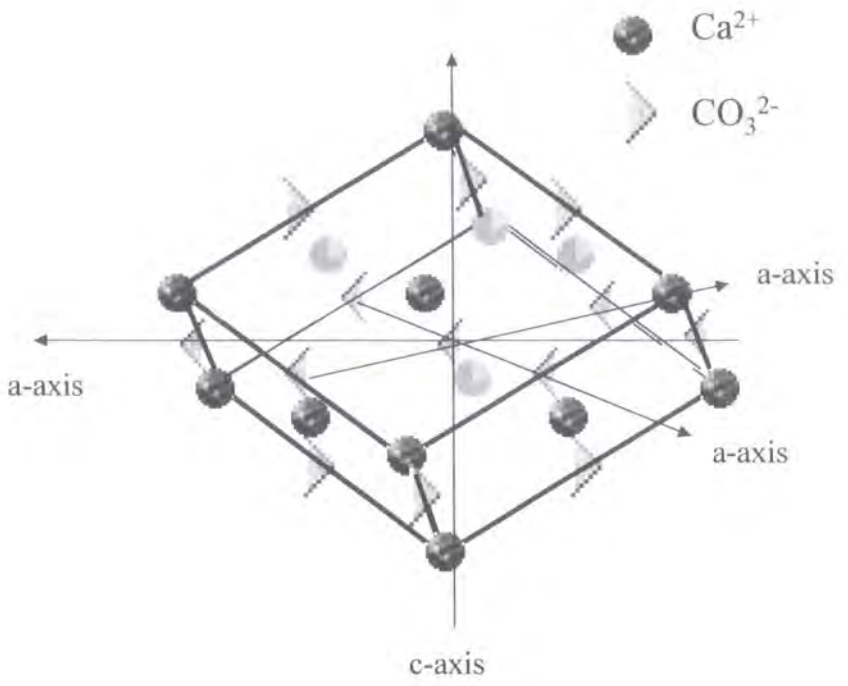

Figure 3.2. Illustration of different axes and lattice positions for calcite.

The precipitation of the metastable forms of calcium carbonate is difficult, but magnesium can be used to inhibit growth of the calcitic form[18]. From an engineering perspective, vaterite has potentially greater applications because it offers high specific surface area, small specific gravity and high solubility/dispersion compared with calcite and aragonite[6].

3.1.3 Naturally Occurring Organic Templates

Naturally occurring organic matrices are studied following dissolution of the calcium carbonate with chelating agents such as EDTA[19] (see EDTA titrations in section 3.3.3). Falini et al.[20] extracted major matrix components from mollusc shells. When placed in supersaturated calcium bicarbonate solutions, they found that the matrix extracted from calcitic structures led to calcite crystallisation, and similarly for vaterite and aragonite matrices, vaterite and aragonite were crystallised from supersaturated calcium bicarbonate solutions, respectively.

Polycationic[21] and neutral polypeptides have little or no ability to regulate calcium carbonate growth, except for poly(asparagine), which suggests that repeating (COX) carbonyl groups impart some activity. Weiner et al.[22,23] showed that the spacing of anionic groups nearly matches the crystal lattice. This was believed to lower the nucleation energy requirement. This idea was developed further[24] to suggest a calcium loaded matrix can adopt a different configuration in order to optimally interact with the incoming carboxylate of the forming crystals.

These observations demonstrate that the polymorph specificity is dependent on the amino acid sequence and imply that a simple artificial template modelled on the naturally occurring matrices might be designed for the controlled nucleation of minerals.

3.1.4 Synthetic Templates and the Oriented Crystallisation of Calcium Carbonate

It is widely accepted that oriented growth can proceed on a solid substrate[25]. This oriented growth of one substance on another is termed epitaxy. Lahav et al.[26-31] first demonstrated that epitaxial growth can also occur beneath monolayers deposited at the air-water interface. Monolayers provide a well-defined matrix for studies of oriented growth, which can be compressed and systematically varied as appropriate.

Xu et al.[32] prepared thin films of thickness range 0.4 - 0.6 μm by use of porphyrin depositor and poly(acrylic acid) inhibitor. This showed calcite oriented with the (001) face (see figure 3.3) parallel to the porphyrin monolayer. Ahn et al.[33] demonstrated that calcite nucleates principally at the (010), (001) and (012) planes under octadecanoic acid, octadecyl sulfate and acidic polydiacetylenic lipid film, respectively. The oriented nucleation of calcite under octadecanoic acid was attributed to tilting of the octadecanoic acid monolayer molecules to better accommodate the (010) calcite plane, whereas for octadecyl sulfate, Ahn reported gradual expansion of the monolayer to better fit the carbonate spacings in the (001) calcite plane.

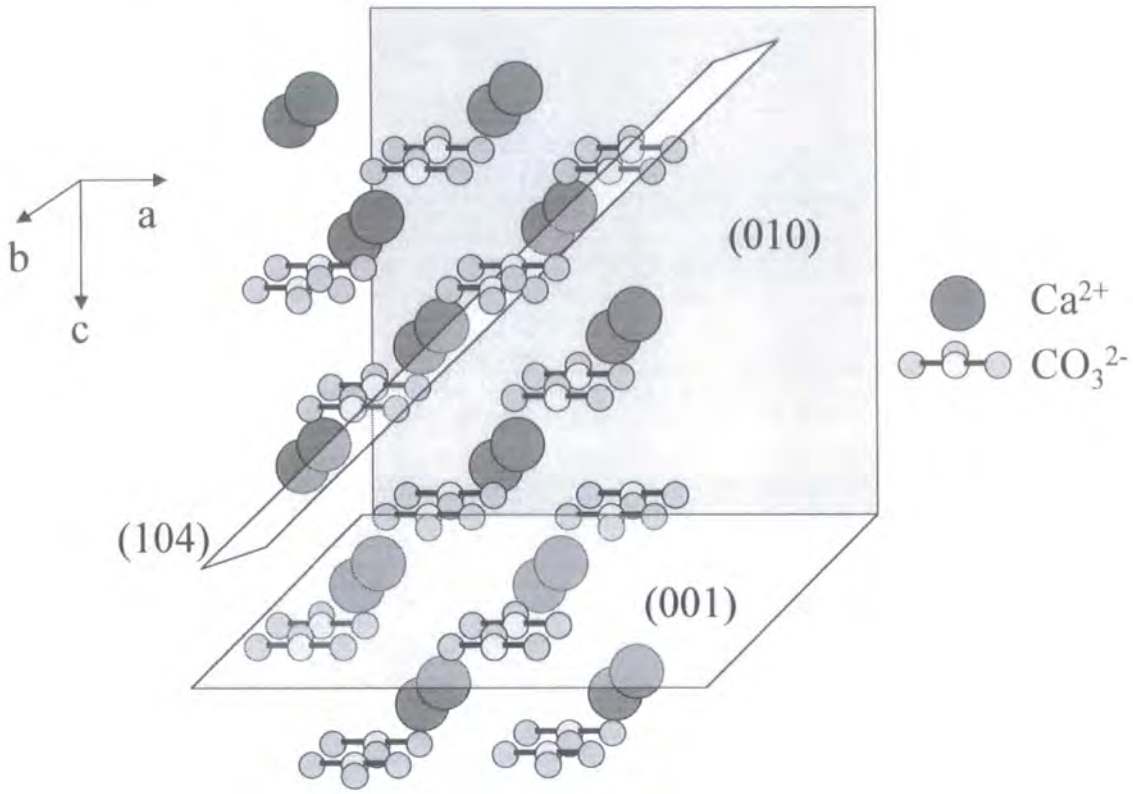

Figure 3.3. Structure of calcite with important faces illustrated.

Heywood et al.[34] reported the oriented growth of calcite and vaterite under charged monolayers and Mann et al.[35,36] first described the oriented (controlled) crystallisation of calcium carbonate from supersaturated solutions under monolayers of octadecanoic acid. In the absence of the monolayer, rhombohedral crystal formation is observed, but the presence of an octadecanoic acid monolayer promotes oriented calcite formation. This is discussed further in section 3.5. At lower calcium bicarbonate concentration, (4.5 mmol dm^{-3}) under monolayers of octadecanoic acid, the metastable polymorph vaterite forms, oriented with the c axis perpendicular to the monolayer surface. Similarly, crystallisation of calcite under conditions where the aragonite formation is generally favoured have been demonstrated by use of crystal-imprinted polymer additives[7].

This suggests stereochemical or electrostatic interactions are responsible for this epitaxial nucleation process. DiMasi et al.[37] recently proposed that the rate of carbon dioxide evolution is the true cause of nucleation of different calcium carbonate polymorphs, and questioned whether polymorph control or oriented growth could really

be achieved at all. Groves et al.[32] proposed a multistep process with calcium carbonate starting with an amorphous precursor, which transforms to the crystalline forms of calcium carbonate with time. Both the hypotheses of Groves et al. and DiMasi et al. will be discussed in more detail later.

3.1.5 Previous Studies of the Structure of Octadecanoic Acid Monolayers on Water and Calcium Rich Aqueous Subphases

GIXD studies of octadecanoic acid monolayers on water[38,39] and Ca^{2+} subphases[40] have been reported. Similar fatty acids have also been studied[41-44]. These typically show a peak in the region $Q_{xy} \sim 1.47$ Å^{-1} at surface pressures of ~15 mN/m with a tilt of the hydrocarbon chains approximately 20° from the surface normal. At surface pressures of $\pi = 10$ mN/m and 21 mN/m, Tippmann-Krayer and Möhwald[44] showed that eicosanoic acid on water gave peaks centred at 1.477 and 1.511 Å^{-1}, respectively. Similarly, Kjaer et al.[41] showed that a weaker peak at $Q_{xy} = 1.47$ Å^{-1} is observed at very low surface pressures of eicosanoic acid, which increases in intensity and moves to $Q_{xy} = 1.53$ Å^{-1} when $\pi = 25$ mN/m.

Shih et al.[40] showed that a peak at $Q_{xy} = 1.43$ Å^{-1} is observed for heneicosanoic acid on an aqueous 0.5 mmol/dm^3 Ca^{2+} subphase for pH ~ 6 and $\pi = 0$ mN/m. This system shows a peak at $Q_{xy} = 1.47$ Å^{-1} for the surface pressure range ~ 7 mN/m to 17 mN/m with a corresponding tilt of ~ 19.3 to 27° from the surface normal. At $\pi = 7$ mN/m, this is characteristic of a rectangular unit cell with parameters a = 5.04 Å, b = 8.11 Å and a tilt of 19.3° from the surface normal. Above surface pressures of ~ 18 mN/m, Shih et al.[40] reported a 0° tilt for fatty acid monolayers on these aqueous Ca^{2+} subphases.

Based on external reflectance FTIR studies, Ahn et al.[33] reported that when an octadecanoic acid monolayer is spread onto a supersaturated calcium bicarbonate subphase, there is reorientation of the monolayer molecules away from the surface normal, evidenced by a decrease in intensity of methylene stretches over time, with no change in band position. This will be discussed again later in this chapter. The same observation is not observed when the subphase is $CaCl_2$, indicating this change is specific to calcium carbonate crystallisation.

3.1.6 Inhibition of Crystal Growth

Calcium carbonate crystal growth is stunted by the presence of carboxylate ions[45] in solution, but nucleation of $CaCO_3$ is not affected. Reddy and Hoch developed this idea further[46], demonstrating that rigid polycarboxylic acids dissolved at low concentrations inhibit calcite crystal growth. Furthermore, they demonstrated that the inhibition is proportional to the number of acid groups present within the additive molecule.
The morphology and size of calcium carbonate crystals can be controlled by block copolymers and the directed synthesis of hollow calcite spheres has been achieved by the use of surfactants and inhibitors[47]. Other have shown how magnesium is able to promote aragonite formation by inhibiting calcite growth[48,49], but to date, this has not been shown in vivo[50].

3.2 Chapter Aims

The aims of this chapter are to investigate the crystallisation mechanisms during the nucleation of calcium carbonate induced by octadecanoic (stearic) acid at the air-water interface. While this has been investigated extensively in recent years, there remains a limited understanding of the mechanisms that cause octadecanoic acid to promote the crystallisation of calcium carbonate so effectively. In particular, crystallisation of the most stable polymorph, calcite, under carboxylate groups is thought to be aided by a stereochemical match between the headgroups at the position of the carbonate groups in the attached calcitic plane. However, there is also a growing body of evidence[33,51,52] to suggest the crystallisation is assisted by reorganisation of the monolayer, particularly at low surface pressures.

The possibility that rearrangement of the monolayer occurs during calcite crystallisation will be investigated by external reflectance FTIR (ER-FTIR) and synchrotron GIXD. Others[32,33] have proposed that calcium carbonate crystallisation begins with an amorphous phase with subsequent transformation to a more stable (calcite) phase. This hypothesis will also be investigated.

3.3 Experimental

3.3.1 Materials

Materials used were as follows. Calcium carbonate, stearic (octadecanoic) acid (99.5%), polyacrylic acid (mol. wt. = 5,000) and chloroform (>99.5%). All were purchased from Aldrich and used with no further purification.

3.3.2 Preparation of Supersaturated Calcium Bicarbonate Solutions

Two methods of preparing supersaturated calcium bicarbonate solutions were explored. These are detailed below, including details of the advantages and disadvantages for each.

Kitano Method[53]

Carbon dioxide gas was bubbled for 1 hour through a stirred aqueous suspension (10 g per dm^3) of $CaCO_3$ at a rate of ~ 0.20 m^3h^{-1}. This allows formation of a more soluble bicarbonate. The resulting suspension was passed through a 0.20 μm Millipore filter and the filtrate purged with CO_2 for a further 30 minutes to remove any remaining undissolved $CaCO_3$.

The concentration of Ca^{2+} was approximately 9 mmol/dm^3 as determined by standard EDTA titrations[54-56] (see section 3.3.3). Similarly, a value of 10 mmol/dm^3 was reported by DiMasi et al.[57] for solutions prepared by the same method.

$CaCl_2$ Method[58]

Equal volumes of 0.005 M aqueous $NaHCO_3/Na_2CO_3$ solution and 0.005 M aqueous $CaCl_2$ solutions were combined and passed through a 0.2 μm Millipore filter to remove any undissolved material. The supersaturation level over time is determined by measuring the pH and comparing to data reported by Spanos and Koutsoukos[14].

The resulting solution was pH adjusted to 9.6 with 0.2 M aqueous NaOH or HCl.

Relative Advantages and Disadvantages of $CaCl_2$ and Kitano Methods

With the $CaCl_2$ method, the crystallisation can be monitored by the change in pH caused by evolution of H^+ (see equations 3.1 and 3.2). The supersaturation of the system can then be calculated by reference to the tables in Spanos and Koutsoukos[14].
The critical reactions observed in this case are:

$$Ca^{2+}_{(aq)} + CO^{2-}_{3(aq)} = CaCO_{3(s)} \qquad \text{[Eqn. 3.1]}$$

$$Ca^{2+}_{(aq)} + HCO^{-}_{3(aq)} = CaCO_{3(s)} + H^{+} \qquad \text{[Eqn. 3.2]}$$

Care must be taken with this method, as a high HCO_3^- to Ca^{2+} ratio favours vaterite formation, whereas a stoichiometric ratio favours calcite formation[59]. The advantage of this method, however, is that unlike the Kitano method, crystallisation is not forced at the surface by evolution of carbon dioxide gas [eqn. 3.3], and the initial supersaturation is known.

$$Ca^{2+}_{(aq)} + 2HCO^{-}_{3(aq)} = CaCO_{3(s)} + CO_{2(g)} + H_2O_{(l)} \qquad \text{[Eqn. 3.3]}$$

The supersaturation or calcium content of solutions prepared by the Kitano method is not known to an exact value, due to its dependence on the rate of carbon dioxide loss.

3.3.3 EDTA Titrations

The typical concentrations of Ca^{2+} in supersaturated solutions prepared by the Kitano method were determined by EDTA titrations. The solution was adjusted to pH 10 with dilute aqueous NaOH, to ensure a sharp endpoint. A known amount of EDTA was dissolved in UHQ water (resistivity = 18 MΩ cm). Eriochromeschwartz-T indicator was added to the supersaturated solution and initiated by addition of a small amount of $MgCl_2$, which causes a red appearance. EDTA forms a weaker complex with Mg^{2+} than

Ca^{2+}, hence addition of EDTA will preferentially complex all the Ca^{2+}. As an excess of EDTA is added, the Mg will be complexed turning the indicator colourless, followed by hydrolysis, resulting in a blue colour.

3.3.4 Monolayer Formation

A full compression cycle of the subphase was completed to ensure a clean surface, before addition of the film solution. Octadecanoic acid was spread from a chloroform solution (1 mg/cm^3), which was added to the subphase by micro-syringe. After evaporation of the chloroform, the trough barrier was adjusted to compress the monolayer to the required initial surface pressure reading reported for each data set.

All crystallisation experiments were performed in PTFE troughs (section 2.3.4). A Nima trough of dimensions 20 cm x 10 cm was used for GIXD studies and a 2 cm x 12 cm equivalent was used for external reflectance FTIR analyses. These troughs were cleaned with dilute HCl, followed by boiling water and chloroform.

3.3.5 External Reflection FTIR (ER-FTIR)

The ER-FTIR equipment used was as described in section 2.3.7. ER-FTIR data were acquired over 512 scans at 4 cm^{-1} resolution. A background spectrum was taken on the clean subphase before addition of the octadecanoic acid monolayer, hence spectra become increasingly affected by subtraction of ageing background as the experiment progresses.

3.3.6 X-Ray Diffraction

This chapter includes data from GIXD and wide angle X-ray scattering (WAXS). A brief introduction to X-ray diffraction and the equipment used in these studies follows.

Introduction to X-Ray Diffraction

X-ray diffraction probes the interaction between X-rays and the electron density surrounding molecules and atoms. For crystalline materials with a regularly repeating lattice, sharp diffraction signals occur.

Bragg's Law is the fundamental equation describing diffraction.

$$n\lambda = 2d\sin\theta \qquad \text{[Eqn. 3.4]}$$

where n is the order number (integers 1, 2, 3.....), λ is the X-ray wavelength, d is the distance between the diffraction planes and θ is the Bragg scattering angle. This is illustrated in figure 3.4.

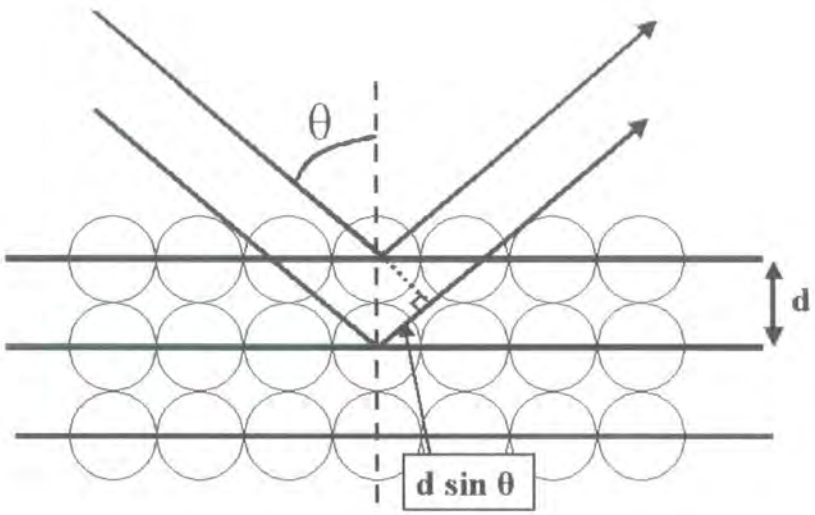

Figure 3.4. Illustration of Bragg's Law.

3.3.6 Grazing Incidence X-ray Diffraction; Daresbury Station 16.2

GIXD data were acquired on Station 16.2 at Daresbury Laboratories, Cheshire. Station 16.2 was designed to study the structure of surfaces and interfaces as it allows horizontal diffractometry and vertical reflectivity for solids. It is particularly suited to the studies of crystal growth at the surface of solutions, electrochemical interfaces, surface melting, thin molecular layers, and semiconductor heterostructures.

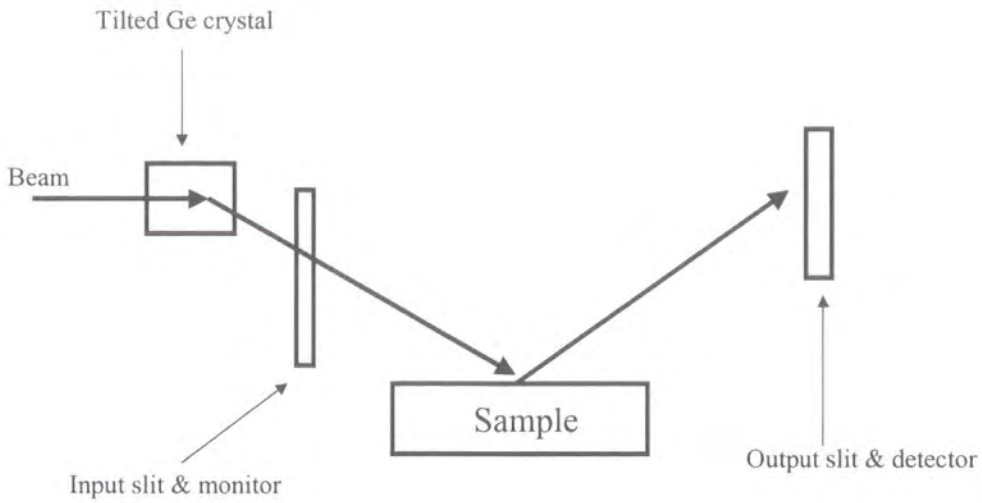

Figure 3.5. Schematic of experimental set-up at Daresbury Station 16.2.

The instrument receives light fixed at an angle of approximately 0.125° from the horizontal. The X-ray wavelength (1.36 Å) is selected by use of Ge (111), (220) and Si (111) & (220) crystals. The incident angle of the beam is fixed, hence 2θ values are achieved via a coupled movement of the stage tilt and detector arm.

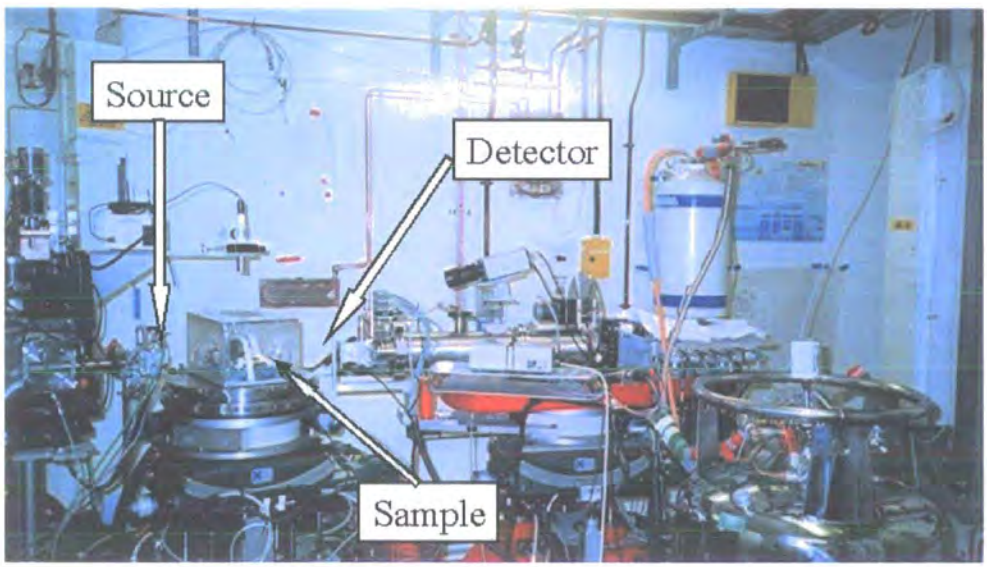

Figure 3.6. Image of experimental set-up on station 16.2.

3.3.8 GIXD Experimental Procedures

Sample Height Optimisation

For the preliminary GIXD studies, the sample height was assessed by placing the detector directly in the path of the beam, and protecting the detector by closing the horizontal and vertical beam slits to 0.04 mm, hence reducing the beam size. The sample height was then adjusted incrementally until a maximum counts reading was measured when the beam passed directly over the top of the sample (trough) and into the detector, see example graph in figure 3.7. Placing the sample at the height that gave half the maximum number of counts would then place the beam on the centre of the sample.

This method is similar to that reported by Richardson and Roser[60], but failed to work perfectly as the incident angle, $\theta_i \neq 0$, but was fixed at approximately 0.125°. The height determined by this method was falling out of the beam quicker than anticipated and in fact meant that the beam landed at the back of the sample area, rather than the centre.

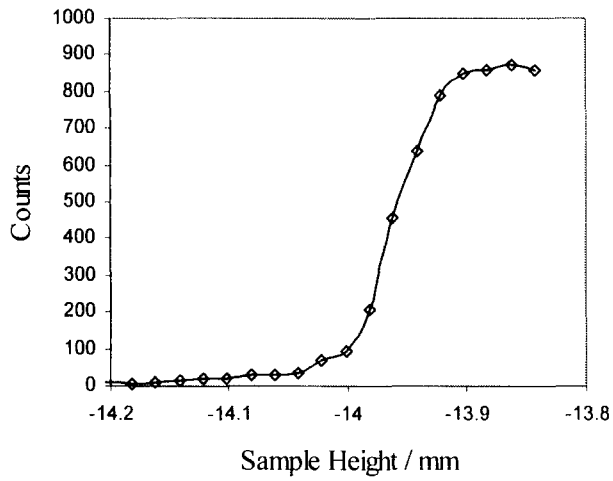

Figure 3.7. Graph illustrating a typical data set for height optimisation by the method of Richardson and Roser[60].

It was calculated that increasing the sample height by an additional 76 μm would give the beam focussed in the centre of the sample area. This is illustrated in figure 3.8. In practice, making this minor height adjustment led to a very significant improvement in data quality.

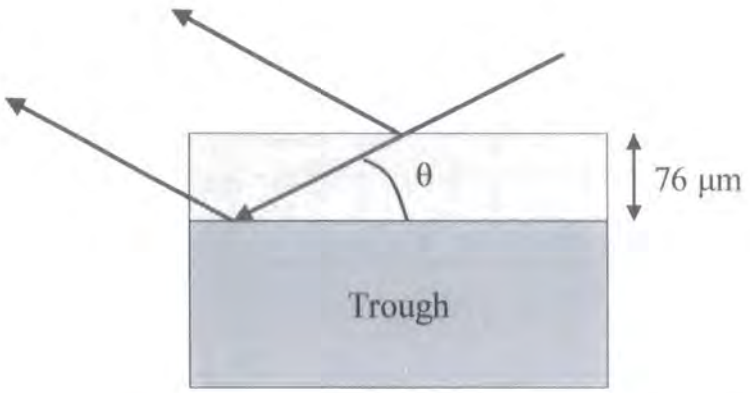

Figure 3.8. Illustration of the height adjustments made during exploratory experiments. Moving the trough up by 76 μm to the position of the light grey area, resulted in the beam landing in the centre of the sample area, rather than the back.

Improved Sample Height Optimisation Method

Better sample height optimisation was achieved by placing the detector directly in the path of the reflected beam, and tilting the detector at an angle approximately twice that of the incident angle, θ_i. In this case, the intensity of reflected signal was monitored with incremental changes in sample height, and the optimal sample height judged as the height corresponding to the maximum counts received at the detector. This better height optimisation method results in a graph such as that illustrated in figure 3.9.

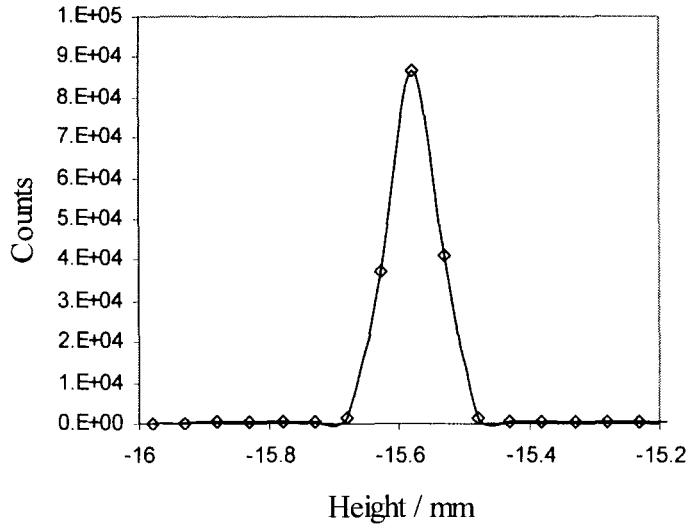

Figure 3.9. Typical data acquired for the height optimisation where the reflected beam is monitored.

Figure 3.9 demonstrates the importance of sample height. A 50 μm error in the height of the sample platform leads to a halving of counts, whilst a 100 μm error leads to a complete loss of signal.

Sample Enclosure and Water Evaporation

The height optimisation methods described above indicated that water loss in open air due to evaporation was approximately 2 μm per minute. With this degree of evaporation, the sample would have changed height after only a very short time, leading to poor signal to noise levels.

Covering the trough with polyethene sheeting and introducing higher humidity through wicking reduced the evaporation rate by half. This indicated that an airtight enclosure would significantly improve the data acquired. A purpose built enclosure (figure 3.10) was made for the Daresbury workstation with an aluminium base to secure the trough to the sample platform and minimise vibrations. The Perspex cover had windows covered with mylar sheets, which have limited crystallinity/orientation, and hence would not cause any significant diffraction of X-rays. The perspex cover fitted into a groove around the edge of the base, and was sealed with Blu-tack. Combined with wicking, this set-up reduced evaporation to only ≈ 0.4 μm/min.

The tensiometer was taped at one corner of the trough and wicking was introduced by water-filled Petri dishes and tissue paper. This provided a humid environment, which was measured as equilibrating between 96-98% saturation by a portable humidity reader. The humidity reader was essentially crude, but found to give correct readings when compared to a Met.Office weather station reading 12 km from Durham.

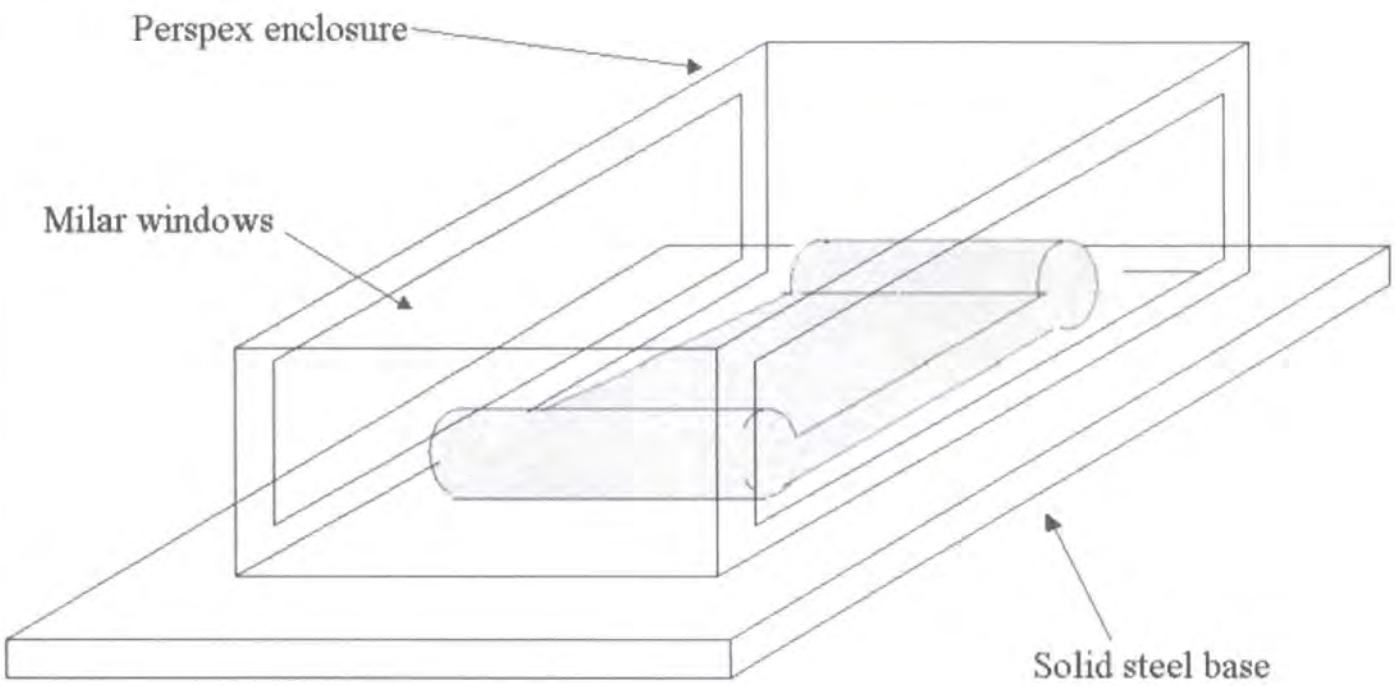

Figure 3.10 Illustration of enclosure designed to minimise evaporation of water.

In principle, the sample platform could be moved incrementally between each data point acquisition, to ensure the best possible data throughout each run, which typically lasted 55 minutes. In practice, the workstation would crash given these greater experimental demands, and evaporation varied according to weather conditions and periodic cooling of the detector with liquid nitrogen. Periodic cooling of the detector caused a temperature change in the hutch, and the resulting condensation on the interior of the Perspex enclosure, inevitably caused additional X-ray scattering.

The sample platform was therefore kept static throughout each run, and the sample height reassessed every time a new data series was acquired.

Image Plates

For the initial studies, following each 2θ scan, an image plate with dimensions 250 mm x 200 mm was exposed in the path of the beam for 4 minutes in order to obtain a diffraction pattern of the crystals nucleating beneath the monolayer.

Drawing semi-circles with a compass through the amorphous halo caused by background and/or mylar enabled location of the primary beam position. This is illustrated in figure 3.11. The distance of each diffraction spot from this reference point and the angle of the spot from the normal at the reference point, were measured for each spot and recorded.

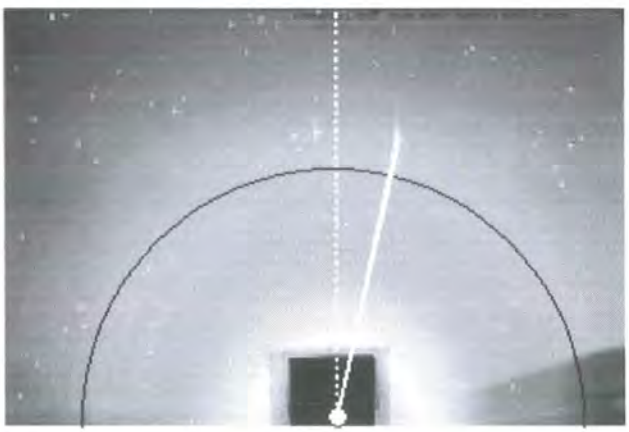

Figure 3.11. Illustration of a typical image plate. A semi-circle is drawn parallel to the halo perimeter to locate the position of the primary beam.

The sample to image plate distance was 188 to 258 mm (front and back of trough). The experimental set up of the image plates is illustrated in figure 3.12.

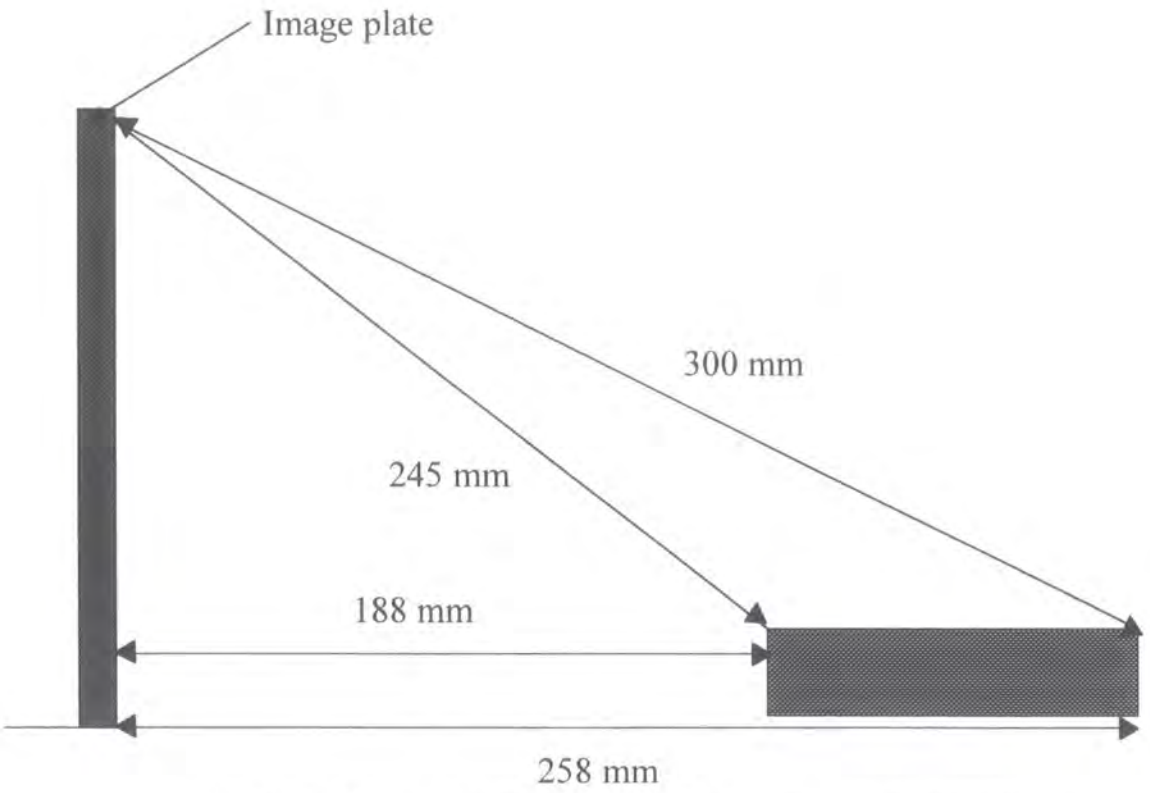

Figure 3.12. Iillustration of distances of the image plate to sample.

The scattering angle 2θ is determined from:-

$$2\theta = \text{Arctan}\left[\frac{\text{Distance of spot from beam position on detector.}}{\text{Horizontal distance of crystal from image plate, assumed initially to be in the trough centre}}\right]$$

[Eqn. 3.5]

GIXD Data Collection

Typically, data were acquired over a 2θ range of 19.7° to 17° at 0.05° resolution with a dwell time at each point of 60 seconds. Following each 2θ scan and image plate exposure (where applicable), the height of the sample stage was reassessed as described earlier, and the process repeated.

Dupres et al.[39] reported a peak for octadecanoic acid on pure water at approximately Q_{xy} = 1.47 to 1.5 $Å^{-1}$ at ambient temperature for $\pi \sim 0$ to 25 mN/m. Initial studies confirmed this, and so studies were focussed with the detector in this region. Data

presented are ratioed against the monitor counts to correct for beam inhomogeneity and decrease in flux, as time passes since the last injection of the beam.

Data are presented as the momentum transfer components within and normal to the layer plane, Q_{xy}:

$$Q_{xy} = \frac{2\pi}{\lambda}\sqrt{\cos^2\alpha + \cos^2\beta - 2\cos\alpha\cos\beta\cos(2\theta)} \qquad \text{[Eqn. 3.6]}$$

where α is the incident angle of the beam and β is the tilt of the detector (figure 3.13).

Approximating for α and β = 0, this gives

$$Q_{xy} = \frac{4\pi}{\lambda}\sin\theta \quad \text{since} \quad 2\sin\theta = \sqrt{2 - 2\cos 2\theta} \qquad \text{[Eqn. 3.7]}$$

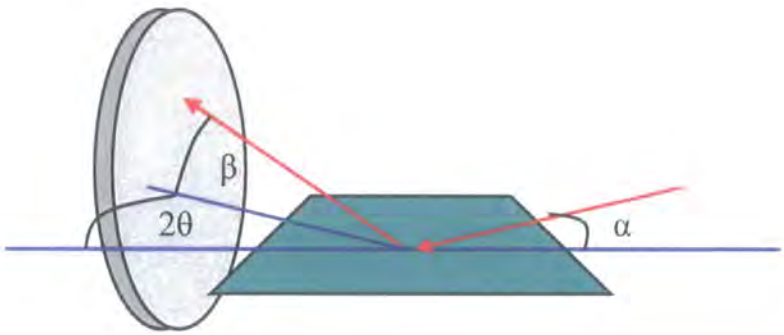

Figure 3.13. Illustration of incoming beam at angle α, the detector tilt, β and 2θ. The blue lines are in the horizontal equatorial plane.

3.3.9 Bruker D8 WAXS Diffractometer

Some in-house X-ray studies were undertaken to support the GIXD data acquired at Daresbury. Wide angle X-ray data were acquired on a Bruker D8 diffractometer. The angle of the source and area detector can be moved on this instrument in order to

facilitate orientation experiments. The sample platform height is variable, with the optimal sample height and sample target area identified by use of a vertical HeNe laser.

The angle of incidence (θ_1), detector arm angle (θ_2) and sample stage (X, Y and Z) are moved by independent stepper motors, controlled via a PC. On the D8, the X-rays are produced from a copper source via a tube-generator typically operating at 40 mA – 40 kV, but the power can be reduced if required to give a lower X-ray flux. The X-ray wavelength is 1.5418 Å, corresponding to CuKα radiation. Goebel mirrors positioned in the horizontal plane help collimate the beam in the vertical direction, so that the X-ray incident angle is well defined.

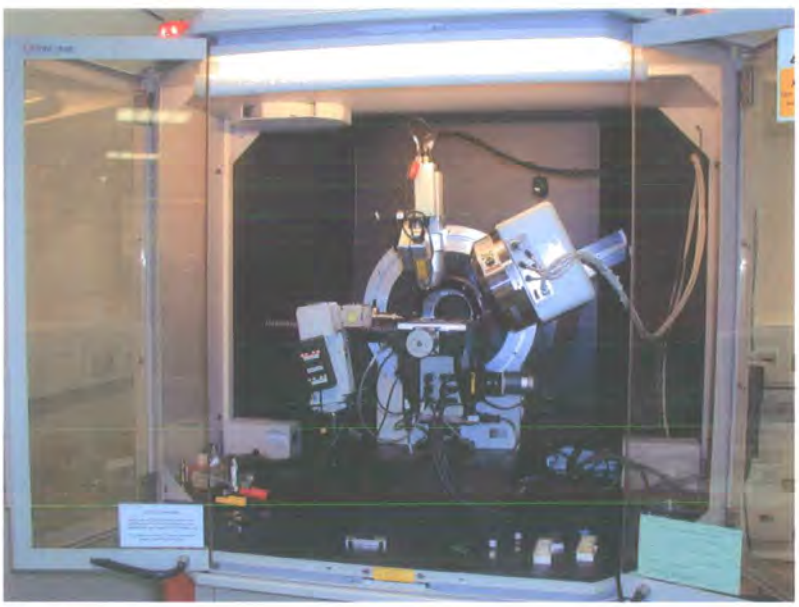

Figure 3.14. Picture of Bruker D8 WAX diffractometer.

3.4 Calcium Carbonate: Experimental Background Information

D-spacings for the metastable polymorphs, aragonite and vaterite are given in table 3.2[61]. Table 3.3 illustrates 2θ values and d-spacings for calcite as expected for λ = 1.5418 Å (CuK_α) and λ = 1.36 Å (Daresbury Synchrotron), and figure 3.15 shows a simulated powder X-ray diffraction pattern. In practice, the scatter from large angles was found to be very low, thwarting any efforts to view strongly diffracting calcite planes with smaller d-spacings. Image plate data for calcium carbonate are presented, however.

Vaterite			Aragonite		
d-spacing/ Å	2θ λ = 1.5418 Å	2θ λ = 1.36 Å	d-spacing/ Å	2θ λ = 1.5418 Å	2θ λ = 1.36 Å
4.245	20.83°	18.44°	4.212	21.00°	18.58°
3.577	24.78°	21.92°	3.396	26.12°	23.10°
3.296	26.93°	23.81°	3.273	27.12°	23.98°
2.735	32.59°	28.79°	2.700	33.03°	29.17°
2.219	40.47°	35.69°	2.481	36.04°	31.81°
2.122	42.41°	37.38°	2.328	38.50°	33.97°
2.065	43.64°	38.45°	2.106	42.75°	37.67°
1.857	48.82°	42.96°	1.977	45.69°	40.24°
1.825	49.74°	43.75°	1.882	48.13°	42.36°
1.648	55.51°	48.74°	1.814	50.06°	44.03°
1.544	59.61°	52.26°	1.698	53.74°	47.21°
1.477	62.62°	54.82°	1.535	60.00°	52.59°
1.351	69.24°	60.44°			
1.331	70.43°	61.45°			
1.286	73.28°	63.84°			

Table 3.2. X-ray peak positions expected for the metastable forms of calcium carbonate, vaterite and aragonite, on the Durham X-ray equipment and at Daresbury.

Miller Plane	d – spacing / Å	Relative Powder Intensity	λ = 1.5418 Å 2 θ Durham	λ = 1.36 Å 2 θ Daresbury
(104)	3.0357	100.0	29.422°	25.888°
(116)	1.8754	22.73	48.542°	42.519°
(113)	2.2848	20.57	39.437°	34.629°
(202)	2.0946	15.73	43.189°	37.888°
(018)	1.9124	14.35	47.544°	41.657°
(110)	2.4950	14.26	35.995°	31.631°
(012)	3.8550	5.34	23.070°	20.320°
(024)	1.9275	4.50	47.149°	41.316°
(006)	2.8435	2.28	31.460°	27.672°

Table 3.3. Peak positions expected for calcite on the Durham X-ray equipment and at Daresbury.

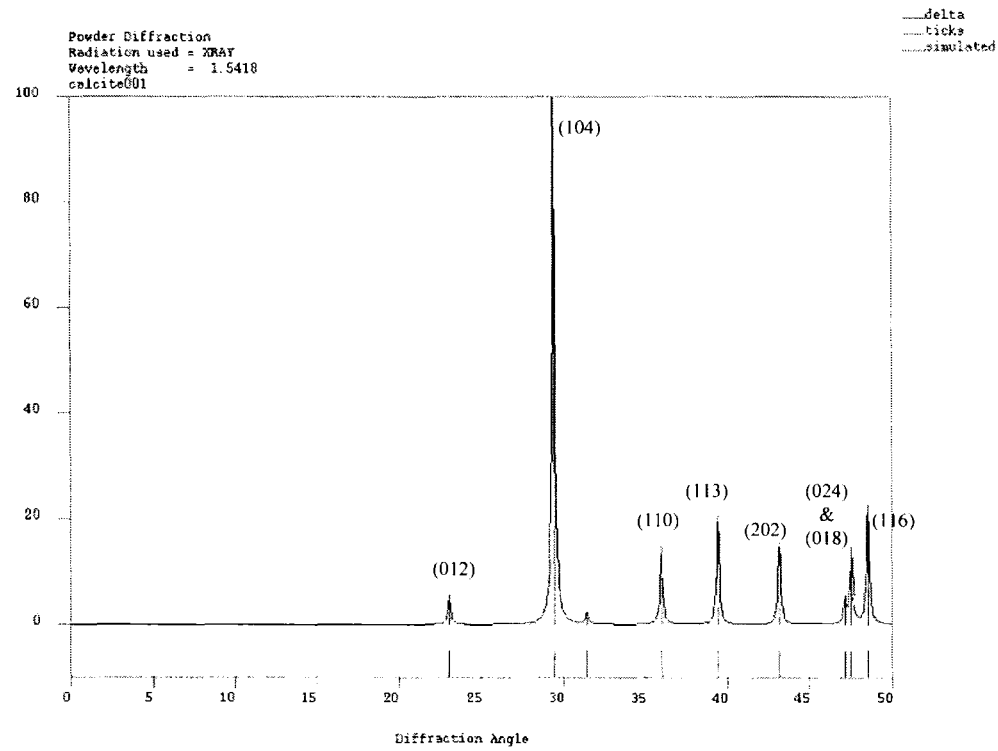

Figure 3.15. Simulated powder X-ray diffraction pattern for calcite from Cerius2 software assuming, λ = 1.5418 Å

In the FTIR, all forms of calcium carbonate show bands in the regions 3400 cm^{-1} (broad), and 870 cm^{-1}. Very broad bands at 3430 cm^{-1} and 1080 cm^{-1} are due to the amorphous form[62]. Some bands can be used to determine the presence of specific polymorphs, as specified in table 3.4. FTIR bands due to the octadecanoic acid monolayer that are relevant to this chapter are detailed in table 3.5.

Bands / cm^{-1}	Specific to	Ref
712, 714	Calcite and Aragonite	32,63
698	Aragonite	63
745	Vaterite and hexahydrate	63
1080	Amorphous form	32

Table 3.4. Bands used to identify specific polymorphs of calcium carbonate by FTIR.

Bands / cm^{-1}	Assignments[33]
2955	Asymmetric methyl stretch
2917	Asymmetric methylene stretch
2850	Symmetric methylene stretch
1704	Carbonyl stretch
1469	Methylene scissoring

Table 3.5 FTIR band assignments for octadecanoic acid.

3.5 Optical Microscopy Studies

Microscopy studies were undertaken of calcium carbonate crystallisation under octadecanoic acid monolayers to confirm the findings of Mann[35,50] and others[33,37]. Good reproducibility of the experiments was ensured, before commencing the GIXD studies at Daresbury.

Use of a $CaCl_2$ with bicarbonate subphase (see section 3.3.2) was attempted under octadecanoic acid monolayers at a variety of surface pressures, but was abandoned entirely. This method never gave surface crystals, even after 24 hours.

Kitano subphases (see section 3.3.2) always gave surface crystals because carbon dioxide is only evolved at the sample surface. As discussed (section 3.3.2), the degree of supersaturation is only known to an approximate value by Kitano preparation, but the method did offer good reproducibility of results. In the absence of the octadecanoic acid monolayer, Kitano solutions give predominantly unoriented rhombahedrons after approximately 15 hours. These are shown in figures 3.16 and 3.17.

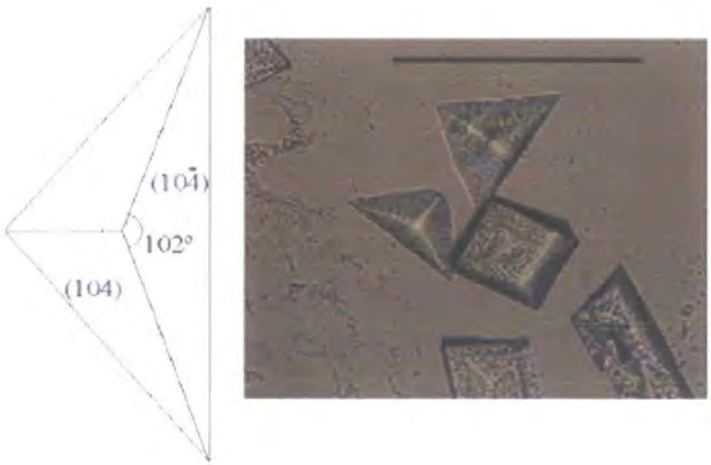

Figure 3.16. Image of unoriented calcite rhombahedra under an octadecanoic acid monolayer. Scale bar = 50 μm.

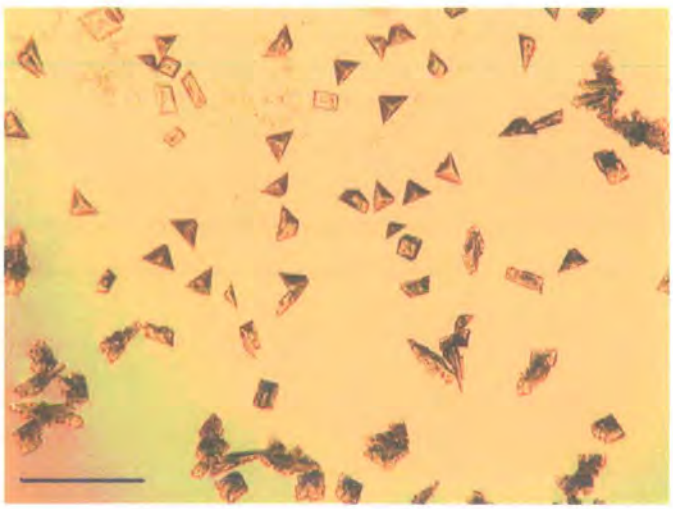

Figure 3.17. Image of unoriented calcite rhombahedrons in absence of an octadecanoic acid monolayer. Scale bar = 250 μm.

For Kitano solutions under octadecanoic acid monolayers compressed to $\pi = 15$ mN/m, mostly (approximately 80%) oriented plates of calcite were found, with crystallisation nucleated at the (010) and minor (104) faces (see figure 3.18) in keeping with earlier studies[33,61]. For a less highly compressed film at $\pi = 10$ mN/m, calcite is still expected, but the orientation is less pronounced and the morphology altered (figure 3.19). For a less concentrated subphase (4.5 mmol/dm^3) much more of the metastable form vaterite is expected (figure 3.20).

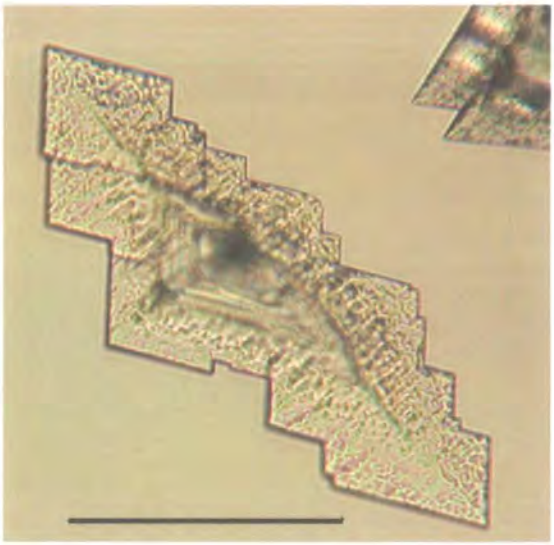

Figure 3.18. Image of oriented calcite under octadecanoic acid monolayer viewed at high magnification. Scale bar = 50 μm.

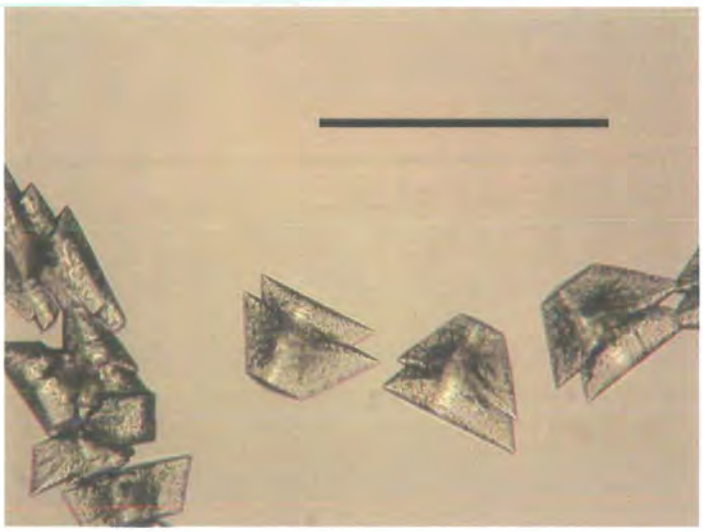

Figure 3.19. Image of calcite formed under a less well-compressed monolayer of octadecanoic acid, showing limited orientation. Scale bar = 50 μm.

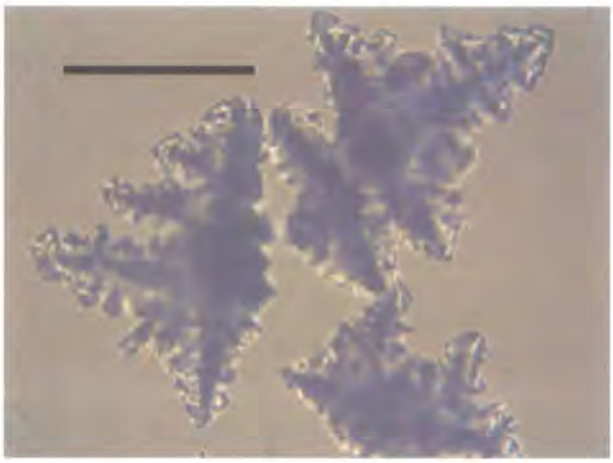

Figure 3.20. Vaterite induced by octadecanoic acid from a less supersaturated phase (4.5 mmol/dm^3) subphase. Scale bar = 50 μm.

Conclusion of Optical Microscopy Work

The $CaCl_2$ method for supersaturated calcium carbonate preparation is unsuitable for further work. Despite numerous attempts, crystals were frequently found at the bottom of the trough, and never at the air-water interface induced by the octadecanoic acid monolayer. This suggests that octadecanoic acid cannot induce nucleation at supersaturations below that at which indiscriminate foreign material such as dust can operate. Solutions prepared by the Kitano method induced crystallisation on all occasions, and the preparation is much simpler. These data confirm the findings published in the literature and are a good grounding for the synchrotron GIXD work described in the next section.

3.6 Initial Synchrotron Studies and ER-FTIR Analysis

Experiments were carried out on Station 16.2 at Daresbury Laboratories, Cheshire. The station manager was Dr. Graham Clark. Solutions were prepared by the Kitano method as described earlier. The emphasis at Daresbury was to study the octadecanoic acid monolayer, which would be invisible to standard X-ray equipment due to low flux. Scattering of X-rays in the equatorial plane only was studied at Daresbury in order to access diffraction signals from the monolayer.

Station 16.2 at Daresbury is equipped with a one-dimensional (point) detector, which could be moved in the horizontal plane over time to give a range of 2θ values. Consequently, this type of detector limited the range of 2θ where data were acquired to the equatorial plane. Data were acquired in the region $Q_{xy} \sim 1.5$ Å^{-1} where a peak for octadecanoic acid was reported by Dupres et al.[39] and for related fatty acids by others[37,57]. Focussing studies in this region maximised the possibility a change in signal for the monolayer would be observed as crystallisation occurred.

3.6.1 Octadecanoic Acid on Pure Water and $CaCl_2$ Subphases

Recall from page 115 that a peak is expected at $Q_{xy} = 1.47$ Å^{-1} for fatty acids on water and Ca^{2+} subphases when compressed to ~ 7 –17 mN/m. This corresponds to a tilt of ~20° from the surface normal and a rectangular lattice structure of a = 5.04 Å and b = 8.11 Å. Consider the data for octadecanoic acid spread on pure water and compressed to 15 mN/m and 20 mN/m in figures 3.21a and b, respectively. These show a peak position centred at $Q_{xy} \sim 1.49$ Å^{-1}, which is consistent with the findings of other authors as discussed in section 3.1.5. The variation in this peak position between the surface pressures of $\pi \sim 7 - 20$ mN/m is therefore limited to the range $Q_{xy} \sim 1.47 - 1.51$ Å^{-1} according to previous studies in the literature. The far weaker peak at $Q_{xy} \sim 1.67$ Å^{-1}, which was observed by some authors[43] and enabled characterisation of the

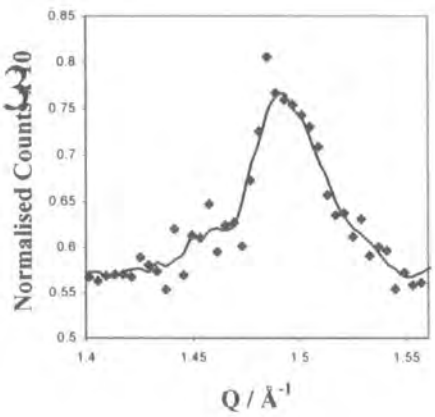

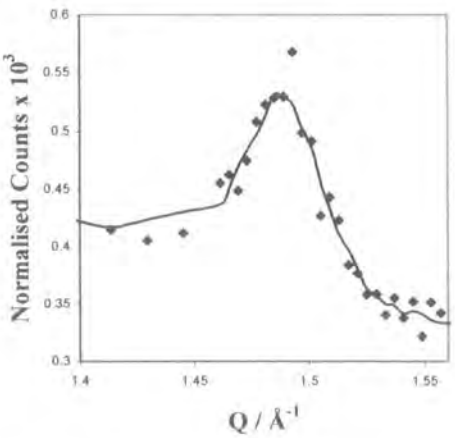

Figure 3.21a (left) and 3.21b (right). GIXD data for octadecanoic acid on water where initial π = 15 mN/m and 20 mN/m, respectively. The solid line is a rolling average of five points.

rectangular structure of the film, was not observable above the noise for these studies at Daresbury station 16.2.

As discussed earlier, Ahn et al.[33] did not observe changes in ER-FTIR spectra over time for octadecanoic acid on aqueous $CaCl_2$ subphase, but did during the crystallisation of calcite from supersaturated solutions of calcium bicarbonate. Rajam et al.[34] reported the crystallisation of calcite from calcium bicarbonate subphases where $[Ca^{2+}] = 9$ mmol/dm^3 and the crystallisation of vaterite when $[Ca^{2+}] = 4.5$ mmol/dm^3.

Figures 3.22a and b show data acquired at $[CaCl_2] = 9$ mmol/dm^3 immediately after film deposition where π was 20 mN/m, and at 10 hours when π had relaxed to 11 mN/m. There is a very subtle change in Q_{xy} from 1.49 to 1.48 Å^{-1} on decreasing surface pressure, but the effect is so small that it is within experimental error.

Figures 3.23 a and b are for octadecanoic acid on a $CaCl_2$ subphase where $[Ca^{2+}] = 4.5$ mmol/dm^3. The surface pressure relaxes from 15 mN/m to 13.1 mN/m over five hours, with no significant shift in the peak position from a value of $Q_{xy} \sim 1.49$ Å^{-1}.

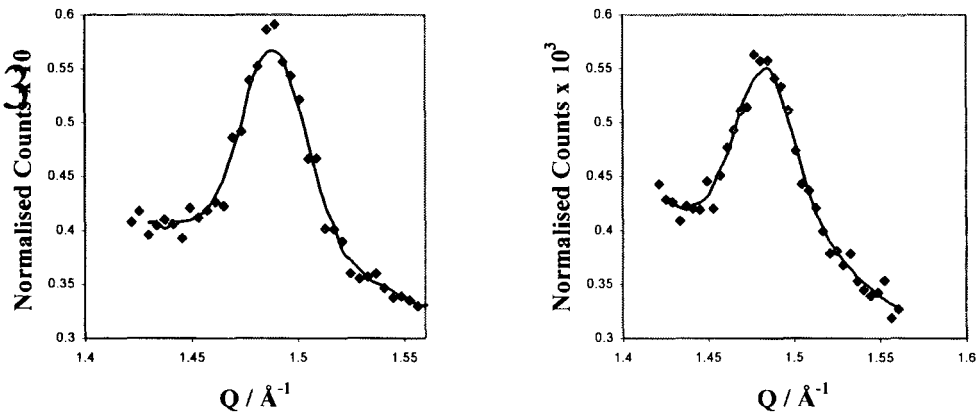

Figure 3.22a (left) and 3.22b (right). GIXD data for octadecanoic acid on 9 mmol $CaCl_2$ at initial where π = 20 mN/m and after 10 hours where π has relaxed to 11 mN/m, respectively. The solid line is a rolling average of five points.

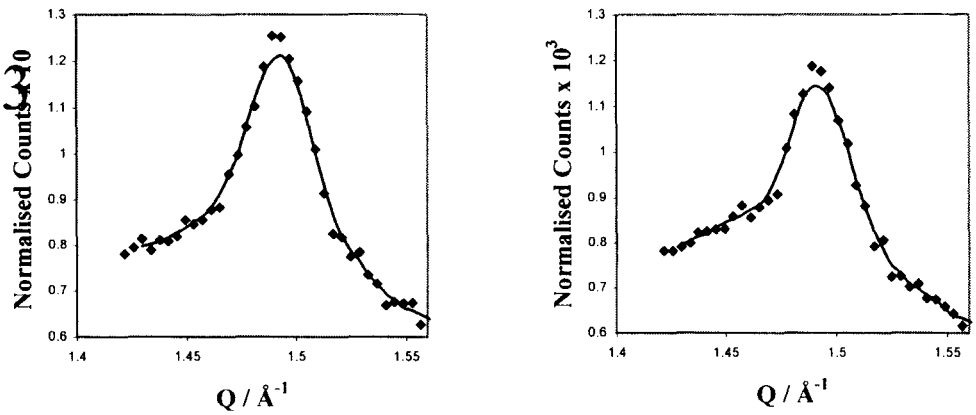

Figure 3.23a & 3.23b. GIXD data for octadecanoic acid spread on 4.5 mmol aq $CaCl_2$ at 0 and 5 hours after monolayer addition where π = 15 mN/m and relaxes to 13.1 mN/m. The solid line is a rolling average of 5 points.

These data for octadecanoic acid on aqueous $CaCl_2$ show no significant difference in peak position or shape for different concentrations of Ca^{2+}, and the peak is in the same position as for octadecanoic acid on pure water. The data on an aqueous Ca^{2+} subphase do show a cleaner/sharper peak, but not significantly so. There is no evidence for a change in peak intensity or position over time. This is consistent with the findings of Shih et al.[40]

3.6.2 Octadecanoic Acid on Kitano Solutions

Data for the crystallising system, octadecanoic acid on Kitano solution ($[Ca^{2+}] \sim 9$ mmol/dm^3), were acquired over a Q_{xy} range of 1.40 to 1.56 Å^{-1}, which captures the peaks reported in the previous section and the peak range reported in the literature for fatty acid monolayers on water. Octadecanoic acid was spread and compressed to a surface pressure of 15 mN/m, initially. This had relaxed to 10 mN/m by the acquisition of the last data set at 8 hours, but from the previous section, we can say this would result in little or no shift in peak position.

The data for this system are presented in figure 3.25, and show significant levels of noise, caused by roughness introduced by growing crystals and the sample falling out of the beam over time due to water evaporation. They do undoubtedly show, however, changes in peak shape/position as crystallisation progresses. At 1 hour (figure 3.25a), a

broad peak from 1.46-1.50 $Å^{-1}$ is observed. The breadth of this feature decreases at the 2nd and 3rd hour, roughly centred at 1.50 $Å^{-1}$ but maintaining a shoulder at 1.46 $Å^{-1}$. At 5 – 8 hours, the peak Q_{xy} = 1.46 $Å^{-1}$ is more apparent.

Figure 3.24 shows a background image plate taken when the sample platform was dropped out of the beam, leaving only the trough enclosure in the X-ray path. This shows some subtle amorphous features, which are due to background scatter and the mylar film over the windows of the Perspex trough enclosure.

Figure 3.24. Image plate taken with sample lowered out of the beam path, showing subtle features due to background and mylar film.

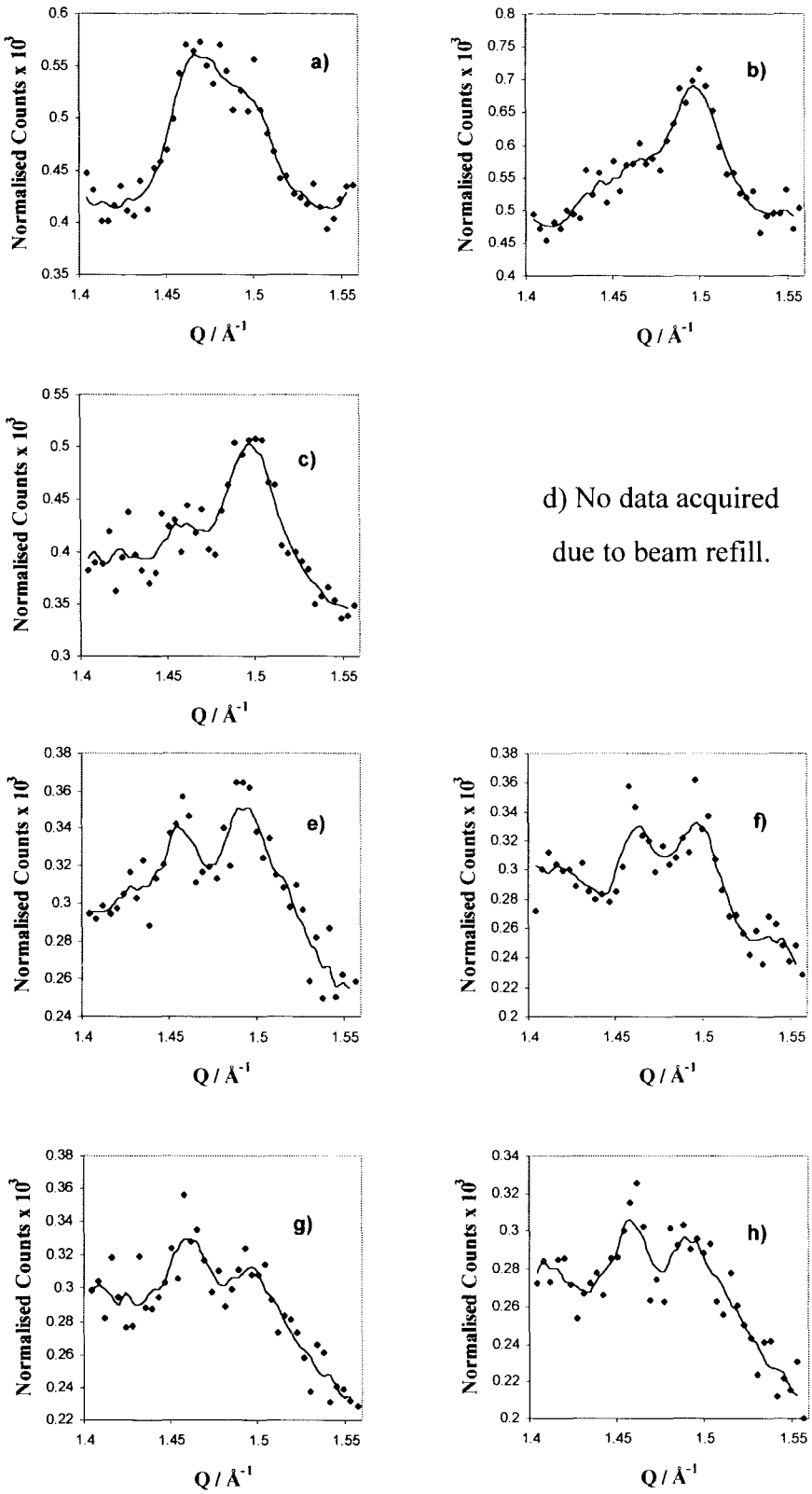

Figures 3.25 a – h GIXD data for octadecanoic acid on pure Kitano solution at hourly timepoints (1 – 8 hours). The solid line is a rolling average of 5 points.

Image plates were placed directly in the path of the beam at hourly points during this series of experiments, and are presented in figure 3.26. The spots on the image plates, which were caused by X-ray diffraction from the growing calcite crystals, were manually numbered and measured as described on pages 127-129. From these measurements, the 2θ values were calculated from equation 3.5 and are represented in the graphs in figures 3.27 a-d. These graphs assume that the crystals were located in the middle of the trough, which is a major drawback with these data.

Table 3.6 shows the maximum error in the calculated 2θ values making the assumption that the crystals are located in the middle of the trough. For instance, a spot calculated at 2θ = 15° could actually be from a crystal at the front of the trough with 2θ = 13.03° or at the back with 2θ = 17.62°.

2θ Assuming the Crystal is at the Middle of the Trough	2θ Assuming the Crystal is at the Front of the Trough	2θ Assuming the Crystal is at the Back of the Trough
15°	13.03°	17.62°
20°	17.48°	23.37°
25°	21.99°	28.99°
30°	26.59°	34.49°
35°	31.20°	39.73°
40°	35.90°	44.82°

Table 3.6. The maximum possible error in calculated 2θ values for image plate data. Each spot on the image plate could be diffracting the X-rays at the range of 2θ values illustrated in the table, depending on where in the trough sample area the crystal is located.

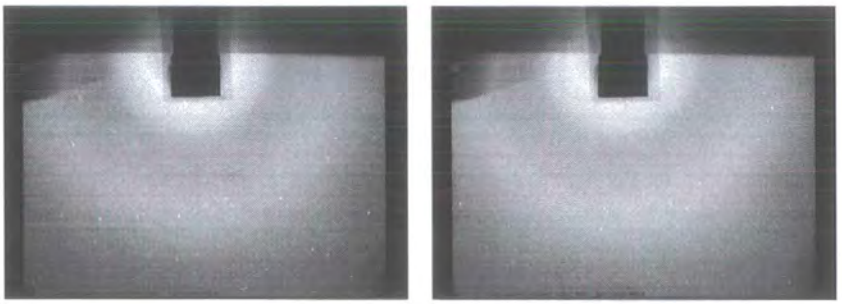

At 1 hour *At 2 hours*

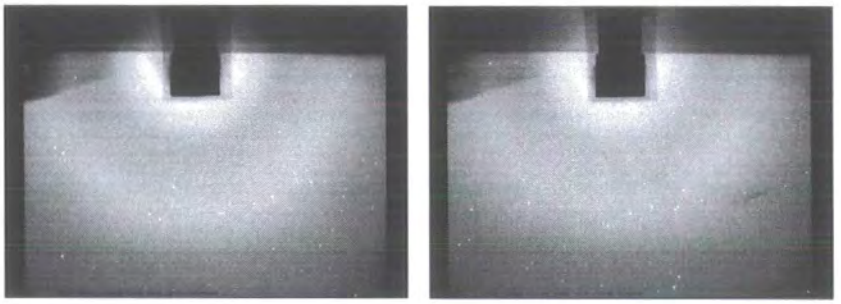

At 3 hours *At 4 hours*

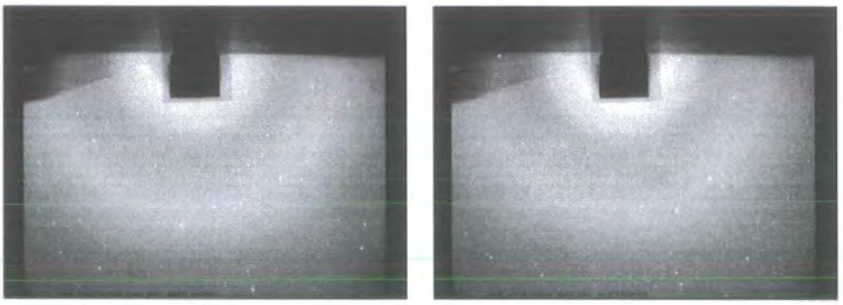

At 5 hours *At 6 hours*

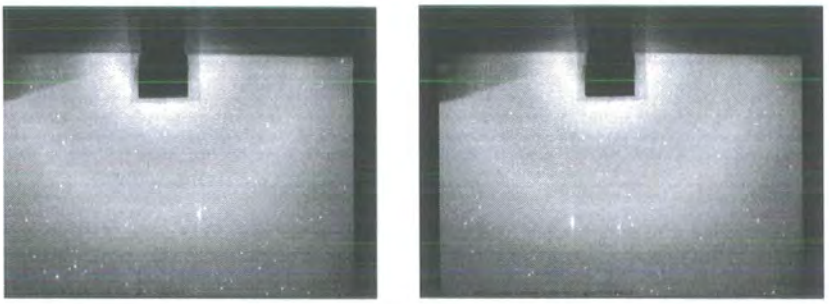

At 7 hours *At 8 hours*

Figure 3.26. Image plates placed in the path of the beam at hourly points (1 – 8 hours).

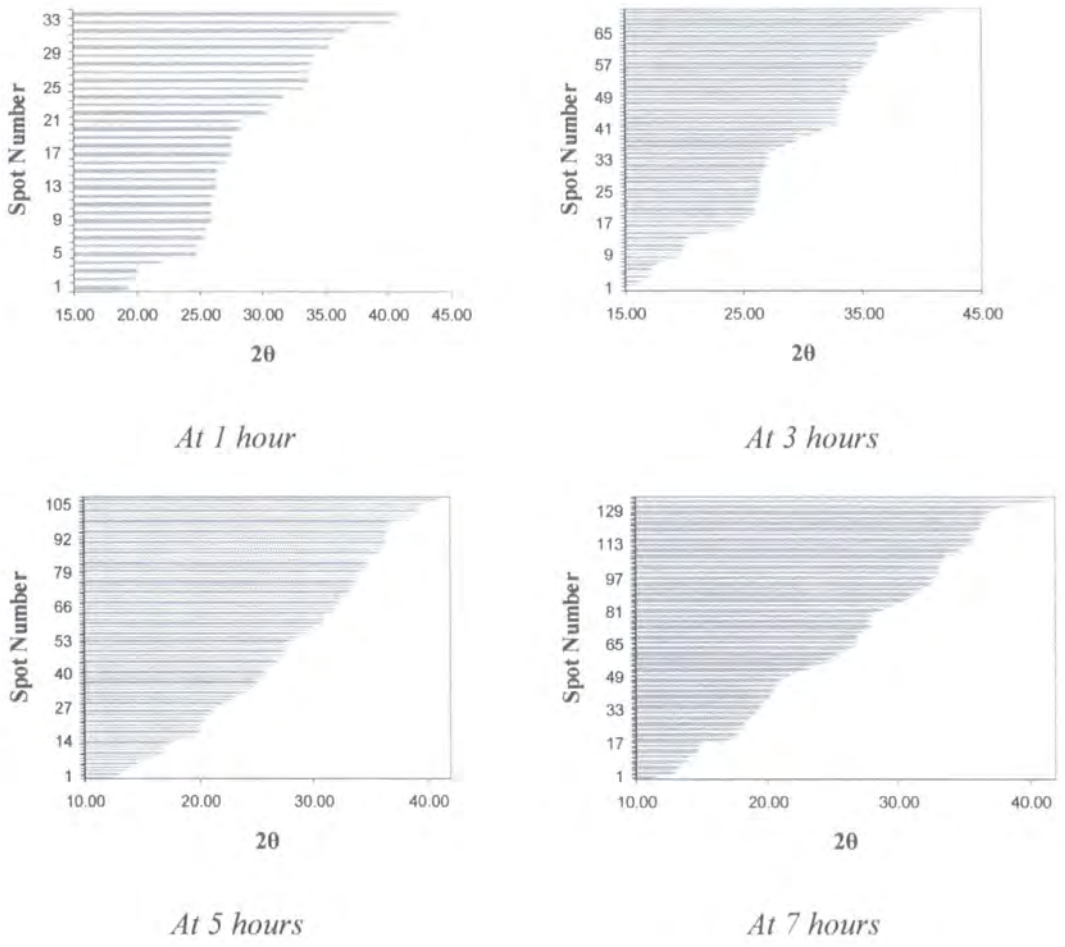

Figures 3.27 a - d. Graphs representing 2θ values calculated for the image plates scanned at 1, 3, 5 and 7 hours, respectively.

The image plate data are difficult to pursue any further without knowing the exact location of the crystal causing each reflection. There are groups of 2θ values, however, at ≈ 18 - 20°, 26 - 28°, 33 - 34° and 37° (figures 3.27a – d). These apparent patterns of diffraction across the image plates are not sufficient to confirm whether calcite is the polymorph of calcium carbonate crystallising, nor which plane is causing each diffraction spot. If a single polymorph and unique orientation did occur, it is certainly not apparent from these image plate data.

3.6.3 ER-FTIR Data for Octadecanoic Acid on Kitano Solutions

ER-FTIR data were acquired as described in section 3.3.5. The subphase was cleaned and the monolayer added by deposition of chloroform solution and allowing evaporation of the solvent. The surface pressure reading was measured at the beginning by a tensiometer and the barrier was moved to compress the monolayer to a surface pressure reading of 15 mN/m. The tensiometer was then removed to allow FTIR data acquisition.

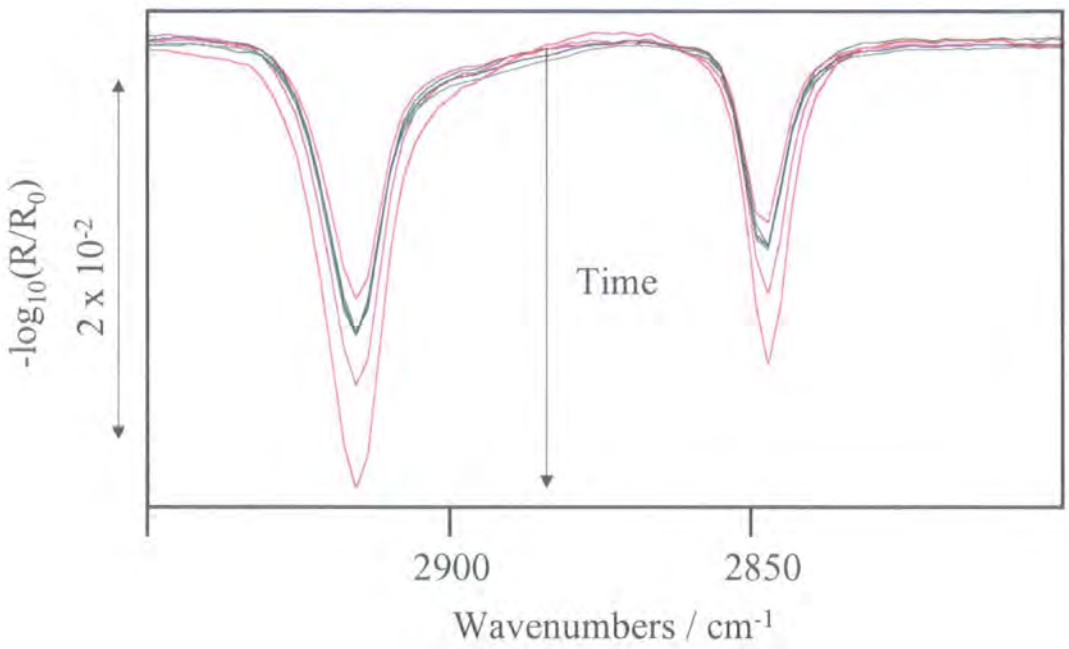

Figure 3.28. ER-FTIR spectra 2950 – 2800 cm^{-1} at 0, 2, 4, 6, 8 & 10 hours, illustrating the increase in C-H band intensity over time as the crystallisation of calcium carbonate progresses.

Over time, the background file becomes less appropriate and subtraction of features due to carbon dioxide and moisture are less successful. This affects the regions 3800 - 3300 cm^{-1} and 1700-1300 cm^{-1} (H_2O) and 2380 – 2300 cm^{-1} (CO_2). As crystals form, there is also more scope for poor subtraction of background.

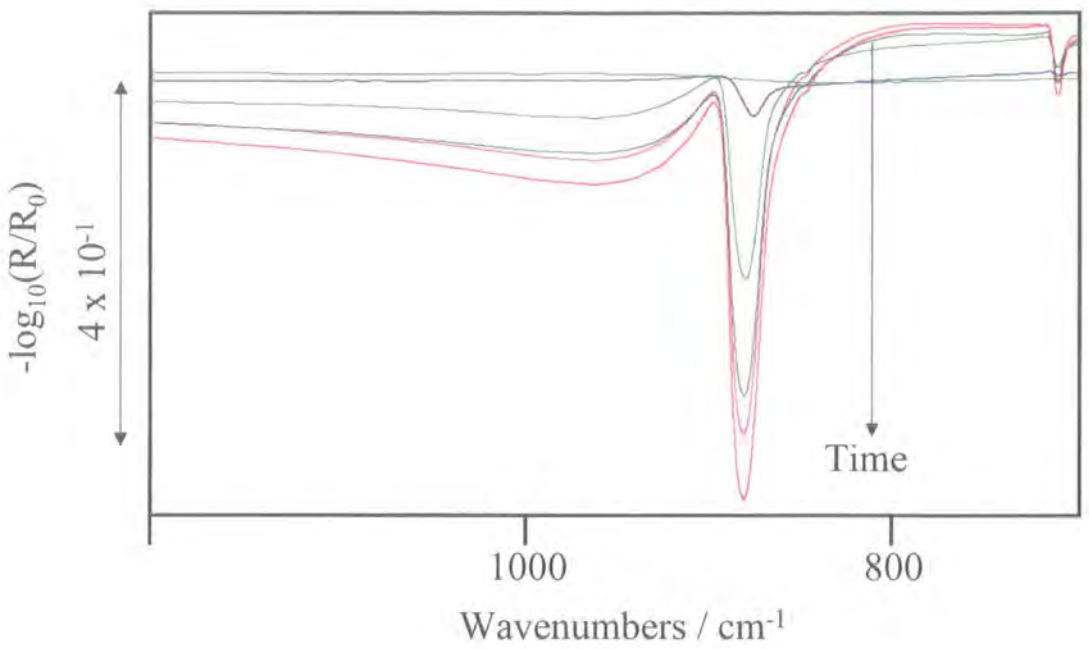

Figure 3.29. ER-FTIR spectra 950 – 650 cm^{-1} at 0, 2, 4, 6, 8 & 10 hours, illustrating the increase in band at 872 cm^{-1}, consistent with calcium carbonate, as the crystallisation of calcium carbonate progresses.

Despite these detrimental background effects, there are significant features in the spectra. There is the emergence and intensity increase over time of a sharp band at 872 cm^{-1}, and the formation of a small band at 712 cm^{-1}. Both bands are attributed to calcium carbonate crystallisation. The sharpness of the band at 872 cm^{-1} and the absence of a feature at 1080 cm^{-1} indicate crystalline character for these crystals and the presence of the 712 cm^{-1} band indicates calcite crystallisation. There is no band discernible at 745 cm^{-1}, which is attributed to vaterite. There is also an increase in the intensity of the C-H stretch bands at approximately 2915 cm^{-1} and 2845 cm^{-1}. This change in C-H band intensity was reported by Ahn et al.[33] as reorientation of the octadecanoic acid hydrocarbon tailgroups relative to the surface normal[33], thus giving a lattice better able to accommodate the (010) structure of calcite, where nucleation occurs. The 872cm^{-1} and 712 cm^{-1} bands are due to out-of-plane and in-plane calcite carbonate deformations, respectively. Therefore, the ratio of these band intensities is indicative of the calcite carbonate orientation, since bands with transition dipole moments parallel to the surface contribute preferentially to the ER-FTIR spectrum, as

detailed in chapter 2. The 872 cm^{-1} band is far more intense than the 712 cm^{-1} band in these spectra, indicating that the carbonate groups orientate preferentially perpendicular to the surface. This orientation is consistent with nucleation of (010) and other planes deviating by not more than 20° from (hk0) orientations as found previously by Ahn et al.[33] for calcite crystallisation beneath octadecanoic acid monolayers. However, in Ahn's data, the C-H band intensity decreased with time, whereas our data show the intensity increasing. This difference may arise because their film is at higher surface pressure and hence more close packed than the system studied here. In addition, Ahn et al. did not consider the possibility that the film was floating as islands on the surface of the subphase or could be relaxing to lower surface pressures due to film dissolution. Band intensity changes in ER-FTIR can be caused by an inhomogeneous spread film or film dissolution. These FTIR data therefore support the GIXD data by showing a possible rearrangement of the octadecanoic acid monolayer as crystallisation progresses. The nature of these changes will be discussed further in section 3.9.

3.6.4 Summary of Initial Studies

These initial studies of octadecanoic acid monolayers deposited on Kitano subphases show changes in features attributed to the octadecanoic acid monolayer by ER-FTIR and GIXD over time. The GIXD data are particularly noisy and increasingly so over time as calcium carbonate crystallisation progresses, which increases the roughness of the sample surface.

On the basis of the initial GIXD and ER-FTIR data presented in this section, additional Daresbury beam-time was awarded to explore in more detail the changes in octadecanoic acid structure as crystallisation progresses. It was also proposed that the effects of polyacrylic acid inhibitor be explored as this will cause formation of an amorphous calcium carbonate film precursor prior to calcite formation.

There have been numerous studies of amorphous[64-66] and crystalline calcium carbonate crystallisation by FTIR. In the absence of PAA, Ahn et al.[33] detailed experiments where ER- FTIR was used to study the composition of octadecanoic acid monolayers during

crystallisation of calcium carbonate[33]. The possibility that the film was floating as islands on the surface of the subphase, or relaxing to lower surface pressures, was not considered, however.

The addition of PAA, known to inhibit calcite growth, was reported by Groves[32]. This results in a thin film of calcium carbonate and more complete surface crystal coverage than observed without use of inhibitor. Greater confidence can be placed in these data, therefore, that changes in peak intensity are not due to islands of film and crystals floating across the path of the beam during data acquisition.

The next section includes data acquired with 10 ppm PAA and in the absence of PAA inhibitor, under octadecanoic acid monolayers at low (~10 mN/m), medium (~15mN/m) and high surface pressures (>20mN/m).

3.7 Further GIXD Studies

3.7.1 Repeat GIXD Studies of Octadecanoic Acid on Kitano Solutions

Repeat data were acquired as described for section 3.6.2, except that the sample height was determined incrementally by placing the detector directly in the path of the reflected beam, see page 124. This better height optimisation method, combined with better wicking and reliability of the beam has given data of significantly better quality, see figure 3.30a – h, with the film peaks more apparent relative to the background scatter. The film was initially compressed to 15 mN/m.

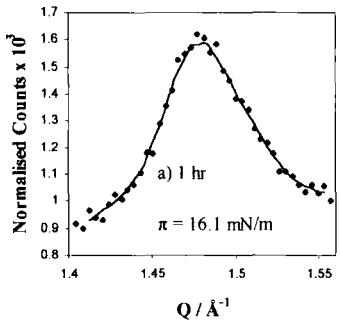

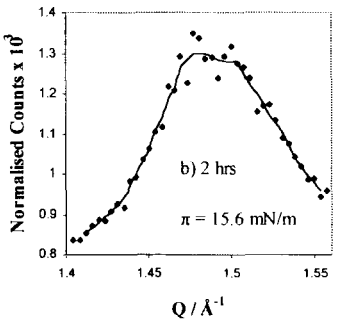

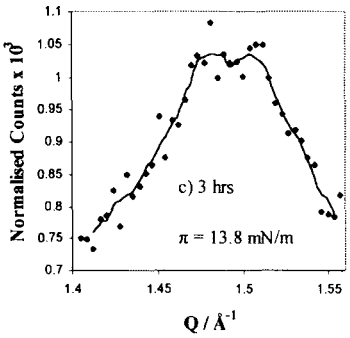

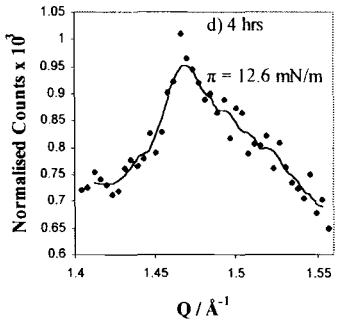

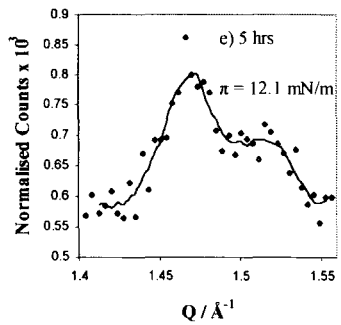

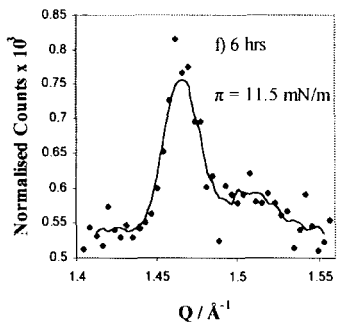

g) 7 hrs (Beam refill).

π = 10.8 mN/m

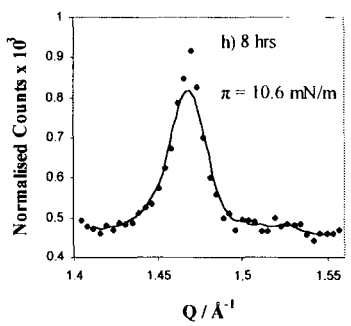

Figure 3.30. GIXD Data for octadecanoic acid on pure Kitano solution at hourly timepoints. The solid line is a rolling average of 5 points.

At one hour there is a broad peak, centred at Q_{xy} = 1.48 Å^{-1}, but extending outwards to 1.46 – 1.50 Å^{-1}. At the 2nd hour, this feature has broadened further, and shows signs of splitting into 2 separate features at Q_{xy} = 1.47 and 1.51 Å^{-1}; this splitting is clearly visible at the 3rd hour. By the 4th hour, the peak at 1.51 Å^{-1}, has reduced in intensity and is now little more than a shoulder to the neighbouring peak. This feature at 1.51 Å^{-1}, continues to reduce in intensity, until it is completely absent at the 8th hour.

Time	Initial Analysis		Repeat Analysis	
	Intensity at Q_{xy} = 1.46 Å^{-1}	Intensity at Q_{xy} = 1.50 Å^{-1}	Intensity at Q_{xy} = 1.47 Å^{-1}	Intensity at Q_{xy} = 1.51 Å^{-1}
1 hour	← Broad →		← Broad →	
2 hours	Shoulder	Strong	← Broad →	
3 hours	Medium	Strong	Strong	Strong
4 hours	Beam refill		Strong	Medium
5 hours	Strong	Strong	Strong	Medium
6 hours	Strong	Strong	Strong	Weak
7 hours	Strong	Medium	Beam refill	
8 hours	Strong	Medium	Strong	Absent

Table 3.7. Comparison of data from the initial and 2nd analysis of calcite crystallisation under an octadecanoic acid monolayer.

Table 3.7 compares the data from the initial study and this repeat study of calcite crystallisation under an octadecanoic acid monolayer compressed to 15 mN/m initially. There are similarities between the data sets, with both showing features at approximately 1.46/1.47 Å^{-1} and 1.50/1.51 Å^{-1}. Both show a broad feature initially, followed by a reduction in the intensity of the signal at ~ 1.50 Å^{-1} over time. The first analysis shows an early reduction in signal intensity at 1.46 Å^{-1} (at 2/3 hours), but this is probably due to slower crystallisation for this system. The repeat analysis showed the complete disappearance of the peak at ~ 1.51 Å^{-1}, whereas the 1st analysis showed only a moderate decrease in the signal intensity in this region, consistent with the different rates of progress over 8 hours for the initial and 2nd experiment.

The narrow peak observed at the 8th hour for the repeat analysis is consistent with octadecanoic acid on aqueous Ca^{2+} subphases at moderate (π = 10 mN/m) surface pressure and neutral pH[40]. The initial broadness of the peak in these crystallising systems is not observed for octadecanoic acid on $CaCl_2$ subphase at equivalent Ca^{2+} concentration (section 3.6.1), hence we can conclude that this peak broadness is specific to this crystallising system. The two data sets indicate that the peak emerging at ~ 1.5 $Å^{-1}$ is due to the film rearranging during the calcium carbonate crystallisation, with this peak then decreasing in intensity with time as the film relaxes back to its initial state.

3.7.2 GIXD Data for High π on Pure Kitano Subphase

The highest surface pressure reading possible was ≈ 20 mN/m. Addition of any further octadecanoic acid solution resulted in visible multilayer formation prior to barrier compression, due to the latter film solution drops not spreading fully due to the amount of film material already present on the surface. The GIXD data in figure 3.31 for octadecanoic acid on a pure Kitano solution compressed to 20 mN/m show no significant change in peak position (Q_{xy} = 1.51 $Å^{-1}$) for the octadecanoic acid peak over time. The intensity of the peak decreases as time and crystallisation progress, due to increased surface roughness. These data are not inconsistent with the data presented at moderate surface pressure (π = 15 mN/m), as firstly we would not expect to see any peak shift since it is already at the ~1.5 $Å^{-1}$ position, which presumably corresponds to the optimal film structure for the crystallisation, and secondly, the increased rigidity of the film would probably prohibit any rearrangement if required. The density of crystals to the naked eye at 8 hours was equivalent to the π = 15 mN/m study.

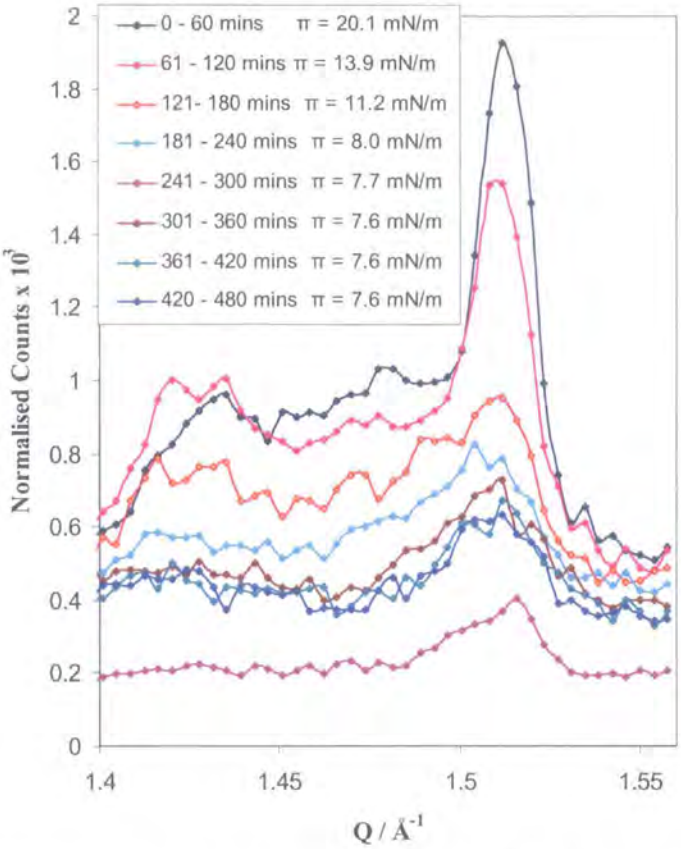

Figure 3.31. GIXD data acquired for high initial surface pressure (20 mN/m) octadecanoic acid on Kitano solution.

3.7.3 GIXD Data for Low π on Pure Kitano Subphase

Data acquired from a system at low (10 mN/m) surface pressure are presented in figure 3.32. Visible crystallisation occurred very rapidly for this sample, but the low density of the octadecanoic acid on the subphase led to very noisy data and a weaker film signal, hardly discernible after 4 hours.

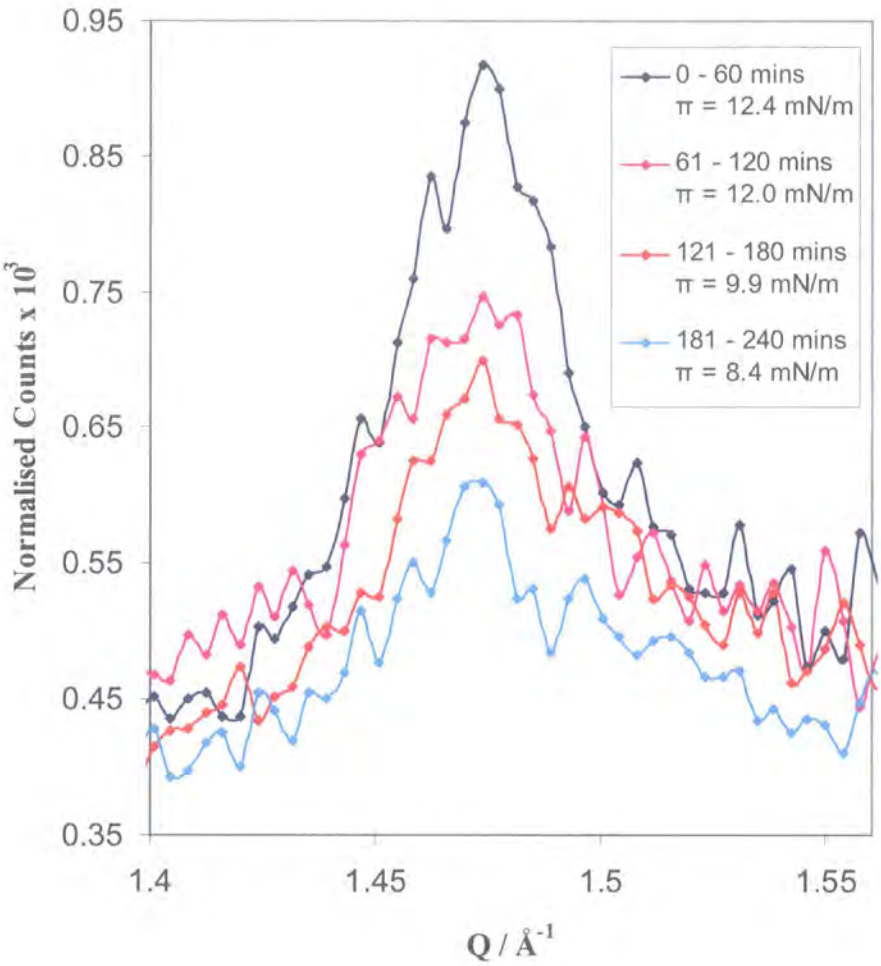

Figure 3.32. GIXD data for low surface pressure octadecanoic acid (initial π = 10 mN/m) on pure Kitano subphase.

3.7.4 GIXD Data for Moderate (15 mN/m) π on Kitano Subphase with Added PAA Inhibitor

Figures 3.33 a – d show GIXD data for octadecanoic acid compressed to 15 mN/m initially on Kitano subphase with 10 ppm PAA inhibitor at 5, 7, 9 and 11 hours. Prior to 5 hours, no change in signal was observed. There is a subtle narrowing of the broad peak (Q_{xy} = 1.43 – 1.53 $Å^{-1}$) between 5 and 11 hours, but this is almost certainly not significant. Surface pressure readings increased over time; these were 18.1, 19.0, 19.6 and 20.3 mN/m at 5, 7, 9 and 11 hours, respectively.

The GIXD data show no evidence for a rearrangement of the monolayer as the calcium carbonate film forms. To the naked eye there is visible formation of a wrinkled surface film due to calcium carbonate growth between the barriers. Outside the barriers in the absence of octadecanoic acid, there was no evidence for thin film or single crystal formation.

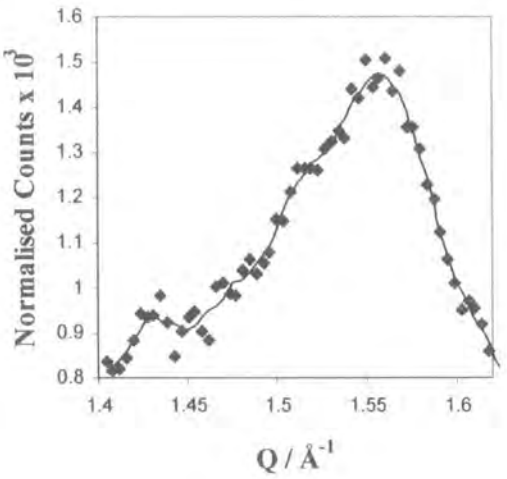

Figure 3.33 a

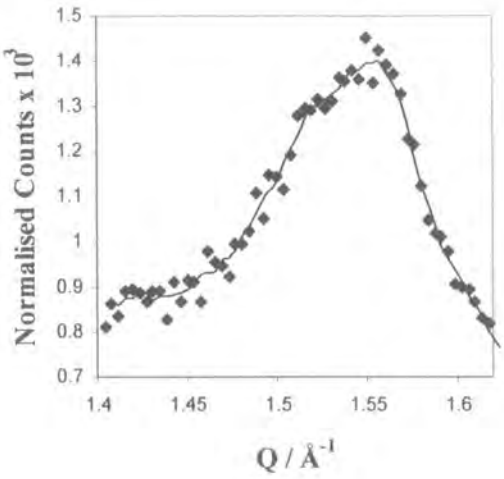

Figure 3.33 b

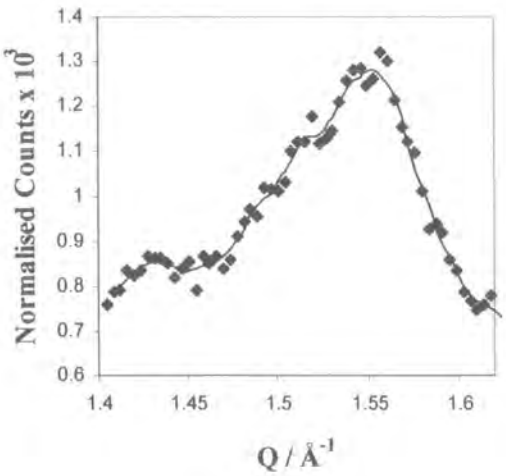

Figure 3.33 c

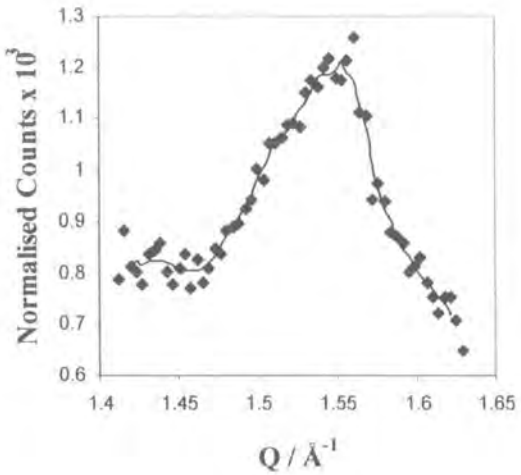

Figure 3.33 d

Figure 3.33a – d. GIXD data for moderate (15 mN/m) octadecanoic acid on Kitano subphase with 10 ppm PAA at 5, 7, 9 and 11 hours respectively.

3.7.5 GIXD Data for High π on Kitano Subphase with PAA Inhibitor

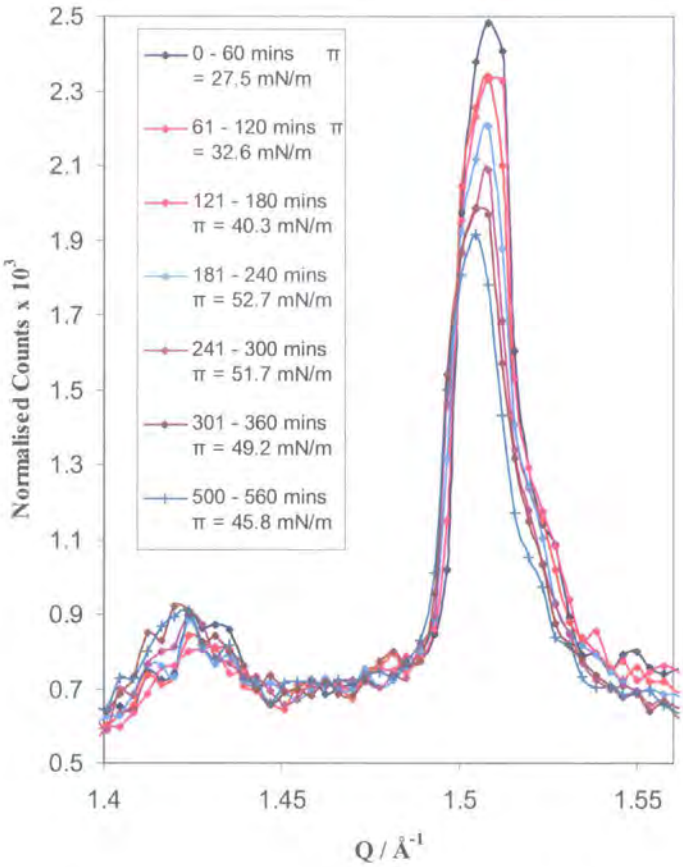

Figure 3.34. Data for octadecanoic acid compressed to high surface pressure (initial π = 20 mN/m) on Kitano subphase with PAA inhibitor.

The GIXD data for the octadecanoic acid system compressed to 20 mN/m on the Kitano subphase with PAA inhibitor initially show no evidence for a rearrangement of the monolayer upon calcium carbonate film formation. Over time the X-ray signal intensity decreases (see figure 3.34), but this can be attributed to increased surface roughness. The position of the peak is similar to that for a pure Kitano subphase at π ~ 20 mN/m, hence the PAA has not significantly affected the packing of the fatty acid headgroups due to a minor change in pH, as reported elsewhere[40]. The peak position is unaltered from its original value of 1.51 $Å^{-1}$ with time, but the surface pressure increases to approximately 50 mN/m as a thin film of calcium carbonate forms under the monolayer. Outside the barriers in the absence of octadecanoic acid monolayer, there was no evidence for thin film or single crystal formation. On compressing the barriers at the

end of the experiment, it was found that the surface was very rigid, forming ridges as the barriers were pushed together.

3.7.6 Data for Low π on Kitano Subphase with PAA Inhibitor

Data for an octadecanoic acid monolayer compressed to only 10 mN/m are presented in figure 3.35. These data show a very weak signal initially due to low surface pressure. The signal position was ~1.51 $Å^{-1}$; this signal decreases very significantly as a thin film forms, causing roughness at the surface of the sample. At 1, 3 and 6 hours, the surface pressure readings were 11.8, 13.0 and 14.3 mN/m respectively, indicating that formation of calcium carbonate thin film did occur.

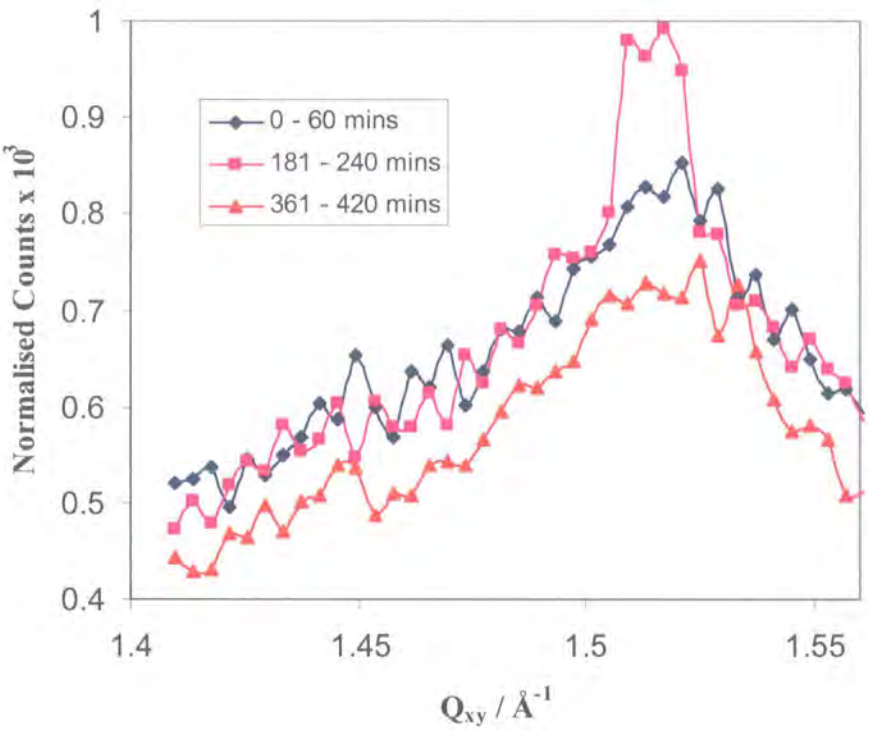

Figure 3.35. GIXD data for octadecoanoic acid compressed to low surface pressure (initial π = 10 mN/m) on Kitano subphase with PAA inhibitor.

3.7.7 Discussion and Conclusions of GIXD Studies

For the pure Kitano solutions under octadecanoic acid at initial surface pressure = 15 mN/m, there is a broadening of the peak initially at Q_{xy} = 1.47 $Å^{-1}$ to reveal at later stages a second peak at Q_{xy} = 1.51 $Å^{-1}$. This second peak decreases in intensity until only the original peak remains at Q_{xy} = 1.47 $Å^{-1}$, which is consistent with octadecanoic acid on Ca^{2+} subphases. At higher surface pressure, no change in signal is observed, but the higher rigidity of the film would prohibit this and the film already has an optimal structure for the crystallisation. At lower surface pressures the signal is too weak to make any reliable assessments, but for this system crystallisation did proceed very rapidly as judged by the naked eye.

In the presence of 10 ppm PAA, the GIXD film signal at Q_{xy} = 1.51 $Å^{-1}$ shows no significant change over time, but there is a significant increase in surface pressure with time, indicating that an amorphous film of $CaCO_3$ is forming under the spread octadecanoic acid monolayer. This will be explored and discussed at greater length later in the chapter.

3.8 ER-FTIR and WAXS Studies of Calcium Carbonate Crystallisation with Added PAA Inhibitor

External reflectance FTIR and WAXS studies were undertaken to assess in more detail the influence of adding PAA inhibitor to calcium bicarbonate solutions. The aim of these studies is to assess the extent of crystallinity of the calcium carbonate films formed.

ER-FTIR

Groves et al.[32] reported a sharp band at 872 cm^{-1} and a small feature at 712 cm^{-1} in FTIR spectra that are specific to crystalline calcite. A small band at ≈ 1086 cm^{-1} and broadening of the band at ≈ 3340 cm^{-1} also indicate an amorphous phase. For transmission measurements, Groves reported that the ratio of the bands (I_{872}/I_{712}) is 3.0 for pure calcite.

Figures 3.36 a & b and 3.37 a & b show ER-FTIR data acquired from octadecanoic acid compressed to 15 mN/m on Kitano solutions with 30 ppm and 6 ppm PAA, respectively. The data with 30 ppm added PAA correspond to the concentration reported by Groves[32].

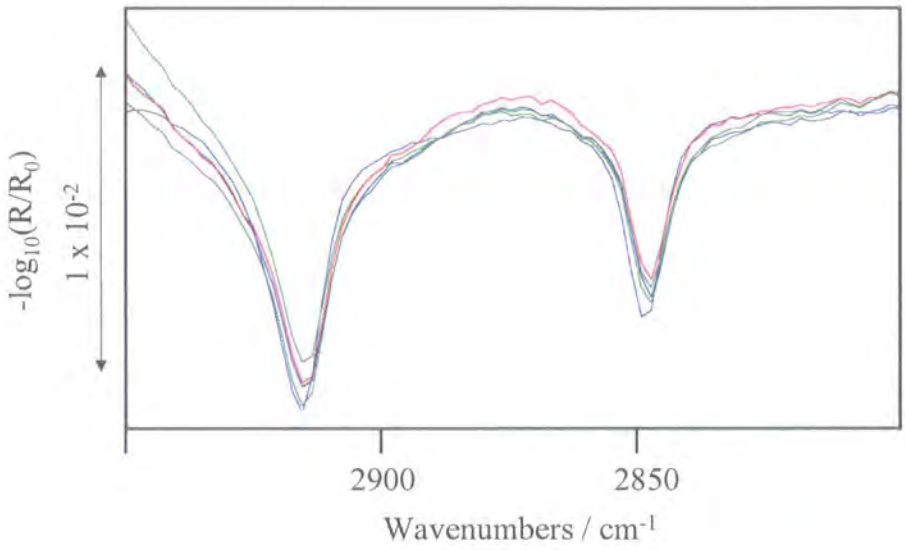

Figure 3.36a ER-FTIR data (2950 – 2800 cm^{-1}) acquired for octadecanoic acid compressed to 15 mN/m on Kitano solution, with 30 ppm PAA inhibitor. Data are presented from 2, 3, 4, 5 and 6 hours.

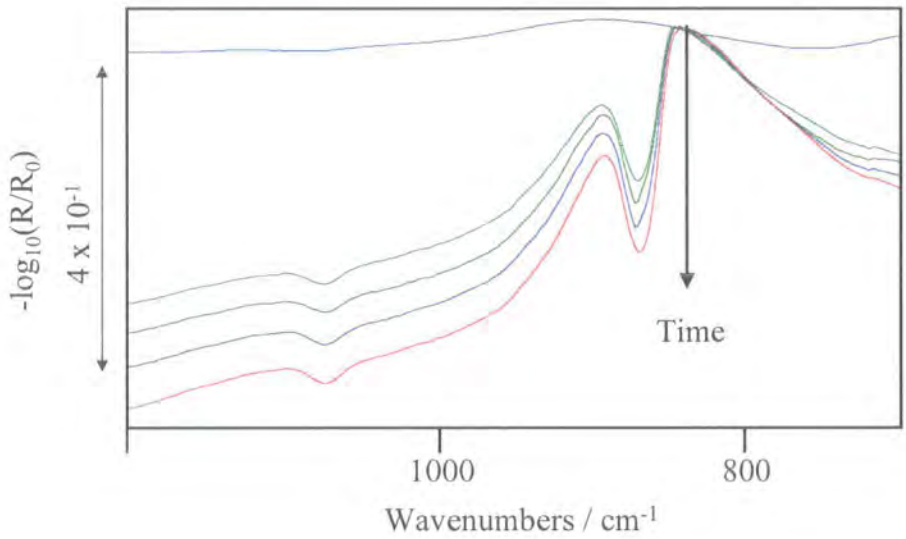

Figure 3.36b ER-FTIR data (1200 – 700 cm^{-1}) acquired for octadecanoic acid compressed to 15 mN/m on Kitano solution, with 30 ppm PAA inhibitor. Data are presented from 2, 3, 4, 5 and 6 hours.

The data presented for the 30 ppm PAA system in figure 3.36a show no significant change in the C-H stretch region over time. Figure 3.36b shows a small band at 1080 cm^{-1} and a broad band at ~ 870 cm^{-1} visible from 3 hours, which indicate the presence of amorphous calcium carbonate. There is no sharp band at either 712 cm^{-1} (calcite) or 745 cm^{-1} (vaterite), again showing that the calcium carbonate film is amorphous.

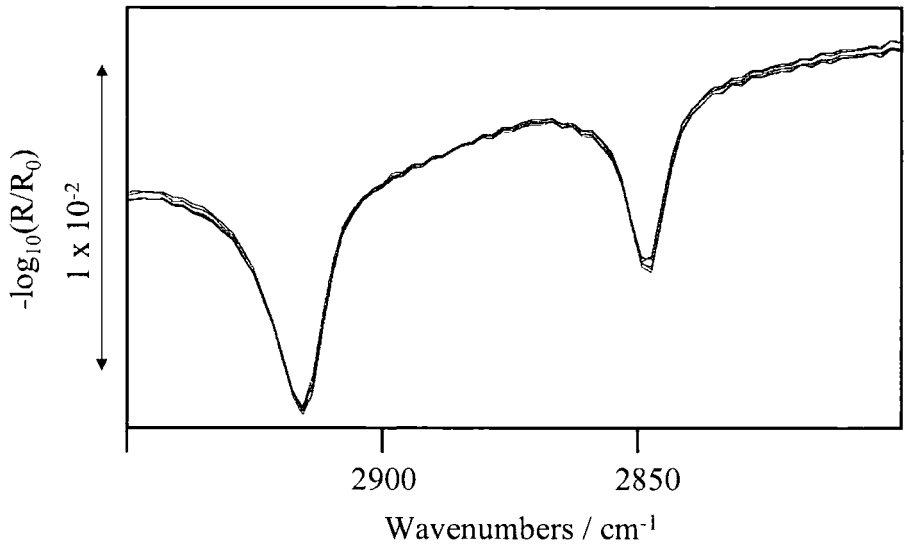

Figure 3.37a ER-FTIR data acquired for 15 mN/m octadecanoic acid on Kitano solution, with 6 ppm PAA inhibitor over 12 hours.

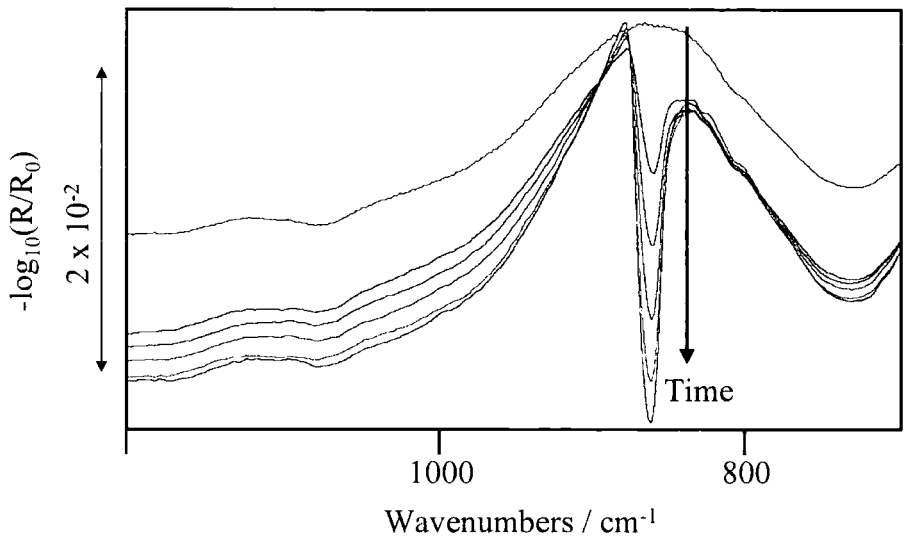

Figure 3.37b ER-FTIR data acquired for 15 mN/m octadecanoic acid on Kitano solution, with 6 ppm PAA inhibitor over 12 hours.

The absence of bands at 712 cm^{-1} and 745 cm^{-1} for the data from the 6 ppm PAA system (figure 3.37b) indicates limited crystallinity of the growing calcium carbonate film, but again there is no increase in C-H stretch intensity (figure 3.37a) as reported in the absence of PAA. The sharpness of the band at 872 cm^{-1} is indicative of lower amorphous character than for the 30 ppm PAA system. Data were acquired at intervening (25, 20, 15, 10 ppm) concentrations of PAA, but no significant change in FTIR spectra was observed until the inhibitor concentration was reduced to 6 ppm, at which point the 872 cm^{-1} band became narrower, indicating a small degree of crystallinity.

WAXS

WAXS data were acquired for the 6 ppm and 30 ppm PAA systems at an incident angle, of 1°, and the detector angle set to 15°. This gives a 2θ range of approximately 3.2 to 37.9°. This shallow incident angle ensures there is limited penetration of the surface and the thin calcium carbonate film is probed.

Figure 3.38 shows data acquired in-situ for octadecanoic acid deposited on a pure Kitano subphase without polyacrylic acid at 6 hours. As expected, there was significant crystal growth, and crystalline diffraction spots are seen on the detector. The superimposed graph in figure 3.38 is an area integration and shows an amorphous hump due to aqueous background, with peaks at ~26.2°, 32° and 35.8° due to crystalline calcium carbonate.

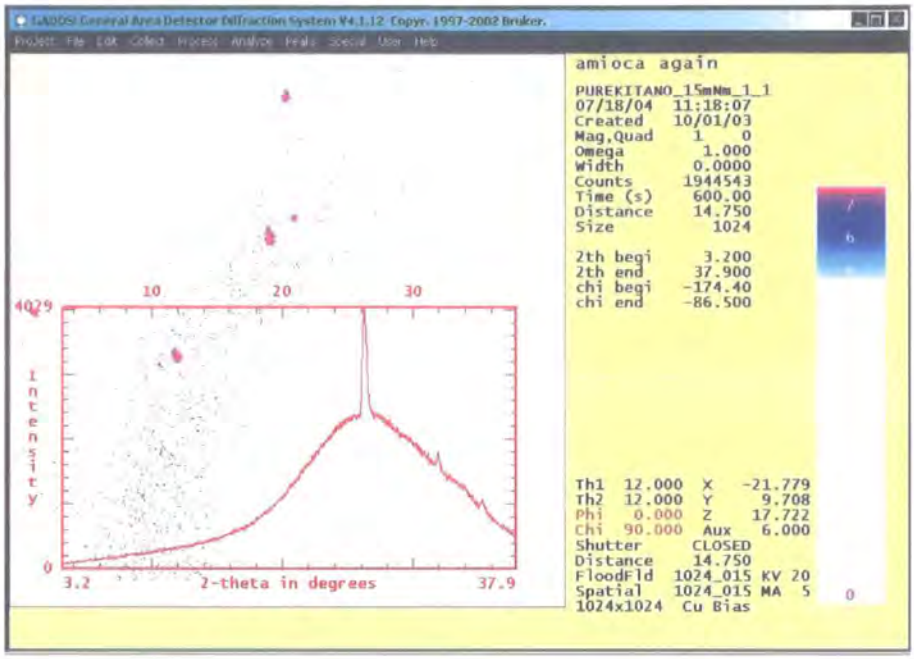

Figure 3.38. WAXS data acquired for octadecanoic acid on Kitano solution after 6 hours. The spots and peaks visible are due to calcium carbonate crystallisation.

Figures 3.39 and 3.40 are equivalent WAXS data for the systems with 30 ppm and 6 ppm PAA inhibitor, respectively. The dark blue curve is of a pure Kitano solution at the initial timepoint. Subsequent data show that the centre of the amorphous hump moves from approximately $2\theta = 28^{\circ}$ to approximately 23°. The movement of this feature is slower for the system with 6 ppm PAA, where ER-FTIR had suggested lower amorphous character (the narrow band at 872 cm^{-1}). The X-ray data for both the 30 ppm and the 6 ppm systems showed no evidence for crystalline character.

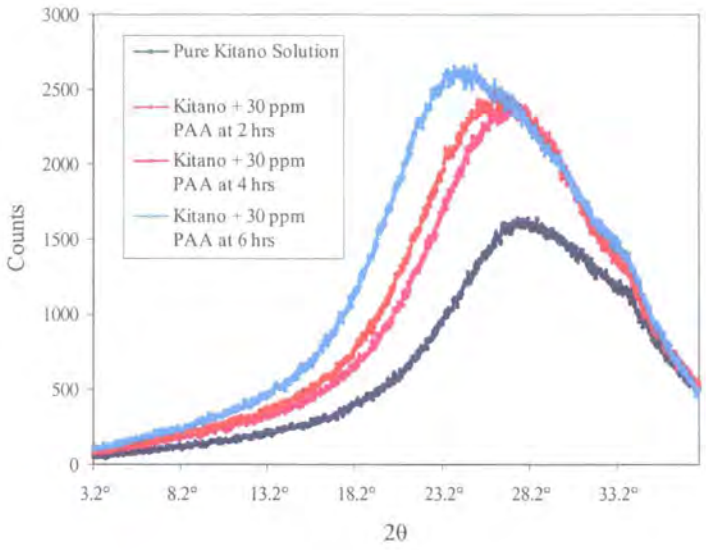

Figure 3.39. WAXS data acquired for octadecanoic acid deposited on a Kitano subphase with 30 ppm PAA inhibitor.

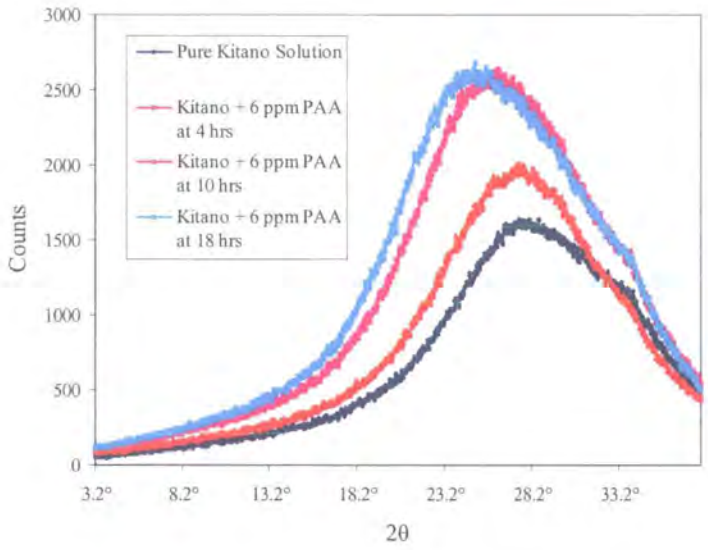

Figure 3.40. WAXS data acquired for octadecanoic acid deposited on a Kitano subphase with 6 ppm PAA inhibitor

3.9 Discussion and Conclusions

Optical microscopy, GIXD and ER-FTIR data have been presented for the crystallisation of calcite under octadecanoic acid monolayers. At moderate (15 mN/m) initial surface pressure in the absence of PAA inhibitor, the GIXD data show a broadening of the peak attributed to the monolayer, which splits into 2 discrete peaks at approximately Q_{xy} = 1.47 and 1.51 $Å^{-1}$. The peak at 1.51 $Å^{-1}$ finally decreases in intensity until it is completely absent, resulting in one narrow peak at 1.47 $Å^{-1}$. The resulting narrow peak is consistent with an octadecanoic acid monolayer on aqueous Ca^{2+} subphase. Since $Q = \frac{2\pi}{d}$, the GIXD data presented for this system imply that the octadecanoic acid molecules have become less tilted upon crystallisation to give a d-spacing of ~ 4.16 Å, compared with ~ 4.25 Å (Q_{xy} = 1.51 and 1.48 $Å^{-1}$ respectively) for the non-crystallising systems. However, we cannot determine the complete film structure since we do not observe the far weaker peak at Q_{xy} ~ 1.67 $Å^{-1}$, which occurs for the rectangular lattice structures expected on Ca^{2+} subphases at π = 7 to 17 mN/m and pH ~ 6.8.

The ER-FTIR data for this system showed an increase in C-H band intensity as crystallisation progressed. Ahn et al.[33] attributed C-H band intensity changes for this system to a change in tilt of the hydrocarbon tailgroup of the octadecanoic acid monolayer relative to the surface normal. In contrast to the results in this chapter, Ahn et al. reported a C-H band intensity decrease with time, due to tailgroup reorientation away from the surface normal, whereas these studies imply a tailgroup reorientiation towards the surface normal for both the GIXD and ER-FTIR data.

The contradiction with Ahn et al.'s findings is unfortunate, but they reported an alkyl chain tilt of only 1° from the surface normal. This is only true for systems compressed to high surface pressure (>18 mN/m) or high pH. Ahn et al. quote the 1° tilt from Böhm et al.[67], which was relevant to systems at alkaline pH, whereas these systems are weakly acidic (pH ~ 5.5). If the octadecanoic acid monolayer really was tilted at 1°, the monolayer has been heavily compressed in which case the decrease in C-H band intensity observed by ER-FTIR could be attributed to dissolution of the film into the subphase. The data presented here are certainly consistent with the alkyl chains being

tilted at ~ 20° from the surface normal, and this tilt decreases upon crystallisation. The ER-FTIR and GIXD data presented here are totally consistent, with both data sets indicating a gradual tilt towards the surface normal.

At higher initial surface pressure (20 mN/m) the peak due to octadecanoic acid is centred at 1.51 $Å^{-1}$ (d = 4.16 Å) and shows only a decrease in counts with time. The film therefore already has a structure akin to the one that develops during the calcium carbonate crystallisation at the lower surface pressures of 10 to 15 mN/m. Furthermore, any film reorganisation that may be favourable for crystallisation would be inhibited by the more rigid film. This system did crystallise, but not at a rate visibly different to the system at moderate initial surface pressure. The system at low initial surface pressure (10 mN/m) crystallised very rapidly; initial GIXD signal was weak due to low surface pressure, and at 4 hours the signal was hardly discernible. All crystallising systems point towards calcite formation. There was no evidence by WAXS for amorphous material, except due to aqueous background, and microscopy studies showed most (> 80%) of crystals formed were calcite.

With 10 ppm PAA inhibitor added, the GIXD data at moderate surface pressure (15 mN/m) show a broad peak centred at Q_{xy} = 1.43 – 1.53 $Å^{-1}$. This system showed no change in the peak up to 5 hours; there is a subtle narrowing at 5 – 11 hours, which corresponds to a slight increase in measured surface pressure (20.3 mN/m at 11 hours).

The equivalent system compressed initially to 20 mN/m shows a rapid increase in surface pressure from 27.5 mN/m to 52.7 mN/m at 4 hours. There is no shift in the peak position (Q_{xy} = 1.51 $Å^{-1}$), but the intensity does fall due to surface roughness. At low initial surface pressure, the GIXD data show few features above the noise, but the surface pressure reading does increase to 14.3 mN/m after 6 hours.
ER-FTIR studies on moderate surface pressure with 30 ppm and 6 ppm added PAA show no change in C-H band intensity with time, though evidence for calcium carbonate precipitation is apparent at 872 cm^{-1} for both systems. At 6 ppm PAA, the 872 cm^{-1} band is sharper, indicating some crystalline character, but the band at 712 cm^{-1} often attributed to calcite is not observed and the band at 1080 cm^{-1} due to amorphous calcium carbonate is apparent. The 30 ppm data show a band at 1080 cm^{-1} attributed to

amorphous calcium carbonate, which is reinforced by the broadness of the band at 872 cm^{-1}, and no crystalline peak at 712 cm^{-1} is seen.

The system with 30 ppm PAA precipitated rapidly after ~ 3 hours and shows no crystalline character by WAXS or ER-FTIR. The 6 ppm system indicates some crystalline character by ER-FTIR, but WAXS did not identify any crystalline order in this system. The WAXS data show a shift in the amorphous hump on calcium carbonate precipitation, indicating little or no crystallinity for either the 30 ppm or 6 ppm system.

Groves et al.[32] proposed an amorphous precursor to calcite and studied this with added PAA (~ 30 ppm) to encourage amorphous calcium carbonate growth. The results in this chapter do not demonstrate the subsequent transformation to calcite reported by Groves et al; much lower concentrations of PAA would be required for this process to be observed on a timescale appropriate for synchrotron experiments. DiMasi et al.[37] recently reported GIXD results for the rearrangement of sodium salts of octadecanoic acid on Kitano solutions, but suggested no resulting epitaxial relation to the $CaCO_3$ planes. The data in this chapter suggest that the monolayer at moderate π changes during the crystallisation process, then relaxes to a structure analogous to that on a Ca^{2+} subphase. In particular, a reduction in the hydrocarbon tail towards the surface normal is indicated by both ER-FTIR and GIXD. It is difficult to understand why the monolayer would change in this way during the crystallisation process, unless a strong or weak epitaxial or stereochemical match actually aids the crystallisation process. In addition, the absence of any film rearrangement for the systems with PAA, in which amorphous calcium carbonate is formed is also consistent with the rearrangement only occurring when a specific ordered crystalline phase is obtained. While DiMasi's conclusions are somewhat contentious given the extensive literature that precedes it, the data presented in this chapter confirm a rearrangement of the octadecanoic acid monolayer at moderate surface pressures during calcium carbonate crystallisation.

The reason why the film structure shown by GIXD relaxes back to its original state after the crystallisation requires further study. It may be that there is significant adsorption of sub-visible calcite clusters beneath the monolayer at early crystallisation times, and then many of these clusters redissolve and precipitate onto the larger visible crystals which

only cover approximately ~ 5 – 15 % of the surface 8 hours after film deposition. This result would be consistent with the neutron reflectivity and ER-FTIR studies on DL-aspartic acid crystallisation presented in chapter 2.

References

(1) Mann, S.; Webb, J.; Williams, R. J. P. *Biomineralization: Chemical and Biochemical Perspectives*; Weinheim, 1989.

(2) Fincham, A. G.; Moradian-Oldak, J.; Simmer, J. P. *J. Struct. Biol.* **1999**, *126*, 270-299.

(3) Wilt, F. H. *J. Struct. Biol.* **1999**, *126*, 216-226.

(4) Nanci, A. *J. Struct. Biol.* **1999**, *126*, 256-269.

(5) Weiner, S.; Wolfie, T.; Wagner, H. D. *J. Struct. Biol.* **1999**, *126*, 241-255.

(6) Naka, K.; Chujo, Y. *Chem. Mat.* **2001**, *13*, 3245-3259.

(7) D'Souza, S. M.; Alexander, C.; Carr, S. W.; Waller, A. M.; Whitcombe, M. J.; Vulfson, E. N. *Nature* **1999**, *398 (6725)*, 312-316.

(8) Falini, G. *Int. J. Inorg. Mat.* **2000**, *2*, 451-461.

(9) Levi, Y.; Albeck, S.; Brack, A.; Weiner, S.; Addadi, L. *Chem Eur. J.* **1998**, *4*, 389-396.

(10) Young, J. R.; Davis, S. A.; Bown, P. R. *J. Struct. Biol.* **1999**, *126*, 195-215.

(11) Malkaj, P.; Chrissanthopoulos, A.; Dalas, E. *J. Cryst. Growth* **2002**, *242*, 233-238.

(12) Lowenstam, H. A. *Science* **1981**, *211*, 1126-1131.

(13) Hall, A.; Taylor, J. D. *Mineral Mag.* **1973**, *38*, 521-525.

(14) Spanos, N.; Koutsoukos, P. G. *J. Phys. Chem. B.* **1998**, *102*, 6679.

(15) Lippmann, F. *Sedimentary Carbonate Materials*; Springer: Berlin, 1973.

(16) Kralj, D.; Brecevic, L.; Nielsen, A. E. *J. Cryst. Growth* **1990**, *104*, 793.

(17) Lowenstam, H. A.; Weiner, S. *On Biomineralization*; Oxford University Press: New York, 1989.

(18) Ahn, J. W.; Kim, H. S.; Kim, H.; Yoon, S. H.; Kim, J. S.; Sung, G. W. *J. Ceramic Processing Res.* **2002**, *3*, 62-65.

(19) Krampitz, G.; Graser, G. *Angew. Chem. Int. Ed. Engl.* **1988**, *27*, 1145.

(20) Falini, G.; Albeck, S.; Weiner, S.; Addadi, L. *Science* **1996**, *271*, 67-69.

(21) Sikes, C. S.; Wheeler, A. P.: USA, 1985; p 4534881.

(22) Weiner, S.; Hood, L. *Science* **1975**, *190*, 987-989.

(23) Weiner, S.; Traub, W. *Phil. Trans. R. Soc. Lond.* **1984**, *304B*, 425-434.

(24) Addadi, L.; Weiner, S. *Proc. Nat. Acad. Sci. USA* **1985**, *82*, 4110-4114.

(25) Gebhard, H.; Neuhaus, A. *Epitaxie-Daten anorganischer und organischer kristalle*; Springer: Berlin, 1972.

(26) Lahav, M.; Landau, E. M. *Nature* **1985**, *318*, 353.

(27) Lahav, M.; Weissbuch, I.; Shimon, J. W.; Landau, E. M.; Popovitz-Biro, R.; Birkovitch-Yellin, Z.; Addadi, L.; Leiserowitz, L. *Pure & Appl. Chem.* **1986**, *58*, 947.

(28) Lahav, M.; Weissbuch, I.; Popovitz-Biro, R.; Levanon, M.; Leiserowitz, L.; Sagiv, J. *Mol. Cryst. Liq. Cryst.* **1986**, *134*, 323-325.

(29) Lahav, M.; Landau, E. M.; Grayer Wolf, S.; Sagiv, J.; Deutch, M.; Kjaer, J.; Als-Nielsen, J.; Leiserowitz, L. *Pure & Appl. Chem.* **1989**, *61*, 673.

(30) Lahav, M.; Landau, E. M.; Grayer Wolf, S.; Levanon, L.; Leiserowitz, L.; Sagiv, J. *J. Am. Chem. Soc.* **1989**, *111*, 1436-1445.

(31) Lahav, M.; Weissbuch, I.; Frolow, F.; Leiserowitz, L. *J. Am. Chem. Soc.* **1990**, *112*, 7718.

(32) Xu, G.; Yao, I.; Aksya, I. A.; Groves, J. T. *J. Am. Chem. Soc.* **1998**, *120*, 11977-11985.

(33) Ahn, D. J.; Berman, A.; Charych, D. *J. Phys. Chem* **1996**, *100*, 12455-12461.

(34) Rajam, S.; Heywood, B. R.; Walker, J. B. A.; Mann, S.; Davey, R. J.; Birchall, J. D. *J. Chem. Soc.; Far. Trans.* **1991**, *87*, 727-734.

(35) Mann, S.; Heywood, B. R.; Rajam, S.; Birchall, J. D. *Nature* **1988**, *334*, 692-695.

(36) Mann, S.; Heywood, B. R.; Rajam, S.; Birchall, J. D. *Proc. R. Soc., London, A* **1989**, 457.

(37) DiMasi, E.; Olszta, M. J.; Patel, V. M.; Gower, L. B. *CrystEngComm* **2003**, *5*, 346-350.

(38) Peterson, I. R.; Brezesinski, G.; Struth, B.; Scalas, E. *J. Phys Chem. B.* **1998**, *102*, 9437-9442.

(39) Dupres, V.; Cantin, C.; Benhabib, F.; Perrot, F.; Fontaine, P.; Goldmann, M. *Langmuir* **2000**, *16*, 10189-10192.

(40) Shih, M. C.; Bohanon, T. M.; Mikrut, J. M.; Zschack, P.; Dutta, P. *J. Chem. Phys.* **1992**, *96*, 1556-1559.

(41) Kjaer, K.; Als-Nielsen, J.; Helm, C. A.; Tippman-Krayer, P.; Möhwald, H. *J. Phys. Chem.* **1989**, *93*, 3200-3206.

(42) Datta, A.; Kmetko, J.; Richter, A. G.; Yu, C.-J.; Dutta, P.; Chung, K.-S.; Bai, J.-M. *Langmuir* **2000**, *16*, 1239-1242.

(43) Jacquemain, D.; Leveiller, F.; Weinbach, S. P.; Lahav, M.; Leiserowitz, L.; Kjaer, J.; Als-Nielsen, J. *J. Am. Chem. Soc.* **1991**, *113*, 7684-7691.

(44) Tippman-Krayer, P.; Möhwald, H. *Langmuir* **1991**, *7*, 2303-2306.

(45) Wada, N.; Kanamura, K.; Umegaki, T. *J. Coll. & Interf. Sci.* **2001**, *233*, 65-72.

(46) Reddy, M. M.; Hoch, A. R. *J. Coll. & Interf. Sci.* **2001**, *235*, 365-370.

(47) Qi, L.; Li, J.; Ma, J. *Adv. Mat.* **2002**, *14*, 300-303.

(48) Kitano, Y.; Park, K.; Hood, D. W. *J. Geophys. Res.* **1962**, *67*, 4873-4874.

(49) Kitano, Y. *Bull. Chem. Soc. Japan* **1962**, *35*, 1973-1980.

(50) Heywood, B. R.; Mann, S. *Chem. Mat.* **1994**, *6*, 311-318.

(51) Cooper, S. J.; Sessions, R. B.; Lubetkin, S. D. *J. Am. Chem. Soc.* **1998**, *120*, 2090-2098.

(52) Backov, R.; Lee, C. M.; Khan, S. R.; Mingotaud, C.; Fanucci, G. E.; Talham, D. R. *Langmuir* **2000**, *16*, 6013-6019.

(53) Kitano, R. *Bull. Chem. Soc. Japan* **1962**, *12*, 1980.

(54) Harris, D. C. *Quantitative Chemical Analysis*, 4th ed.; W.H. Freeman & Co., 1995.

(55) Vogel, A. I. *Textbook of Quantitative Inorganic Analysis*, 4th ed.; Longman Group Ltd., 1978.

(56) Welcher, F. J. *The Analytical Uses of Ethylenediaminetetraacetic Acid.*; D. Van Nostrand Co. Inc., 1957.

(57) DiMasi, E.; Patel, V. M.; Sivakumar, M.; Olszta, M. J.; Yang, Y. P.; Gower, L. B. *Langmuir* **2002**, *18*, 8902-8909.

(58) Rodriguez-Clemente, R.; Lopez-Macipe, A.; Gomez-Morales, J. *J. Cryst. Growth* **1996**, *166*, 1015.

(59) Turnball, A. G. *Geochim. Cosmochim. Acta.* **1973**, *37*, 1593.

(60) Richardson, R. M.; Roser, S. J. *Liquid Crystals* **1987**, *2*, 797.

(61) Rajam, S. In *PhD thesis, Controlled Crystallisation of Calcium Carbonate under Langmuir Monolayers*; Univ. of Bath, 1990.

(62) Pobeguin, T. *Ann. Sc. Nat. Bot.* **1954**, *15*, 29.

(63) Dedek, J. *Le Carbonate de Chaux*; Librarie Universitaire Louvain: Louvain (France), 1966.

(64) Aizenberg, J.; Lambert, G.; Addadi, L.; Weiner, S. *Adv. Mat.* **1996**, *8*, 222-226.

(65) Beniash, E.; Aizenberg, J.; Addadi, L.; Weiner, S. *Proc. R. Soc., London, B* **1997**, *264*, 461-465.

(66) Brecevic, L.; Nielsen, A. E. *J. Cryst. Growth* **1989**, *98*, 504-510.

(67) Böhm, C.; Leveiller, F.; Jacquemain, D.; Möhwald, H.; Kjaer, J.; Als-Nielsen, J.; Weissbuch, I.; Leiserowitz, L. *Langmuir* **1994**, *10*, 830-836.

Chapter 4

Ice Crystallisation in Oil-in-Water Emulsions

4.1 Introduction

4.1.1 Background

The ability of Langmuir monolayers to act as 2 dimensional templates for inducing the heterogeneous crystallisation of organic and inorganic materials was introduced in Chapter 1. Results of crystallisation studies for DL-aspartic acid under nylon 6 and calcium carbonate under octadecanoic acid were presented in chapters 2 and 3, respectively. This chapter considers the effect of interfacial curvature and additive density on ice crystallisation in emulsions.

Popovitz-Biro at el.[1] demonstrated that self-assembled monolayers of long chain alcohols effectively nucleate supercooled water into ice at the air-water interface. Alcohols of type $C_nH_{2n+1}OH$ (where $16 \leq n \geq 31$) were investigated and the longer chain species found to be most effective at inducing ice formation. In addition, an odd/even effect was found, with species where n is odd inducing ice formation at temperatures approximately 3 °C higher than neighbouring species where n is even. This better ice nucleating ability of species where n is odd, is believed to be due to a better epitaxial match between the ice and the monolayer, whose lattice parameters were measured by GIXD. Experimental observations of ice crystallised under atmospheric pressure show a hexagonal structure[2,3], with a = b = 4.5 Å and c = 7.3 Å. GIXD measurements[1,4] of $C_{21}H_{43}OH$ on water at 0 °C show that the film structure can be represented as a rectangle where a = 5 Å and b = 7.42 Å. Thus a good epitaxial match is expected between the (001) face of crystalline water and long chain odd alcohols. Long chain alcohols where n is even are believed to have a poorer epitaxial match to ice and an unfavourable OH group orientation at the interface.

Davey et al.[5] were the first to explore kinetics of nucleation by Langmuir monolayers for the case of ice nucleation induced by triacontanol ($nC_{30}H_{61}OH$) at the air-water interface. The ability of these long chain alcohols to induce heterogeneous crystallisation in emulsions has not been reported and there has been no systematic study on interfacial curvature effects to-date, despite its crucial role in determining whether a particular additive will promote or inhibit crystallisation. Consequently, these issues are addressed here.

The following information is relevant to this work. Homogeneous ice nucleation in emulsions in the absence of additives that induce nucleation has been reported at temperatures as low as -39 °C [6,7]. In comparison, for non-specific heterogeneous nucleators, such as glass slides, container walls, etc, ice nucleation is expected in the temperature range -18 °C to -20 °C [8].

4.1.2 Aims of this Chapter

Crystallisation induced by surfactants in emulsions has been reported[9-13], but the effect of droplet size on interfacial crystallisation has not been studied. Typically, crystallisation within emulsion droplets has been studied, but Lim et al.[14] showed the use of an active surfactant to induce crystallisation around, as opposed to within, emulsion droplets. These studies have shown that greater crystallisation control can be achieved using interfacial nucleators in emulsion systems, however, none has quantified the effect of interfacial curvature to-date. In recent weeks, Davey[15] has highlighted the need for experiments in this area, following a computer simulation[16] on the effects of different substrate shapes and sizes on crystallisation of colloidal particles.

As will be discussed at the end of this chapter, an extension of classical nucleation theory already predicts that interfacial heterogeneous nucleation on a smaller droplet where curvature is high (i.e. nanoemulsions) will give a lower crystallisation temperature (T_{cryst}) than for crystallisation on an emulsion droplet of larger droplet size where curvature is very low. In this chapter the aim is to explore whether classical nucleation theory accurately describes heterogeneous nucleation on a curved substrate, or whether additional factors must be considered.

Recall from chapter 1 that emulsions fall into three main categories; microemulsions where droplet size is typically 10 nm, nanoemulsions where droplet size range is 50 - 500 nm and emulsions where droplet diameter exceeds 500 nm.

Stable emulsion systems of different droplet size will be developed and the effect of long chain alcohol additives investigated. The development of stable emulsions systems of various droplet diameters will enable an assessment of the effect of interfacial curvature.

The longest linear alcohol readily available where n is odd, is 1-heptacosanol ($C_{27}H_{55}OH$) obtainable from Aldrich. This will be the species used for most studies in this chapter, but 1-nonadecanol ($C_{19}H_{39}OH$) and 1-eicosanol ($C_{20}H_{41}OH$) will also be used for comparison in some studies. The surfactant used was Brij 30 for the reasons outlined below.

The Brij® series of surfactants are polyoxyethylene fatty ethers derived from lauryl, cetyl, stearyl and oleyl alcohols. They are resistant to acid and alkaline conditions at a more extreme pH range than ester type emulsifiers. This resistance makes them useful for paints and coatings, adhesives and other industrial applications. Hydrophilic and lipophilic Brij surfactants are available, making both oil-in-water (o/w) emulsions and water-in-oil (w/o) emulsions possible.

Brij 30 (polyoxyethylene-4-lauryl ether) is a lipophilic form that is well understood[17-21]. The phase diagram published by Forgiarini et al.[22] is illustrated in figure 4.1. Both small and large droplet oil-in-water emulsions can be stabilised with this surfactant, as can water-in-oil microemulsions at room temperature.

The structure of Brij 30 is $C_{12}H_{25}O(CH_2CH_2O)_4OH$, which is often represented as $C_{12}E_4$ or $C_{12}EO_4$ in the literature. The non-ionic structure of Brij 30 suggests it would be passive, i.e. it will not nucleate ice. This is greatly advantageous in these studies where it is hoped nucleation of the ice will be solely induced by the long chain alcohol additive.

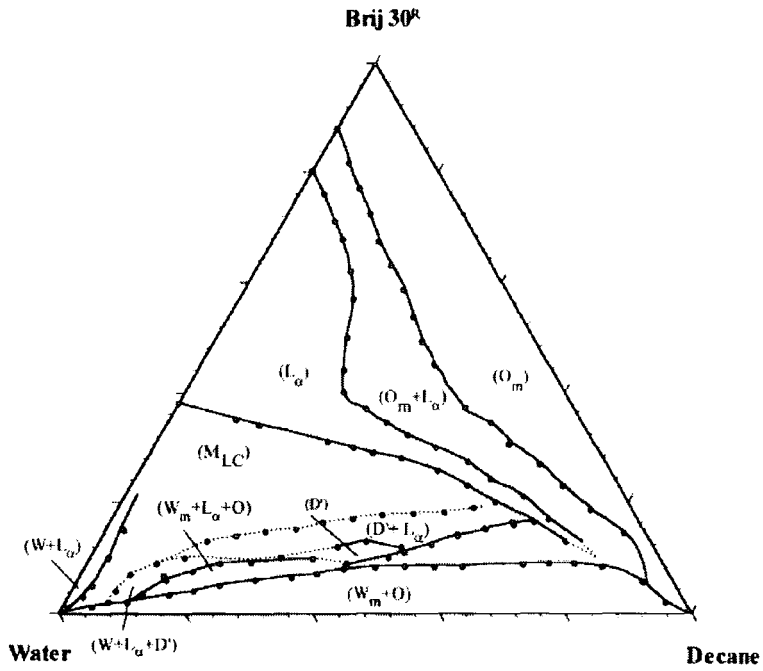

Figure 4.1. Phase diagram[22] for decane-water emulsions stabilised with Brij 30 at 25 °C. O_m is an isotropic liquid phase, Lα a lamellar liquid crystalline phase, D' a shear birefringent liquid phase, W_m a bluish liquid phase (O/W microemulsion), W an aqueous liquid phase, O an oil liquid phase and M_{LC} a multiphase region including lamellar liquid crystal.

4.2 Experimental Procedures

4.2.1 Materials

The materials used were as follows. 1-heptacosanol, 1-nonadecanol, 1-eicosanol, decane and Brij 30 (polytetraoxyethylene dodecyl ether) were obtained from Aldrich and used with no further purification. Ultrapure water with a resistivity of 18 MΩ cm was provided by a UHQ water filtration unit.

4.2.2 Differential Scanning Calorimetry (DSC)

Introduction to DSC

Differential scanning calorimetry is the standard technique for studies of thermal transitions of a sample. The technique is used to determine glass transitions, melting temperatures and many other thermal changes in a sample with changing temperature. The technique operates by measuring the amount of energy absorbed or released by a sample as it is heated or cooled.

DSC was used in this work to study the crystallisation temperature of ice in emulsions. A typical DSC trace for the crystallisation of ice is pictured in figure 4.2. This shows a sharp exotherm caused by ice crystallisation and a broader endotherm at the point of sample melting.

DSC data were collected on a Pyris 1 Perkin Elmer system (figure 4.3) managed by Mr. W. D. Carswell. This is a power compensation instrument, which operates with two individual furnaces that maintain a reference and the sample at the same temperature throughout the analysis. The difference in heatflow between the reference and the sample with temperature is the fundamental variable with this technique. The instrument can operate across a temperature range of -170 °C to 730 °C and can heat or cool at controlled rates of up to 500 °C/min.

Two identical aluminium pans are positioned on a sample platform connected to a furnace by a common heat flow path. The sample is placed in one pan, while the other pan is left empty for reference purposes. The furnace temperature is controlled by the software, which ensures that both the sample and the reference pan heat at the same rate.

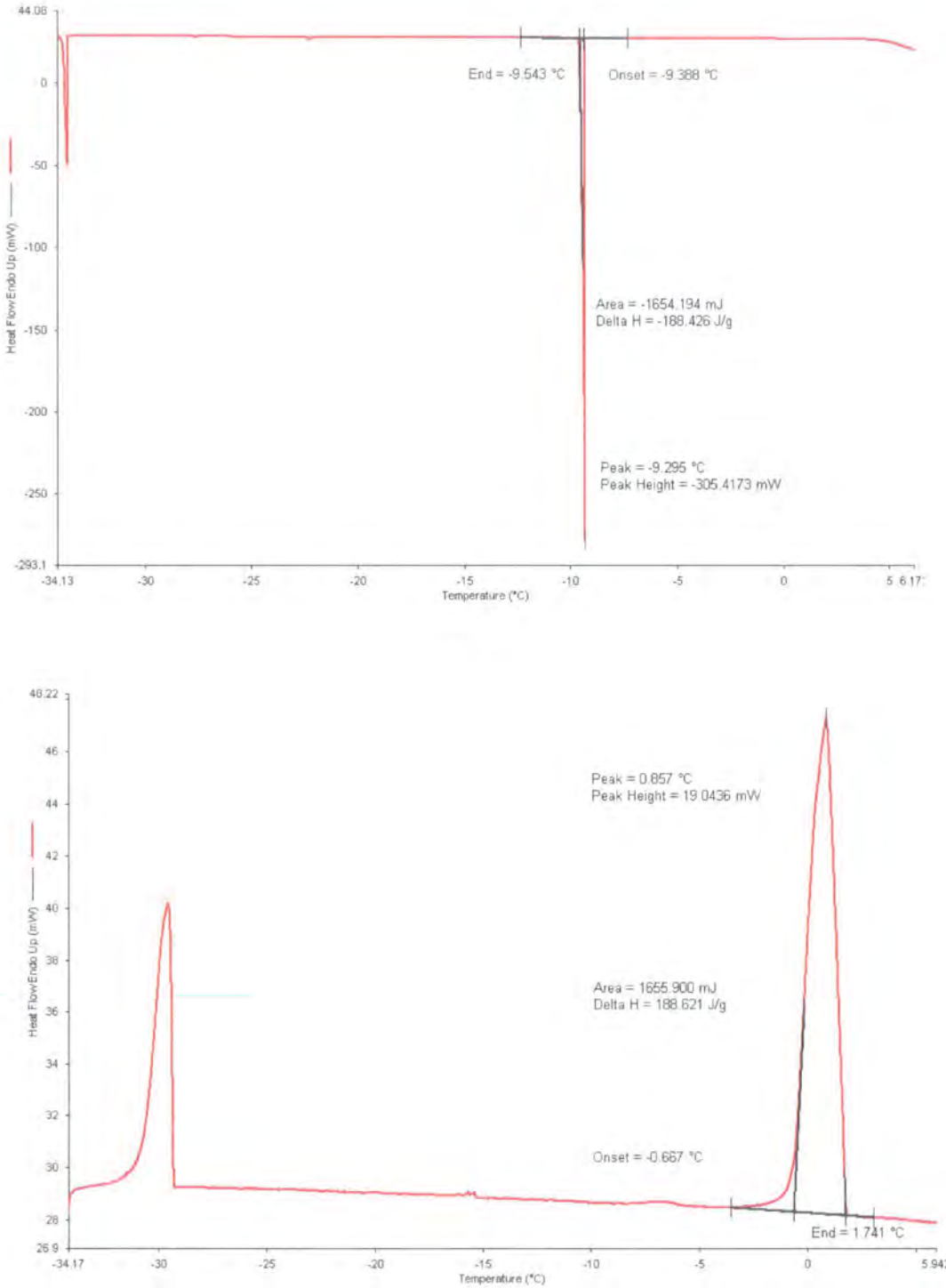

Figure 4.2. Typical DSC traces for ice crystallisation, exotherm (top) and endotherm (bottom). The additional peaks at the left side of the plots are due to the freezing and melting of decane.

Figure 4.3. Image of Perkin Elmer Pyris 1 DSC. The liquid nitrogen dewar required for the sub-ambient temperature studies detailed in this chapter is visible at the bottom left of the image.

Figure 4.4 shows the two furnaces in the sample environment. The furnace is cooled by liquid nitrogen and the sample chamber is purged with nitrogen gas to eliminate oxidation of samples at elevated temperatures.

Figure 4.4. Picture of sample environment in the DSC instrument.

DSC Data Collection

Crystallisation temperatures of ice, T_{cryst} ,were assessed by DSC at heating and cooling rates of 1 °C/min across a temperature range of 10 °C to -30 °C. Samples of ≈ 5 to 20 mg were accurately weighed and analysed in hermetically sealed aluminium pans under a nitrogen purge. A single sharp exotherm peak, and a broader endotherm peak, attributable to ice crystallising and melting, respectively, were observed on the cooling and subsequent heating runs. Data are presented here as ΔT where:

$$\Delta T = T_{cryst} - T_{melt} \qquad \text{[Eqn. 4.1]}$$

T_{melt} is the observed temperature of the melt and T_{cryst} is the observed crystallisation temperature.

T_{melt} was always 0 °C ± 1 °C, indicating a maximum error of 1 °C in the measurements. However, T_{cryst} readings from the instrument were found to be changing for identical samples, by approximately ±2 °C, principally due to the stochastic nature of nucleation. Two different UHQ water samples analysed by DSC gave ΔT values of -20.7 °C and -24.2 °C. This is actually lower than the values quoted in the literature[8] (approximately -18 to -20 °C) for non-specific heterogeneous nucleation. This indicates that the aluminium pans used in the DSC analysis do not have a significant effect on the nucleation of ice.

4.2.3 Optical Microscopy Equipped with a Linkam Controlled Temperature Stage

The optical microscope was coupled with a Linkam controlled temperature stage for the cooling and heating of samples at a controlled rate. This enables the user to assess T_{cryst} and T_{melt}, in addition to valuable visual information upon cooling or heating of samples.

Samples were cooled to T_{cryst} and then heated to the melt at a rate of 4 °C/min. In optical microscopy studies this cooling rate better enables the user to determine the freezing

point, T_{cryst}. Slower cooling rates made it very difficult to determine the onset of birefringence at T_{cryst}. The quicker rate of cooling gives a more abrupt visual change in the sample upon crystallisation.

Table 4.1 compares readings from an electronic thermometer applied to a glass coverslip on the Linkam sample platform with the temperature readings on the Linkam control panel. There is good agreement between the values, deviating only in excess of 0.4 °C when temperatures below -16 °C are reached.

The sample platform is cooled by liquid nitrogen, which is circulated through the sample platform and recycled to purge the sample chamber. This eliminates condensation and crystallisation of water vapour from the atmosphere. Approximately 20 mg of sample was placed on a glass coverslip and placed directly on the sample platform.

In order to demonstrate the effectiveness of the purge, a blank cover slip was cooled to -40 °C. No ice formation was observed, but in absence of the purge, ice forms at approximately -18 °C. We can therefore be confident that the ice formation observed and T_{cryst} values reported here are due to genuine sample changes and not condensation from the atmosphere.

Using the Linkam controlled temperature stage, a drop of UHQ water placed on a glass coverslip froze at -17.0 °C, which is comparable to the literature values[8] of -18 to -20 °C.

Linkam Reading / °C	Measured Temperature / °C
18.0	18.3
15.0	15.1
10.0	10.3
5.0	4.9
0.0	0.0
-2.0	-2.2
-3.9	-4.3
-6.1	-6.1
-8.0	-8.1
-10.0	-9.8
-12.0	-11.8
-14.0	-14.0
-16.0	-15.8
-18.0	-17.4
-20.0	-19.3
-22.0	-20.9
-24.0	-22.6

Table 4.1. Measured sample temperature readings versus digital readings on the Linkam controlled temperature stage.

4.2.4 X-Ray Diffraction Data Acquisition

While optical microscopy provided useful visual information and helped to gain an understanding of thermal effects on emulsion structure, there was sometimes ambiguity as to whether birefringent development was from liquid crystalline surfactant or localised crystallisation of water.

Use of the Linkam controlled temperature stage with the D8 diffractometer demonstrated that the birefringence differences observed are principally due to the nucleation of ice in

these systems and not a lamellar or liquid crystalline phase, since diffraction spots consistent with ice were observed. The occurrence of lyotropic liquid crystal phases is discussed in more detail later.

As the Linkam housing would have prevented shallow angle incident radiation reaching the sample, the active cooling/heating block was removed and placed directly on the X-ray sample platform. Samples were cooled at a rate of 4 °C/min, corresponding with the microscopy studies. At this cooling rate, a test run with no sample showed that crystallisation of water from the atmosphere was not observed until -22 °C.

X-ray data were acquired with a 15 seconds acquisition time, an incident angle, $\theta_1 = 20°$ and detector angle, $\theta_2 = 10°$. This gave a 2θ range of approximately 20 - 47°, capturing most of the reflections expected for crystalline water (see tables 4.2 and 4.3). Each X-ray diffraction pattern acquired represents an approximate 1 °C change in temperature, and the T_{cryst} data represented in the graphs later in this chapter are the temperatures recorded at the end of the trace where diffraction spots consistent with ice are observed.

Crystallographic Plane	d-spacing / Å	2 θ	Intensity / %
(110)	3.8989	22.807°	100.00
(002)	3.6640	24.291°	86.16
(111)	3.4420	25.884°	65.00
(020)	3.8990	22.807°	56.96
(130)	2.2511	40.053°	55.83
(113)	2.0700	43.729°	51.09
(021)	3.4421	25.883°	30.88
(200)	2.2510	40.054°	28.67
(112)	2.6700	33.563°	27.68
(132)	1.9180	47.397°	23.94
(023)	2.0700	43.729°	23.61
(022)	2.6701	33.562°	16.19
(202)	1.9180	47.398°	12.45
(221)	1.8839	48.309°	7.31
(220)	1.9494	46.587°	6.44
(041)	1.8840	48.307°	4.24
(131)	2.1518	41.985°	2.11
(040)	1.9495	46.586°	1.92
(004)	1.8320	49.769°	0.18

Table 4.2. Expected powder X-ray diffraction peaks for cubic ice.
Wavelength = 1.5418 Å

Crystallographic Plane	d-spacing / Å	2 θ	Intensity / %
(100)	3.9110	22.736°	100.00
(101)	3.4530	25.800°	58.89
(002)	3.6770	24.204°	54.13
(110)	2.2580	39.925°	43.55
(103)	2.0771	43.572°	34.93
(102)	2.6789	33.448°	24.53
(112)	1.9242	47.236°	15.01
(201)	1.8898	48.148°	6.35
(200)	1.9555	46.435°	2.76
(004)	1.8385	49.581°	0.35

Table 4.3. Expected powder X-ray diffraction peaks for hexagonal ice. Wavelength = 1.5418 Å

Hexagonal and cubic structures for ice are possible, but the free energy barrier for the cubic lattice is 100 J mol^{-1} greater than the hexagonal case[23]. Tables 4.2 and 4.3 show the expected reflections for cubic and hexagonal ice, respectively, as derived from the Cerius2 software.

X-ray Results

This chapter includes T_{cryst} data as assessed by DSC and optical microscopy. The data acquired from the X-ray coupled with the cold stage largely back up these conclusions, but a repetition of some samples results in anomalous results. This technique is inevitably less accurate than DSC and optical microscopy, because the onset of crystallisation can only be judged within a 1 °C window. The samples with anomalous results were largely those of higher long chain alcohol content. This could mean that the air-water interface has become contaminated with a 1-heptacosanol monolayer that then induces surface crystallisation. X-ray diffraction data are inevitably more susceptible to this surface phenomenon because the systems are not well purged with nitrogen gas, the way to which would help disrupt surface nucleation should surface contamination occur.

Section 4.3.2 (see later) details studies that the concentration of 1-heptacosanol at the air-water interface in these emulsions is sufficiently low not to induce ice nucleation. X-ray data are not therefore presented, as they add little value to this work where a quantitative measure of the onset of crystallisation is desired. As expected, however, the X-ray data were consistent with the hexagonal structure of ice only.

4.2.5 Droplet Size Measurements

Malvern Mastersizer

Droplet size measurements were made on a Malvern Mastersizer model 2000, which is based at the School of Engineering. This is a laser diffraction system capable of measuring the diameters of solids and emulsion droplets, in the range 0.020 μm to 2000 μm. The main laser bench is equipped with a Hydro 2000S dispersion unit, which is designed for solvent based suspensions and pharmaceuticals. The sample unit has a variable stirrer, which drives the sample through the quartz cell, through which the laser beam passes. The instrument has a dual wavelength sensitive detector, which allows use of a second blue laser to improve sensitivity at sub-micron size range.

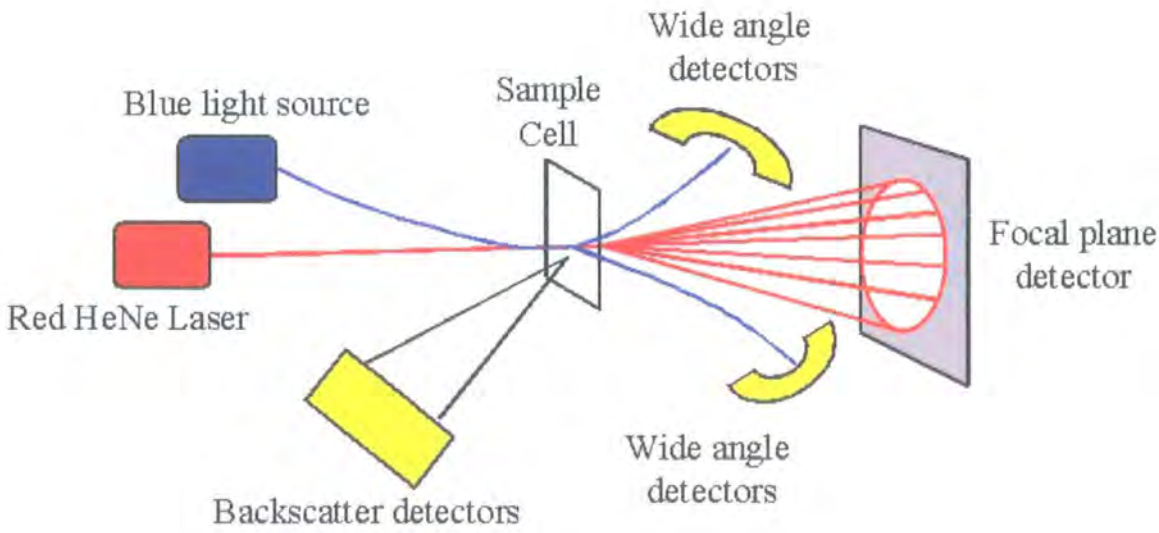

Figure 4.5. Illustration of Malvern Mastersizer and major components.

The particles/droplets scatter the laser light at an angle roughly inversely proportional to their size. The angle and intensity of this scattered light is measured by numerous detectors, which are positioned to give a broad size range sensitivity for the instrument. The size of the features is then determined by a Mie scattering model[24].

The instrument is operated through a PC, with the standard data output being a volume distribution. While volume fraction measurements are the standard output with this type of instrument, surface area and number based data were preferred, as these are not skewed by the presence of large material, such as air bubbles. These data are processed in the Malvern software by means of Hatch-Choate[25] transformations to give distributions in terms of number, and surface area of the emulsion droplets.

The Hatch-Choate model assumes a spherical distribution for the sample, which is unsuitable for solid samples. For the measurements of emulsions presented here, however, the number and surface area transformations are expected to be relatively accurate. Diameter measurements, d, are presented as d(0.1), d(0.5) and d(0.9) with d(x) denoting the droplet diameter value for which a number/volume/surface area fraction, x, of droplets have a smaller value.

Malvern Mastersizer Data Acquisition

Samples were added dropwise to the sample chamber until an obscuration of 5% was recorded. Data were acquired assuming an optical index of 1.410 for the droplets, which corresponds to the value for decane.

The stirring speed was 1500 rpm and 5 sequential acquisitions were made, each lasting 5 seconds. All data presented here are from the first acquisition. Only very small changes were observed over 5 acquisitions for the white emulsions and no changes were observed for the blue or white nanoemulsions, showing good reproducibility was obtained in all cases.

4.2.6 Preparation of Emulsions

Emulsions were prepared by "Method B", as described by Forgiarini et al[22]. "Method B" where Brij 30 surfactant and decane are premixed and the water subsequently added, produces more monodisperse emulsions. For "Method A", the surfactant is added to the water, mixed and then decane added. "Method A" is described by Forgiarini et al.[22] as producing emulsions of larger droplet size, whereas "Method C" (no binary premixing) gives emulsions of variable structure.

In all cases the ratio, F_O, of oil to water is quoted where:

$$F_O = \frac{O}{O+W} \qquad \text{[Eqn. 4.2]}$$

O is the mass of oil, and W is the mass of water.
Surfactant concentration is quoted here as the percentage mass of total emulsion, and is usually in the order of 5%.

Nanoemulsions (where F_O is 0.019) were always prepared by "Method B". Attempts to generate nanoemulsions by "Method A" resulted in emulsions with droplet diameters of approximately 4.8 to 6.2 μm. This is probably because the decane has been unable to disperse properly by this method and has remained in large pockets.

4.2.7 Hydrophobised Glass Coverslips

In order to limit the nucleation of ice by the glass, attempts were made to create a hydrophobic surface on the coverslips used in microscopy studies. This glass treatment method was based on the one reported by Sagiv et al.[26,27] and is described below.

The coverslips were sonicated in UHQ water with detergent at approximately 95 °C for 60 minutes. These were sonicated for a further 5 minutes in concentrated acid and then in dilute (0.005M) NaOH for 10 minutes. The slides were dried in an oven and remained covered until required for the next step.

The cleaned slides were immersed for 2 minutes in a solution of 0.05 g n-octadecyl trichlorosilane predissolved in a 1:3 carbon tetrachloride/n-hexadecane solution. This silane solution was stable for approximately 1 hour, after which time oxidation of the silane occurs. Slides were used on the day of preparation.

Water added to these glass slides had a high contact angle compared to water on untreated coverslips, and moved freely without wetting the surface.

4.2.8 Heptacosanol Solubility Studies

Solubility studies for 1-heptacosanol in decane and water were undertaken at various temperatures. Ambient solubility studies were also undertaken for nanoemulsions (F_O = 0.019) and emulsions (F_O = 0.70). The experimental method of Yano et al[10] was followed, as described below.

Approximately 1 mg of heptacosanol was weighed on a microbalance. A known quantity of liquid/emulsion was added and the mixture briefly vortexed and sonicated at the appropriate temperature for approximately 5 minutes. These were stored overnight at the temperature of interest in the case of emulsion samples and for one hour in the case of decane-heptacosanol and water-heptacosanol samples. These were then analysed visually for evidence of undissolved material. If necessary, more emulsion/liquid was added and the process repeated until all the heptacosanol appeared to have dissolved. This method was found to be inaccurate for the determination of heptacosanol in emulsions and nanoemulsions due to their opaque and translucent appearance, respectively. Consequently, laser diffraction measurements were also undertaken on these systems, with the solubility limit considered to be exceeded when particles in excess of 100 μm were consistently found in the emulsions.

4.3 Proof of Concept: Long Chain Alcohol Induced Ice Nucleation in Emulsions

4.3.1 Planar Studies of Long Chain Alcohols

Popovitz-Biro et al.[1] undertook ice nucleation studies of long chain alcohols at the air-water interface using a controlled temperature stage. The alcohols were dissolved in chloroform and added to a drop of water, whereupon evaporation of the chloroform left a spread alcohol film.

To verify these results, long chain alcohols were pre-dissolved in chloroform at concentrations of 0.5 mg/ml. 20 µl of the chloroform solutions were added by microsyringe to approximately 15 mg UHQ water in a DSC pan. The chloroform was allowed to evaporate (approximately 5 minutes) before the DSC pan was sealed.

Table 4.4 shows the DSC data acquired for C19 (1-nonadecanol), C20 (1-eicosanol) and C27 (1-heptacosanol) long chain alcohols spread on UHQ water.

Sample	DSC Results ΔT / °C
$C_{19}H_{39}OH$	-14.7
$C_{20}H_{41}OH$	-12.4
$C_{27}H_{55}OH$	-10.7

Table 4.4 DSC data acquired for long chain alcohols spread on UHQ water.

Popovitz-Biro et al.[1] reported T_{cryst} of approximately -7 °C, -11 °C and -2 °C for the C19, C20 and C27 alcohol species, respectively. While the T_{cryst} data in table 4.4 do not demonstrate the better ability of C19 versus C20 to nucleate ice (odd/even effect), they do confirm that long chain alcohols induce ice crystallisation before the non-specific heterogeneous nucleation temperature of approximately -20°C[8]. The values are significantly lower than that of Popovitz-Biro et al.[1], which is probably due to monolayer

disruption by the nitrogen purge. The data also confirm that 1-heptacosanol is better able to induce nucleation of supercooled water into ice than the shorter C19 and C20 variants.

4.3.2 Planar Studies with Brij 30, Decane and 1-Heptacosanol

In order to verify whether Brij 30/decane would be passive, i.e. they would not induce nucleation of ice, planar investigations were undertaken with 1-heptacosanol at various concentrations.

Approximately 15 mg of UHQ water was weighed into a DSC pan and 1 drop (~3 μl) of the decane/Brij 30/1-heptacosanol mixtures described in table 4.5 added by microsyringe. T_{cryst} was assessed in triplicate by DSC. A new sample from the same sample batch was used for the repeat analyses. The alcohol component in decane/Brij 30/alcohol samples precipitates after a few hours, hence fresh samples were prepared and analysed within 30 minutes to verify the data acquired.

There is variation between the three ΔT (T_{cryst}) values for each sample again attributed mainly to the stochastic nature of nucleation, but despite this, the data acquired (see table 4.5) show once more the strong ability of 1-heptacosanol to nucleate ice. The nucleating ability of 1-heptacosanol is much enhanced in the presence of Brij 30 and decane, but Brij 30 and decane alone do not induce ice nucleation. The Brij 30, water and decane samples represent the planar interface analogous to the curved interfaces in the emulsion crystallisation studies, and shows a crystallisation temperature as high as approximately ~ -5 °C in many instances.

Sample added to UHQ water	DSC Results #1 ΔT / °C	DSC Results #2 ΔT / °C	DSC Results #3 ΔT / °C
Decane:Brij 30 (95:5)	-17.9	-21.0	-19.7
3% $C_{27}H_{55}OH$ in decane:Brij 30 (95:5)	-4.5	-7.0	-8.4
1% $C_{27}H_{55}OH$ in decane:Brij 30 (95:5)	-5.6	-7.9	-7.5
0.5% $C_{27}H_{55}OH$ in decane:Brij 30 (95:5)	-4.8	-5.2	-7.9
0.3% $C_{27}H_{55}OH$ in decane:Brij 30 (95:5)	-5.6	-7.0	-9.5
0.05% $C_{27}H_{55}OH$ in decane:Brij 30 (95:5)	-7.0	-8.3	-10.2
Brij 30	-17.6	-17.8	-18.0
3% $C_{27}H_{55}OH$ in Brij 30	-10.5	-10.0	-6.2
1% $C_{27}H_{55}OH$ in Brij 30	-10.4	-9.6	-10.7
0.5% $C_{27}H_{55}OH$ in Brij 30	-14.3	-14.5	-13.4
0.05% $C_{27}H_{55}OH$ in Brij 30	-20.8	-19.3	-19.4
Decane	-19.0	-17.9	-21.1
3% $C_{27}H_{55}OH$ in decane	-10.2	-8.8	-6.8
1% $C_{27}H_{55}OH$ in decane	-11.2	-6.6	-9.9
0.5% $C_{27}H_{55}OH$ in decane	-12.0	-11.2	-10.6
0.05% $C_{27}H_{55}OH$ in decane	-12.3	-8.1	-10.6

Table 4.5 Crystallisation temperatures (ΔT) for Brij 30, decane and 1-heptacosanol mixtures absorbed at the planar interface.

4.3.3 1-Heptacosanol Dispersed in Water

The effectiveness of crystalline 1-heptacosanol in water to induce ice nucleation was explored. 1 mg of 1-heptacosanol was weighed and 1 cm^3 UHQ water added. The long chain alcohol was insoluble in water, so samples were vortex mixed for 10 seconds immediately before analysis, to ensure a good mixing of the insoluble alcohol. Two samples were prepared in this way and analysed by DSC.

Each sample was then analysed again after further vortex mixing in order to reduce the particle size of the insoluble alcohol, and ensure it was well mixed within the water.

ΔT after 1st vortex mixing / °C	ΔT after 2nd vortex mixing / °C
-12.6	-10.8
-10.9	-7.7

Table 4.6. DSC data acquired for 1-heptacosanol dispersed in water.

The T_{cryst} data illustrated in table 4.6 show that the addition of solid 1-heptacosanol has increased T_{cryst} initially to -12 to -8 °C in contrast to approximately -20 °C for pure water. In addition, as expected, the ΔT values have decreased after further vortexing, due to a greater number of 1-heptacosanol particles, and hence 1-heptacosanol surface area, upon which heterogeneous ice nucleation can occur. It is interesting to note that the solid 1-heptacosanol is not able to induce ice nucleation at the high temperatures of ~ -1 °C and -5 °C found for the monolayers at the air-water[1] and decane-water interfaces respectively. Presumably, this is because the solid 1-heptacosanol is not able to rearrange to better accommodate the nucleating ice, which the less rigid monolayer is able to do.

4.4 Preliminary Crystallisation in Emulsion Studies

4.4.1 n-Hexadecane Based Emulsions

Preliminary emulsion studies were undertaken with Brij 30 at a mass fraction of 4.8%. 1-Heptacosanol was present at a relatively high mass fraction of 3.4% for all samples, (except for its absence in the control samples) and so the combined mass fraction of oil and water was 91.8%.

Initially, hexadecane was employed as the oil, as this would solidify just below room temperature (~16°C), thus minimising motion and droplet coalescence. It was subsequently realised, however, that the droplets will not necessarily maintain spherical

structure as crystallisation progresses, and rigidity of the sample could not be excluded from the factors inducing ice crystallisation. For this reason, and the instability of emulsions in absence of 1-heptacosanol at oil fraction, F_O = 0.10 and 0.90, n-hexadecane emulsions were not explored any further. The data are presented here, however, as the first demonstration that 1-heptacosanol is a potent nucleator of ice in emulsions.
Both control (no alcohol added) and samples doped with 3.4% (w/w) 1-heptacosanol were prepared by "Method B" at a range of F_O from 0.10 to 0.90. The T_{cryst} values found by DSC are presented in table 4.7.

The instability of samples in the absence of 1-heptacosanol, where F_O = 0.10 and 0.90, indicates a high surface activity of the alcohol. This interfacial activity of the alcohol will be discussed at greater length later in this chapter.

No logical pattern can be discerned with increasing oil fraction, F_O, and repeated measurements would need to be undertaken for any trend to be observable, but the data do demonstrate the ability of 1-heptacosanol to increase the crystallisation temperature of ice from approximately –18 °C for the control sample to approximately -4 to -8 °C with 1-heptacosanol added.

Oil Fraction, F_O	Control ΔT /°C	Doped with 3.4% 1-heptacosanol ΔT /°C
0.10	Not stable	-8.3
0.20	-17.3	-6.1
0.40	-17.3	-4.2
0.60	-20.4	-3.9
0.80	-17.1	-4.6
0.90	Not stable	-3.6

Table 4.7 T_{cryst} (ΔT) values for n-hexadecane based emulsions.

4.4.2 n-Pentanol Based Emulsions

Pentanol based emulsions were explored and prepared by "Method B", as 1-heptacosanol displayed greater solubility in pentanol than in n-alkanes, which it was hoped would ensure a good interfacial concentration. In these samples, the 1-heptacosanol was pre-dissolved in the pentanol, hence the concentrations of 1-heptacosanol quoted with the DSC results in table 4.8 refer to the mass percentage as a concentration in the pentanol fraction only. These samples were prepared at an oil fraction, F_O, of 0.019. The overall concentration of Brij 30 surfactant was 4.7%. These emulsions had a blue/white appearance, indicating a small (approximately 50 – 200 nm) droplet size. The ice crystallisation temperatures once more indicate the potent ability of 1-heptacosanol to nucleate ice.

Wt% 1-heptacosanol in Pentanol	DSC ΔT / °C
2.40%	-8.3
0.75%	-8.5
0.50%	-6.8
0.25%	-11.5
0.075%	-14.8
0.025%	-20.7
0.010%	-19.5

Table 4.8 T_{cryst} data acquired by DSC for pentanol based nanoemulsions doped with various concentrations of 1-heptacosanol.

While nanoemulsions (judged by the translucent appearance) were easily produced and stable, white pentanol emulsions of larger droplet size could not be stabilised for any significant period. Hence further studies on these systems were abandoned and, instead, decane was employed as the oil.

4.4.3 n-Decane Based Emulsion Studies

Initial Studies

Decane based emulsions prepared by "Method B" were stable for many days, and in most cases appear unchanged after many weeks. Samples were analysed in duplicate for $C_{19}H_{39}OH$, $C_{20}H_{41}OH$ and $C_{27}H_{55}OH$, with a constant, relatively high alcohol concentration of 3.4% for all samples. Brij 30 was present at 4.7% by total mass of the emulsion. The total mass of decane and water (O + W) was 91.9%. These samples were analysed in duplicate by DSC only; the T_{cryst} values are displayed in table 4.9.
Many conclusions are derived from the data acquired. Firstly, there are wide variations in the data for equivalent samples. This is due not only to the stochastic nature of nucleation, but also to a lack of sample homogeneity, due to excess amounts of alcohol in many of these systems. Indeed, for most samples, the alcohol sinks to the bottom of the vial, though viscosity of the emulsions delays this process for many hours.

Oil Fraction F_O	No alcohol ΔT		$C_{19}H_{39}OH$ ΔT		$C_{20}H_{41}OH$ ΔT		$C_{27}H_{55}OH$ ΔT	
	Sample #1 / °C	Sample #2 / °C	Sample #1 / °C	Sample #2 / °C	Sample #1 / °C	Sample #2 / °C	Sample #1 / °C	Sample #2 / °C
0.10	-18.6	-17.9	-13.7	-8.9	-8.2	-11.6	-12.2	-13.4
0.20	-19.7	-14.3	-9.3	-11.3	-8.2	-12.8	-9.4	-12.2
0.40	-23.3	-15.9	-6.6	-7.0	-13.8	-13.9	-6.9	-9.1
0.60	-21.5	-15.6	-6.6	-6.5	-7.1	-12.7	-7.9	-11.4
0.80	-19.8	-16.3	-8.6	-8.1	-8.1	-11.9	-6.3	-7.0
0.90	-16.9	-19.5	-7.6	-8.2	-12.7	-6.1	-4.3	-5.0

Table 4.9 DSC (ΔT) data acquired from preliminary decane based emulsions.

The data do demonstrate, though, the more potent ice-nucleating ability of 1-heptacosanol compared to its shorter analogues. The best nucleating ability is where $F_O = 0.90$ for which a ΔT less than -5 °C is recorded in both analyses. It must be noted, though, that samples where $F_O = 0.90$ are very viscous, whereas all other samples are

relatively mobile, even when cooled. This high viscosity cannot be discounted as a factor assisting the nucleation of ice.

The stability of the decane-based emulsions across a wide range of oil fractions indicated that a range of droplet sizes might be possible. The apparent ability of these emulsions to induce crystallisation of ice by solubilised alcohols, without high viscosity, is also useful. These properties led to the system being studied much more extensively to try and understand the effects of interfacial curvature on ice nucleation.

4.5 Physical Characteristics of Brij 30/Water/Decane Emulsions

4.5.1 Droplet Size Indicators for Emulsions and Nanoemulsions

Emulsions without the 1-heptacosanol additive were prepared at various oil fractions, F_O, and analysed on the Malvern Mastersizer to gain an accurate measurement of droplet sizes. Until this stage, the sample colour and optical microscopy were the only indicators of droplet size in the emulsions. As discussed in section 4.2.5, number and surface based droplet size data were preferred to the volume distribution, as these are not skewed by large features such as air bubbles or undissolved long chain alcohol.

Droplet size data determined on the Mastersizer are presented in table 4.10 in terms of number, volume and surface area fractions, with d(x) denoting the droplet diameter value for which a number/volume/surface area fraction, x, of droplets have a smaller value.

Oil Fraction, F_O	Number Fractions			Volume Fractions			Surface Area Fractions		
	d (0.1) / μm	d (0.5) / μm	d (0.9) / μm	d (0.1) / μm	d (0.5) / μm	d (0.9) / μm	d (0.1) / μm	d (0.5) / μm	d (0.9) / μm
0.019	0.035	0.064	0.122	0.076	0.181	1.52	0.053	0.107	0.249
0.40	0.213	0.288	0.425	0.259	0.387	0.626	0.238	0.344	0.519
0.50	1.23	2.14	4.57	2.73	5.51	10.1	1.92	4.16	8.09
0.70	1.07	1.59	3.64	2.39	6.35	12.6	1.47	3.90	9.30
0.78	1.23	1.79	3.15	1.73	3.09	4.93	1.47	2.57	4.36

Table 4.10. Measured droplet diameters for emulsions of various oil fractions, F_O.

These preliminary studies showed that 3 classes of emulsion can be produced with Brij 30 surfactant, for which the number based median, d (0.5) droplet diameters were approximately 64 nm (F_O = 0.019), 300 nm (F_O = 0.40) and 1.9 μm (F_O = 0.50, 0.70 and 0.78).

The nanoemulsions with diameter ~ 67 nm have a blue translucent appearance, due to the predominant Rayleigh scattering that occurs for particles of size much smaller than the wavelength of visible light. The emulsions of diameter ~ 300 nm are technically nanoemulsions, but their larger droplet size gives a white appearance. This group of emulsions will therefore be referred to in this chapter as "white nanoemulsions".

4.5.2 Polarised Optical Microscopy of Different Phases for Brij 30/Water/Decane Emulsions

The decane/water/Brij 30 emulsion system has been studied by Forgiarini et al[22] who reported the multiphase nature of these emulsions. The significant presence of additional phases within conventional emulsions could compromise studies of the effect of interfacial curvature by introducing various curvature material. Compositions that give rise to lamellar liquid crystal (Lα), w/o microemulsion/isotropic region (O_m) and samples

of a bicontinuous or sponge type structure (D') are indicated in the phase diagram published by Forgiarini et al.[22]. A selection of these were prepared and studied by optical microscopy.

As would be expected due to the very small droplet sizes, nothing significant was observed by polarised optical microscopy for w/o microemulsions. Bicontinuous samples also showed the absence of any significant structure.

The compositions of the lamellar Lα samples presented here are given in table 4.11.

Sample	Weight Fraction			Phase Type	Figures
	Water	Brij 30	Decane		
A	0.475	0.48	0.045	Lα	4.6 a & b
B	0.329	0.61	0.061	Lα	4.7 a & b

Table 4.11 Composition of emulsions with significant amounts of lamellar liquid crystalline phase.

The images in figures 4.6 and 4.7 are of lamellar phases viewed through crossed polarisers in the microscope. Sample A (fig. 4.6) shows many birefringence colours, which was typical of samples prepared where the concentration of Brij 30 is approximately 50%, in the presence of significant fractions of water. Much less inherent colour is observed where higher or lower Brij 30 concentration is present for lamellar phase samples. Sample B is a typical example with >60% Brij 30 but no inherent colouring observed.

The ability of Brij 30 to form colourful liquid crystals in mixed water and oil systems is widely reported[17,22]. Borne et al.[28] reported the unusual feature of lamellar crystals to appear spherulitic Very small "spherulitic droplets" (Maltese cross appearance) were observed for Brij 30 in water by optical microscopy and are shown in figure 4.8.

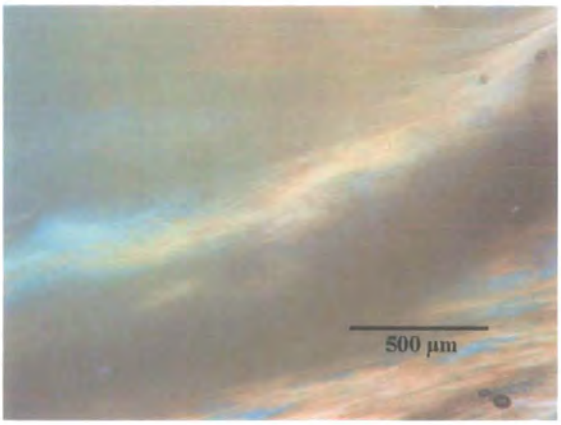

Figure 4.6a Sample A (Lα) viewed with high magnification.

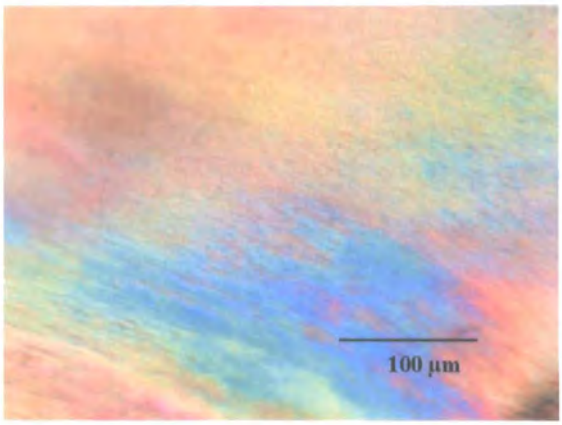

Figure 4.6b Sample A (Lα) viewed with low magnification.

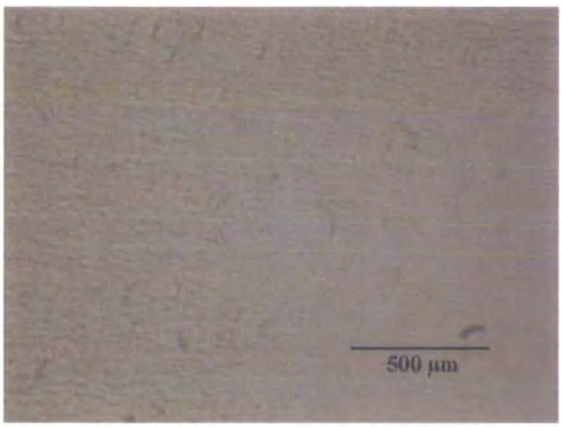

Figure 4.7a Sample A (Lα) viewed with high magnification.

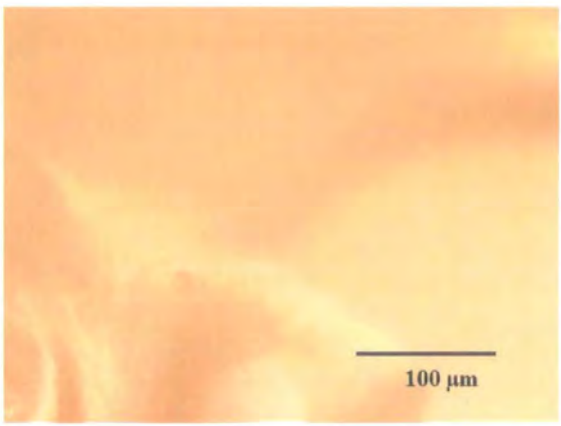

Figure 4.7b Sample A (Lα) viewed with low magnification.

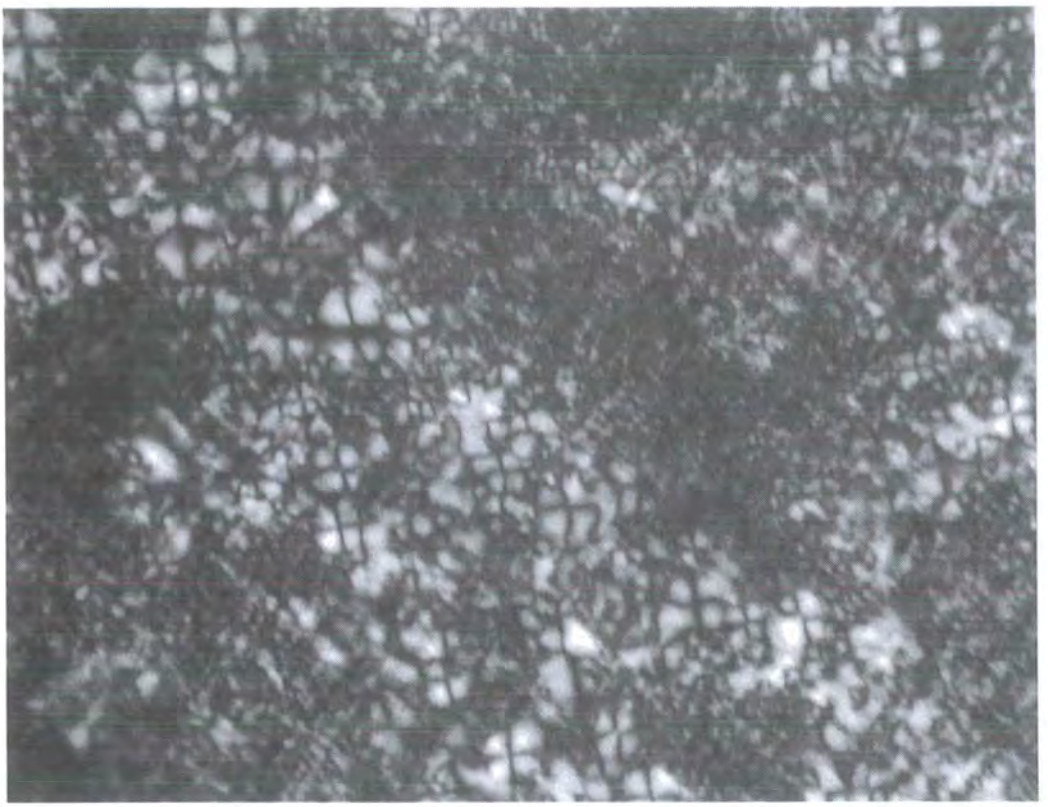

Figure 4.8. An image of liquid crystals in Brij 30 in water viewed with high magnification with crossed polarisers, showing a Maltese cross appearance. Scale 1:300.

4.5.3 *Emulsions with Lamellar Liquid Crystalline Component*

In order to assess the impact of lamellar phases on ice crystallisation, a relatively large amount of 1-heptacosanol (3 wt%) was added to sample A and analysed in triplicate by DSC. The T_{cryst} data are presented in table 4.12 and show that 1-heptacosanol adsorbed at lamellar interfaces is no better able to induce ice nucleation than undissolved 1-heptacosanol dispersed in water.

	T_{cryst} Measured by DSC		
	ΔT #1 / °C	ΔT #2 / °C	ΔT #3 / °C
Sample A	-9.9	-9.3	-11.9

Table 4.12. T_{cryst} values from DSC for 1-heptacosanol added to lamellar samples.

Figures 4.9a and b show samples with oil fraction, $F_O = 0.78$ with a 10% concentration of Brij 30. This sample shows features not dissimilar to the Lα data presented in figure 4.7 and will introduce minor quantities of unwanted planar elements to the sample. Figures 4.10a and b show images of samples prepared at 5% Brij 30 concentration, which shows no evidence for liquid crystalline phases. All studies of interfacial curvature were therefore undertaken at 5% Brij 30 concentration to minimise the presence of lamellar (planar) material.

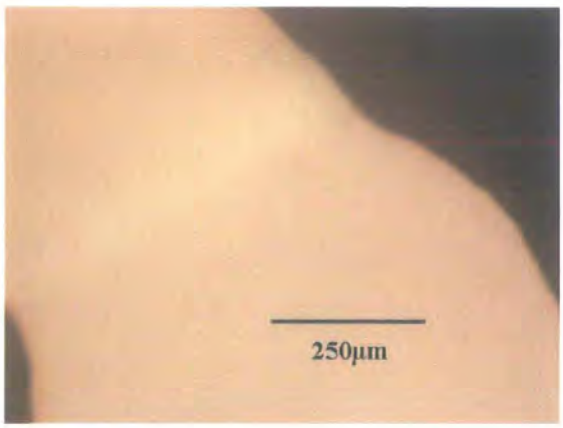

Figure 4.9a Optical micrograph (low magnification) of sample where $F_O = 0.78$ with 10 % Brij 30

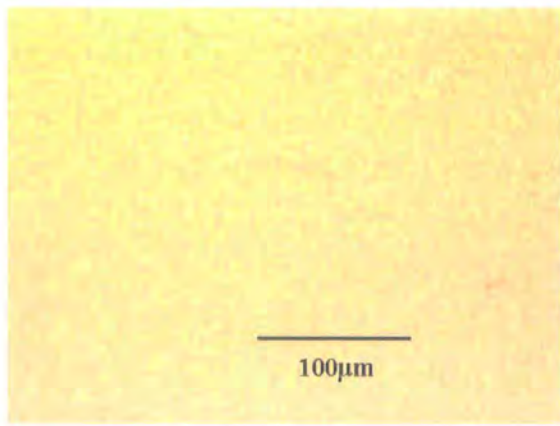

Figure 4.9b Optical micrograph (high magnification) of sample where $F_O = 0.78$ with 10 % Brij 30

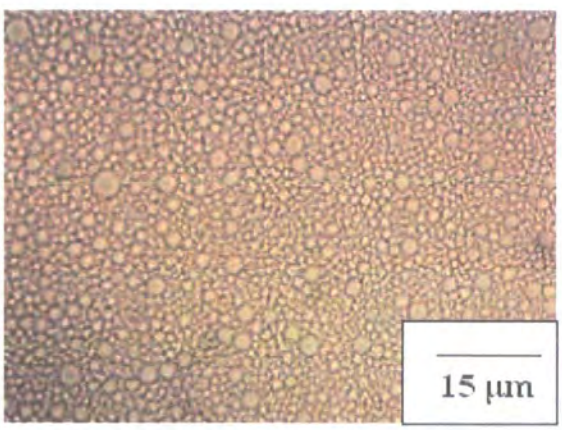

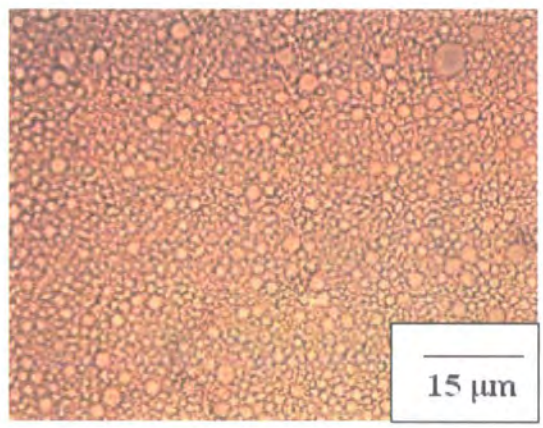

Figure 4.10a & b. Optical micrograph of sample where $F_O = 0.78$ with 5 % Brij 30

4.5.4 Solubility Studies

In order to proceed with a better understanding of the emulsion systems, experiments were undertaken as described in section 4.2.8 to assess the solubility of 1-heptacosanol in emulsions and nanoemulsions.

Yano et al.[10] used this experimental method for colourless microemulsions where it will be relatively accurate. For the coloured nanoemulsions and emulsions described in this chapter, it is difficult to confirm the presence of crystalline material. The solubility data assessed by this method are expected to overestimate the solubility of 1-heptacosanol in emulsions, as the colour of the emulsion will mask the presence of undissolved 1-heptacosanol. Laser diffraction experiments on emulsions with 1-heptacosanol up to this concentration then enabled more accurate solubility assessments.

The solubility of 1-heptacosanol in decane was found to fit the linear relationship (figure 4.11):

$$\ln S = (-10926/T) + 34.161 \qquad \text{[Eqn. 4.3]}$$

where S = weight percentage solubility of 1-heptacosanol in decane at temperature, T (K). Consequently, there is limited solubility of the 1-heptacosanol in decane at temperatures below 0 °C; for instance at -5 °C, the solubility is ~ 0.0012 %.

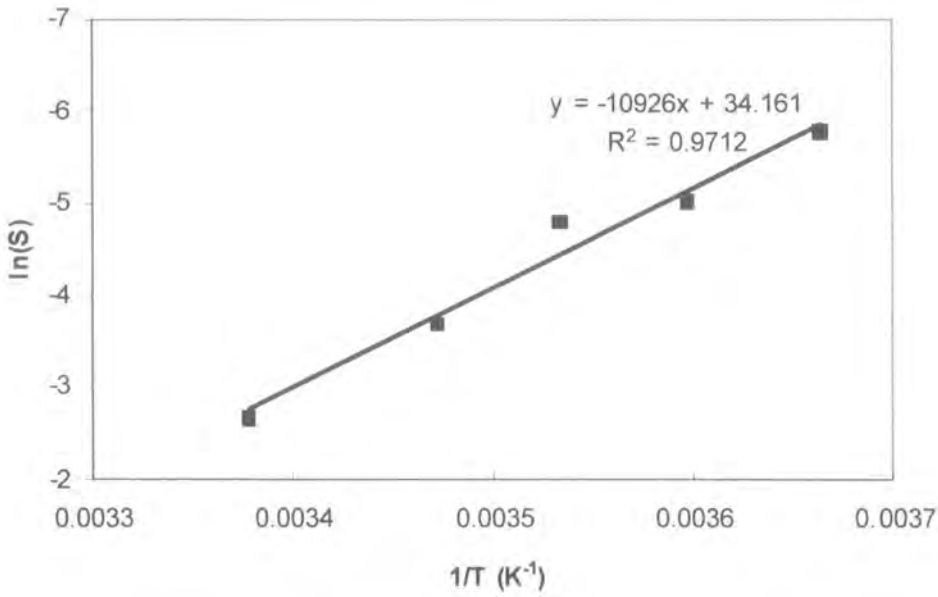

Figure 4.11. Graph indicating the solubility of 1-heptacosanol in decane at different temperatures. At 296 K, S = 0.069%; at 288 K, S = 0.025%, at 283 K, S = 0.0081%, at 278 K, S = 0.0066%, and at 273 K, S = 0.0031%.

Based on this relationship, the solubility of 1-heptacosanol in decane at –10 °C is < 0.001%, i.e. negligible. The solubility of 1-heptacosanol in water at ambient temperature was assessed as lower than 0.0011% by mass, at which point hardly any of the alcohol initially added appeared to have dissolved. The solubility of 1-heptacosanol in water is therefore considered negligible.

By the Yano[10] visual determination method, the ambient solubility of 1-heptacosanol in nanoemulsions and white emulsions was overestimated as 22% and 2%, respectively. Given that 1-heptacosanol is virtually insoluble in decane and water, these data indicate a very high interfacial activity for the alcohol. Hence water/decane emulsions stabilised by 1-heptacosanol only were attempted (see section 4.6.1).

Given the high 1-heptacosanol interfacial activity suggested by the solubility studies, it is useful to consider the 1-heptacosanol percentage coverage, Interface%, at the emulsion interface, using the equation:

$$\text{Interface}\% = \frac{\text{No. of } C_{27}H_{55}OH \text{ molecules at interface} \times A_{C27H55OH}}{A_{emulsion}} \times 100\%$$

[Eqn. 4.4]

which is determined from:

$$\text{Interface}\% = \frac{(W - S)N_A \rho_{decane} A_{C27H55OH} V_{droplet}}{M_W A_{droplet}}$$

[Eqn. 4.5]

and simplified to:

$$\text{Interface}\% = \frac{(W - S)N_A \rho_{decane} A_{C27H5OH} r}{3M_W}$$

[Eqn. 4.6]

where $A_{C27H55OH}$ = area per molecule of a close-packed 1-heptacosanol monolayer, taken as 20 Å^2, $A_{Emulsion}$ = total interfacial area of the emulsion, W = weight percentage of 1-heptacosanol added to the decane, S is the percentage solubility of 1-heptacosanol in decane, N_A = Avogadro constant, ρ_{decane}= density of decane = 730 kg m^{-3}, M_w = molecular weight of 1-heptacosanol = 0.396 kg mol^{-1}, $A_{droplet}$ = interfacial area of a single droplet, $V_{droplet}$ = volume of a single droplet and r = radius of a droplet, taken as the surface area average value determined from the laser diffraction experiments.

Using the solubility values determined by the visual observation method, this gives estimated interfacial coverages of 53% and 135% at ambient temperature for the F_O = 0.019 nanoemulsion and F_O = 0.70 emulsion, respectively which have droplet radii of 33 nm and 950 nm respectively. These values are unrealistically high, showing that more accurate solubility limits needed to be determined by laser diffraction.

4.5.5 Laser Diffraction Experiments to Determine 1-Heptacosanol Emulsion Solubilities and the Effect of 1-Heptacosanol Additive on Droplet Radius

Blue nanoemulsions ($F_O = 0.019$)

The ambient temperature solubility of 1-heptacosanol in the decane fraction of nanoemulsions was assessed optically as 21.5%. This is an over-estimate of the true solubility, as the previous section indicated this would give an unrealistically high interfacial coverage. Therefore nanoemulsions were prepared at this additive concentration and various lower concentrations, in order to determine the effect of 1-heptacosanol on the droplet radius, and a more accurate 1-heptacosanol solubility limit. The resulting number fraction, surface area fraction and volume fraction droplet diameters are listed in table 4.13.

The surface area fraction data for these nanoemulsions consistently show a median surface area droplet radius of ~ 65 nm (average d(0.5) = 129 nm), showing that added 1-heptacosanol does not perturb the droplet size. As stated earlier, the volume fraction data are skewed by the presence of large material; the 0.25% data show evidence for air bubbles, which are not seen for the 3.5% sample. At 4.3% added 1-heptacosanol, the volume fraction d(0.9) is 326 μm, which is evidence for undissolved alcohol additive.

So it can be seen that these droplet size data offer valuable information about the true solubility of 1-heptacosanol. The volume fraction d(0.9) remains >100 μm for concentrations of 1-heptacosanol above 4.3%. All the 1-heptacosanol appears to be dissolved at 3.5%, while the data at 4.3% undoubtedly show large undissolved material, so the true solubility of 1-heptacosanol is between these values. These 1-heptacosanol concentration values correspond to an estimated maximum interfacial coverage of 16 - 20% at ambient temperature.

The ratio of the volume to number average values provides a convenient measure of the polydispersity of the nanoemulsions systems. The 3.5% data provides a volume to number average ratio of 2, which is consistent with the cloudy blue appearance of these

nanoemulsions due to the white light scattering by a smaller number of larger diameter nanoemulsion droplets.

$[C_{27}H_{55}OH]$ in weight% in decane	Number Fractions			Volume Fractions			Surface Area Fractions		
	d (0.1) / μm	d (0.5) / μm	d (0.9) / μm	d(0.1) / μm	d(0.5) / μm	d(0.9) / μm	d(0.1) / μm	d(0.5) / μm	d(0.9) / μm
21.5	0.036	0.067	0.137	0.115	0.704	151	0.059	0.131	0.350
17.2	0.036	0.067	0.137	0.115	0.653	176	0.059	0.133	0.375
12.9	0.035	0.065	0.125	0.085	0.248	143	0.054	0.111	0.260
8.6	0.035	0.064	0.120	0.082	0.245	173	0.052	0.104	0.232
4.3	0.034	0.063	0.117	0.094	7.186	326	0.051	0.102	0.232
3.5	0.038	0.067	0.118	0.069	0.134	0.261	0.055	0.134	0.351
2.7	0.036	0.067	0.140	0.102	0.214	7.00	0.059	0.142	0.396
1.85	0.036	0.066	0.146	0.110	0.271	5.96	0.062	0.164	0.352
1.00	0.036	0.069	0.152	0.115	0.350	2.85	0.064	0.165	0.459
0.50	0.035	0.066	0.132	0.086	0.224	1.80	0.056	0.123	0.305
0.25	0.035	0.067	0.136	0.095	0.277	32.8	0.058	0.129	0.331
0.0	0.035	0.064	0.122	0.076	0.181	1.52	0.053	0.107	0.249
Average up to 3.5% heptacosanol	0.0359	0.0666	0.1351				0.057	0.129	0.324

Table 4.13. Droplet diameters measured for blue nanoemulsions (F_O = 0.019) at various concentrations of 1-heptacosanol.

White Nanoemulsions (F_O = 0.40)

The number fraction, surface area fraction and volume fraction droplet diameters for the white nanoemulsions are listed in table 4.14, and show that added 1-heptacosanol has little effect on the droplet sizes. The surface area data show an average droplet radius value of ~ 0.17 μm, whilst the volume fraction data indicate that this data set is not affected by the presence of air bubbles, and that the 1-heptacosanol solubility lies

between 0.5 and 0.6 % by weight in decane. This corresponds to an estimated maximum interfacial coverage of 5 - 7% at ambient temperature. These white nanoemulsions are relatively monodisperse, since the volume to number average ratio is ~1.2.

[$C_{27}H_{55}OH$]	Number Fractions			Volume Fractions			Surface Area Fractions		
in weight% in decane	d(0.1) / μm	d(0.5) / μm	d(0.9) / μm	d(0.1) / μm	d(0.5) / μm	d(0.9) / μm	d(0.1) / μm	d(0.5) / μm	d(0.9) / μm
0.70	0.179	0.245	0.405	0.320	4.88	201	0.206	0.346	1.05
0.60	0.168	0.235	0.399	0.343	5.28	276	0.200	0.351	1.61
0.50	0.226	0.305	0.488	0.284	0.480	0.969	0.255	0.394	0.711
0.40	0.206	0.284	0.427	0.255	0.387	0.596	0.233	0.345	0.525
0.30	0.219	0.293	0.463	0.268	0.438	0.776	0.243	0.371	0.630
0.20	0.199	0.265	0.357	0.231	0.313	0.414	0.218	0.296	0.394
0.10	0.220	0.290	0.390	0.252	0.339	0.446	0.242	0.322	0.430
0.05	0.225	0.294	0.396	0.259	0.348	0.476	0.246	0.327	0.442
0.00	0.213	0.288	0.425	0.259	0.387	0.626	0.238	0.344	0.519
Average up to 0.5% heptacosanol	0.206	0.278	0.417				0.239	0.343	0.522

Table 4.14. Droplet diameters measured for white nanoemulsions (F_O = 0.40) at various concentrations of 1-heptacosanol.

Emulsions (F_O = 0.70)

Table 4.15 shows the number fraction, surface area fraction and volume fraction droplet diameters for emulsions (F_O = 0.70) at a range of 1-heptacosanol concentrations in decane from 2% (solubility limit as assessed optically) to 0%. The number fraction data indicate that 1-heptacosanol weight percentages in decane in excess of 0.10% perturb the emulsion structure, leading to an average droplet radius similar to that for the white nanoemulsions (F_O = 0.40) for 1-heptacosanol values above 0.3%. As a consequence of this, 1-heptacosanol concentrations above 0.10% were not included in subsequent ice

nucleation studies. From the volume fraction data, the 1-heptacosanol solubility is between 0.5 and 1.0%, giving an estimated maximum interfacial coverage of 5 - 11% for the smaller droplet diameter of 0.24 μm. In comparison, at 0.1% 1-heptacosanol concentrations, where the number average diameter = 1.9 μm, the estimated interfacial coverage is 4% at ambient temperature. Assuming that the consistency of the volume fraction data for emulsions with <0.2 % 1-heptacosanol means the data are little affected by the presence of air bubbles, then the volume to number average ratio of ~2.5 - 3 shows that these emulsions are more polydisperse than the nanoemulsions.

$[C_{27}H_{55}OH]$ in weight% in decane	Number Fractions			Volume Fractions			Surface Area Fractions		
	d(0.1) / μm	d(0.5) / μm	d(0.9) / μm	d(0.1) / μm	d(0.5) / μm	d(0.9) / μm	d(0.1) / μm	d(0.5) / μm	d(0.9) / μm
2.00	0.227	0.285	0.371	0.312	6.40	244	0.245	0.320	1.72
1.50	0.182	0.243	0.368	0.342	3.46	169	0.210	0.346	3.23
1.00	0.194	0.254	0.370	0.356	103	202	0.216	0.319	2.66
0.50	0.169	0.232	0.352	0.340	5.41	15.5	0.198	0.320	4.28
0.40	0.151	0.210	0.332	0.348	5.36	11.8	0.181	0.313	4.65
0.30	1.02	1.35	5.52	5.57	11.1	20.6	1.69	7.90	16.1
0.20	0.938	1.32	2.45	1.34	2.67	4.75	1.11	2.05	3.93
0.10	1.25	2.22	4.65	2.77	5.50	9.98	1.56	3.806	7.44
0.08	1.11	1.75	4.02	2.46	5.49	10.3	1.55	3.66	7.85
0.06	1.07	1.76	3.99	2.44	5.39	10.1	1.38	3.28	6.58
0.04	1.11	1.77	3.99	4.42	5.33	10.0	1.21	2.47	5.14
0.02	1.20	1.94	4.33	2.61	5.64	10.6	1.71	4.08	8.20
0.00	1.23	2.15	4.57	2.73	5.51	10.1	0.212	1.14	7.07
Mean Up to 0.1%	1.161	1.931	4.259				1.27	3.07	7.05

Table 4.15. Droplet diameters for emulsions where F_O = 0.70, at various concentrations of 1-heptacosanol in decane.

4.5.6 Interfacial 1-Heptacosanol Density

The laser diffraction experiments show that the addition of 1-heptacosanol does not alter the droplet size of the blue and white nanoemulsions, and for the emulsions, no/little effect was observed up to 1-heptacosanol weight percentages of 0.10%. The number average and surface area average droplet radii for these different systems are listed in table 4.16, together with the estimated maximum interfacial 1-heptacosanol coverage achievable for these systems at ambient temperature. All the emulsions and nanoemulsions appeared stable upon cooling, and there was no evidence for any large change in droplet sizes, when viewed through the microscope. However, some small perturbation from the ambient temperature values obtained cannot be ruled out.

	Blue Nanoemulsions	White Nanoemulsions	Emulsions
Oil Fraction, F_O	0.019	0.40	0.70
Brij 30 Fraction	0.049	0.049	0.049
Number Average Droplet Diameter / nm	67	280	1900
Surface Area Average (up to the solubility limit) / nm	130	340	3100
Estimated Maximum Interfacial 1-Heptacosanol Coverage at Ambient Temperature.	16 - 20	5 - 7	4
Weight % of 1-Heptacosanol in Decane Required for Maximum Interfacial Coverage	3.5 - 4.3	0.5 - 0.6	0.10

Table 4.16. Summary of the properties of Brij 30 and added 1-heptacosanol o/w nanoemulsions and emulsions.

The enhanced solubility of 1-heptacosanol in emulsions and nanoemulsions indicate a high interfacial activity for the 1-heptacosanol, so that ~ 4 – 20 % of the interfacial region can be covered by 1-heptacosanol at ambient temperatures. This is further shown

by the fact that 1-heptacosanol can stabilise decane/water emulsions in the absence of surfactant for many hours. These 1-heptacosanol-stabilised emulsions are sufficiently stable for immediate ice crystallisation studies, as discussed in section 4.6.1.

4.6 Ice Crystallisation Temperatures

4.6.1 Emulsions in Absence of Brij 30 Surfactant

Emulsions generated without Brij 30 surfactant were prepared by predissolving 1-heptacosanol in decane by heating, then adding water. These mixtures were vortexed for approximately 30 seconds each.

Two emulsions were successfully made and remained stable for many hours. These were at oil fraction, F_O, of 0.091 and 0.25. Samples made at oil fractions of 0.50 and 0.75 were not stable. Both samples contained 0.34% heptacosanol in decane, and gave ΔT values of -7.6 °C (F_O = 0.091) and -7.4 °C (F_O = 0.25)

The droplet diameters measured for these samples are illustrated in table 4.17.

F_O	Number Fractions			Volume Fractions			Surface Area Fractions		
	d(0.1) / μm	*d*(0.5) / μm	*d*(0.9) / μm	*d*(0.1) / μm	*d*(0.5) / μm	*d*(0.9) / μm	*d*(0.1) / μm	*d*(0.5) / μm	*d*(0.9) / μm
0.25	0.808	1.14	1.87	1.07	1.95	5.02	0.947	1.54	3.11
0.091	0.715	1.47	1.93	1.19	2.14	5.62	0.854	1.48	3.95

Table 4.17. Droplet size data for emulsions successfully stabilised with 1-heptacosanol in the absence of Brij 30 surfactant.

This success in generating samples with 1-heptacosanol as surfactant, demonstrates further the high interfacial activity for this long chain alcohol.

4.6.2 Nanoemulsions, Diameter ~ 67 nm

Crystallisation temperatures for decane based nanoemulsions were assessed mainly at 1-heptacosanol concentrations up to and including the solubility limit (4.3%), although studies were also conducted at much higher heptacosanol concentrations to verify the effect of solid heptacosanol on the T_{cryst} values. The concentration of Brij 30 was 4.9% by mass and oil fraction, F_O, was 0.019. The droplet size data presented earlier indicate that these blue samples have a median number droplet diameter in the order of 67 nm. These samples were prepared by "Method B" and the 1-heptacosanol was pre-dissolved in the decane by heating.

Optical microscopy data were initially assessed using hydrophobised glass coverslips. Table 4.18 presents data acquired using hydrophobic and standard coverslips.

The data acquired using hydrophobic slides was not considered enhanced at all, however. The borosilicate glass slides used for "standard" microscopy measurements were already relatively hydrophobic when compared to standard glass coverslips. The hydrophobising procedure succeeded in giving water droplets with a higher contact angle than for standard coverslips, but the roughness and unevenness introduced by the method potentially introduces sites for heterogeneous nucleation and often led to poorly reproducible results. Borosilicate glass coverslips were considered sufficiently inert given that UHQ water was observed to crystallise at -20 to -18 °C, hence the use of hydrophobised slides was abandoned. The data presented in figure 4.12 are from standard untreated glass coverslips.

[$C_{27}H_{55}OH$] in Decane	Microscopy Hydrophobised Coverslip T_{cryst} / °C	Microscopy Normal Coverslip T_{cryst} / °C
21.5%	-10.6	-12.4
17.2%	-12.0	-9.7
12.9%	-17.3	-14.7
8.6%	-12.6	-14.6
4.3%	-7.8	-14.7
0.00%	-12.3	-19.0

Table 4.18 T_{cryst} data acquired for nanoemulsions using hydrophobised glass coverslips and unmodified borosilicate coverslips.

The crystallisation temperatures for the nanoemulsions as assessed by DSC and optical microscopy are presented in figure 4.12. DSC data were acquired in triplicate, and microscopy data in duplicate. Samples were re-prepared on each occasion from the same batch.

As illustrated in figure 4.12, the T_{cryst} values for a particular system once more show variation due to the stochastic nature of nucleation. The following trends, though, are readily apparent. In the absence of 1-heptacosanol, the crystallisation temperature is -18 to -15.4 °C, which is consistent with weak non-specific nucleators. As the heptacosanol concentration is increased from 0.5 to 2.7 %, there is a significant increase in crystallisation temperature, at which point the value plateaus, giving an average T_{cryst} of approximately -13 °C for the DSC data, although some individual DSC values were as high as -11.2 °C. Above the solubility limit of 4.3%, crystallisation temperatures of -9.7 to -12.4 °C were found, which were consistent with solid 1-heptacosanol being present. So, since the T_{cryst} values are typically lower than the values for the planar Brij 30 + 1% 1-heptacosanol on water system (section 4.3.2), this shows that the 1-heptacosanol adsorption at the planar nitrogen/water interface is very limited in comparison with the Brij 30. Indeed even at much higher 1-heptacosanol concentrations up to 21%, well above its solubility limit, T_{cryst} values were ~ -10 °C, i.e. typical of the values expected

for ice nucleation induced by solid 1-heptacosanol or weak 1-heptacosanol adsorption at the nitrogen-water planar interface; the higher values of -5 to -7 °C attributable to significant adsorption of 1-heptacosanol at the nitrogen-water planar interface (section 4.3.2) were never attained.

Assuming T_{cryst} is at -12 °C, this corresponds to interfacial coverage of 9 - 21 % for the emulsions with 1.8 to 4.3 wt% 1-heptacosanol, assuming the droplet sizes remain unchanged on cooling (which appeared to be the case when viewed through the microscope), and the 1-heptacosanol solubility in decane is given by equation 4.3.

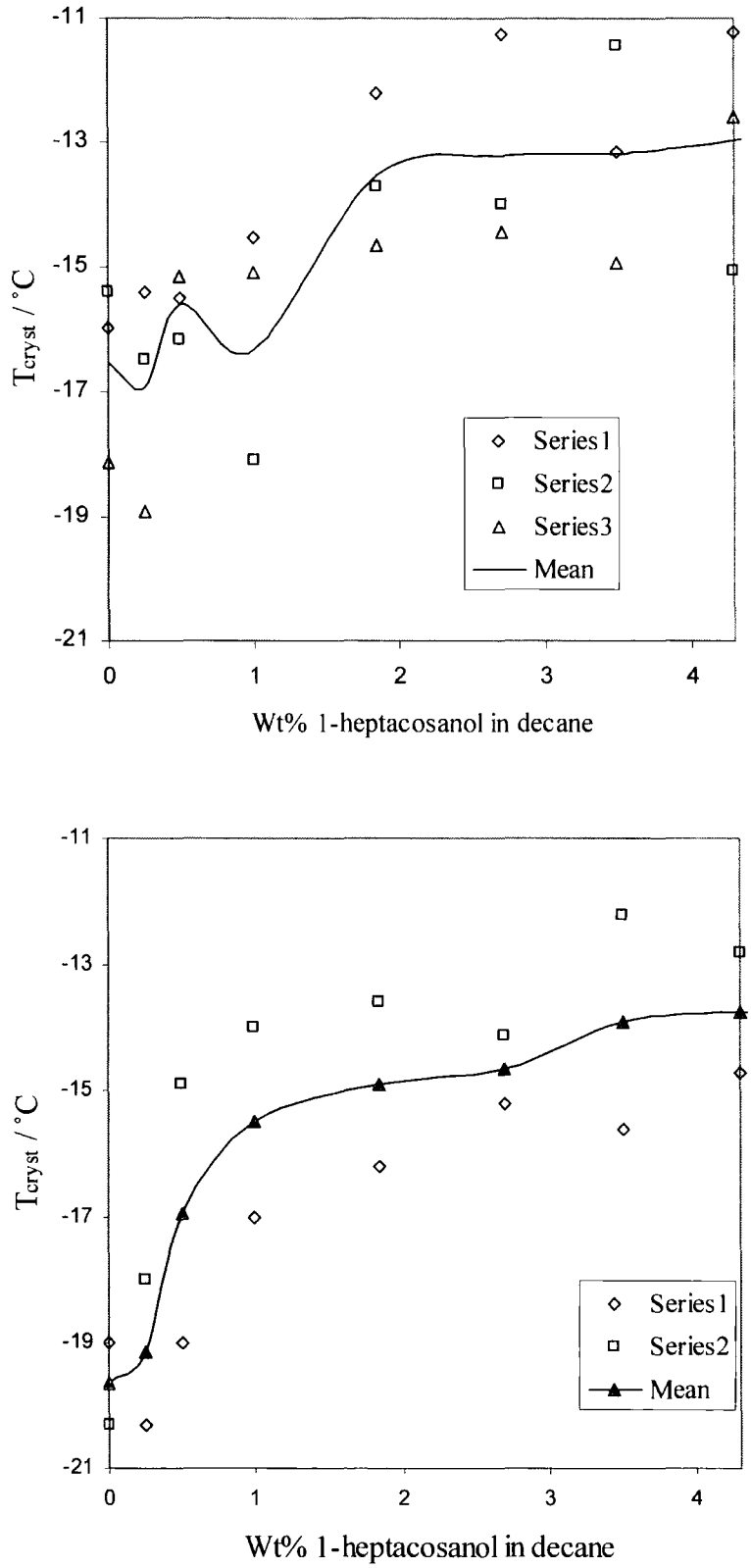

Figure 4.12. T_{cryst} as assessed by DSC (top) and microscopy (bottom) for nanoemulsions (d ~ 67 nm) at various concentrations of 1-heptacosanol.

4.6.3 White Nanoemulsions

Following the results that showed emulsions of droplet size of 300 nm is possible at F_O = 0.40, samples were prepared at F_O = 0.40 by "Method B" with various concentrations of 1-heptacosanol. The 1-heptacosanol concentration range was chosen to give an approximate equivalent additive density at the interface as for emulsions of droplet size in the micrometer range. T_{cryst} values of these samples were assessed in triplicate by DSC and in duplicate by microscopy. The results are presented in figure 4.13.
As observed for the blue nanoemulsions and emulsions, these samples show a crystallisation temperature consistent with weak nucleators, in the absence of 1-heptacosanol. The DSC and optical microscopy data show similar trends, with the T_{cryst} values tending to plateau at 1-heptacosanol concentrations of approximately 0.20%. The combined data consistently show the highest T_{cryst} at approximately -8 °C at heptacosanol concentrations between 0.20 and 0.50%. This corresponds to an interfacial coverage of approximately 3 - 6% at these temperatures assuming the droplet sizes remain unchanged on cooling (which appeared to be the case when viewed through the microscope), and the 1-heptacosanol solubility in decane is given by equation 4.3.

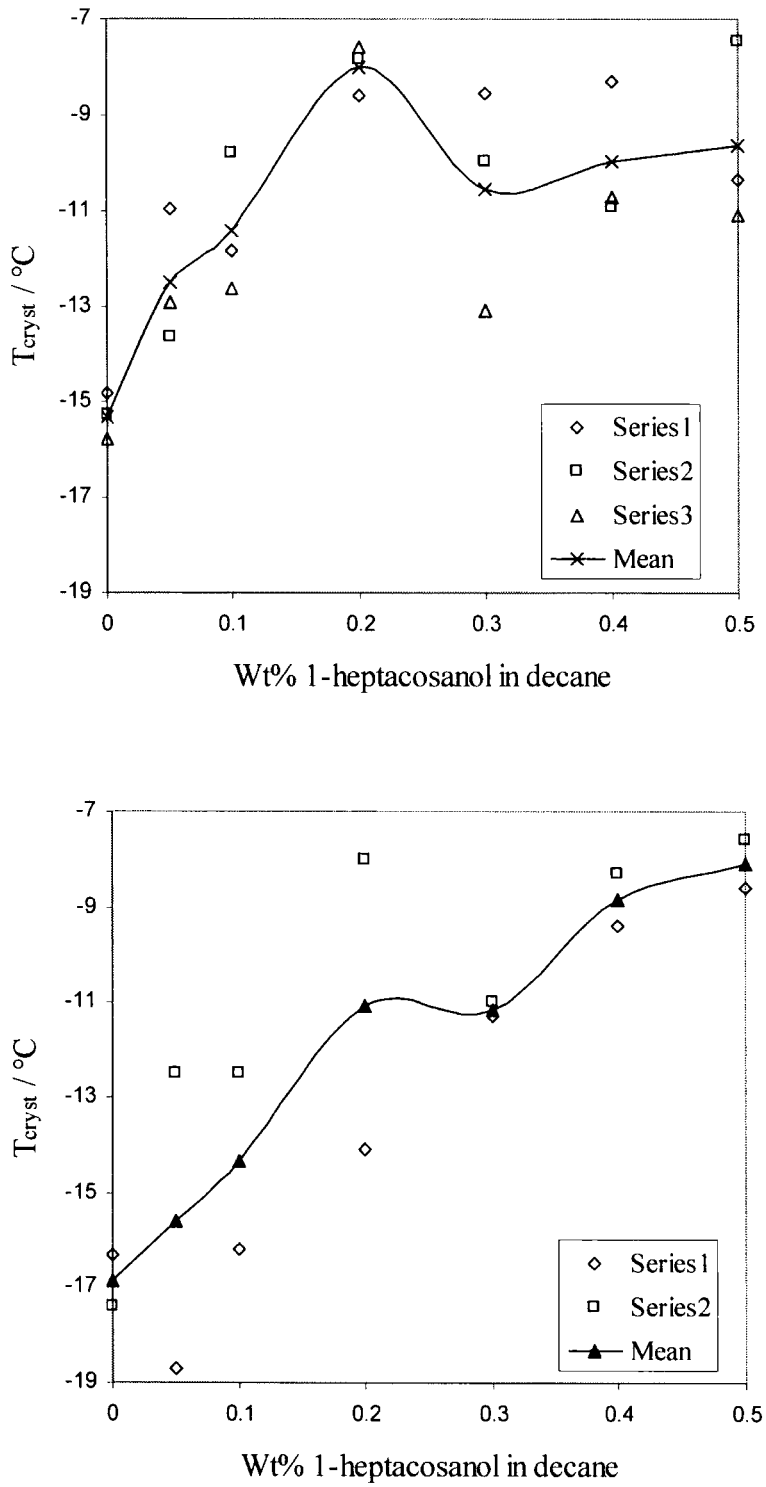

Figure 4.13. T_{cryst} as assessed by DSC (top), optical microscopy and XRD (bottom) for white nanoemulsions (d ~ 300 nm) at various concentrations of 1-heptacosanol.

4.6.4 Emulsions, Diameter ~ 1.9 μm

The droplet size data presented earlier indicate that for emulsions where F_O = 0.50, 0.70 or 0.78, a median number based droplet diameter of approximately 1.9 μm is expected at low concentrations of 1-heptacosanol. Emulsions were prepared at 1-heptacosanol concentrations in decane up to 0.10%, as above this range the droplet diameters were perturbed.

Figures 4.14, 4.15 and 4.16 present crystallisation temperatures as assessed by DSC and optical microscopy for emulsions of oil fraction, F_O = 0.70, 0.78 and 0.50 respectively.

All three systems show a highest mean T_{cryst} value in the order of approximately -8 °C, with some individual values as high as ~ - 5.5 °C. There is more scatter in these data sets than for the smaller droplet systems. Along with the usual variation expected for nucleation studies, there could be further scatter due to sample homogeneity within the samples, or perhaps due to time elapsed, as some samples were approximately one month old when all the analyses were completed.

In the absence of 1-heptacosanol, all systems show a value for T_{cryst} consistent with weak, non-specific nucleators. As expected, higher values for T_{cryst} are found with increasing concentrations of 1-heptacosanol, with the most effective concentration being between 0.06 and 0.10%. This corresponds to interfacial coverages of approximately 7 - 11% at these temperatures, assuming the droplet sizes remain unchanged on cooling (which appeared to be the case when viewed through the microscope), and the 1-heptacosanol solubility in decane is given by equation 4.3.

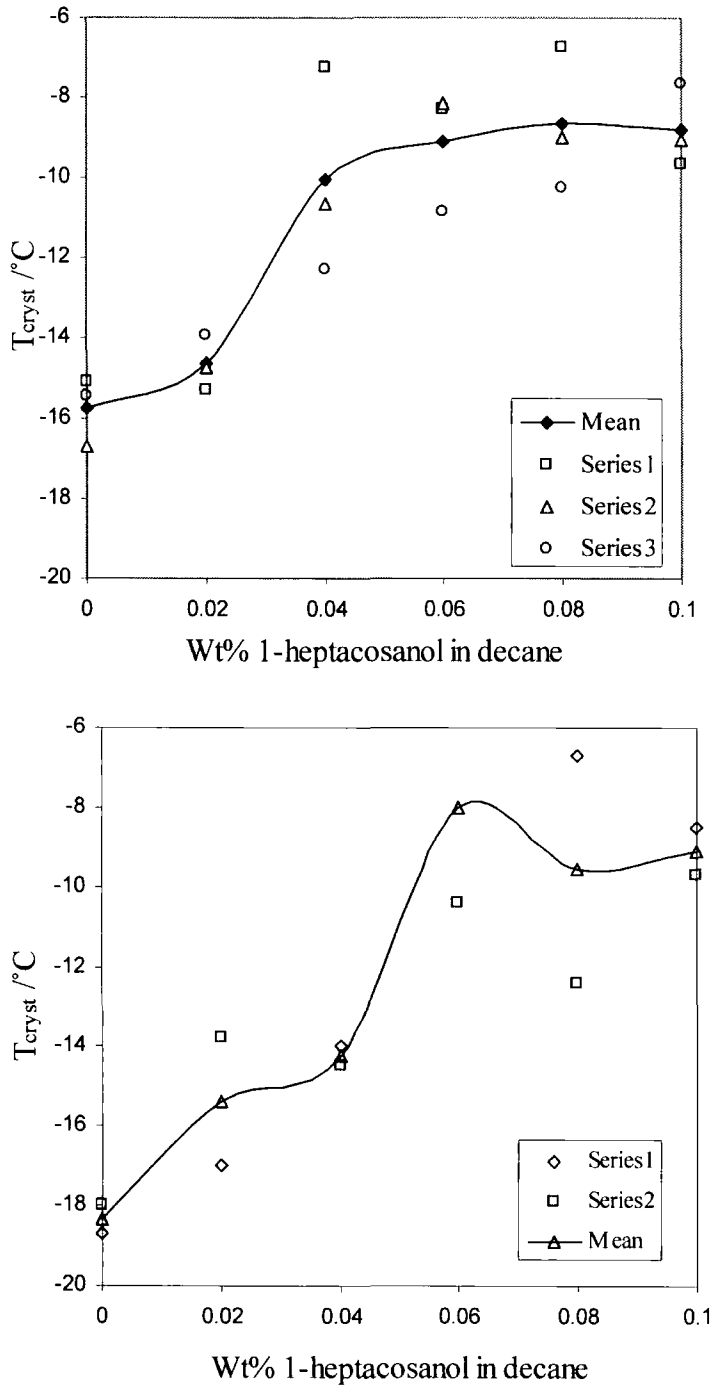

Figure 4.14. T_{cryst} as assessed by DSC (top) and microscopy (bottom) for F_O = 0.70 emulsions at various concentrations of 1-heptacosanol.

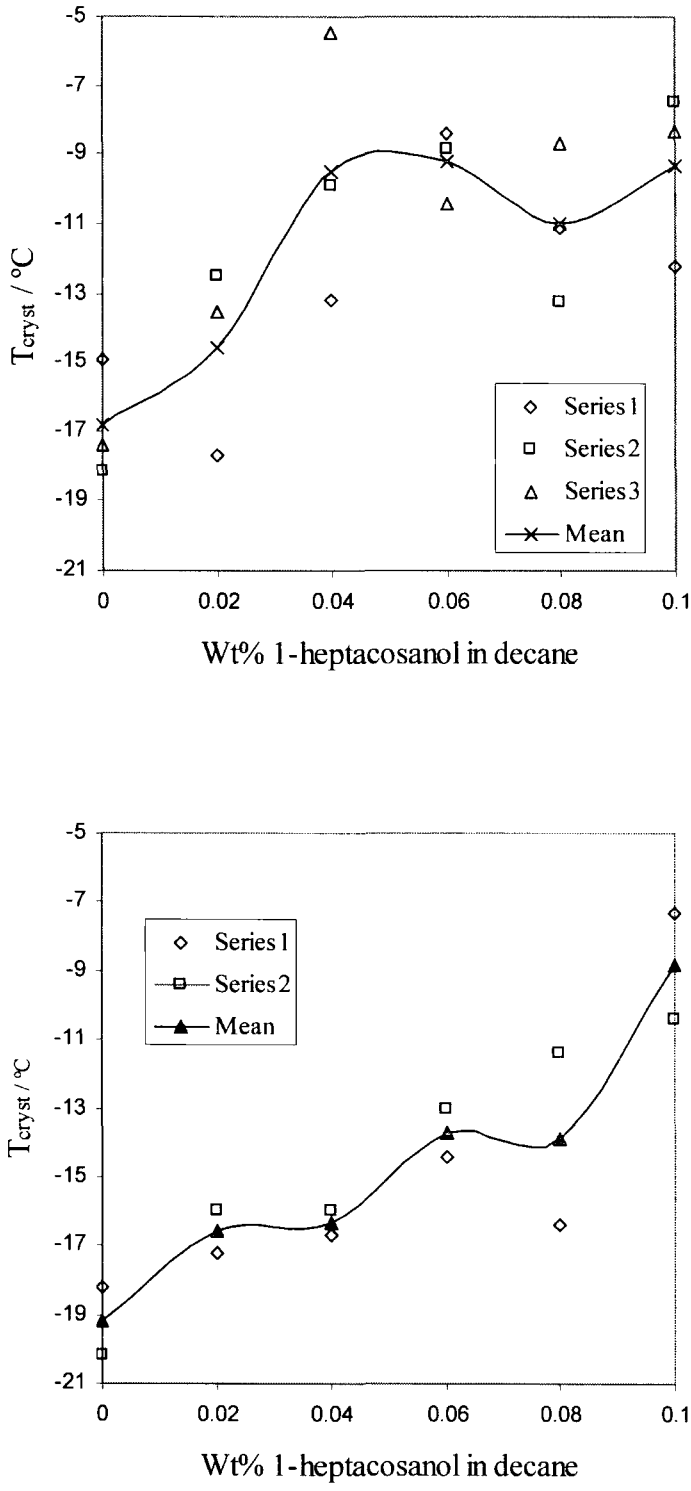

Figure 4.15. T_{cryst} as assessed by DSC (top) and microscopy (bottom) for $F_O = 0.78$ emulsions at various concentrations of 1-heptacosanol.

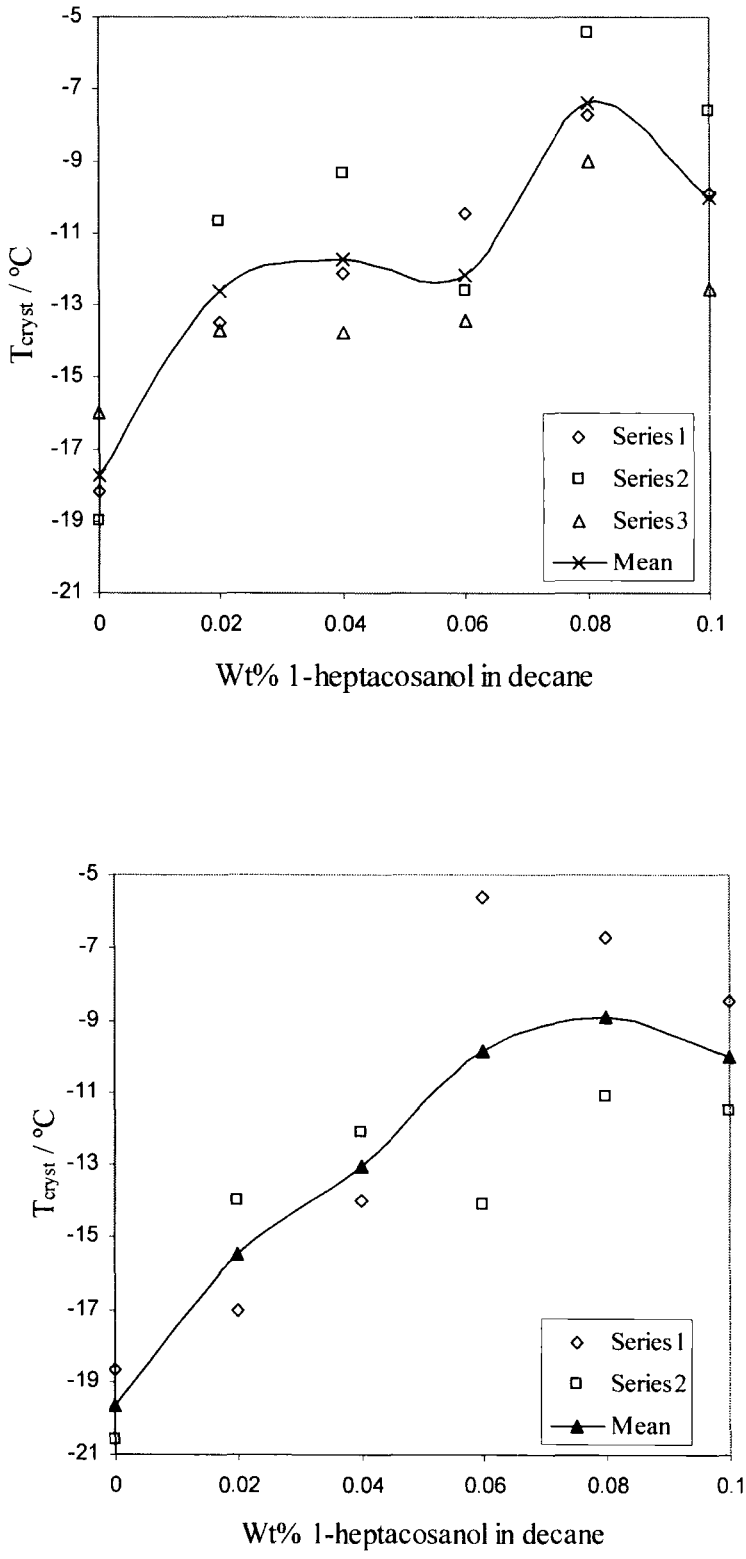

Figure 4.16. T_{cryst} as assessed by DSC (top), microscopy and XRD (bottom) for F_O = 0.50 emulsions at various concentrations of 1-heptacosanol.

4.7 Discussion

The T_{cryst} data illustrated for nanoemulsions, white nanoemulsions and emulsions show a great deal of scatter due to the stochastic nature of nucleation. The similarity in data acquired between DSC and optical microscopy, however, increase confidence that the patterns observed are genuine. The DSC data were acquired in triplicate and the optical microscopy data in duplicate. The latter of these showed no discernable evidence for additional phases, such as lamellar liquid crystals; the samples studied are principally oil droplets in water and maintain this structure on cooling to the crystallisation temperature.

There might be some small change in droplet size on cooling, but no evidence for this was observed for the emulsions when viewed through a microscope. The nanoemulsions when cooled in a waterbath show no bulk change, and maintain the blue translucent appearance, which is indicative of a small (<100 nm) droplet size.

All the data show that heptacosanol is an effective nucleator of ice, which is able to raise very significantly the crystallisation temperature from approximately -18 °C for the case of non-specific heterogeneous nucleation for both planar and curved interfaces in emulsions.

With comparable amounts of interfacially adsorbed 1-heptacosanol, high curvature, blue nanoemulsion systems are significantly poorer ice nucleators than the white nanoemulsion and emulsion systems. The highest T_{cryst} values obtained for the blue nanoemulsion systems were typically ~ -13 to -15 °C, with a few values as high as -11 °C. In comparison, T_{cryst} values of ~ -8 °C were typically obtained for the low curvature emulsions and white nanoemulsions, with a few values as high as -5 °C. Consequently, a difference of at least 3 °C is observed, and this value in fact could be considered as high as 6 °C.

The poorer nucleating ability of the nanoemulsions is clearly seen in figure 4.17, which shows the average DSC crystallisation temperatures compared to the estimated interfacial 1-heptacosanol coverage at T_{cryst} for the 3 curvature systems studied in this chapter.

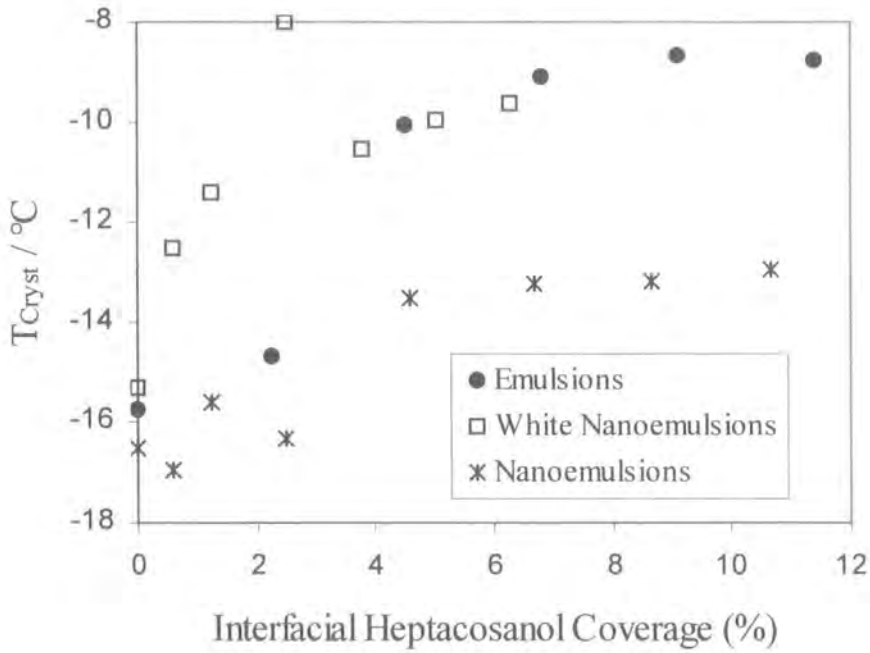

Figure 4.17. Mean values of T_{cryst}, as assessed by DSC, plotted against calculated interfacial 1-heptacosanol coverage.

Figure 4.17 shows that 1-heptacosanol is an effective ice nucleator at low (< 10%) interfacial coverage. This suggests that the 1-heptacosanol molecules are forming close-packed islands at the interface, with a lattice structure presumably similar to that of the (001) plane of hexagonal ice, as was found by Popovitz-Biro et al. in the air-water interface studies[1]. It is unlikely that the 1-heptacosanol molecules form permanently close-packed islands at the decane-water interface since the van der Waals interactions between 1-heptacosanol molecules will be similar to those between 1-heptacosanol and decane/Brij 30 molecules. This will result in a reduced drive for close-packed island formation at the decane-water interface, compared to the air-water interface. So, the ability of 1-heptacosanol to promote ice nucleation at low interfacial concentrations might be aided by a synergic interaction between the 1-heptacosanol and water molecules. This would occur where pre-critical nuclei of ice adsorb onto a few

1-heptacosanol molecules at the interface, causing impinging 1-heptacosanol molecules to adopt a close-packed structure akin to ice because the increased ice nuclei-heptacosanol interactions will lower the energy of the system. This will promote further growth of the ice nuclei to critical nuclei sizes and above, causing ice crystallisation. Similar synergic interactions have been suggested to explain nucleation promotion at low additive concentrations in other systems[29-31]. The pre-critical nuclei of ice exist, albeit transiently, in increasing concentrations below the ice melting temperature of 0 °C, and can be adsorbed at the interface either by singly adsorbed molecules aggregating together, or by impingement of clusters from the droplet exterior onto the interface, as suggested by Davey et al.[9]

Assuming the mechanism outlined above occurs, then the ability of 1-heptacosanol to nucleate ice would depend upon the following factors:

1. The frequency of 1-heptacosanol molecule impingement upon the pre-critical ice nuclei and their residency times. Hence this would increase with 1-heptacosanol interfacial concentrations, but would not prevent low concentrations from exhibiting a marked nucleation promotion effect.

2. The ability of the 1-heptacosanol headgroups to adopt a structure similar to ice. This ability has been shown for a planar interface, but is likely to be compromised by increasing interfacial curvature.

3. The size of the critical ice nuclei, which will change not only with the temperature of the system, but also, if classical nucleation theory is obeyed, with the interfacial curvature of the system.

The impingement rate and residency time would be affected by the viscosity of the system and differences in the dynamical freedom of the interfacial molecules in the nanoemulsion and emulsion systems. The blue nanoemulsions are slightly less viscous than the white nanoemulsions, which in turn are slightly less viscous than the R = 0.50 and R = 0.70 emulsions. Viscosity may be having an effect on these systems, however, the R = 0.78 emulsion is noticeably more viscous than the R = 0.50 and R = 0.70

emulsions and yet they have similar ice-nucleating abilities. Consequently, at present there is no systematic evidence that the viscosity or differences in interfacial dynamics are dominant factors in these systems. The next section proposes that the reduced nucleating ability of the blue nanoemulsions arises primarily due to the increased interfacial curvature of this system causing not only a slightly larger critical nucleus size, but also a reduction in the ability of 1-heptacosanol molecules to adopt a structure similar to that of hexagonal ice.

4.7.1 Calculation of T_{cryst} Using Classical Nucleation Theory

The theory detailed below and the calculated T_{cryst} values are based on the work of my supervisor, Dr. S.J. Cooper.

Recall from chapter 1, that the equation for the formation of a critical nucleus is:

$$\Delta G^*_{Het} = \frac{16\pi\gamma^3 v_c^2}{3\Delta\mu^2} f(\theta_p) = \Delta G^*_{Hom} f(\theta_p) \qquad \text{[Eqn. 1.22]}$$

where ΔG^*_{Het} and ΔG^*_{Hom} are the Gibbs free energy barrier to formation of a critical nucleus for the heterogeneous and homogeneous nucleation cases, respectively, $\Delta\mu$ is the supersaturation, γ is interfacial tension and v_c is the molecular volume. θ_p is the contact angle (see figure 4.18) and:

$$f(\theta) = \frac{2 - 3\cos\theta + \cos^3\theta}{4} \qquad \text{[Eqn. 1.20]}$$

ΔG^*_{Het} is related to the corresponding homogeneous and heterogeneous critical nuclei volumes, V^*_{Hom} and V^*_{Het} by:

$$\Delta G^*_{Het} = \Delta G^*_{Hom} V^*_{Het} / V^*_{Hom} = \Delta G^*_{Hom} f(\theta_p) \qquad \text{[Eqn. 1.22]}$$

For a spherical nucleus:

$$\Delta G^*_{Hom} = \frac{16\pi\gamma_{lx}^{\ 3} v_c^{\ 2} T_{cryst}^{\ 2}}{3\Delta H_{melt}^{\ 2} \Delta T^2} \qquad \text{[Eqn. 4.7]}$$

where γ_{lx} is the liquid-nucleus interfacial tension.

4.7.2 Extension of Classical Heterogeneous Nucleation Theory to Account for Interfacial Curvature

The classical nucleation theory outlined above can be applied to curved interfaces as follows. The nucleation rate, *J*, is given by:

$$J = \Omega \exp\left(\frac{-\Delta G^*}{k_B T}\right) \qquad \text{[Eqn. 1.16]}$$

Hence the nucleation rate, J, increases as the critical nucleus size decreases. A larger critical nucleus occurs on the spherical, convex curvature surface of radius, r_{subst}, present in an o/w emulsion than on the analogous planar surface, see figure 4.18. In particular, the critical nucleus volume on the planar surface $V_{HetPlanar}$ (represented by the light grey shaded area) is equal to:

$$V_{HetPlanar} = \frac{4\pi r^{*}_{nuc}{}^3}{3} f(\theta_p) \qquad \text{[Eqn. 4.8]}$$

The critical nucleus volume $V_{HetSphere}$ on the spherical surface is represented by the light and darker grey shaded areas and is equal to:

$$V_{HetSphere} = \left[\frac{4\pi r^{*}_{nuc}{}^3 f(\theta_{s1})}{3}\right] - \left[\frac{4\pi r_{subst}{}^3 f(\theta_{s2})}{3}\right] \qquad \text{[Eqn. 4.9]}$$

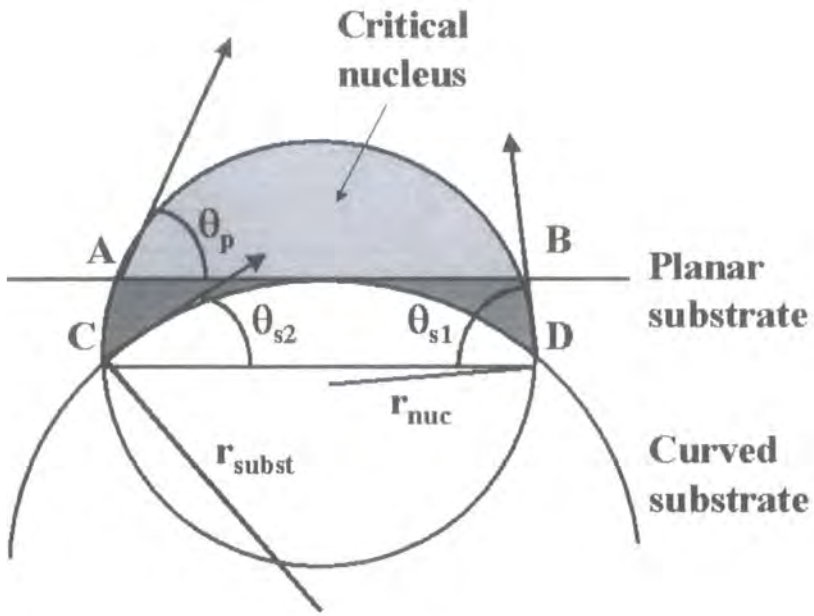

Figure 4.18. Diagram illustrating nucleation of a critical nucleus (of radius r^*_{nuc}) on a convex substrate (of radius r_{subst}). Angles pertinent to the calculations in this section are also illustrated.

So, for a spherically curved interface, the Gibbs free energy of formation, $\Delta G^*_{\text{Het Sphere}}$ of the critical nucleus, is

$$\Delta G^*_{\text{Het Sphere}} = \Delta G^*_{Hom}[f(\theta_{s1}) - (r_{subst}{}^3 f(\theta_{s2})/r^*_{nuc}{}^3)]$$

$$= [f(\theta_{s1}) - (r_{subst}{}^3 f(\theta_{s2})/r^*_{nuc}{}^3)](16\pi\gamma_{lx}{}^3 v_c{}^2 T_{cryst}{}^2)/3(\Delta H_{melt}\Delta T)^2$$

[Eqn. 4.10]

The ratio of the nucleation rates $J_{\text{Het Plane}}$ and $J_{\text{Het Sphere}}$ on planar and spherical substrates, respectively becomes:

$$= \frac{(1-\cos\theta_p)}{(1-\cos\theta_{s1})} \exp\left[\frac{\Delta G^*_{Hom}[f(\theta_{s1}) - \{f(\theta_{s2}) r_{subst}{}^3/r^*_{nuc}{}^3\} - f(\theta_p)]}{kT}\right]$$

[Eqn. 4.11]

The pre-exponential factor is equal to the surface area ratio of the critical nuclei at the planar and curved interfaces. θ_{s1} and θ_{s2} are related via the common chord length CD, such that:

$$r^*_{nuc}\sin\theta_{s1} = r_{subst}\sin\theta_{s2} \qquad \text{[Eqn. 4.12]}$$

Consideration of the perpendicular distance of the chords AB and CD from the critical nuclei and emulsion droplet spherical surfaces gives

$$\cos\theta_p = \cos\theta_{s1} + (r_{subst} / r^*_{nuc})(1 - \cos\theta_{s2}) \qquad \text{[Eqn. 4.13]}$$

Experimental determination of T_{cryst} for the planar case allows calculation of θ_p by the process outlined below. Once θ_p is known, θ_{s1} and θ_{s2} are calculated for different r_{subst}/r^*_{nuc} values and hence the increase in ΔG^*_{Het} in changing from a planar to a curved substrate can be determined.

For a concave curvature w/o system, similar considerations show a reduction in the critical nucleus volume, and hence a nucleation rate increase compared to planar substrates, provided the droplets contain sufficient material to create the critical nucleus.

Critical Nucleus Shape

Equation 4.11 above is strictly only valid for cap-shaped nuclei, which will become increasingly inaccurate as r_{subst} decreases. An alternative derivation, which considers the actual critical nucleus shape on the curved substrate can be obtained by considering ΔG_i, the Gibbs free energy of formation of a nucleus containing i molecules, with respect to r^*_{nuc}.

ΔG_i is given in classical nucleation theory by the sum of the volume and surface energy terms, i.e.

$$\Delta G_i = -\frac{4}{3v_c}\pi r^*_{nuc}{}^3 \Delta\mu[(f(\theta_{s1}) - (r_{subst}/r^*_{nuc})^3 f(\theta_{s2})]$$

$$+ 2(1-\cos\theta_{s1})\pi r^*_{nuc}{}^2 \gamma_{vx} + 2(1-\cos\theta_{s2})\pi r_{subst}{}^2(\gamma_{sx} - \gamma_{sv})$$

[Eqn. 4.14]

But $$\cos\theta_p = \frac{\gamma_{sv} - \gamma_{sx}}{\gamma_{vx}}$$ [Eqn 1.17]

So

$$\Delta G_i = -\frac{4}{3v_c}\pi r^*_{nuc}{}^3 \Delta\mu[(f(\theta_{s1}) - (r_{subst}/r^*_{nuc})^3 f(\theta_{s2})]$$

$$+ 2(1-\cos\theta_{s1})\pi r^*_{nuc}{}^2 \gamma_{vx} - 2(1-\cos\theta_{s2})\cos\theta_p \pi r_{subst}{}^2 \gamma_{vx}$$

[Eqn. 4.15]

Then we find $\Delta G^*_{\text{Het Sphere}}$ by substituting $r^*_{nuc} = \frac{2\gamma v_c}{\Delta\mu}$ into Eqn. 4.15.

This gives:

$$\Delta G^*_{Het} = \frac{32}{3\Delta\mu^2}\pi\gamma_{vx}{}^3 v_c{}^2[(-f(\theta_{s1}) + (r_{subst}/r^*_{nuc})^3 f(\theta_{s2})]$$

$$+\frac{8}{\Delta\mu^2}\pi\gamma_{vx}{}^3 v_c{}^2[(1-\cos\theta_{s1}) - (1-\cos\theta_{s2})\cos\theta_p (r_{subst}/r^*_{nuc})^2]$$

[Eqn. 4.16]

which simplifies to:

$$\Delta G^*_{\text{Het Sphere}} = \frac{8}{3\Delta\mu^2}\pi\gamma_{vx}{}^3 v_c{}^2[1 - \cos^3\theta_{s1} + 4(r_{subst}/r^*_{nuc})^3 f(\theta_{s2})$$

$$- 3(1-\cos\theta_{s2})\cos\theta_p (r_{subst}/r^*_{nuc})^2]$$

$$= \Delta G^*_{\text{Hom}} \frac{[1-\cos^3\theta_{s1}+4(r_{subst}/r^*_{nuc})^3 f(\theta_{s2})-3(1-\cos\theta_{s2})\cos\theta_p(r_{subst}/r^*_{nuc})^2]}{2}$$

[Eqn 4.17]

4.7.3 Determination of θ_p, θ_{s1}, θ_{s2} and T_{cryst} for a Spherical Substrate Using Classical Nucleation Theory

Recall from chapter 1 that using the experimental T_{cryst} value for the planar case, the supersaturation, $\Delta\mu$, is calculated from:

$$\Delta\mu = \frac{\Delta H_m}{T_m}\Delta T = \Delta H_m\left(\frac{T_m - T_{cryst}}{T_m}\right) \qquad \text{[Eqn. 1.3]}$$

where ΔH_m is the enthalpy of melting and T_m is the normal melting temperature of bulk material.

At T_{cryst}, we assume the nucleation rate $J = \Omega\exp(-\Delta G^*_{Het}/k_BT) = 1$ nuclei cm^{-2}, hence:

$$\Delta G^*_{Het} = k_B T_{cryst} \ln\Omega \qquad \text{[Eqn. 4.18]}$$

This assumption is valid because the rapid increase in nucleation above the Ostwald metastable limit (section 1.2.3) ensures that at the highest temperature at which crystallisation occurs (i.e. T_{cryst} in this study), we can set $\ln J = 0$, corresponding to a rate of 1 nucleus cm^{-2} sec^{-1} with little loss of accuracy.

Substituting in equation 4.18 for ΔG^*_{Het} using equations 1.22 and 4.7 and for $\Delta\mu$ using equation 1.3 above gives:

$$f(\theta_p) = \frac{3\Delta H_m{}^2 k_B \ln\Omega(T_m - T_{cryst})^2}{16\pi\gamma^3 v_c{}^2 T_{cryst}} \qquad \text{[Eqn. 4.19]}$$

Solving equation 4.19 using a value of 268.5 K for T_{cryst} on a planar substrate, which is consistent with the experimental data presented here, and setting a value of 1×10^{-20} cm^{-2} s^{-1} for Ω gives a value for θ_p of 26.0°. Typical values of Ω_{Het} are $\sim 10^{17}$ -10^{22} cm^{-2} s^{-1} for heterogeneous nucleation from aqueous solutions. In fact we find that any Ω value between $\sim 10^{15}$ to 10^{30} cm^{-2} s^{-1} will produce the same variations between T_{cryst} values for these different interfacial curvature systems to within ±0.02 °C.

We can use this θ_p value of 26.0° to calculate θ_{s1} and θ_{s2} and then determine the expected T_{cryst} for a spherical substrate by the following iterative method. As in the planar heterogeneous case, $\Delta G^*_{\text{Het Sphere}}$ is set equal to $k_B T_{Cryst} \ln\Omega$. This gives:

$$f(\theta_{s1}) - \frac{r_{subst}^{\ 3} f(\theta_{s2})}{r^*_{nuc}{}^3} = \frac{3\Delta H_m^{\ 2} k_B \ln\Omega (T_m - T_{cryst})^2}{16\pi\gamma^3 v_c^{\ 2} T_{cryst}} \qquad \text{[Eqn. 4.20]}$$

for $\Delta G^*_{\text{Het Sphere}}$ given by equation 4.11 for a cap shaped nucleus. Alternatively considering volume and surface energy terms relevant to non-cap shaped nuclei, we find:

$$\frac{1 - \cos^3\theta_{s1} + 4(r_{subst}/r^*_{nuc})^3 f(\theta_{s2}) - 3(1-\cos\theta_{s2})\cos\theta_p (r_{subst}/r^*_{nuc})^2}{2} = \frac{3\Delta H_m^{\ 2} k_B \ln\Omega (T_m - T_{cryst})^2}{16\pi\gamma^3 v_c^{\ 2} T_{cryst}} \qquad \text{[Eqn. 4.21]}$$

for $\Delta G^*_{\text{Het Sphere}}$ given by equation 4.17 for an alternative shaped nucleus.

Initially, $r^*_{nuc} = \frac{2\gamma v_c}{\Delta\mu}$ is calculated at the planar T_{cryst} temperature, and this value is substituted into either expression 4.20 or 4.21 to determine an initial T_{cryst} value for the spherical interface, which is then used to recalculate r^*_{nuc}. The recalculated r^*_{nuc} value is then used to determine a more accurate T_{cryst} value for the spherical interface. This process of determining increasingly accurate r^*_{nuc} and T_{cryst} values is repeated until convergence is achieved. Table 4.19 shows the resulting T_{cryst} values obtained for the case of $\theta_p = 26.0°$ by using equations 4.20 and 4.21. The T_{cryst} values obtained from

equation 4.21 are slightly lower than those obtained from equation 4.20, with the difference becoming more apparent for smaller r_{subst} values. Application of this extended theory, however, predicts that the ice crystallisation temperature is significantly altered when the emulsion droplet radius $r_{subst} \sim r^*_{nuc}$, irrespective of whether equation 4.20 or 4.21 is adopted. The values in bold in table 4.19 are relevant to the systems detailed in this chapter.

Provided there is little variation in the ice nucleating ability with droplet size, it can be assumed that nucleation occurs on the droplets presenting the greatest total interfacial area, i.e. those droplets with diameter, d_{max}, where d_{max} is the value which maximises nd^2, and n is the number of droplets with size d. For the (near) symmetrical, unimodal number distribution of droplet diameters found in these emulsion and nanoemulsion systems, d_{max} will be greater than the number $d(0.5)$ value, whilst for a symmetrical, unimodal interfacial area distribution function, it is equal to the interfacial area $d(0.5)$ value. A large increase/decrease in nucleating ability with droplet size will then displace the nucleating d range to higher/lower values.

As shown above and detailed in table 4.19, classical nucleation theory predicts a slight increase in the nucleation rate with droplet size for these nanoemulsion and emulsion systems. For this theory to be obeyed quantitatively, the increase in T_{cryst} with droplet size must be less than that predicted using the number $d(0.5)$ values, and should in fact be similar to that predicted using the interfacial area d(0.5) values. So the T_{cryst} variation should be ~ 0.4 - 0.7 °C from the interfacial area values (-4.92 °C versus -4.51 °C using equation 4.20 or -5.26 °C versus -4.53 °C using equation 4.21, see table 4.19), and should certainly be less than the ~1.4 °C value difference predicted using the number $d(0.5)$ values and equation 4.21 (-5.91 °C versus -4.55 °C, see table 4.19). Thus, classical nucleation theory provides qualitative agreement with these data presented in this chapter, but is not sufficient to explain the ~3 °C variation generally found between the nucleating ability of the blue nanoemulsions and emulsions.

Emulsion diameter /μm	Parameters calculated from equation 4.20				Parameters calculated from equation 4.21			
	r_{subst}/ r^*_{nuc}	θ_{s1} / °	θ_{s2} / °	T_{cryst}/ °C	r_{subst}/ r^*_{nuc}	θ_{s1} / °	θ_{s2} / °	T_{cryst}/ °C
∞	∞	26.01	0.00	-4.50	∞	26.01	0.00	-4.50
10	388	26.04	0.06	-4.50	389	26.04	0.06	-4.51
5.0	194	26.08	0.13	-4.51	195	26.08	0.13	-4.52
3.1	**121**	**26.11**	**0.21**	**-4.51**	**121**	**26.11**	**0.21**	**-4.53**
1.9	**74.1**	**26.18**	**0.34**	**-4.52**	**74.6**	**26.18**	**0.34**	**-4.55**
1.0	39.2	26.34	0.65	-4.55	39.7	26.33	0.64	-4.60
0.50	19.8	26.68	1.29	-4.60	20.3	26.65	1.27	-4.70
0.34	**13.7**	**27.98**	**1.90**	**-4.66**	**14.1**	**26.95**	**1.84**	**-4.80**
0.28	**11.3**	**27.19**	**2.31**	**-4.69**	**11.8**	**27.14**	**2.22**	**-4.86**
0.13	**5.53**	**28.60**	**4.97**	**-4.92**	**5.91**	**28.41**	**4.62**	**-5.26**
0.1	4.37	29.42	6.45	-5.06	4.74	29.11	5.90	-5.47
0.067	**3.10**	**31.23**	**9.61**	**-5.35**	**3.43**	**30.60**	**8.53**	**-5.91**
0.05	2.46	33.18	12.87	-5.67	2.75	32.12	11.13	-6.34
0.02	1.36	46.41	32.23	-7.78	1.54	41.45	25.41	-8.80
0.01	1.06	73.48	65.31	-11.70	1.15	59.15	48.42	-12.89

Table 4.19. Calculated crystallisation temperatures for ice using classical nucleation theory for different size emulsions.

The amount of 1-heptacosanol present at the decane-water interface in the blue nanoemulsion systems is more than sufficient to enable ice nucleation at high temperatures and so this cannot explain the discrepancy. Classical nucleation theory predicts that for crystallisation at -5.5 °C, the critical nucleus would occupy ~0.9 % of the emulsion surface, and at temperatures of -8 °C and -11 °C this value would fall to ~0.4 % and ~0.2 %, respectively. In comparison, the 1-heptacosanol can occupy up to ~21% of

this region in the blue nanoemulsions, providing >20 times as much 1-heptacosanol as would be required for a fully close-packed 1-heptacosanol island to induce ice crystallisation at these temperatures, if indeed a fully close-packed arrangement is required. Hence we suggest that another factor besides the intrinsic curvature of the system probably limits the ice nucleating potential of the blue nanoemulsions. In particular, the ability of 1-heptacosanol to pack into structures suitable for inducing ice crystallisation is thought to be compromised with increasing surface curvature, as indicated below.

4.7.4 Calculation of Interfacial Additive Density and the Effect of Curvature

If each interfacially adsorbed additive molecule is considered as a block (see figure 4.19), the angle, ø, between each, assuming 100% coverage is:

$$\phi = 180 - 2\sin^{-1}\left(\frac{\sqrt{A}}{d}\right) \qquad \text{[Eqn. 4.22]}$$

where A is the limiting area of the additive molecule and d is the emulsion diameter.

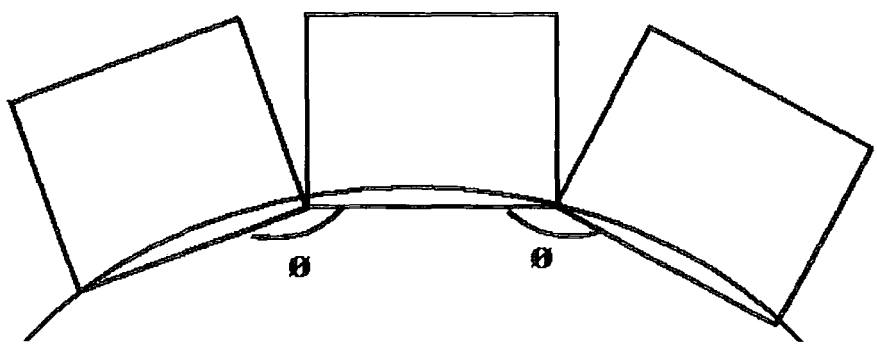

Figure 4.19. Illustration of angle, ø, between each interfacially adsorbed alcohol molecule.

Droplet diameter / nm	$\sqrt{A}/d$ /10^{-3}	Angle, ø, between adjacent interfacially adsorbed 1-heptacosanol headgroups	(180 – ø)
1900	0.235	179.972°	0.028°
280	1.60	179.829°	0.171°
67	6.67	179.224°	0.776°

Table 4.20. Calculation of angles between interfacially adsorbed heptacosanol for the three sizes of emulsion studied in this chapter.

The angle, ø, that arises is illustrated in figure 4.19, and the values of $\sqrt{A}/d$ and ø obtained for the blue nanoemulsion, white nanoemulsion and emulsion systems are listed in table 4.20. For both the white nanoemulsion and emulsion systems, the values of $\sqrt{A}/d$ and ø are so low, that only a minor impact is expected on the ability of 1-heptacosanol to close-pack into a structure suitable for inducing ice crystallisation.

For the blue nanoemulsion systems, the parameters indicate that a reduced nucleating ability can occur. The relatively large size of the critical nucleus predicted by classical nucleation theory at temperatures between -8 °C and -5.5 °C means that ~ 190 to 770 close-packed 1-heptacosanol molecules would be required to induce nucleation (assuming a close-packed structure is required) resulting in an accumulated angular deviation from linearity of ~10.7° to 21.5°. In contrast for nucleation between -13 °C and -11 °C, islands of only ~ 64 to 93 1-heptacosanol molecules would produce ice nucleation, resulting in a significantly smaller accumulated angular deviation of ~6.2° to 7.5°.

The hypothesis of a reduced nucleating ability for 1-heptacosanol as the interfacial curvature increases is reinforced by the inability of classical nucleation theory to predict the extent of the decreased ice nucleating power of the blue nanoemulsions.

4.8 Conclusions

Reproducible decane-in-water emulsions with droplet diameters, *d*, of approximately 67 nm, 280 nm and 1.9 μm have been produced with estimated interfacial 1-heptacosanol concentrations between 0 and ~ 21%. 1-heptacosanol was found to be an excellent nucleator of ice, and was able to substantially raise the ice crystallisation temperature in the planar and the lower interfacial curvature systems with $d \sim 280$ nm and 1.9 μm, despite it being typically present in relatively low interfacial concentrations of typically less than 10%. In particular, the white nanoemulsions (d ~ 280 nm) induced ice crystallisation at temperatures as high as -7 to -8 °C, with typical values between -8 to -11 °C for estimated 1-heptacosanol interfacial concentrations between ~ 2 to 8%. The emulsions (d ~ 1.9 μm) formed ice at temperatures as high as -6 to -7 °C, with typical values between -8 and -9 °C for estimated 1-heptacosanol interfacial concentrations between 7 - 11 %. In contrast, the blue nanoemulsions (d ~ 67 nm) were significantly poorer nucleators, inducing ice crystallisation at temperatures no higher than ~ -11 °C, with typical values of -13 to -15 °C, despite there being higher 1-heptacosanol interfacial concentrations of between ~9 to 21 %.

The finding of excellent ice nucleating ability at low 1-heptacosanol concentrations is consistent with a nucleation mechanism in which a synergic interplay exists between the water and 1-heptacosanol molecules. In this mechanism, interfacial 1-heptacosanol molecules adsorb pre-critical nuclei size ice clusters, which then promote impingement of additional interfacial 1-heptacosanol molecules into a structure favouring ice nucleation.

The ability of the 1-heptacosanol to pack into a structure that will induce ice nucleation is expected to decrease as the interfacial curvature increases, whilst classical nucleation theory predicts that the critical nucleus size will increase. Hence both these factors would make ice crystallisation less favourable in the smaller droplet, blue nanoemulsion systems.

References

(1) Popovitz-Biro, R.; Wang, J. L.; Majewski, J.; Shavit, E.; Leiserowitz, L.; Lahav, M. *J. Am. Chem. Soc.* **1994**, *116*, 1179-1191.

(2) Pauling, L. *J. Am. Chem. Soc.* **1935**, *57*, 2680-2684.

(3) Peterson, W.; H.A., L. *Acta. Cryst.* **1957**, *10*, 70.

(4) Barton, S. W.; Thomas, B. N.; Flom, E. B.; Rice, S. A.; Lin, B.; Peng, J. B.; Ketterson, J. B.; Dutta, P. *J. Chem. Phys.* **1988**, *89*, 2257-2270.

(5) Davey, R. J.; Maginn, S. J.; Steventon, R. B.; Ellery, J. M.; Murell, A. V.; Booth, J.; Godwin, A. D.; Rout, J. E.-. *Langmuir* **1994**, *10*, 1673-1675.

(6) Johari, G. P. *J. Chem. Phys.* **1997**, *107*, 10154-10165.

(7) Clausse, D.; Babin, L.; Broto, F.; Aguerd, M.; Clausse, M. *J. Phys. Chem.* **1983**, *87*, 4030-4034.

(8) Wilson, P. W.; Heneghan, A. F.; Haymet, A. D. *Cryobiology* **2003**, *45*, 88-98.

(9) Allen, K.; Davey, R. J.; Ferrari, E.; Towler, C.; Jones, M. O.; Pritchard, R. G. *Cryst. Growth & Design* **2002**, *2*, 523-527.

(10) Yano, J.; Furedi-Milhofer, H.; Wachtel, E.; Garti, N. *Langmuir* **2000**, *16*, 9996-10004.

(11) Furedi-Milhofer, H.; Garti, N.; Kamyshny, A. *J. Cryst. Growth* **1999**, *198/199 Pt II*, 1365-1370.

(12) Skoda, W.; van den Tempel, M. *J. Coll Sci.* **1963**, *18*, 568-584.

(13) Coupland, J. N. *Current Opinion Coll. Interface Sci.*, *7*, 445-450.

(14) Lim, G. K.; Wang, J.; Ng, S. C.; Gan, L. M. *Langmuir* **1999**, *15*, 7472-7477.

(15) Davey, R. J. *Nature* **2004**, *428*, 374-375.

(16) Cacciuto, A.; Auer, S.; Frenkel, D. *Nature* **2004**, *428*, 404-406.

(17) Lopez-Montilla, J. C.; Herrera-Morales, P. E.; Shah, D. O. *Langmuir* **2002**, *18*, 4258-4262.

(18) Forgiarini, A.; Esquena, J.; González, C.; Solans, C. *Prog. Colloid Polym. Sci.* **2000**, *115*, 36-39.

(19) Mitchell, D. J.; Tiddy, G. J. T.; Waring, L.; Bostock, T.; McDonald, M. P. *J. Chem. Soc., Far. Trans. 1* **1983**, *79*, 975-1000.

(20) Izquierdo, P.; Esquena, J.; Tadros, T. F.; Dederen, C.; Garcia, M. J.; Azemar, N.; Solans, C. *Langmuir* **2002**, *18*, 26-30.

(21) Caldararu, H.; Caragheorgheopol, A.; Vasilescu, M.; Dragutan, I.; Lemmetyinen, H. *J. Phys. Chem* **1994**, *98*, 5320-5331.

(22) Forgiarini, A.; Esquena, J.; González, C.; Solans, C. *Langmuir* **2001**, *17*, 2076-2083.

(23) Tanaka, H.; Okabe, I. *Chem Phys. Lett* **1996**, *259*, 593-598.

(24) van de Hulst, H. C. In *Light Scattering by Small Particles*; Dover Publ. Inc.: New York, 1981; pp 114-128.

(25) Hatch, T.; Choate, S. P. *J. Franklin Inst.* **1929**, *207*, 369-387 or Harvard Eng. School, Publ. Vol. 335 pp 369-387.

(26) Maoz, R.; Sagiv, J. *J. Colloid Interf. Sci.* **1984**, *100*, 465-496.

(27) Sagiv, J. *J. Am. Chem. Soc.* **1980**, *102*, 92-98.

(28) Borne, J.; Nylander, T.; Khan, A. *Langmuir* **2001**, *17*, 7742-7751.

(29) Ahn, D. J.; Berman, A.; Charych, D. *J. Phys. Chem* **1996**, *100*, 12455-12461.

(30) Cooper, S. J.; Sessions, R. B.; Lubetkin, S. D. *J. Am. Chem. Soc.* **1998**, *120*, 2090-2098.

(31) Backov, R.; Lee, C. M.; Khan, S. R.; Mingotaud, C.; Fanucci, G. E.; Talham, D. R. *Langmuir* **2000**, *16*, 6013-6019.

Chapter 5

Crystallisation of Glycine in Emulsions

5.1 Introduction

The previous chapter demonstrated the effect of interfacial curvature on the crystallisation of ice. The crystallisation of glycine, a polymorphic organic species is explored in this chapter.

5.1.1 Chapter Aims

Heterogeneous classical nucleation theory predicts that a convex surface is less efficient at inducing crystallisation than a planar surface, while in principle, a concave surface will be more efficient than a planar surface, provided the emulsion droplet contains sufficient crystallising material to form a critical nucleus. The crystallisation of glycine is examined at the planar interface and in emulsions. The former system is well understood, but crystallisation at the curved interfaces in oil-in-water (o/w) and water-in-oil (w/o) emulsions have been studied less extensively. The crystallisation of glycine in emulsions prepared at the o/w to w/o phase inversion will also be studied. In addition, additives will be included in order to try to alter the glycine polymorph or morphology obtained.

5.1.2 Choice of Glycine

Glycine was chosen because it is a simple molecule, but offers 3 polymorphs. These are commonly labelled α, β, and γ. The α form was described by Iitaka[1] as the "usual form". It is formed by evaporation from aqueous solution and is usually elongated in the c-axis.

The β polymorph is the least stable, and this form transforms into the α polymorph in air or water but is stable indefinitely in a dry environment. It is synthesised by slow cooling of ethanol in water and its morphology is often needle-like. The γ form[2] is now believed to be the most stable at room temperature[3], and is usually synthesised by slow cooling of supersaturated aqueous solution acidified with acetic acid. It can also be made by crystallising from solution doped with sodium chloride[4] and by laser-induced nucleation[5].

The space group and lattice parameters of each glycine polymorph are listed in table 5.1.

Form	Space Group	a / Å	b / Å	c / Å	Angle γ	No. of Molecules in Unit Cell	Ref.
α	$P2_1/n$	5.102	11.9709	5.4575	111.425°	4	6
β	$P2_1$	5.077	6.268	5.38	113.2°	2	1
γ	$P3_1$ or $P3_2$	7.037	7.037	5.483	120°	3	7

Table 5.1 Lattice parameters for the α, β, and γ polymorphs of glycine.

5.2 Experimental Procedures

5.2.1 Polymorph Identification

The polymorph of the crystals was assessed by XRD. The characteristic peaks[4,8] for each polymorph are detailed in table 5.2.

	Polymorphic Form		
	α	β	γ
Characteristic XRD Peaks / 2θ	19°, 21°, 30°	18°, 24°, 28°	22°, 25°

Table 5.2. Characteristic X-ray peaks (2θ) for polymorphs of glycine.

In the X-ray diffraction analyses in this chapter, the peaks typically observed were at 2θ = 18° and 24° (β) and 30° (α), these being the most intense.

5.2.2 Preparation of Supersaturated Solutions

The solubility of glycine is calculated from[8]:

$$S = 13.63 + 0.49T \qquad \text{[Eqn. 5.1]}$$

where S is the solubility of glycine in 100 g water and T is the temperature in Celsius.

Solutions were prepared by weighing the required amount of UHQ water and solute and then treating in a hot (~ 70 °C) ultrasonic bath for at least 2 hours. This more aggressive method was described by Garetz et al.[9] and gave supersaturated glycine solutions that were stable for a much longer period than those prepared by the heating and filtration method. Garetz et al. did not explain why this method was pursued, but its effectiveness may be due to degassing or breaking down of impurities.

All the supersaturated solutions detailed in this chapter contained 28.5 g of glycine in 100 g of UHQ water, which corresponds to a supersaturation of 10% at 25 °C. If undisturbed, the 10% supersaturated solutions were stable for many weeks without spontaneously nucleating. The ease with which the glycine crystallised was assessed by cooling the sample on the Linkam stage at a rate of 1 °C/min and noting the temperature at which crystallisation occurred.

5.3 Choice of Surfactant for Emulsion Crystallisation Studies

5.3.1 Surfactant Experiments

A variety of surfactants were tested for the ability to stabilise emulsions, with decane fractions, F_O, = 0.25, 0.50 and 0.75. The surfactant concentration was 10% of the overall emulsion mass. Supersaturated glycine is significantly more viscous than water, therefore the choice of surfactant was likely to be limited. Some of the surfactants

explored induce crystallisation of the glycine at the 10% supersaturation level, whilst others did not produce stable emulsions or gave lyotropic liquid crystal phases. The results are summarised in table 5.3.

Surfactant	Remarks
Tween 20	Spontaneous glycine crystallisation (see section 5.6.1).
Tween 80	Spontaneous glycine crystallisation with liquid crystals (see section 5.6.1).
Span 80	Stable emulsions, w/o and o/w.
Tween 60	Spontaneous α/β-glycine crystallisation.
Tergitol	Spontaneous α-glycine crystallisation.
Lauryl sulfate (SDS)	Formed liquid crystals.
Pluronic F127	Surfactant was insoluble.
Span 65	Separated into two phases.
Span 60	Viscous gel formed.
AOT	Stable for a short time (~5 mins).
Sodium Butyrate	Unstable, settled into two phases.
Sodium n-octyl sulfate	Very stable; oil-in-water.
Brij 30	Separated into two phases.

Table 5.3. Surfactants tested for the ability to stabilise emulsions of aqueous supersaturated glycine with decane.

Sodium n-octyl sulfate was extremely effective at stabilising the emulsion, but gave the oil-in-water phase only, and so is of limited interest for the purposes of this chapter.

Allen et al.[8] reported the ability to generate glycine crystals of controlled morphology and size from water-in-oil emulsions stabilised with a mixture of Span surfactants. This controlled morphology was reproduced at Durham with ease, using decane as the oil phase and just Span 80 as the surfactant. These emulsions were stable for many hours. Furthermore, Span 80 can stabilise water-in-oil and oil-in-water emulsions

depending on the aqueous content. This would enable a comparison of the effect of a concave and a convex interface on crystallisation processes. Consequently, Span 80 was used for many of the glycine emulsion studies.

5.3.2 Surfactant Mixtures and the Phase Inversion

The phase diagrams for mixed Span and Tween surfactants are well known[10-13]. As was reported for Brij 30 in the previous chapter, an inversion between o/w and w/o can be achieved with Span and Tween surfactants, simply by changing the weight fraction of the oil or aqueous phase. This is often labelled "catastrophic inversion" because it is deemed irreversible. In the previous section, Tween surfactants were shown to cause rapid crystallisation of glycine. Span surfactants also induce glycine crystallisation, but much less effectively[8].

Sajjadi et al[10] showed that for Span 20/Tween 20 emulsions there is a phase inversion from w/o to o/w emulsions at constant HLB, simply by changing the oil fraction, F_O. On changing F_O, for Span 20/Tween 20 stabilised emulsions, a reduction in droplet diameter is reported on approaching the inversion boundary, such that the droplets are very small at the phase inversion point[14]. This can be complicated by the presence of multiple emulsions, however. Vander Kloet and Schramm[15] reported that for Span 80/Tween 80, at high (~13) or low (~6) HLB, w/o or o/w emulsions are possible depending on the water fraction. This is illustrated further in section 5.6.

This inversion between oil-in-water and water-in-oil provides an opportunity to assess the impact of changing the droplet curvature on the interfacial crystallisation of glycine. While supersaturated aqueous glycine is more viscous than water, initial studies suggested the phase diagrams[10,11] reported for oil and pure water with Span/Tween surfactants are a good guide to generating o/w and w/o emulsions and samples close to the phase inversion boundary with 10% supersaturated glycine substituted for water.

5.4 Span Stabilised Emulsions

A Span 20/Span 80 surfactant mixture was used by Allen et al.[8] to generate w/o emulsions of diameter ~ 10 – 15 μm. The work in this section is closely related to Allen's publication, but the aim here is to see if additives can induce crystallisation of a different glycine polymorph, or whether variable droplet diameters or phase inversion can be achieved to study the effect of interfacial curvature, as in the previous chapter.

5.4.1 Span 80 Stabilised Emulsions

Vander Kloet et al. published a phase diagram that suggested there would be a phase inversion at an oil fraction, $F_{O,}$ = 0.64 for kerosene/water emulsions stabilised with 15% Span 80. This implies that studies of convex and concave interfaces will be possible.

Samples were prepared that would be o/w and w/o. Another sample was prepared at oil fraction, F_O = 0.64, i.e. the point at which inversion between o/w and w/o occurs. These samples were cooled on a Linkam stage and the temperature noted at which crystallisation was observed.

Samples Prepared at the Phase Inversion

A sample was prepared with oil fraction, F_O = 0.64, with 10% supersaturated aqueous glycine. Glycine crystallisation was not observed in this sample, even on cooling to 0 °C. While the sample should have been at the phase inversion at ambient temperature, it is also likely to have been a mixture of o/w and w/o emulsions, as the sample showed a mixture of droplet sizes of ~ 20 μm and ~ 80 μm. This kind of multiple emulsion was described by Zerfa et al.[14] for samples close to the inversion boundary.

Water-in-Oil Emulsion

Figure 5.1 a & b show images of crystallisation from a w/o emulsion prepared at oil fraction, F_O = 0.70. The typical droplet diameter is 25 – 40 μm. Crystallisation occurred on cooling to 10 °C, which corresponds to a supersaturation of 54%. The

spheres are an agglomeration of crystals, which have grown within the droplets to approximately 10 – 15 μm in diameter.

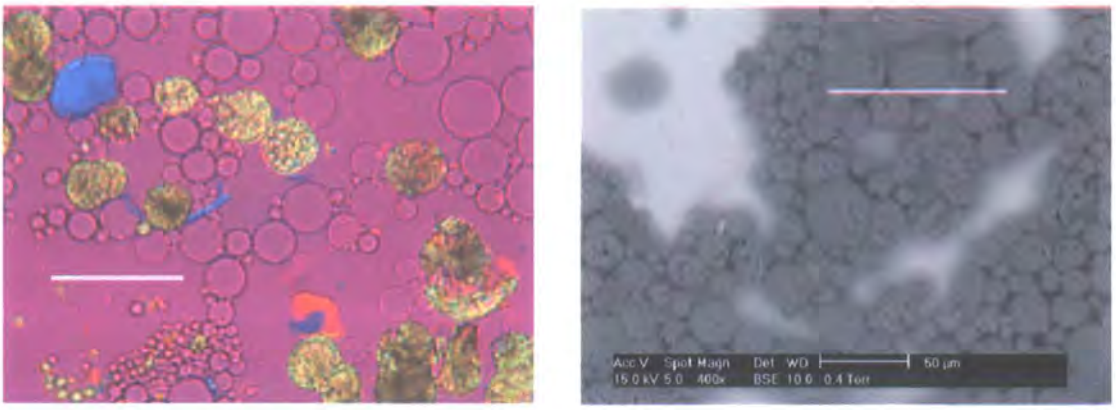

Figure 5.1 a & b. Microscopy image (left) of w/o emulsion cooled to 10 °C viewed at high magnification with red tint plate and ESEM image (right) of the same sample. (White Scale bars = 100 μm).

These spherical agglomerates are as reported by Allen et al.[8]. X-ray diffraction analysis of these spherical agglomerations showed that this was the β polymorph of glycine, also consistent with Allen's findings. In contrast, however, these showed no sign of transformation to the α form, even after a few days. This is probably due to residual surfactant coating the crystals, thus preventing any solvent-mediated transformation.

Oil-in-Water Emulsions

Oil-in-water emulsions were prepared at oil fraction, $F_{O,}$ = 0.30, where the typical droplet size was ~ 30 μm. Crystallisation in this case progressed very rapidly, typically on cooling by only approximately 3 °C to ~ 20 °C, which corresponds to a supersaturation of 22%. Given that water is the continuous phase for this emulsion, there is no constraint on the growth of the crystals other than depletion of glycine solute. This explains the size of the crystals pictured in figures 5.2 a & b, which exceed 1 cm in length.

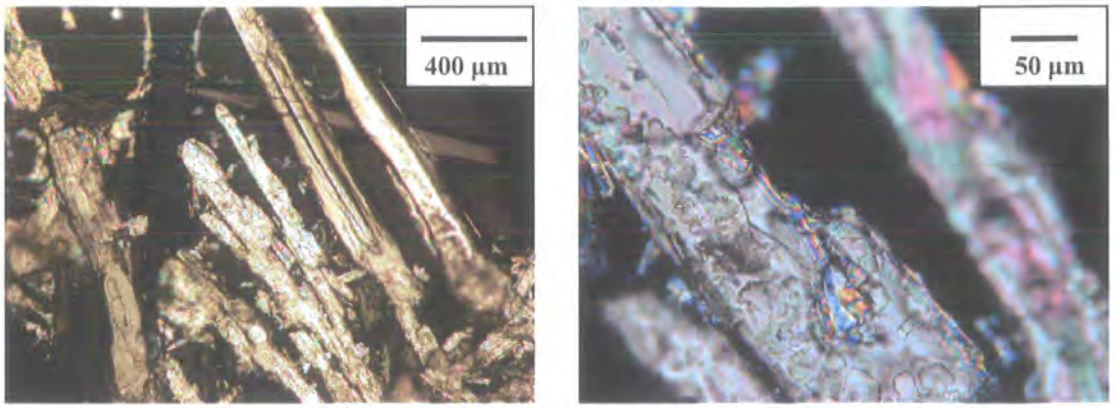

Figure 5.2 a & b. Image of glycine crystallised in Span 80 stabilised o/w emulsion viewed through crossed polarisers. These are viewed with low (left) and high magnification (right).

This sample was remade and cooled under X-ray diffraction analysis. In keeping with the findings of Allen et al.[8], the resulting crystals showed peaks characteristic of the β form of glycine.

5.4.2 Variation in Droplet Size for Span 80 Stabilised Emulsions

For these studies, as was the case in chapter 4, it would be useful to generate samples of different droplet sizes. Attempts were made to achieve this for o/w emulsions by increasing the aqueous content. Figures 5.3 a & b show images of emulsions prepared at $F_O = 0.50$ and 0.20, respectively. The mass percentage of Span 80 surfactant was 9%.

At $F_O = 0.50$, (figure 5.3a) there is a more coherent droplet size of approximately 25 - 40 µm. At $F_O = 0.20$ (figure 5.3b) there is a mixture of droplet sizes from 25 – 50 µm plus a significant number of larger droplets of ~ 80 µm diameter. At higher F_O, samples appear as shown for w/o earlier (section 5.4.1), and for higher aqueous content there was immediate crystallisation of glycine.

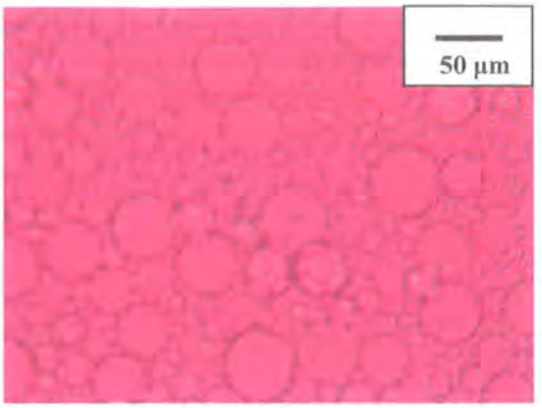

Figure 5.3 a. Oil-in-water emulsion where F_O = 0.50 viewed through crossed polars with a red tint plate.

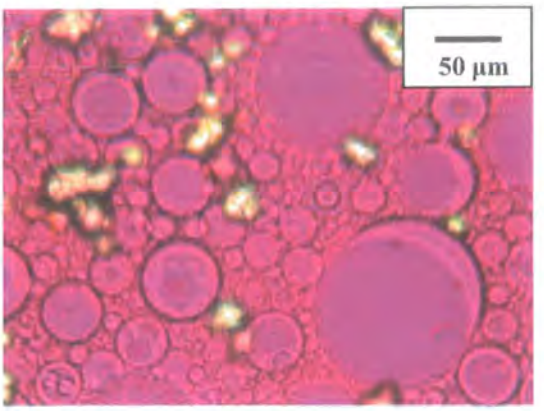

Figure 5.3 b. Oil-in-water emulsion where F_O = 0.20 viewed through crossed polars with a red tint plate.

This work shows that there is unlikely to be a range of droplet sizes of significant interest for these studies, as the droplet sizes observed are relatively large and are effectively planar at a molecular level.

5.4.3 Addition of NaCl or Acetic Acid to the Aqueous Phase

As was stated in the introduction to this chapter, crystallisation of glycine from the bulk aqueous phase in the presence of sodium chloride or acetic acid gives the γ polymorph. The acetic acid method is universally accepted; the sodium chloride method is relatively new. A bulk test of 4% NaCl in supersaturated aqueous glycine did yield the γ form of glycine, however.

The o/w and w/o experiments detailed above were repeated with these additives added at 4 wt% of the aqueous phase. XRD analysis of the resulting glycine crystals showed evidence for the β form only, and the crystal morphologies were as illustrated in the absence of these additives, see section 5.4.1.

5.4.4 Pure Span 20

For pure Span 20 stabilised emulsions, the phase inversion between o/w and w/o was reported[10] at oil fraction, $F_O \approx 0.60$ for the p-xylene/water system. Samples prepared at

the phase inversion and also the w/o emulsions were stable for only a few minutes, giving insufficient time for crystallisation studies. The o/w sample gave the β form of glycine and the same needle morphology as seen for Span 80 stabilised emulsions.

5.5 α-Amino Acid Additives

The term "tailor made" is used in cases where the crystal modifier is similar to the host molecule[16], and is applicable to α-amino acids when considering glycine crystallisation. Soluble α-amino acids are well known to modify the crystal habit of the α form of glycine, typical examples are illustrated in figure 5.4. D-amino acids inhibit the growth of the (010) face, while L-amino acids inhibit growth of the $(0\bar{1}0)$ face[17]. At high concentrations (8 mg/ml) of L-leucine, the additive adsorbs on the $(0\bar{1}0)$ face of glycine while the growth rate of the (010), (011) and $(01\bar{1})$ faces increases. This leads to pairing at the basal plane $(0\bar{1}0)$ where the additive is bound.

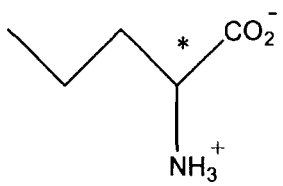

Figure 5.4a Leucine

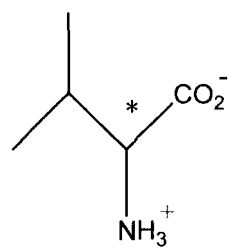

Figure 5.4b Norleucine

The manner in which a racemic mixture of theses tailor made molecules can adsorb to the growing glycine crystal, hence inhibiting growth of both the (010) and $(0\bar{1}0)$ face is illustrated in figure 5.5.

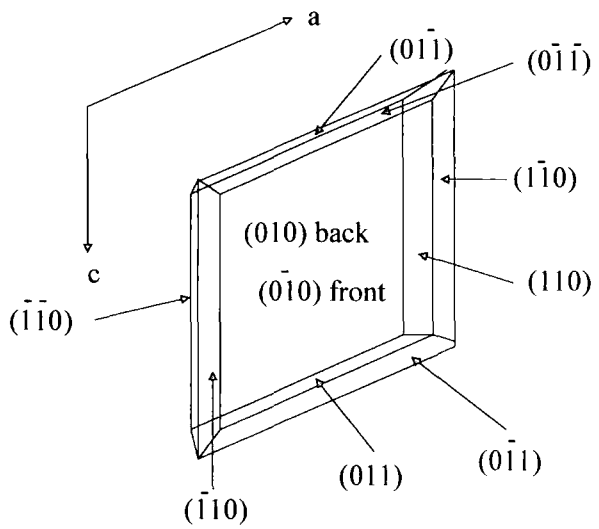

Figure 5.5 α -glycine plate nucleated in the presence of DL-norleucine where both the (010) and (0$\bar{1}$0) faces are "protected" or the growth inhibited by the adsorption of racemic additive. This image is based on examples by Addadi et al[26] and Lee et al[27].

For the case of the optically pure tailor-made additives, the resulting glycine morphologies are shown in figures 5.6a and b, which are based on examples by Addadi et al[26] and Lee et al[27].

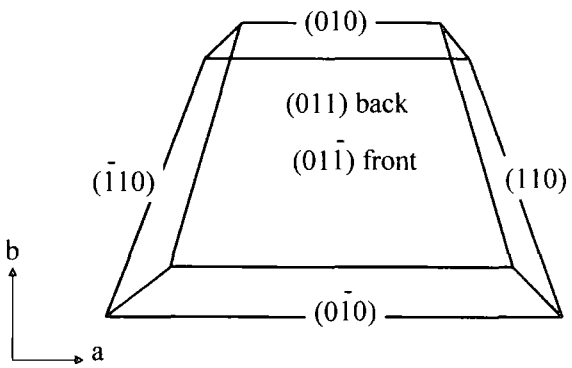

Figure 5.6a. α -glycine nucleated in the presence of D-α-amino acid where growth at the (010) face is inhibited.

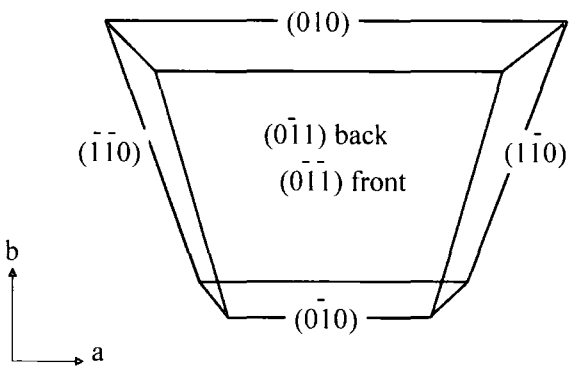

Figure 5.6b. α -glycine nucleated in the presence of L-α-amino acid where growth at the (0$\bar{1}$0) face is inhibited.

It should therefore be noted that dimeric glycine species can form, which are fused at the (0$\bar{1}$0) and (010) faces.

A pioneering paper by Landau et al.[18] illustrated the ability of 12 α-amino acid monolayers to selectively induce oriented crystallisation of the α polymorph of glycine when present at the air-aqueous interface. Hence in solution, α-amino acids typically inhibit glycine growth[19], but when immobilised at an interface, they promote oriented nucleation by assuming a structure similar to, or identical to, that of one of the (010) faces of the α form of glycine[20]. Generally speaking, hydrophobic α -amino acids will induce formation of the α form of glycine.

Allen et al.[8] used DL-norleucine as a crystallisation modifier for α-glycine in some of their glycine emulsion crystallisation studies. As was shown for the pure Span 80 images earlier, this is not an essential factor for the formation of spherical β-phase aggregates, however, in its absence I have seen no crystallisation at all for some w/o emulsions. Cases where crystallisation did not occur were never observed for w/o emulsions with added DL-norleucine, hence it might be concluded DL-norleucine assists the growth of spherical crystal aggregates.

5.5.1 Glycine Crystallisation Induced at the Planar Air-Aqueous Interface

2-aminononanoic acid and 2-aminohexadecanoic acid (see figure 5.7) were chosen for my initial planar studies, because they are readily available from Fluka and have structures similar to the compounds studied by Landau et al. It would be expected that these compounds display similar abilities to nucleate glycine, and in particular it was hoped these compounds would show interfacial activity at the oil-water interface, as illustrated for 1-heptacosanol in chapter 4. Planar studies were undertaken to confirm that these water insoluble α-amino acids would nucleate glycine as demonstrated by Landau et al. Both 2-aminononanoic acid and 2-aminohexadecanoic acid were dissolved in chloroform (1 mg/cm^3) and spread on a 10% supersaturated subphase.

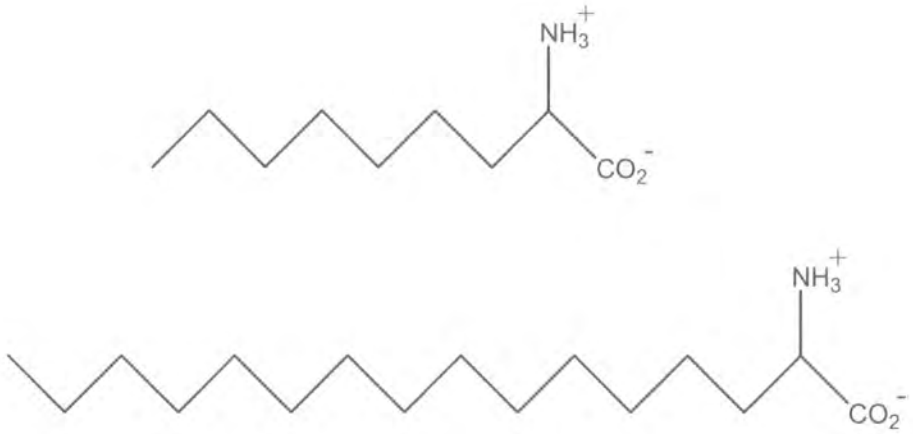

Figure 5.7 α -aminononanoic acid (top) and α-aminohexadecanoic (bottom)

The shorter variant, 2-aminononanoic acid did not produce a good monolayer and also did not induce glycine crystallisation. The longer C16 variant demonstrated a good ability to form monolayers with a limiting area of 22Å^2 and did nucleate the α-phase of glycine.

Figure 5.8 is typical of the α-phase glycine crystals grown under a monolayer of 2-aminohexadecanoic acid. The image shows the (010) face attached to the monolayer. Over time the crystals generate and then sink to the bottom of the trough. Outside the barriers of the trough, in the absence of monolayer, only a few very large (~ 1 cm) crystals form, as expected for non-specific or spontaneous nucleation of glycine from supersaturated aqueous solutions.

Figure 5.8. Glycine crystal grown under a monolayer of 2-aminohexadecanoic acid viewed with high magnification. Scale : 1 cm = 50 μm.

5.5.2 Crystallisation in Emulsions with Crystallisation Promoters and Modifiers, Stabilised with Span 80

Following the success of 2-aminohexadecanoic acid to nucleate glycine at the air-aqueous interface, oil-in-water and water-in-oil emulsions were prepared with 0.10 Wt% 2-aminohexadecanoic acid, which was added to the decane phase. It was hoped this molecule would be interfacially active and could induce the α form of glycine as reported by Landau et al.[18]. Other additives, namely L-leucine and DL-leucine (0.4 g in 100 cm^3 10% supersaturated glycine) and acetic acid and NaCl (5 g in 100 cm^3 10% supersaturated glycine) were also used for interest. The temperature at which crystallisation was observed is listed in table 5.4, with the corresponding supersaturation at that temperature.

Oil-in-Water Emulsions

For the oil-in-water samples, the average droplet diameter was ~ 20 - 40 μm. These were prepared with an oil fraction, $F_O = 0.20$. The Span 80 surfactant was present at 10% of total emulsion mass and was premixed with the decane. The composition of the samples is given in table 5.4.

In the absence of water-soluble additives (see figures 5.9a and 5.10a), the crystals showed an elongated morphology, of dimensions approximately 1000 μm x 100 μm. The sample with only L-leucine added also shows an elongated morphology, (see figures 5.9b and 5.10b) and in this case the crystal growth would have been inhibited at the $(0\bar{1}0)$ face only. All other samples show elongated dendritic-like morphology, except for sample I (figures 5.9i and 5.10i), which shows a mixture of dendritic-like crystals and elongated crystals.

Sample	Soluble Additive	Polymorph	T_{cryst} / °C	$\Delta\mu$ at T_{cryst}	Crystal morphology	Figure
A	None	β	21	19%	High density elongated crystals.	5.9a & 5.10a
B	L-Leucine	β	20	22%	Elongated crystals.	5.9b & 5.10b
C	DL-Leucine	β	17	30%	Small elongated crystals.	5.9c & 5.10c
D	Acetic acid	β	14	39%	Dendritic like	5.9d & 5.10d
E	NaCl	β	12 to 8	46-62%	Small elongated crystals.	5.9e & 5.10e
F	L-Leucine Acetic acid	β	16	33%	Dendritic like	5.9f & 5.10f
G	L-Leucine NaCl	β	18	27%	Dendritic intergrowth	5.9g & 5.10g
H	DL-Leucine Acetic acid	β	16	33%	Small intergrown crystals.	5.9h & 5.10h
I	DL-Leucine NaCl	β	15	36%	Dendritic like	5.9i & 5.10i

Table 5.4. Composition of oil-in-water emulsions, prepared with 2-aminohexadecanoic acid and various water-soluble additives.

X-ray diffraction analysis indicated that all crystals formed were of the β polymorph. Hence this suggests that the soluble additives were all decreasing the growth rate of the β-crystals, such that secondary nucleation on the crystals became favourable, leading to the formation of indistinct, agglomerated and mostly non-facetted crystals, and that the 2-aminohexadecanoic acid was ineffective at inducing α-phase glycine at the oil-water interface in the presence of Span 80.

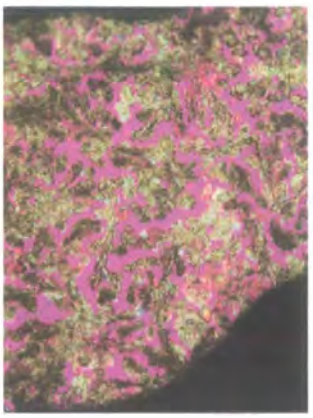

Figure 5.9c. Sample C.

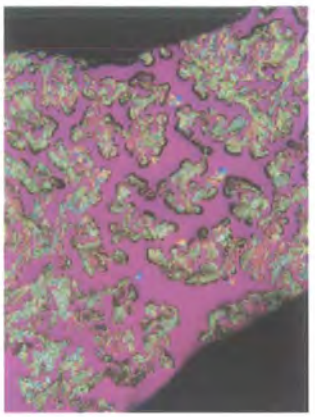

Figure 5.9f. Sample F.

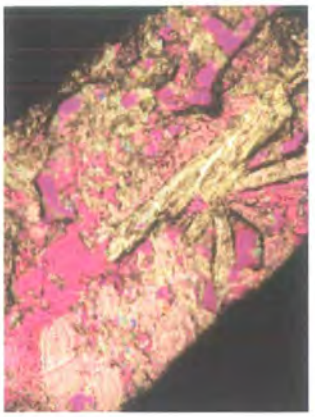

Figure 5.9l. Sample I.

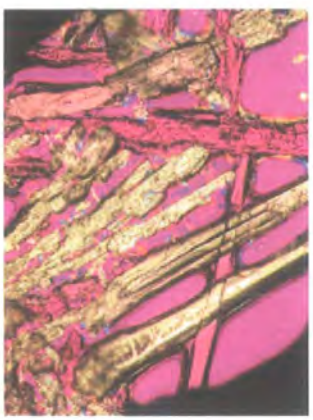

Figure 5.9b. Sample B.

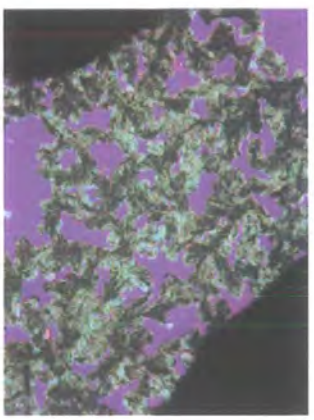

Figure 5.9e. Sample E.

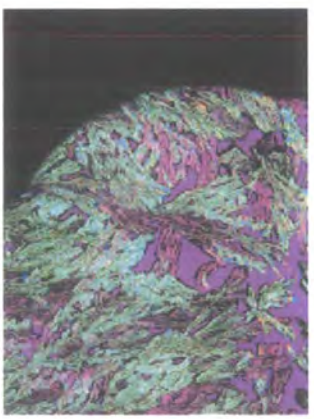

Figure 5.9h. Sample H.

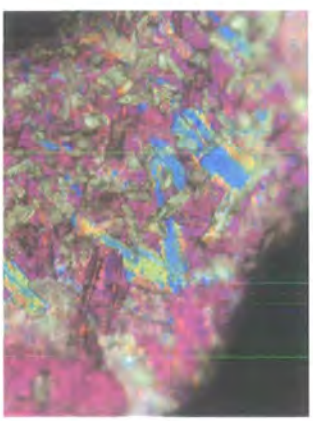

Figure 5.9a. Sample A.

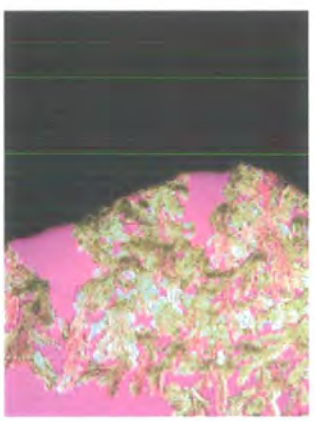

Figure 5.9d. Sample D.

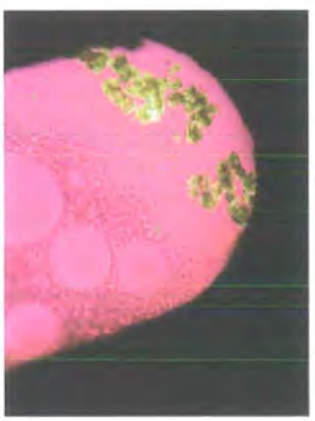

Figure 5.9g. Sample G.

Figures 5.9a –5.9 i. Images viewed at low magnification with crossed polarisers and a red tint plate of crystal growth in oil-in-water emulsions doped with 2-aminohexadecanoic acid and various water soluble additives. Scale 1 cm = 400 μm.

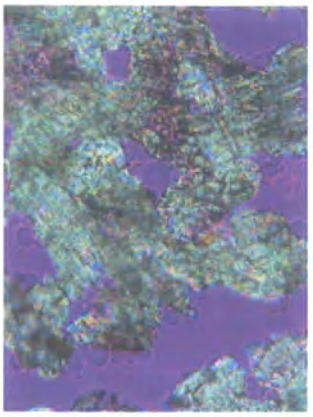

Figure 5.10c. Sample C.

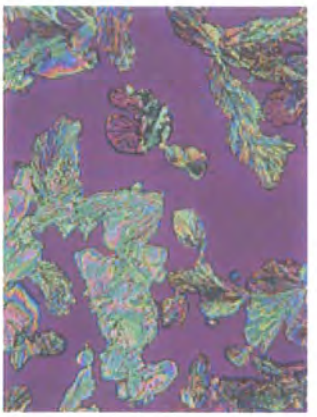

Figure 5.10f. Sample F.

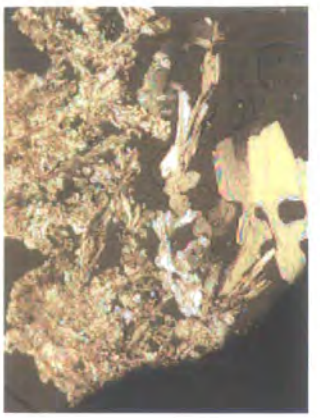

Figure 5.10i. Sample I.

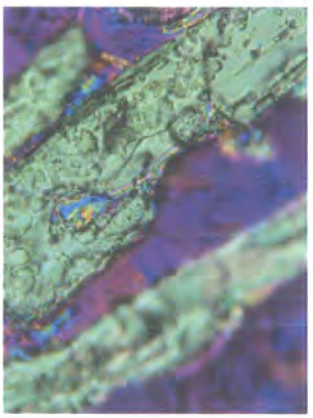

Figure 5.10b. Sample B.

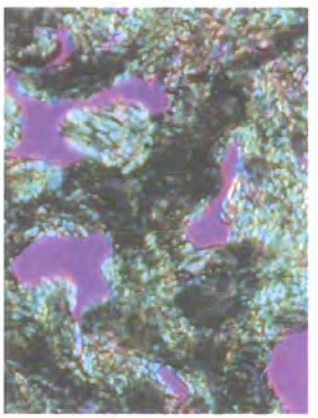

Figure 5.10e. Sample E.

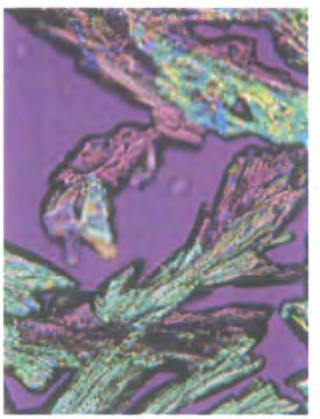

Figure 5.10h. Sample H.

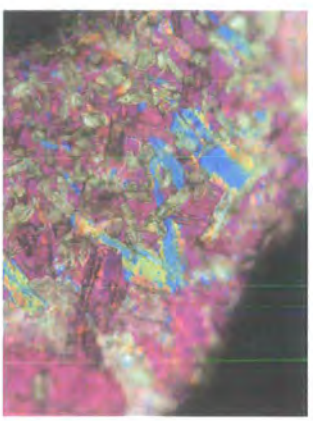

Figure 5.10a. Sample A.

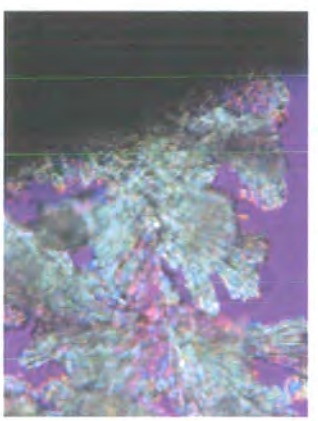

Figure 5.10d. Sample D.

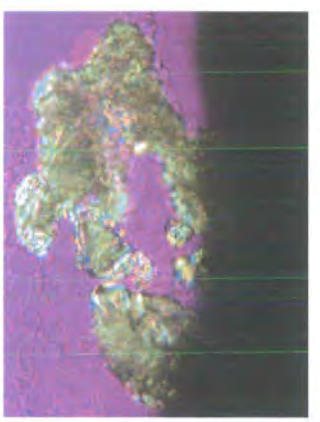

Figure 5.10g. Sample G.

Figures 5.10a –5.10i. Images viewed at high magnification with crossed polarisers and a red tint plate of crystal growth in oil-in-water emulsions doped with 2-aminohexadecanoic acid and various water soluble additives. Scale 1 cm = 80 μm.

Water-in-Oil Emulsions

Water-in-oil emulsions were prepared at an oil fraction $F_O = 0.80$ with 0.1 wt% 2-aminohexadecanoic acid. The amount of Span 80 surfactant used was 10% of total emulsion mass, which was premixed with the decane. The typical droplet size range was 40 - 100 μm, and the results of the glycine crystallisation are summarised in table 5.5.

Sample	Additive	Polymorph	T_{cryst} / °C	Δμ at T_{cryst}	Crystal morphology	Figure
J	None	β	15	36%	High density of spherical aggregates.	5.11a & 5.12a
K	L-Leucine	β	-	-	No crystal growth.	5.11b & 5.12b
L	DL-Leucine	β	17	30%	Spherical aggregates.	5.11c & 5.12c
M	Acetic acid	β	12	46%	Spherical aggregates.	5.11d & 5.12d
N	NaCl	β	18	27%	Spherical aggregates.	5.11e & 5.12e
O	L-Leu AcOH	β	10	54%	Chunky in drops.	5.11f & 5.12f
P	L-Leucine NaCl	β	-	-	No crystal growth.	5.11g & 5.12g
Q	DL-Leucine Acetic acid	β	15 - 12	36-46%	Small spherical aggregates.	5.11h & 5.12h
R	DL-Leucine NaCl	β	16	33%	Spherical aggregates.	5.11i & 5.12i

Table 5.5. Composition of water-in-oil emulsions, prepared with 2-aminohexadecanoic acid and various water soluble additives.

Some of the samples (K & P) show no crystallisation at all, even on cooling to 0 °C. Those samples that have crystallised show evidence of restricted growth, resulting in spherical aggregates. Significantly, not one of these samples gives X-ray diffraction data consistent with the α form of glycine, as would have been expected had the insoluble 2-aminohexadecanoic acid additive induced the crystallisation.

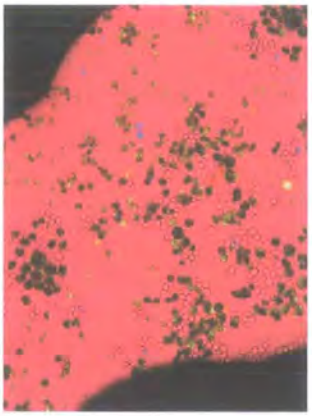

Figure 5.11a. Sample J.

No crystal growth observed.

Figure 5.11b. Sample K.

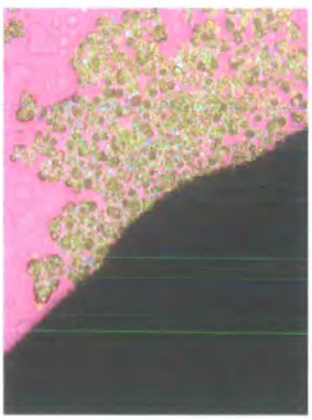

Figure 5.11c. Sample L.

Figure 5.11d. Sample M.

Figure 5.11e. Sample N.

See figure 5.13.

Figure 5.11f. Sample O.

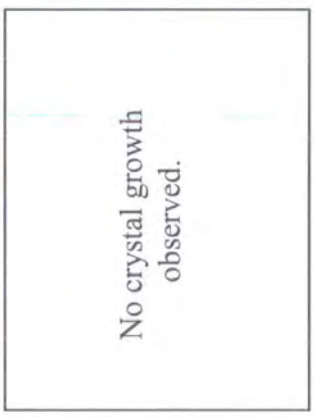

Figure 5.11g. Sample P.

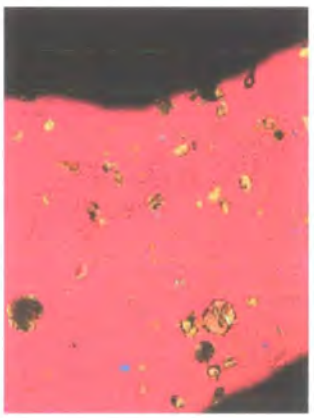

Figure 5.10h. Sample Q.

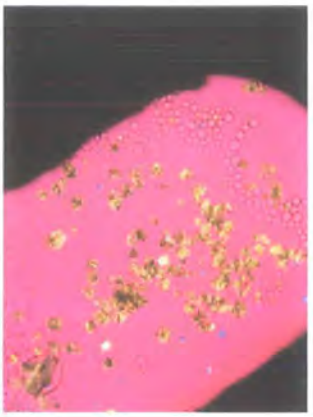

Figure 5.11i. Sample R.

No crystal growth observed.

Figures 5.11a –5.11i. Images viewed at low magnification with crossed polarisers and a red tint plate of crystal growth in water-in-oil emulsions doped with 2-aminohexadecanoic acid and various water soluble additives. Scale 1 cm = 400 μm.

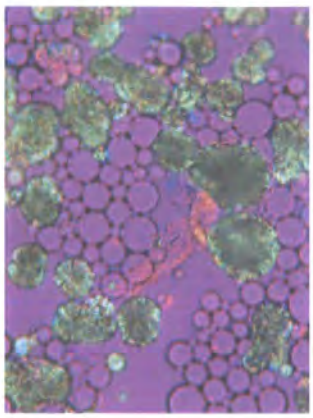

Figure 5.12c. Sample L.

See figure 5.13.

Figure 5.12f. Sample O.

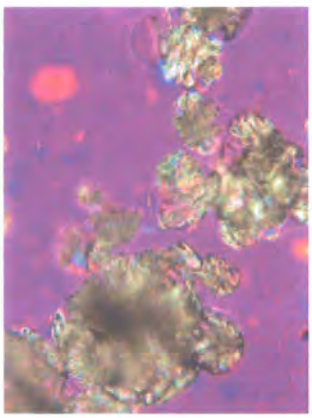

Figure 5.12i. Sample R.

No crystal growth observed.

Figure 5.12b. Sample K.

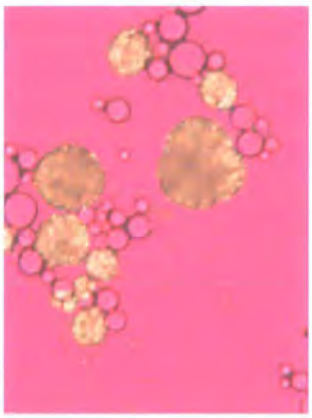

Figure 5.12e. Sample N.

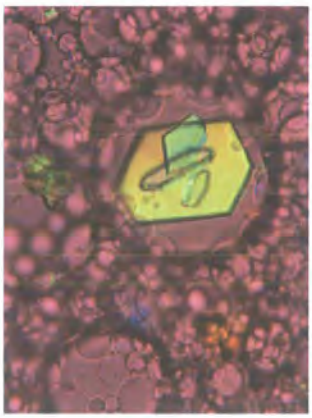

Figure 5.12h. Sample Q.

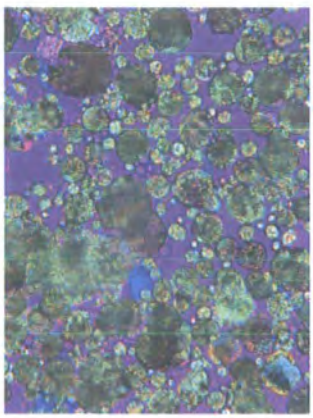

Figure 5.12a. Sample J.

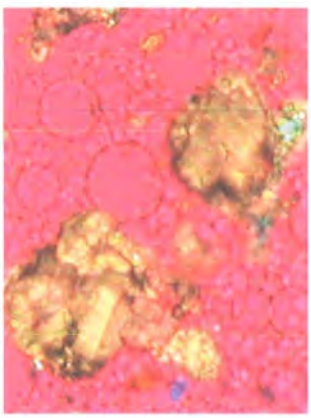

Figure 5.12d. Sample M.

No crystal growth observed.

Figure 5.12g. Sample P.

Figures 5.12a –5.12i. Images viewed at high magnification with crossed polarisers and a red tint plate of crystal growth water-in-oil emulsions doped with 2-aminohexadecanoic acid and various water soluble additives. Scale 1 cm = 80 μm.

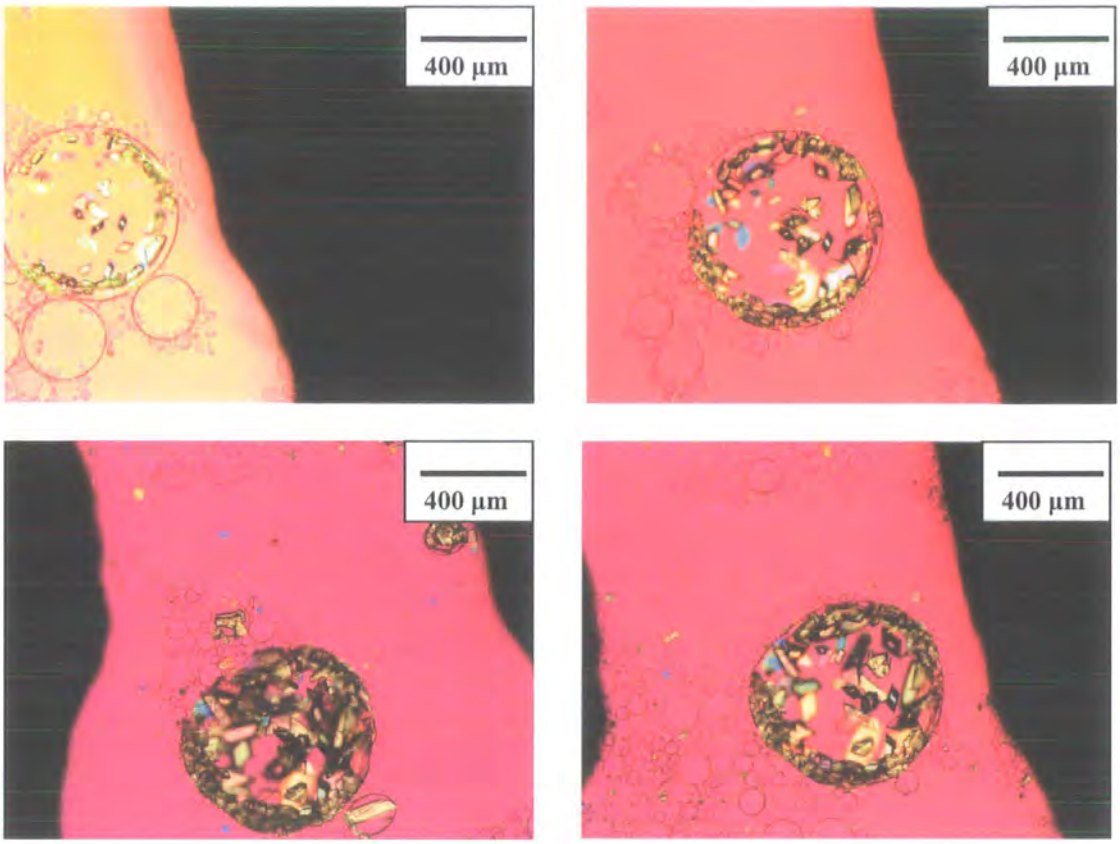

Figures 5.13 a – d (clockwise from top left). Sample O. Crystallisation within a large aqueous droplet over time, which indicates the interfacial nature of the crystallisation. These are viewed with crossed polarisers and a red tint plate.

The images from sample O, which contains the additives L-leucine and acetic acid provide a particular insight into the source of the crystallisation. Figures 5.13a – d show the gradual crystallisation of glycine, which does appear to be induced at the oil-aqueous interface. This would imply that the crystallisation is induced by the Span 80 surfactant, or less likely, the 2-aminohexadecanoic acid. The nucleation is more likely to be induced by the Span 80, however, because this is present at a much higher concentration, and the β polymorph rather than the α-polymorph of glycine is obtained. A similar occurrence was viewed in one area of sample R, see figure 5.14.

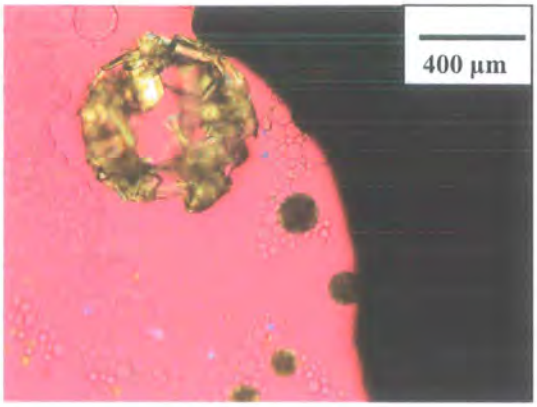

Figure 5.14. Crystal growth induced inside an aqueous droplet, with the crystallisation probably induced by the Span 80 surfactant at the oil-aqueous interface. These are viewed with crossed polarisers and a red tint plate.

Figure 5.15 shows crystallisation within a large droplet (diameter ~ 400 µm). In contrast to figures 5.13 and 5.14, this would appear to have been induced by an impurity within the droplet, followed by crystal growth of a number of crystallites towards the droplet edge.

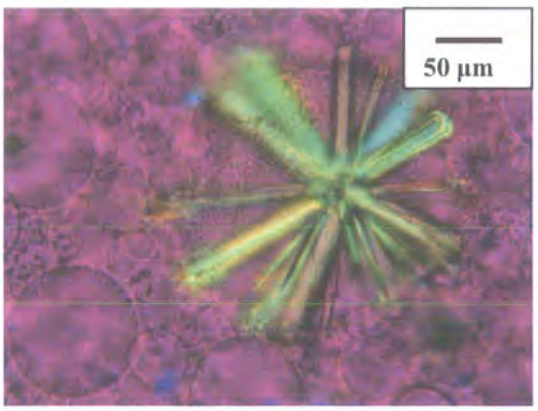

Figure 5.15. Glycine crystallisation induced by an impurity. Viewed with crossed polarisers and a red tint plate.

5.5.3 Decane/Supersaturated Aqueous Glycine Emulsions Stabilised with 2-Aminohexadecanoic Acid and Decanol

Medium chain length alcohols are commonly used as cosurfactants[21-23], particularly in the case of microemulsions. Samples were made to investigate whether decanol can

stabilise decane/aqueous supersaturated glycine emulsions with 2-aminohexadecanoic acid, without needing the Span 80 surfactant that induced the β-nucleation.

Table 5.6 shows the composition of the samples prepared.

2-Aminohexadecanoic acid	Decanol	F_O	Comments
13.8 mg	20.5 mg	0.25	White, viscous
12.8 mg	22.4 mg	0.50	White, viscous
10.0 mg	20.0 mg	0.75	White, less viscous.

Table 5.6. Composition of emulsions prepared that were stabilised by 2-aminohexadecanoic acid and decanol.

To the naked eye, these samples were stable, white emulsions, albeit rather viscous. When viewed under the microscope, however, the samples show a gritty appearance at the oil-aqueous interface due to undissolved 2-aminohexadecanoic acid (figure 5.16). Reducing the amount of amino acid simply destabilised the emulsions.

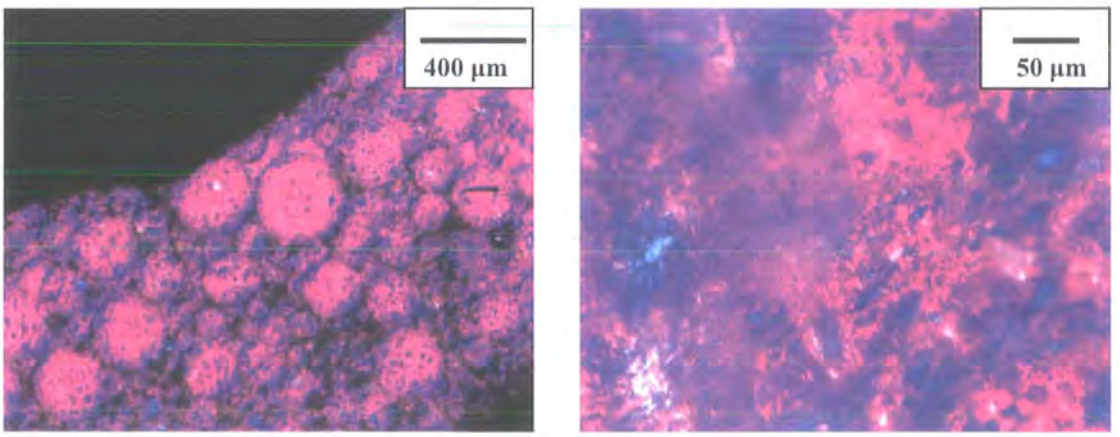

Figure 5.16. 2-aminohexadecanoic acid and decanol stabilised emulsions. Undissolved 2-aminohexadecanoic acid is pictured. Viewed with crossed polarisers and a red tint plate.

One of these decanol stabilised samples did show crystallisation on cooling to 10 °C, but for most samples is was not possible to see the change in birefringence due to the presence of undissolved 2-aminohexadecanoic acid. The 2-aminohexadecanoic acid studies were not therefore pursued further, as there is no evidence in these studies that it has successfully induced glycine crystallisation at the oil-water interface.

5.6 Mixtures of Span and Tween Surfactants

The previous work suggests that the polymorph of glycine nucleated cannot be modified with water-soluble additives or the 2-aminohexadecanoic acid, because the Span 80 surfactant dominates the interfacial areas where the crystallisation is induced. It would be interesting, however, to consider a combination of Span/Tween surfactants, especially as a combination of surfactants typically stabilises emulsions better than one surfactant alone, see e.g. reference[24], and the phase inversion can also be studied.

5.6.1 Pure Tween Surfactants

Tween surfactants were shown in section 5.3.1 to be effective nucleators of glycine. Figure 5.17 shows the extensive crystallisation for this case. The crystals were thickly embedded in the emulsion, and had to be removed for XRD analysis, which showed evidence for mostly α-glycine, but a weak feature due to the β-form was also observed.

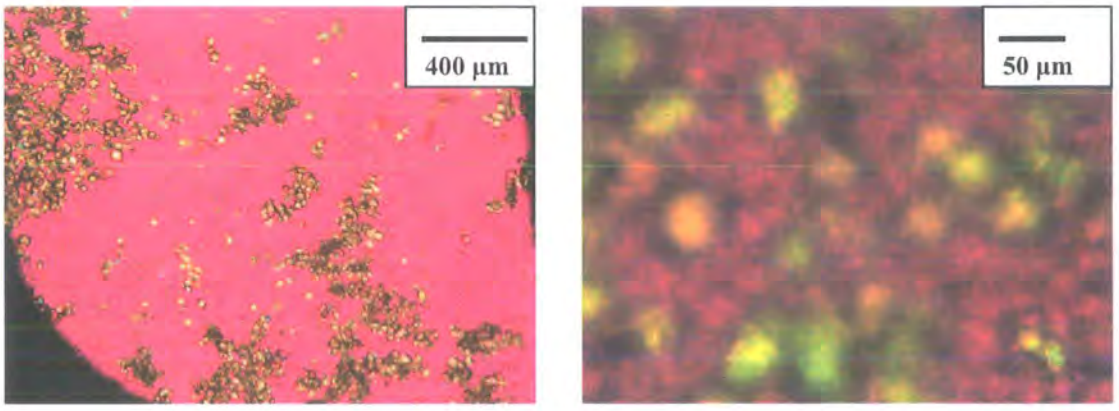

Figure 5.17 a & b. Crystallisation in a Tween stabilised emulsion viewed with low (left) and high (right) magnification with a red tint plate and crossed polarisers.

Figure 5.18 shows the Tween 20 stabilised emulsion, which also shows the presence of lyotropic phase liquid crystals. Once again, these systems gave X-ray diffraction data consistent with α-glycine, but a weak feature due to the β-form was also observed. The initial crystals appear to be of the α form; unfortunately the possibility that the crystals have changed from the β form after removal from the emulsion cannot be discounted entirely, however, especially given the presence of a weak peak at $2\theta = 24^{\circ}$ attributed to the β-form of glycine.

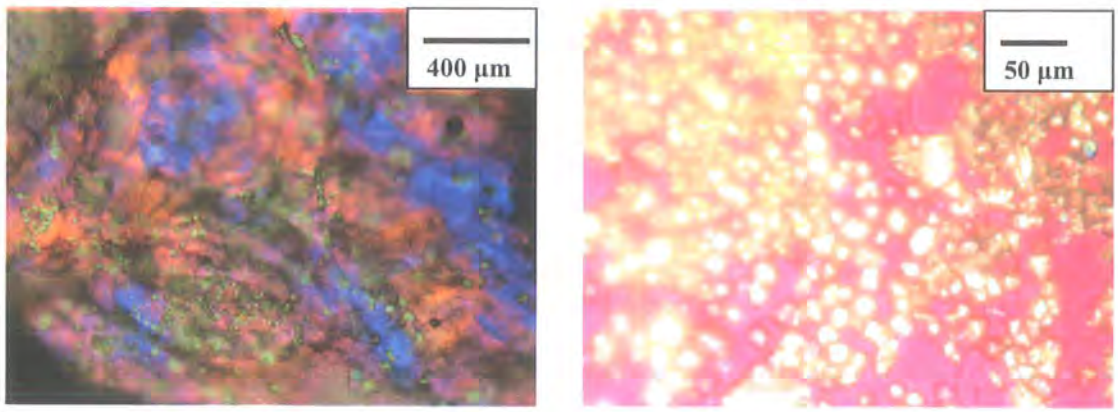

Figure 5.18 a & b. Crystallisation in a Tween stabilised emulsion with some lyotropic liquid crystal character viewed with low (left) and high (right) magnification with a red tint plate and crossed polarisers.

5.6.2 Span 80/Tween 80

The inversion from a water-in-oil to an oil-in-water emulsion was represented by Vander Kloet and Schramm[11] as a linear line between oil fractions, F_O of 0.27 and 0.63. This o/w to w/o inversion at a given HLB (mixture of Span 80/Tween 80 surfactant) can therefore be related to the oil fraction by:

$$F_O = -0.0264HLB + 0.746 \qquad \text{[Eqn. 5.2]}$$

Oil-in-water and water-in-oil emulsions were made in duplicate and the crystallisation temperatures on cooling noted. The polymorph of the resulting crystals was determined by X-ray diffraction, and samples were also made in duplicate at the point where inversion from o/w to w/o is expected.

Span 80/Tween 80 HLB = 6.4

An HLB of 6.4 for the Span 80/Tween 80 surfactant mixture corresponds to a composition of 80% Span. The surfactant was 10% by mass of the total emulsion. The w/o and o/w emulsions show droplet diameters of 50 and 60 μm, respectively. As discussed earlier, the sample prepared at the phase inversion shows a mixture of droplet sizes of approximately 20 and 80 μm. The results of the glycine crystallisation in these systems are summarised in table 5.7.

F_O	Droplet Diameter / μm	Phase	1st Analysis		2nd Analysis		Polymorph
			T_{cryst} / °C	Δμ at T_{cryst}	T_{cryst} / °C	Δμ at T_{cryst}	
0.58	20 & 80	Inversion	None	-	None	-	-
0.80	50	w/o	~10	54%	None	-	α + β
0.20	60	o/w	15	36%	15	36%	α + β

Table 5.7. Summary of observations for different phases of samples stabilised with Span 80/Tween 80 (HLB = 6.4).

For this system, an oil fraction, F_O, of 0.58 is required to give a sample at the phase inversion. The samples prepared at this composition did not crystallise, even on cooling to 0 °C, where significant separation of the oil and water is observed.

The w/o (figure 5.19) and o/w (figure 5.20) systems give crystal morphologies similar to that for the pure Span 80 stabilised systems presented earlier. The w/o are restricted agglomerates of crystals, while the o/w samples have enjoyed unrestricted growth, and have an elongated morphology, although the morphology is less distinct than the rod-like shapes obtained in pure Span 80 o/w emulsions. X-ray diffraction analysis reveals these crystals are a mixture of the α and β polymorph.

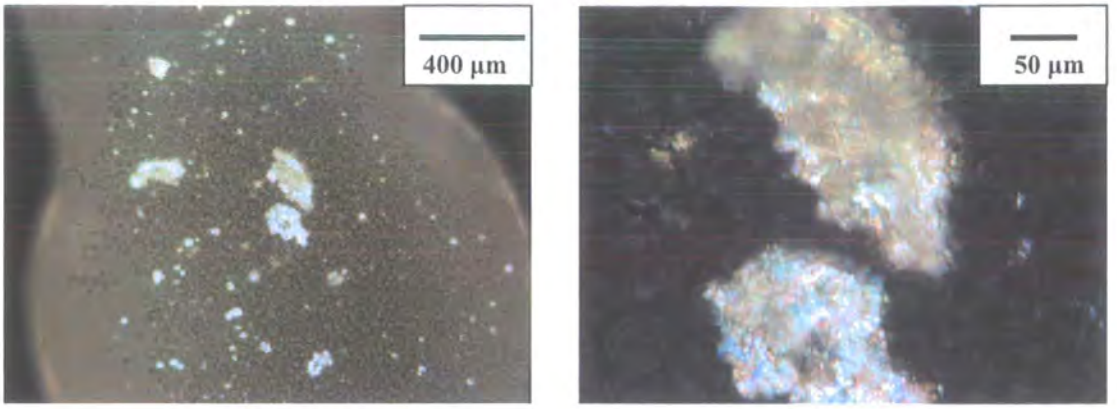

Figure 5.19 a & b. Crystallisation in w/o emulsion viewed with low and high magnification with crossed polarisers.

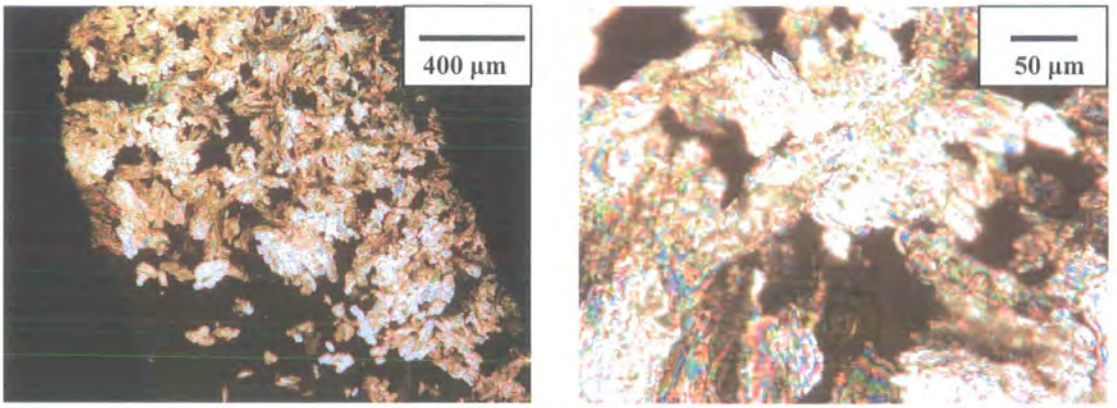

Figure 5.20 a & b Crystallisation in o/w emulsion viewed with low and high magnification with crossed polarisers.

Span 80/Tween 80 HLB = 13.9

An HLB of 13.9 for the Span 80/Tween 80 corresponds to a composition of only 10% Span 80. The surfactant was present at 10% of total emulsion mass. The data acquired for this system are summarised in table 5.8.

F_O	Droplet Diameter / μm	Phase	1st Analysis		2nd Analysis		Polymorph
			T_{cryst} / °C	Δμ at T_{cryst}	T_{cryst} / °C	Δμ at T_{cryst}	
0.38	20, 100	Inversion	19	24%	Ambient	10%	α
0.90	40	w/o	Ambient	10%	Ambient	10%	α
0.30	30	o/w	Ambient	10%	Ambient	10%	α + β

Table 5.8. Summary of observations for different phases of samples stabilised with Span 80/Tween 80 (HLB = 13.9).

This system shows rapid crystallisation, which was observed under the microscope as samples were studied immediately after preparation. This spontaneous crystallisation is almost certainly caused by the high (90%) percentage of Tween surfactant.

All samples show an elongated morphology, though the sample prepared at the inversion point and also the w/o emulsions show much smaller crystals. The o/w sample, once again shows unrestricted growth and these crystals show features in the X-ray diffraction consistent with the α-polymorph of glycine; the o/w sample also produces some β polymorphs as well as the α-phase, with the majority of crystals confined to the emulsion droplet size.

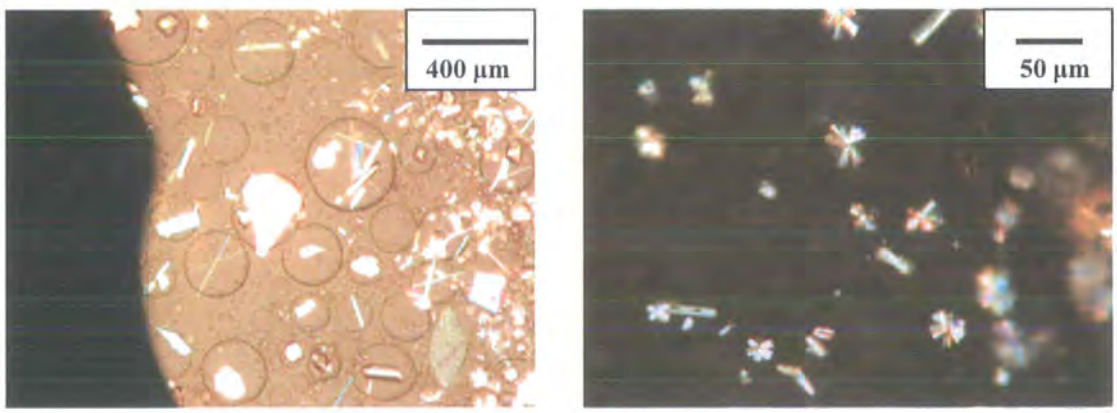

Figure 5.21. Glycine crystallisation at the phase inversion viewed with low and high magnification with crossed polarisers.

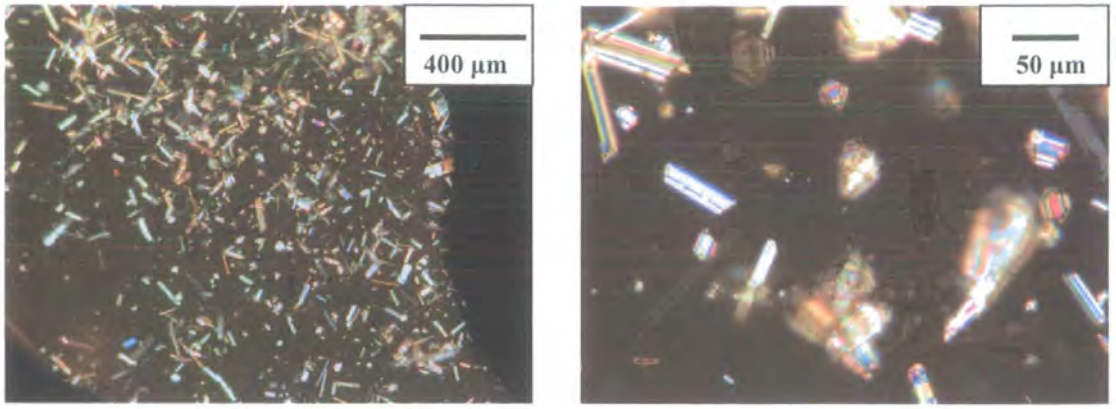

Figure 5.22. Glycine crystallisation in a w/o emulsion viewed with low and high magnification with crossed polarisers.

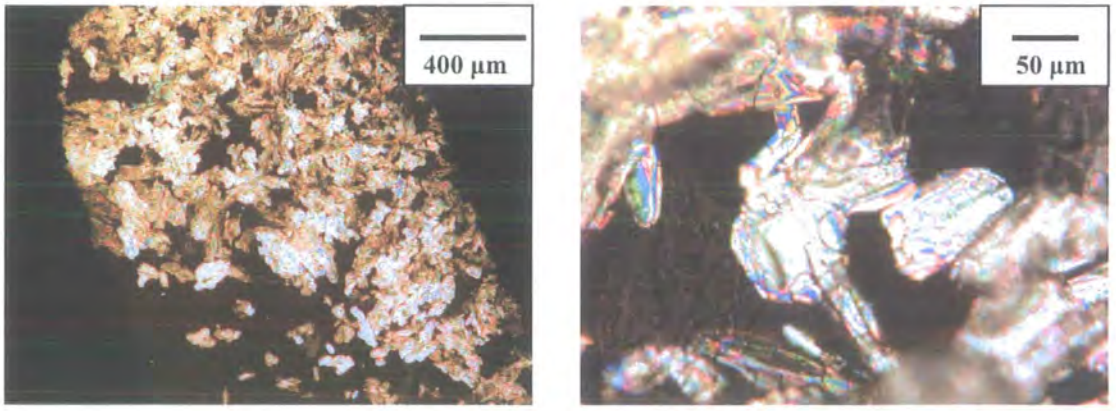

Figure 5.23. Glycine crystallisation in an o/w emulsion viewed with low and high magnification with crossed polarisers.

5.6.3 Span 20/Tween 20

The phase diagram for Span 20/Tween 20 surfactants is more complex and is shown in figure 5.22. Experiments were undertaken to exploit the phase inversion illustrated by arrow 4 in figure 5.24. The transition illustrated by arrow 3 was not attempted, as this requires a large proportion of Tween surfactant, which is a powerful nucleator of glycine.

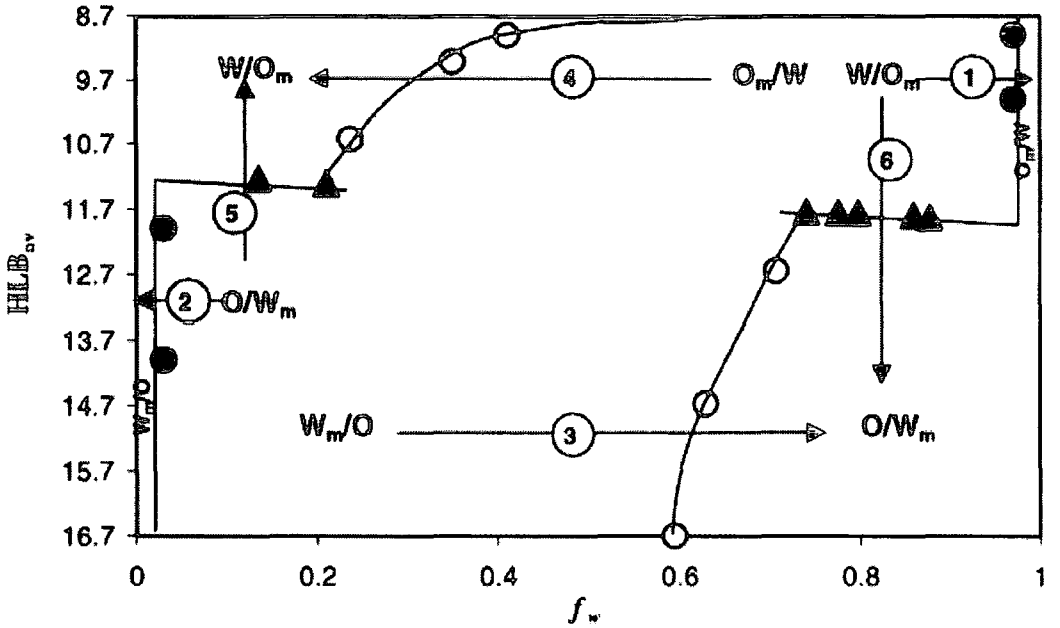

Figure 5.24. Phase behaviour map[10] for p-xylene/water emulsions with 5.0 wt% Span 20/Tween 20. Included with the kind permission of Prof. Brian Brooks, Dept. of Chemical Engineering, University of Loughborough.

Span 20/Tween 20 HLB = 10.7

An HLB of 10.7 for the Span 20/Tween 20 surfactant mixture corresponds to 75% Span 80. The surfactant was present at 10% of total emulsion mass and the results are summarised in table 5.9.

F_O	Droplet Diameter / μm	Phase	1st Analysis		2nd Analysis		Polymorph
			T_{cryst} / °C	Δμ at T_{cryst}	T_{cryst} / °C	Δμ at T_{cryst}	
0.75	30-80	Inversion	None	-	None	-	N/A
0.80	40	w/o	16	33%	5	77%	β
0.60	30	o/w	22	17%	17	30%	β

Table 5.9. Summary of observations for different phases stabilised by Span 20/Tween 20 (HLB = 10.7).

For this system, the o/w to w/o inversion is expected at ~75% oil, where crystallisation did not occur on cooling the sample, until the sample settled into separate decane and aqueous phases. The w/o emulsion (see figure 5.25) showed rapid crystallisation, which gives constricted β-phase crystals, albeit at a very high density, and not confined to the emulsion droplet size.

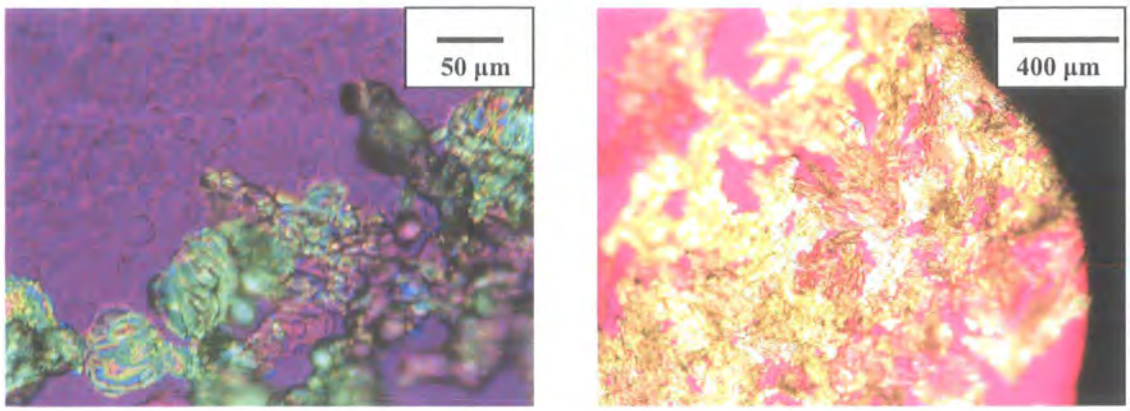

Figure 5.25. Glycine crystallisation in a w/o emulsion stabilised with Span 20/Tween 20 (HLB = 10.7) viewed with low and high magnification with crossed polarisers.

Figure 5.26 shows crystallisation from an o/w emulsion, where crystallisation occurred with less aggressive cooling and resulted in needle formation. This is typical of β-phase glycine, which was confirmed by a peak observed at $2\theta = 24°$ in the X-ray analysis.

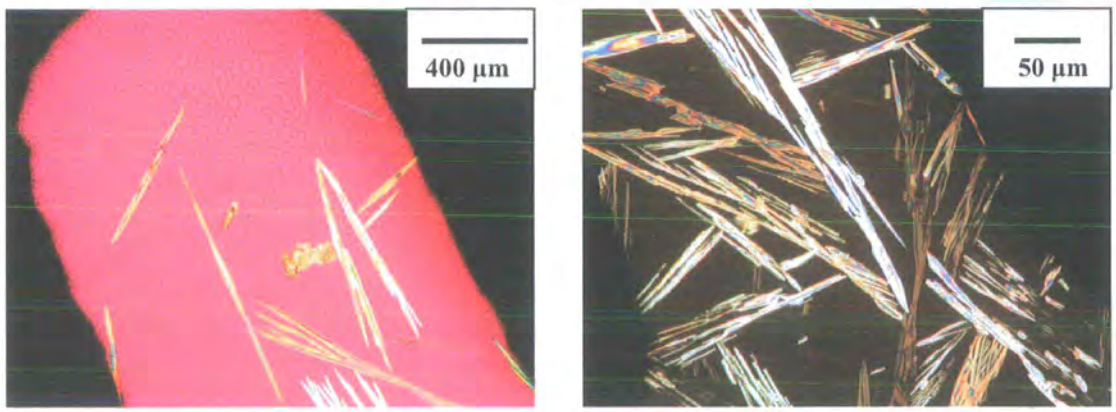

Figure 5.26. Glycine crystallisation in an o/w emulsion stabilised with Span 20/Tween 20 (HLB = 10.7) viewed with low and high magnification with crossed polarisers.

Span 20/Tween 20 HLB = 9.7

Tween 20 alone induces α-phase glycine crystallisation, hence this mixed system at HLB = 9.7 was attempted as there is less Tween required. The surfactant composition is 87.5% Span 20, and the surfactant is present at 10% of total emulsion mass.

The results from this experiment are summarised in table 5.10.

F_O	Droplet Diameter / μm	Phase	1st Analysis		2nd Analysis		Polymorph
			T_{cryst} / °C	Δμ at T_{cryst}	T_{cryst} / °C	Δμ at T_{cryst}	
0.70	20 & 80	Inversion	None	-	5	77%	N/A
0.78	40	w/o	13	43%	10	54%	β
0.55	30	o/w	18	27%	16	33%	β

Table 5.10. Summary of observations for different phases stabilised with Span 20/Tween 20 (HLB = 9.7).

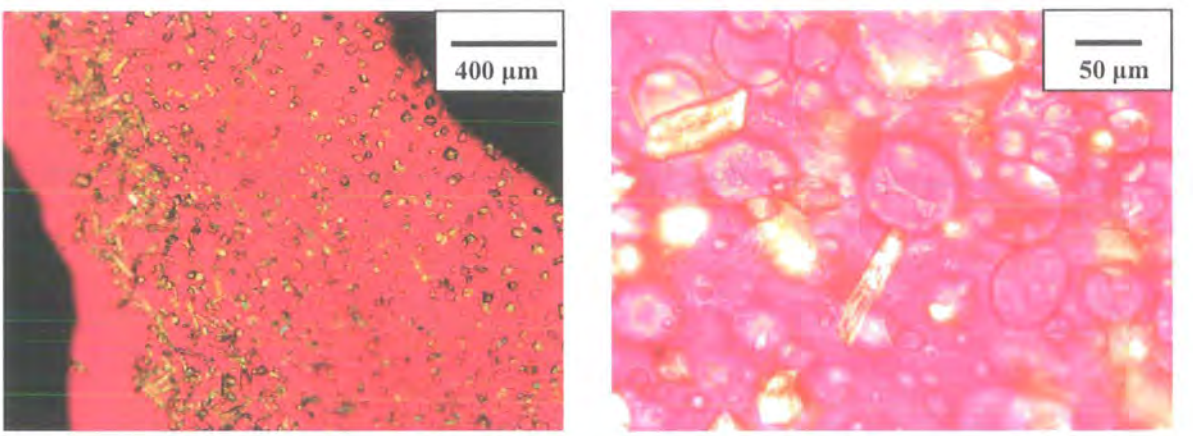

Figure 5.27. Glycine crystallisation at the phase inversion stabilised with Span 20/Tween 20 (HLB = 9.7) viewed with low and high magnification with crossed polarisers.

Figure 5.27 shows some crystallisation for the phase inversion sample, on aggressive cooling to 5 °C. The w/o emulsions in figure 5.28 show needles, or side-on oriented plates confined to the aqueous droplets, whereas an equivalent w/o sample pictured in figure 5.29 shows the familiar spherical aggregates, with subsequent crystallisation

around the perimeter of the spherical aggregates. The o/w emulsion (figure 5.30) gives crystals that are elongated, due to unrestricted growth.

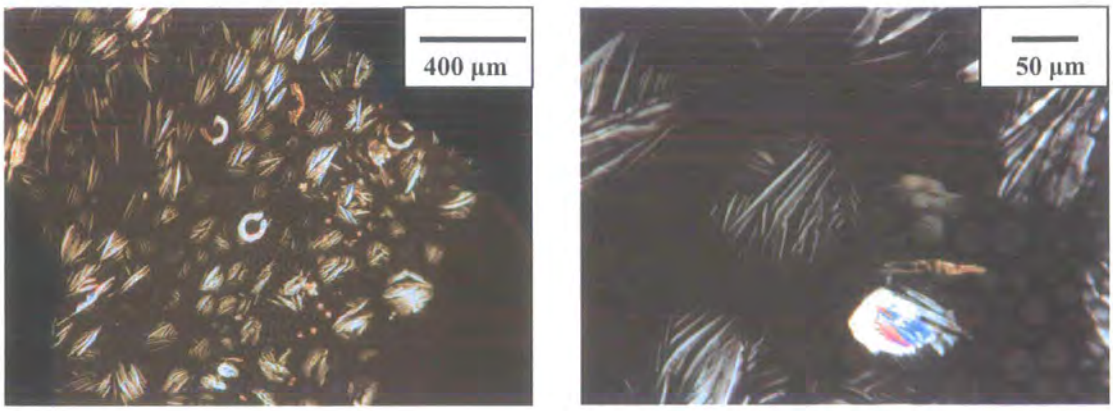

Figure 5.28. Glycine crystallisation in a w/o emulsion stabilised with Span 20/Tween 20 (HLB = 9.7) viewed with low and high magnification with crossed polarisers.

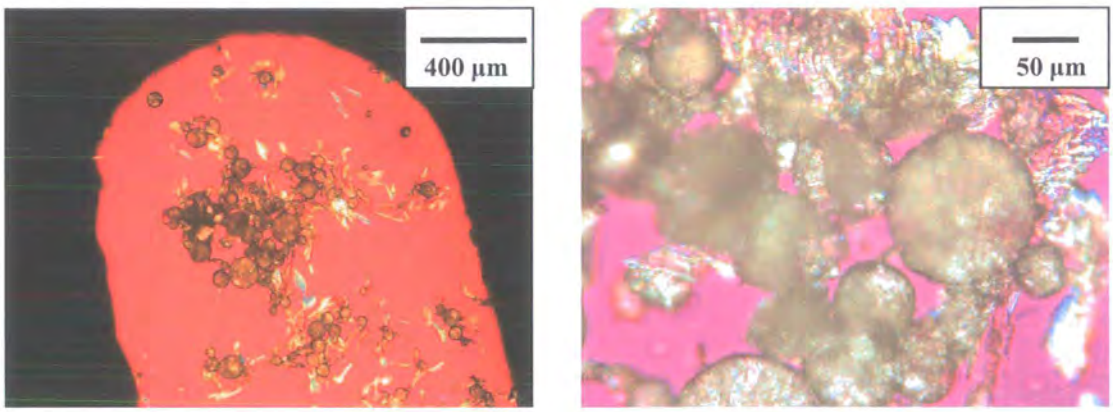

Figure 5.29. Glycine crystallisation in a w/o emulsion stabilised with Span 20/Tween 20 (HLB = 9.7 viewed with low and high magnification with crossed polarisers.

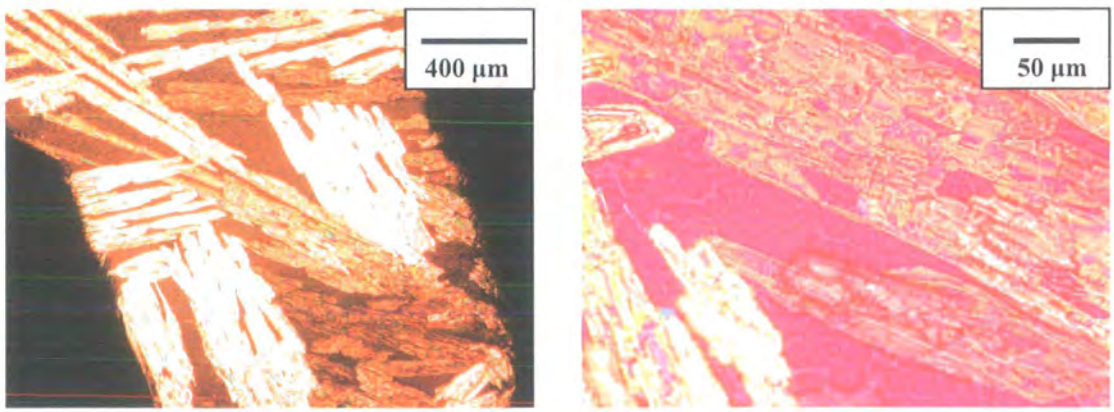

Figure 5.30. Glycine crystallisation in an o/w emulsion stabilised with Span 20/Tween 20 (HLB = 9.7) viewed with low and high magnification with crossed polarisers.

5.6.4 Conclusions of Mixed Surfactant Experiments

Consider the data summary detailed in table 5.11, which provides the supersaturation at the crystallisation temperatures reported for each system stabilised by Span/Tween surfactants. Excluding the data for Span 80/Tween 80 (HLB = 13.9), where crystallisation is virtually instantaneous, the supersaturation at T_{cryst} is lower in all cases for the oil-in-water emulsions than the water-in-oil emulsions. The data must be treated with some caution, however, because it is more challenging to assess T_{cryst} for the w/o emulsions where nucleation occurs in localised pockets, whereas crystallisation in cases where the aqueous phase is continuous, proceeds rapidly and is less subjectively assessed.

System	Emulsion Type	$\Delta\mu$ at T_{cryst} # 1	$\Delta\mu$ at T_{cryst} # 2
Span 80 /	PI	-	-
Tween 80	w/o	54%	-
HLB = 6.4	o/w	36%	43%
Span 80 /	PI	24%	10%
Tween 80	w/o	10%	10%
HLB = 13.9	o/w	10%	10%
Span 20 /	PI	-	-
Tween 20	w/o	33%	77%
HLB = 10.7	o/w	17%	30%
Span 20 /	PI	-	77%
Tween 20	w/o	43%	54%
HLB = 9.7	o/w	27%	33%

Table 5.11. Summary of the supersaturation values at the point where crystallisation is observed.

These data are discussed in more detail in the Discussion (section 5.8).

5.7 Octanoic Acid Based Emulsions

It is well known that additives can promote or inhibit crystallisation if a sufficiently strong interaction exists between the additive and part of the crystalline species. If the additive aggregates to form an ordered surface, nucleation is favoured provided that the crystallising material is adsorbed onto this surface. Cooper[25] showed the effect of carboxylic acids on the crystallisation of L-asparagine monohydrate, and showed that octanoic acid inhibited L-asparagine monohydrate crystal growth.

The aim of this section is to investigate whether octanoic acid acts as a glycine crystallisation promoter or inhibitor in emulsions. Samples were prepared as oil-in-water and water-in-oil emulsions with pure Span 80 and Span 20/Tween 20 surfactants.

5.7.1 Emulsions Stabilised with Span 80 Only

Emulsions containing 10% supersaturated aqueous glycine and stabilised with Span 80 were prepared at oil (octanoic acid) fractions of 0.78 and 0.22, which correspond to the water-in-oil and oil-in-water cases, respectively. The mass percentage of surfactant was 9 %, which was premixed with the octanoic acid. The o/w samples show a droplet diameter of typically 20 – 40 μm and for the w/o samples, larger droplets of 50 – 70 μm are observed.

Oil-in-Water Emulsion

Rapid crystallisation occurred on cooling this o/w emulsion sample to 20 °C. When viewed at low magnification, the sample shows elongated crystals, see figure 5.31. This is consistent with the data presented for the decane based emulsions. Examination with higher magnification, however, reveals holes, or a subtle honeycomb structure for the majority of the crystals, presumably where octanoic acid droplets once resided. XRD analysis showed features for this sample consistent with both the α and β polymorphs of glycine.

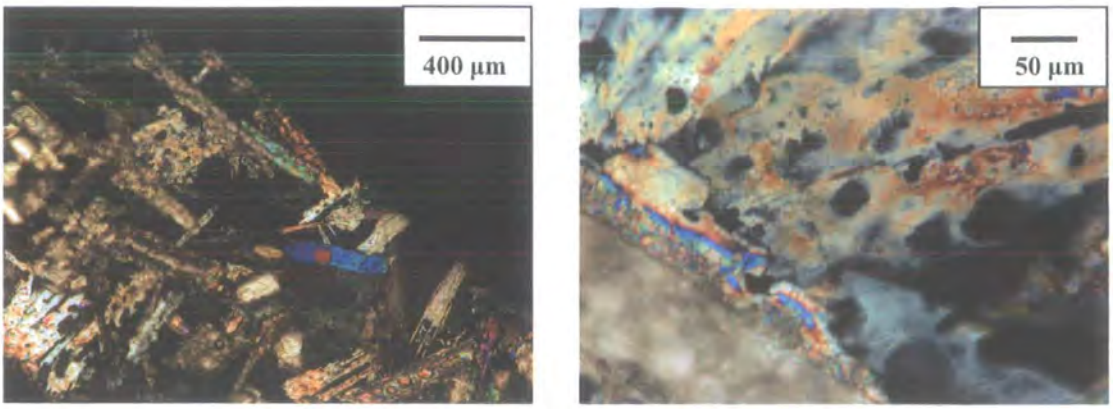

Figure 5.31. Glycine crystals grown in an octanoic acid based o/w emulsion stabilised with Span 80 and viewed with crossed polarisers.

Water-in-Oil Emulsion

For the water-in-oil case, crystallisation was spontaneous with no cooling required. This sample gave crystals of significantly less elongated morphology than the o/w case, see figure 5.32. The crystals showed no evidence for a honeycombed structure, presumably because crystal growth is restricted to the aqueous droplets. As for the oil-in-water case, this sample gave X-ray diffraction features consistent with both the α and β polymorphs of glycine.

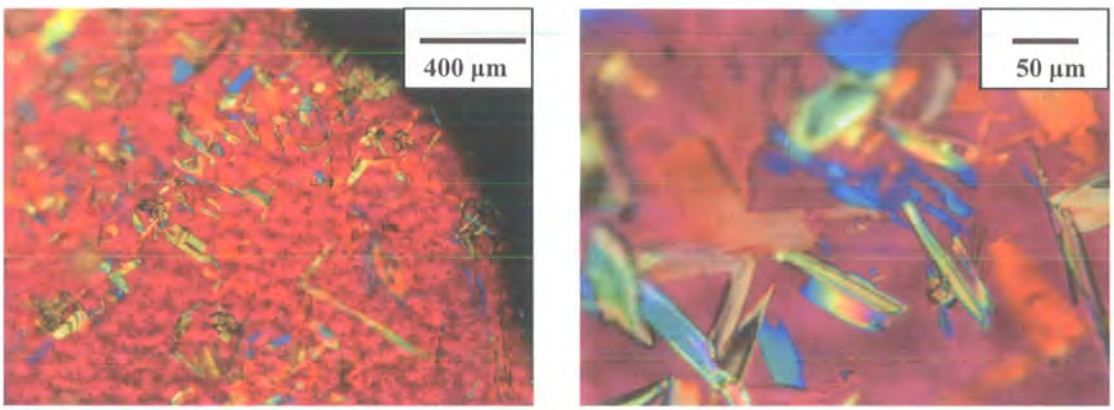

Figure 5.32 Glycine crystals grown in an octanoic acid based w/o emulsion stabilised with Span 80 and viewed with crossed polarisers and a red-tint plate.

Water-in-Oil Emulsion with Added DL-Norleucine

Equivalent samples were prepared with DL-norleucine (0.4 g / 100 cm^3), to see if this would encourage the growth of β-phase spherical aggregates. Crystallisation from the water-in-oil emulsion with this additive results in large, ill defined crystals, see figure 5.33.

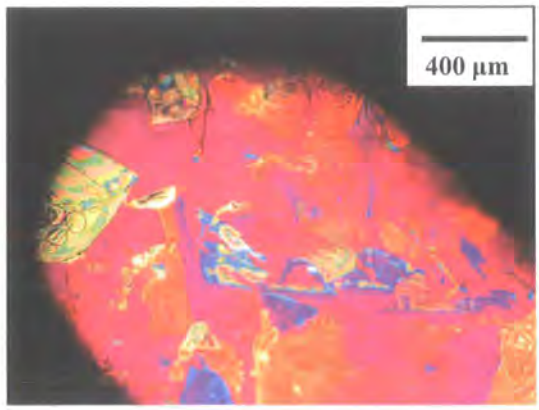

Figure 5.33. Glycine crystals grown in an octanoic acid based w/o emulsion stabilised with Span 80, viewed with crossed polarisers and a red tint plate. The crystal modifier, DL-norleucine was dissolved in the aqueous phase.

These crystals gave X-ray diffraction data consistent with both the α and β polymorphs of glycine.

Oil-in-Water Emulsion with Added DL-Norleucine

The oil-in-water emulsion with added DL-norleucine yielded large platelets of approximately ~ 80 μm along each side (figure 5.34). This sample gave XRD features consistent with the α polymorph of glycine only.

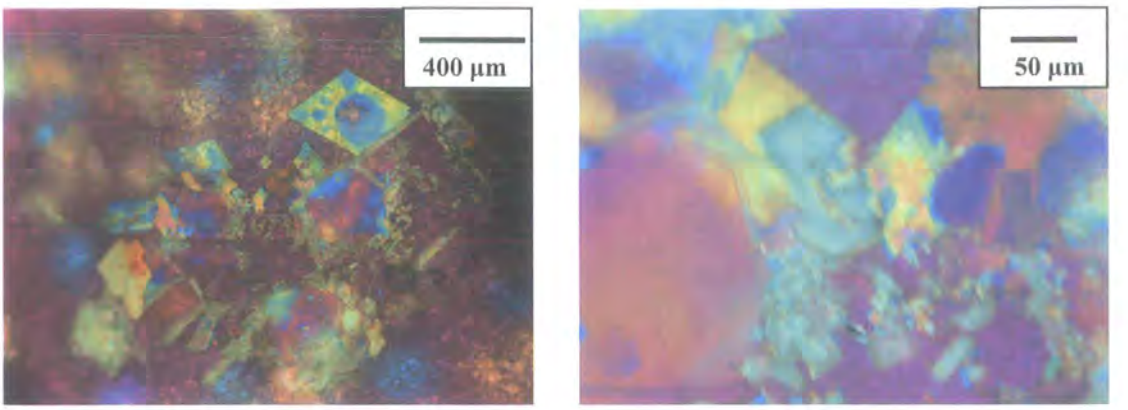

Figure 5.34. Glycine crystals grown in an octanoic acid based o/w emulsion stabilised with Span 80 viewed with crossed polarisers and a red tint plate. The crystal modifier, DL-norleucine was dissolved in the aqueous phase.

5.7.2 Span 20/Tween 20 with Octanoic Acid

The Span 20/Tween 20 mixture had an HLB of 9.7, which corresponds to 87.5% Span 20. The o/w and w/o samples showed a droplet diameter of typically 40 – 60 µm, whereas the samples prepared at the phase inversion show mixed features of approximately 20 and 80 µm diameter.

Oil-in-Water Emulsion

The oil-in-water emulsion was prepared at an oil fraction of 0.30. This sample showed rapid crystallisation on cooling to ~ 22 °C. Approximately 10% of the resulting crystals result in a honeycombed structure such as the one pictured in figure 5.35. X-ray diffraction analysis revealed both the α and β polymorphs of glycine.

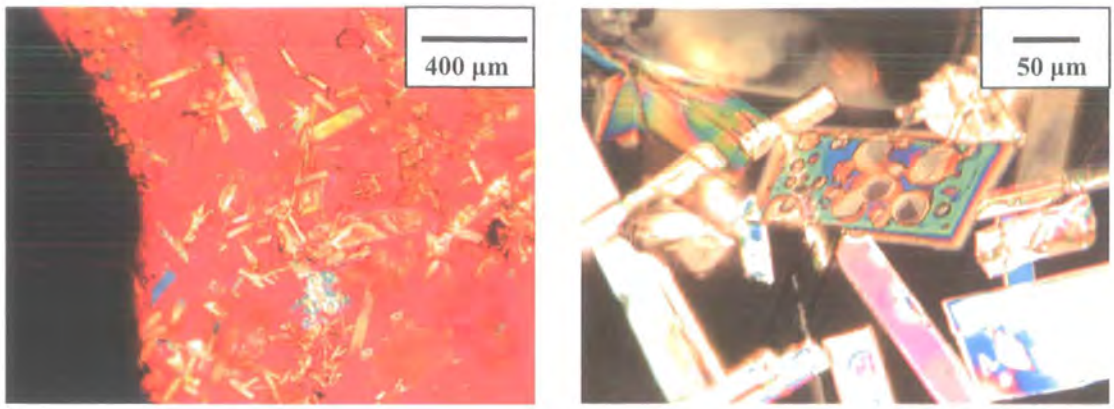

Figure 5.35. Glycine crystals grown in an octanoic acid based w/o emulsion stabilised with Span 20/Tween 20 (HLB = 9.7). These are viewed with crossed polarisers and a red tint plate.

Water-in-Oil Emulsion

The water-in-oil emulsion was prepared at an oil fraction of 0.78.
This sample showed spontaneous crystallisation, see figure 5.36. X-ray analysis reveals both the α and β polymorphs of glycine.

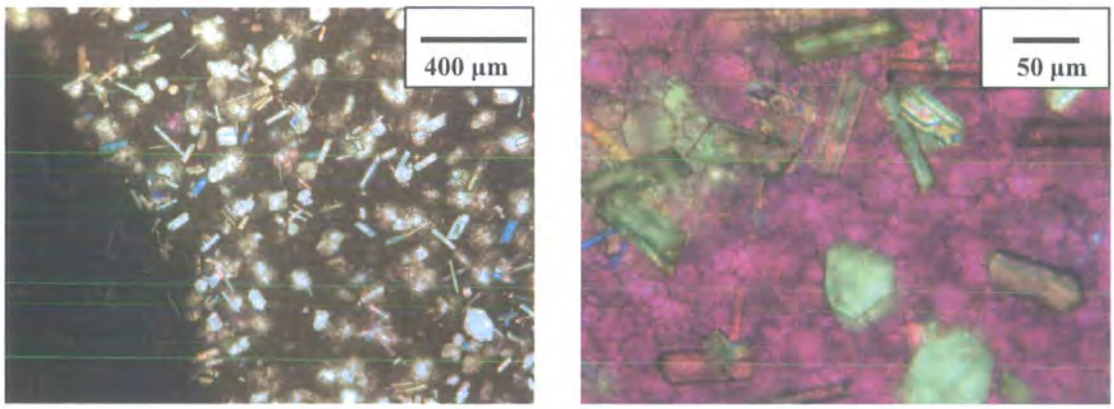

Figure 5.36. Glycine crystals grown in an octanoic acid based o/w emulsion stabilised with Span 20/Tween 20 (HLB = 9.7).

Emulsion at the Phase Inversion

This sample was prepared at an oil fraction = 0.60. This system resulted in extremely rapid crystallisation at room temperature, quicker than the o/w case, which resulted in elongated crystals (figure 5.37), which have encapsulated numerous holes where presumably the octanoic acid emulsion droplets previously resided. At least 70% of the crystals showed this structure.

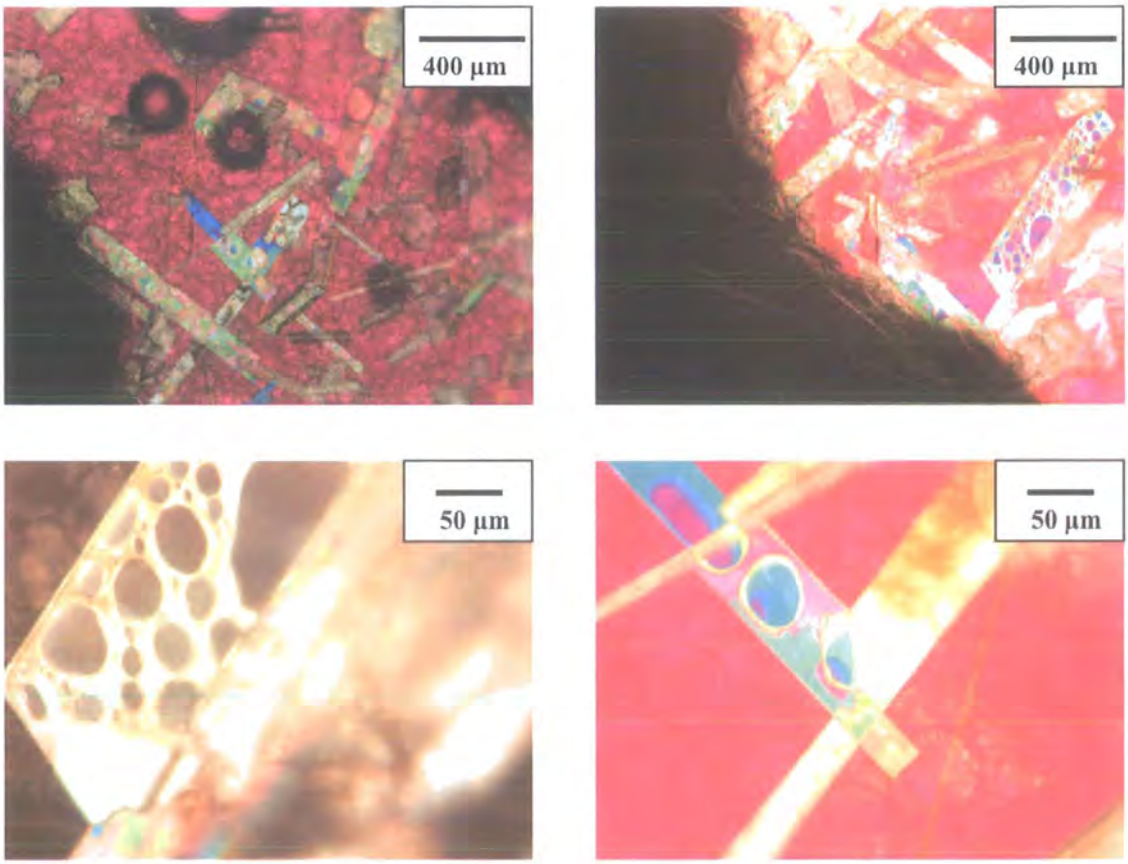

Figure 5.37. Glycine crystals grown in an octanoic acid based sample prepared at the o/w to w/o inversion composition, stabilised with Span 20/Tween 20 (HLB = 9.7). These are viewed through crossed polarisers with a red tint plate.

The density of holes within the crystals is approximately equal to the density of oil droplets in the surrounding emulsion. Consequently, there is no evidence that the crystals are attracting octanoic acid droplets towards its growing matrix, nor is there evidence for significant expulsion of oil droplets from the growing crystal, which occurs for all the glycine crystals previously studied. This finding is consistent with the studies

of Cooper[25] on L-asparagine monohydrate growth from octanoic acid emulsions in which there was sufficient attraction between the growing crystals and emulsion droplets for the droplets to adhere onto the L-asparagine monohydrate crystals and in this case strongly affects the growth morphology. In the glycine studies, all visual evidence implied that the crystal growth proceeds rapidly around the oil droplets, resulting in this unusual morphology. X-ray diffraction analysis of this sample revealed that both α and β glycine crystals were formed.

5.7.3 Conclusions of Octanoic Acid Based Emulsions

Emulsions prepared with Span 80 or Span 20/Tween 20 surfactants with octanoic acid substituted for the decane, show very rapid crystallisation. Samples were studied under the microscope and by X-ray diffraction within moments of sample preparation, and show unusual morphologies. The octanoic acid appears to be acting as a powerful crystallisation promoter, and also adsorbs onto the growing crystals, hence causing the honeycomb structure. The results from the pure Span 80 stabilised emulsions imply that the octanoic acid is promoting crystallisation of the α polymorph, as features for the α polymorph were never seen by X-ray diffraction for the decane based emulsions stabilised by pure Span surfactants. The Span 80 surfactant is still successfully nucleating the β polymorph, though, despite the rapid α-form crystallisation induced by the octanoic acid.

5.8 Discussion of Crystallisation Temperatures

Based on the work of my supervisor, Dr. S.J. Cooper, let us consider the effect of a concave system, i.e. the aqueous-in-oil emulsions on heterogeneous nucleation. Crystallisation in this system can be considered in a similar manner as the convex systems in chapter 4.

5.8.1 Application of Heterogeneous Classical Nucleation Theory to Concave Interfaces

Recall that the volume of a critical nucleus on a planar substrate is given by:

$$V_{HetPlanar} = \frac{4\pi r^{*}_{nuc}{}^{3}}{3} f(\theta_p) \qquad \text{[Eqn. 4.8]}$$

The volume of the critical nucleus at a concave interface is the sum of the dark and light grey areas illustrated in figure 5.38, which is given by:

$$V_{HetConcave} = \frac{4\pi r_{subst}{}^{3}}{3} f(\theta_{p2}) + \frac{4\pi r^{*}_{nuc}{}^{3}}{3} f(\theta_s) \qquad \text{[Eqn. 5.3]}$$

The angles θ_s and θ_{p2} are related via the common chord length CD hence:

$$r^{*}_{nuc} \sin\theta_{p2} = r_{subst} \sin\theta_s \qquad \text{[Eqn. 5.4]}$$

Consideration of the perpendicular distance of the chords AB and CD from the critical nuclei and emulsion droplet spherical surfaces gives:

$$\cos\theta_p = \cos\theta_{p2} - (r_{subst} / r^{*}_{nuc})(1 - \cos\theta_s) \qquad \text{[Eqn. 5.5]}$$

So, knowledge of r_{subst}/r^{*}_{nuc} and θ_p (obtained from the emulsion droplet radius range and the results of the crystallisation behaviour at the planar interfaces) are sufficient to determine θ_s and θ_{p2} and hence the decrease in ΔG^{*}_{Het} in changing from a flat to a spherical substrate.

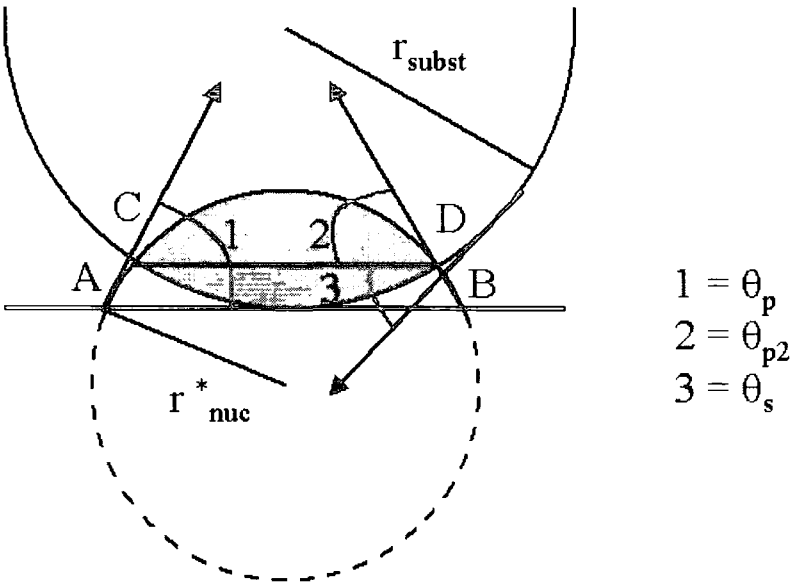

Figure 5.38. Diagram illustrating nucleation of a critical nucleus (of radius r^*_{nuc}) on a concave substrate (of radius r_{subst}). Angles pertinent to the calculations in this section are also illustrated.

Hence for a spherical concave substrate:

$$\Delta G^*_{\text{Het Sphere}} = \frac{16\pi\gamma^3 v^2}{3\Delta\mu^2}\left\{f(\theta_{p2}) + \frac{r_{subst}{}^3 f(\theta_s)}{r^*_{nuc}{}^3}\right\} = \Delta G^*_{Hom}\left\{f(\theta_{p2}) + \frac{r_{subst}{}^3 f(\theta_s)}{r^*_{nuc}{}^3}\right\}$$

[Eqn. 5.6]

and the ratio of the nucleation rates is:

$$\frac{J_{\text{Het Plane}}}{J_{\text{Het Sphere}}} = \frac{\Omega_{\text{Het Plane}}}{\Omega_{\text{Het Plane}}}\exp\left[\frac{\Delta G^*_{Hom}[f(\theta_{p2}) + \{f(\theta_s) r_{subst}{}^3 / r^*_{nuc}{}^3\} - f(\theta_p)]}{kT}\right]$$

[Eqn. 5.7]

$$= \frac{(1-\cos\theta_p)}{(1-\cos\theta_{p2})} \exp\left[\frac{\Delta G_{Hom}{}^{*}[f(\theta_{p2}) + \{f(\theta_s) r_{subst}{}^{3} / r_{nuc}{}^{*3}\} - f(\theta_p)]}{kT}\right]$$

[Eqn. 5.8]

As explained in chapter 4, equation 5.6 is only valid for cap shaped nuclei. The alternative derivation for ΔG^{*}_{Het} that considers the nucleus shape with surface energy and volume terms is illustrated for the concave case below. This is achieved by substituting $(r_{subst} / r^{*}{}_{nuc})^3 f(\theta_{s2})$ for $-(r_{subst} / r^{*}{}_{nuc})^3 f(\theta_s)$ in equation 4.14.

Hence

$$\Delta G_i = -\frac{4}{3v_c}\pi r^{*}{}_{nuc}{}^{3}\Delta\mu[(f(\theta_{p2}) + (r_{subst} / r^{*}{}_{nuc})^3 f(\theta_s)] + 2(1-\cos\theta_{p_2})\pi r^2\gamma_{vx} + 2(1-\cos\theta_s)\pi r_{subst}{}^{2}(\gamma_{sx} - \gamma_{sv})$$

[Eqn. 5.9]

But $$\cos\theta_p = \frac{\gamma_{sv} - \gamma_{sx}}{\gamma_{vx}}$$ [Eqn. 1.17]

so

$$\Delta G_i = -\frac{4}{3v_c}\pi r_{subst}{}^{3}\Delta\mu[(f(\theta_{p2}) + (r_{subst} / r^{*}{}_{nuc})^3 f(\theta_s)] + 2(1-\cos\theta_{p2})\pi r^{*}{}_{nuc}{}^{2}\gamma_{vx} - 2(1-\cos\theta_s)\cos\theta_p\pi r_{subst}{}^{2}\gamma_{vx}$$

[Eqn. 5.10]

Then, for the critical nucleus $r = r^{*} = \frac{2\gamma_{vx}v_c}{\Delta\mu}$

Hence:

$$\Delta G^{*}_{Het} = \frac{8}{3\Delta\mu^2}\pi\gamma_{vx}{}^{3}v_c{}^{2}[1-\cos^3\theta_{p2} - 4(r_{subst}/r_{nuc}{}^{*})^3 f(\theta_s) - 3(1-\cos\theta_s)\cos\theta_p(r_{subst}/r_{nuc}{}^{*})^2]$$

[Eqn. 5.11]

Recall that

$$\Delta G^*_{Het} = k_B T_{cryst} \ln \Omega \qquad \text{[Eqn 4.18]}$$

and

$$\Delta G^*_{Het} = \frac{16\pi\gamma^3 v_c^2}{3\Delta\mu^2} f(\theta_p) = \Delta G^*_{Hom} f(\theta_p) \qquad \text{[Eqn. 1.22]}$$

Hence as in chapter 4, for the cap shaped nucleus:

$$f(\theta_p) + \frac{r_{subst}{}^3 f(\theta_s)}{r^*{}_{nuc}{}^3} = \frac{k_B T_{cryst} \ln \Omega 3\Delta\mu^2}{16\pi\gamma^3 v_c{}^2} \qquad \text{[Eqn. 5.12]}$$

or for the alternative method, considering the volume and surface area terms of the critical nucleus:

$$\frac{1 - \cos^3\theta_{s1} - 4(r_{subst}/r^*{}_{nuc})^3 f(\theta_s) - 3(1-\cos\theta_s)\cos\theta_p (r_{subst}/r^*{}_{nuc})^2}{2} = \frac{k_B T_{cryst} \ln \Omega 3\Delta\mu^2}{16\pi\gamma^3 v_c{}^2} \qquad \text{[Eqn. 5.13]}$$

For the solute case we can substitute for:

$$\Delta\mu = k_B T \ln\left(\frac{s}{s_{sat}}\right) = \frac{\Delta H_{sol}}{N_A}\frac{\Delta T}{T_{sat}} \qquad \text{[Eqn. 5.14]}$$

where ΔH_{sol} is the molar enthalpy of solution and T_{sat} is the saturation temperature.

For the melt case:

$$\Delta\mu = \frac{\Delta H_m}{N_A}\frac{\Delta T}{T_m} \qquad \text{[Eqn. 5.15]}$$

Ω is set to 1 x 10^{-20} $cm^{-2}s^{-1}$ as in chapter 4 and initially, $r^*_{nuc} = \frac{2\gamma v_c}{\Delta\mu}$ is calculated at the planar T_{cryst} temperature and this value is substituted into either equation 5.12 or 5.13 to determine an initial T_{cryst} value for the spherical interface, which is then used to recalculate r^*_{nuc}. The recalculated r^*_{nuc} is then used to determine a more accurate T_{cryst} value for the spherical interface. This process of increasingly accurate r^*_{nuc} and T_{cryst} values is repeated until convergence is achieved.

5.8.2 Calculation of Crystallisation Temperatures

First consider the calculated crystallisation temperatures for ice in table 5.12. As in the previous chapter, these values were calculated assuming T_{cryst} at a planar interface is -4.50 °C. For both the concave and convex cases, the T_{cryst} values predicted by classical nucleation theory only deviate beyond experimental error when a diameter as small as ~250 nm is achieved. At a 250 nm droplet diameter, T_{cryst} at a convex interface is at -4.71 to -4.91 °C depending on whether equation 5.12 or 5.13 is used or at -4.21 to -4.04 °C for the concave case.

Droplet Diameter	Convex (o/w)		Concave (w/o)	
	Using Eqn. 5.12 T_{cryst} / °C	Using Eqn. 5.13 T_{cryst} / °C	Using Eqn. 5.12 T_{cryst} / °C	Using Eqn. 5.13 T_{cryst} / °C
50 nm	-5.67	-6.34	-3.53	-2.04
250 nm	-4.71	-4.91	-4.29	-4.04
1 μm	-4.55	-4.60	-4.44	-4.39
5 μm	-4.51	-4.52	-4.49	-4.47
10 μm	-4.50	-4.51	-4.49	-4.49
50 μm	-4.50	-4.50	-4.50	-4.49

Table 5.12. Calculated crystallisation temperatures for ice at convex (o/w) and concave (w/o) interfaces.

As discussed earlier, these data show that crystallisation at a concave interface is more efficient, assuming sufficient crystallising molecules exist in the droplet to form the critical nucleus.

Table 5.13 illustrates equivalent data for glycine solute crystallisation, assuming a planar crystallisation temperature of 20 °C. This gives a θ_p value of 37.5°. At a diameter of 250 nm, classical nucleation theory predicts T_{cryst} values of 19.73 to 19.51 °C at a convex and 20.19 to 20.43 °C at a concave interface.

The diameters of the emulsions in this chapter are 20 – 80 μm, which is virtually planar at a molecular level. Differences in crystallisation temperatures between the o/w and w/o cases are not therefore expected, and this is borne out by the calculation results shown for the 10 μm and 50 μm diameter data sets, which show no discernible difference in T_{cryst} values irrespective of whether an o/w or w/o system is considered.

Droplet Diameter	Convex (o/w)		Concave (w/o)	
	Using Eqn. 5.12 T_{cryst} / °C	Using Eqn. 5.13 T_{cryst} / °C	Using Eqn. 5.12 T_{cryst} / °C	Using Eqn. 5.13 T_{cryst} / °C
50 nm	18.77	17.88	21.07	22.91
250 nm	19.73	19.51	20.19	20.43
1 μm	19.90	19.84	20.01	20.08
5 μm	19.95	19.94	19.97	19.98
10 μm	19.95	19.95	19.96	19.97
50 μm	19.96	19.96	19.96	19.96

Table 5.13. Calculated crystallisation temperatures for glycine at convex (o/w) and concave (w/o) interfaces.

5.9 Discussion and Conclusions

It is disappointing that a wider variety of emulsion diameters could not be developed for the samples discussed in this chapter. The data do indicate that crystallisation in the water-in-oil emulsions is less favourable than for the oil-in-water ones, but the crystallisation begins in pockets in the former system, hence it is difficult to assess the exact point of crystallisation. In contrast, for oil-in-water systems the crystallisation is rapid and the onset of crystallisation easily identified. Classical nucleation theory predicts only a very small difference between the large diameter convex and concave systems discussed in this chapter, hence if the tentative finding here that a concave interface actually inhibits crystallisation is correct, the theory requires significant improvement. It is interesting that systems at or close to, the phase inversion boundary were typically the poorest nucleators, and this aspect would warrant further studies.

All attempts to modify the polymorph of glycine crystallised in emulsions stabilised by Span surfactants failed, as the β-phase crystallisation is induced at the interfacial region, by the Span surfactants. Emulsions stabilised with Tween surfactants appeared to give the α form, but these emulsions were viscous, hence the crystals were lifted out with a needle. This sample treatment could have exposed the sample to moist air, causing a solvent mediated transformation. However, the fact that mixed Tween and Span surfactant systems also give X-ray diffraction data consistent with α-phase crystals along with β-phase crystals during in-situ XRD analysis does suggest that the Tween surfactants nucleate the α form of glycine. Emulsions made with octanoic acid substituted for decane showed rapid crystallisation, with mostly α form crystals nucleated. In addition, an unusual glycine morphology could be observed for this system, whereby the crystals were perforated with holes, due to adsorbed octanoic acid droplets.

References

(1) Iitaka, Y. *Acta. Cryst.* **1960**, *13*, 35 - 45.

(2) Iitaka, Y. *Proc. Japan Soc.* **1954**, *30*, 109-112.

(3) Chongprasert, S.; Knopp, S. A.; Nail, S. J. *J. Pharm. Sci.* **2001**, *90*, 1720-1728.

(4) Narayan Bhat, M.; Dharmaprakash, S. M. *J. Cryst. Growth* **2002**, *236*, 376-380.

(5) Zaccaro, J.; Matic, J.; Myerson, A. S.; Garetz, B. A. *Crystal Growth & Design* **2001**, *1*, 5-8.

(6) Marsh, R. E. *Acta. Cryst.* **1958**, *11*, 654 - 663.

(7) Iitaka, Y. *Acta. Cryst.* **1961**, *14*, 1 - 10.

(8) Allen, K.; Davey, R. J.; Ferrari, E.; Towler, C.; Jones, M. O.; Pritchard, R. G. *Cryst. Growth & Design* **2002**, *2*, 523-527.

(9) Garetz, B. A.; Matic, J.; Myerson, A. S. *Phys. Rev. Letts.* **2002**, *89*, Art. No. 175501.

(10) Sajjadi, S.; Zerfa, M.; Brooks, B. W. *Colloids & Surfaces A: Physicochem Eng. Aspects.* **2003**, *218*, 241-254.

(11) Vander Kloet, J.; Schramm, L. L. *J. Surfactants & Detergents* **2002**, *5*, 19-24.

(12) Lin, T. J. *J. Soc. Cosmetic Chemists* **1979**, *30*, 167-180.

(13) Takamura, A.; Minowa, T.; Noro, S.; Kubo, T. *Chem. & Pharm. Bulletin* **1979**, *27*, 2921-2926.

(14) Zerfa, M.; Sajjadi, S.; Brooks, B. W. *Coll. & Surf. A: Physicochem. Eng. Aspects.* **1999**, *155*, 323-337.

(15) Kloet, J. V.; Schramm, L. L. *J. Surfactants & Detergents* **2002**, *5*, 19-24.

(16) Li, L.; Lechuga-Ballesteros, D.; Szkudlarek, B.; Rodriguez-Hornedo, N. *J. Coll & Interf. Sci.* **1994**, *168*, 8-14.

(17) Weissbuch, I.; Addadi, L.; Berkovitch-Yellin, Z.; Gati, E.; Weinstein, S.; Lahav, M.; Leiserowitz, L. *J. Am. Chem. Soc.* **1983**, *105*, 6615.

(18) Lahav, M.; Landau, E. M.; Grayer Wolf, S.; Levanon, L.; Leiserowitz, L.; Sagiv, J. *J. Am. Chem. Soc.* **1989**, *111*, 1436-1445.

(19) Addadi, L.; Berkovitch-Yellin, Z.; Weissbuch, I.; Lahav, M.; Leiserowitz, L. *Top. Stereochem.* **1986**, *16*, 1.

(20) Weissbuch, I.; Berfeld, M.; Bouwman, W.; Kjaer, K.; Als-Nielsen, J.; Lahav, M.; Leiserowitz, L. *J. Am. Chem. Soc.* **1997**, *119*, 933-942.

(21) Kahlweit, M.; Strey, R.; Busse, G. *J. Phys. Chem* **1991**, *95*, 5344-5352.

(22) Guo, R.; Tianqing, L.; Weili, Y. *Langmuir* **1999**, *15*, 624-630.

(23) Kahlweit, M.; Strey, R.; Busse, G. *J. Phys. Chem.* **1991**, *95*, 5344-5352.

(24) Barbetta, A.; Cameron, N. R. *Macromol.* **2004**, *37*, 3202-3213.

(25) Cooper, S. J. *CrystEngComm* **2001**, *56*, 1-4.

(26) Lee, A. Y.; Ulman, A.; Myerson, A. S. *Langmuir*, **2002**, *18*, 5886-5898.

(27) Addadi, L.; Berkovitch-Yellin, Z.; Weissbuch, I.; van Mil, J.; Shimon, L. J. W.; Lahav, M.; Leiserwitz, L. *Ang. Chem. Int. Ed.* **1985**, *24*, 466-485.

Chapter 6

Conclusions and Further Work

6.1 Thesis Conclusions

This thesis has investigated crystallisation induced at the air-water planar interface and the oil-water interface in emulsions, by a variety of analytical techniques. The crystallisation of DL-aspartic acid under nylon 6 spread films at the air-water interface was studied by neutron reflectivity, external-reflection FTIR and optical microscopy and showed the gradual incorporation of crystalline DL-aspartic acid within, rather than beneath the nylon 6 spread film, which results in a swelling of the nylon 6 layer. Neutron reflectivity studies showed the composition of this swollen nylon 6 surface layer at 8 hours to be over 50% by volume DL-aspartic acid. This is substantially higher than the percentage coverage determined by optical microscopy, which was judged as 1 - 5%. This discrepancy can only be explained by the presence of sub-visible crystalline DL-aspartic acid nuclei, which was confirmed by the observation of ER-FTIR bands attributed to DL-aspartic acid, in areas of the sample where no DL-aspartic acid was visible to the naked eye. Reversible accumulation of nylon 6 film material around the growing DL-aspartic acid crystals was observed, and is consistent with the mutual attraction between the film and DL-aspartic acid material inhibiting the growth of the latter.

The studies of calcium carbonate crystallisation induced by octadecanoic acid monolayers at moderate surface pressure (~ 10 – 15 mN/m) show a change in monolayer structure with time. At the moderate surface pressures, both GIXD and ER-FTIR show evidence for the tilting of the octadecanoic acid hydrocarbon chain towards the surface normal. For the more compressed monolayers, GIXD showed no differences upon calcium carbonate crystallisation, but greater initial packing of the monolayer could have prohibited this and the monolayer would already be in an optimal state for crystallisation. Polyacrylic acid was added to the subphase to encourage

growth of the amorphous calcium carbonate precursor, which resulted in the formation of a rigid film. In this case, no differences in octadecanoic acid monolayer were observed by GIXD or ER-FTIR, suggesting the amorphous film can form without rearrangement of the monolayer. Lower concentrations of PAA might enable transformation of this amorphous film to crystalline calcite on a timescale commensurate with the X-ray diffraction studies. Both the DL-aspartic acid and calcium carbonate planar studies show a rearrangement of the substrate during solute crystallisation, which provides a useful insight into the processes that control crystallisation.

Crystallisation in emulsions is also studied, which is not well understood. Extended classical nucleation theory predicts that crystallisation will proceed more favourably at a concave interface, provided enough crystallising molecules are present to form the critical nucleus. At the other extreme, a convex interface induces crystallisation less efficiently, whereas a planar surface is somewhere between the convex and concave cases. The ice crystallisation studies outlined here for a convex system, i.e. an oil-in-water emulsion, confirm convex crystallisation is less efficient than the planar case and demonstrate that crystallisation is less efficient for the smaller droplet sizes than the large droplet sizes where the interface is more planar.

The ice crystallisation was induced by 1-heptacosanol adsorbed at the oil-water interface. Despite a higher interfacial density of this long chain alcohol, high curvature systems displayed a poorer ice nucleating ability. This is attributed to the larger critical nucleus size predicted by classical nucleation theory, coupled with the inability of 1-heptacosanol to pack into a structure that will induce ice nucleation. These ice data show that while classical nucleation theory correctly predicts a poorer nucleating ability for convex systems than a planar interface, the effect of the curved system is more detrimental to crystal nucleation than classical nucleation theory predicts.

The crystallisation of glycine was investigated at concave and convex interfaces and is believed to be induced by the surfactant, but did not offer the range of droplet sizes required to offer a systematic study as shown for the ice. The glycine crystallisation did appear to proceed less efficiently for the concave case, but the onset of crystallisation was difficult to assess. The poor nucleating ability of systems at or close to the phase

inversion boundary was particularly interesting. These emulsion crystallisation studies go some way to understanding crystallisation induced at curved interfaces, but of all the studies detailed in this thesis, it provides the greatest opportunity for further studies.

6.2 Suggestions for Further Work

In terms of understanding crystallisation processes and developing classical nucleation theory, the emulsion crystallisation studies offer the greatest scope for further work. The ice studies in this thesis show the effect of a convex interface; systematic studies of a similar concave nature would assess further the extent to which classical nucleation theory adequately models crystallisation for these systems. Solute crystallisation in the Brij 30 stabilised convex system detailed here should also be possible, especially if a solute of lower solubility is identified that does not perturb the range of droplet sizes attainable.

The glycine crystallisation studies have failed to give a systematic study on interfacial curvature effects as was hoped, because only large (~ 20 – 80 μm) droplet sizes could be developed. This system was not therefore suited to determining the validity of classical nucleation theory to emulsion crystallisation, even though concave and convex systems (oil-in-water and water-in-oil, respectively) were successfully made. All efforts to modify the glycine polymorph by use of soluble and insoluble additives were also unsuccessful, although the use of octanoic acid as the oil phase did promote α-phase crystallisation along with β-phase induced by the Span surfactant. These glycine studies were somewhat limited by the very high water solubility of glycine (28.5 g per 100 g water), which results in high viscosity of the aqueous phase, hence emulsion manufacture is challenging. Less soluble amino acids, e.g. leucine and valine (solubility ~ 4 g and 8 g in 100g water, respectively) are sufficiently water soluble, but not so soluble that the water viscosity will be detrimentally affected. Equally, the Tween surfactants could be explored further with aqueous glycine, if the supersaturation is reduced so that spontaneous crystallisation is not observed.

The planar study of DL-aspartic acid crystallisation under nylon 6 requires no further work, but the use of neutron reflectivity in these studies was relatively successful and is

likely to be attempted by other scientists. Another crystallising system such as the calcium carbonate under octadecanoic acid might provide a more predictable result, but nonetheless an interesting insight into the growth of different layers, perhaps even coupled with an increase in thickness of the monolayer as the hydrocarbon chain tilt occurs during the crystallisation process. Crystallisation of discrete layers under the monolayer, if it occurs, will result in discrete maxima and minima by neutron reflectivity, resulting in data that are simpler to model fit than the smooth curves that result for a diffuse layer as in the nylon 6/DL-aspartic acid crystallisation studies detailed here.

The GIXD studies of calcium carbonate crystallisation could be studied at much lower PAA concentration, which might result in subsequent transformation to calcite or metastable crystalline forms. These studies were particularly challenging given the age of the Daresbury synchrotron, which results in limited beam lifetime and frequent beam collapse/involuntary beam dumping. A great deal of extra beamtime was generously awarded to compensate for these difficulties, but lengthy experiments were impossible. Modern GIXD facilities with a more reliable beam and, in particular, an area detector, could potentially give enhanced data for this crystallising system.